An Innovative Fabrication Route to Machining Micro-Tensile Specimens Using Plasma-Focused Ion Beam and Femtosecond Laser Ablation and Investigation of the Size Effect Phenomenon Through Mechanical Testing of Fabricated Single Crystal Copper Micro-Tensile Specimens

By: Betty Huang

A Thesis Submitted to the School of Graduate Studies in Partial Fulfillment of the Requirements for the Degree of Master of Applied Science

M.A.Sc. Thesis- Betty Huang

McMaster University- Material Science and Engineering

MASTER OF APPLIED SCIENCE (2023) McMaster University

(Material Science and Engineering) Hamilton, Ontario

TITLE: An Innovative Fabrication Route to Machining Micro-Tensile Specimens Using Plasma-Focused Ion Beam and Femtosecond Laser Ablation and Investigation of the Size Effect Phenomenon Through Mechanical Testing of Fabricated Single Crystal Copper Micro-Tensile Specimens

AUTHOR: Betty Huang, M.A.Sc. 2nd Year (McMaster University)

SUPERVISOR: Dr. Nabil Bassim

Committee Member: Dr. David Wilkinson

I. Lay Abstract

Hydro-Quebec is an energy utilities company that operates the design of Francis hydro-turbines to supply hydroelectric power across the province of Quebec. The hydro-turbines have an expected service life of 70 years. Unfortunately, the turbines can get replaced by new ones prior to reaching half of its service life, due to the development of severe fatigue crack growth in the primary components of the turbines. A solution proposed by the researchers at the Hydro-Quebec Research Institute (IREQ) is to determine a linkage between the turbine's steel's microstructure and the mechanical behaviour of the turbine steels. Deformation of the material starts at the microstructure level, where dislocations glide through the material lattice, causing both reversible (elastic) and irreversible (plastic) deformation. Therefore, a solution was proposed by the researchers at IREQ to create computational models of the steel microstructure to predict the deformation of the steel's microstructure. Being able to predict the deformation mechanisms through the simulation models of the microstructures allows for engineers at Hydro-Quebec to schedule regular maintenance of the turbines more efficiently and provide metallurgists the knowledge on what is occurring at the microstructure level and what can be done to improve the chemical and physical composition of the steel. To develop the digital twin models, experimental data must be collected through mechanical testing of miniature mechanical test specimens of the turbine steels. The mechanical properties of the single phases and interphase interface specimens are fed into the models as building blocks to building a microstructure map of the turbine steels. Micro-tension testing of micro-tensile specimen provides direct information about the material's mechanical properties. In this work, a reliable and efficient fabrication route for micro-tensile specimens was developed for the purpose of extracting mechanical properties of single phase and interphase interface turbine steel specimens using focused ion beam (FIB) and femtosecond laser machining.

II. Abstract

This project is in collaboration with the Hydro-Quebec Research Institute (IREQ) and the Canadian Centre for Electron Microscopy (CCEM) on the mechanical test performance of miniature-scale micro-tensile specimens. The objective of the thesis project is to create an efficient and reliable fabrication route for producing micro-tensile specimens and to validate the accuracy of a newly custom-built micro-tensile bench at IREQ. The fabrication techniques developed and outlined in this thesis use the underlying fundamental physical mechanisms of secondary electron microscopy (SEM), focused-ion beam (FIB), and the femtosecond (fs)-laser machining for producing optimal quality micro-tensile specimens.

The mechanical testing of the specimens is geared towards studying the localized deformation occurring in the microstructure when the size of the specimen only limits a number of grains and grain boundaries in order to target the specific detailed measurement of the mechanical behaviour of individual grains and interfaces. The goal for creating an optimal fabrication route for micro-tensile specimens is to carry out micro-mechanical testing of the primary turbine steels of 415 martensitic stainless steel used in the manufacture of Francis turbine components at Hydro-Quebec. The mechanical testing of single phase and interphase interface 415 steel micro-tensile specimens are considered building blocks to developing digital twin models of the steel microstructure. The experimental data from the mechanical tests would be fed into the crystal plasticity finite element models (CPFEM) that are currently being developed by researchers at IREQ. With the development of digital twin models, engineers at IREQ would be able to predict crack initiation at the microstructure level (prior to crack propagation into macro-scale cracks) by observing the evolution of the grain's crystallographic orientation and morphology, as well as deformation mechanisms such as martensite formation and twinning produced from localized induced strains in the microstructure. In addition, self-organized dislocation processes such as dislocation nucleation and dislocation escape through the free surface can also be studied using the CPFEM models for size-limited mechanical deformation behaviour of miniature-scale mechanical test specimens.

The fabrication routes studied in this thesis project use the combination of the fs-laser and plasma focused ion beam (PFIB) to machine the micro-tensile specimens. (100) single crystal copper was the ideal material chosen to validate the accuracy of the micro-tensile bench and quality of the fs-laser-machined tensile specimens, due to its ductile nature and well-characterized properties studied in literature. A mechanical size effect was studied for single crystal copper specimens with different gauge thicknesses. It was observed from the micro-tension testing that the strength of the specimens increased with decreasing gauge thickness occurring in the size-limited tensile gauges. In addition, it was determined there was negligible differences in the size effect seen between the PFIB-machined copper micro-tensile specimens and the fs-laser-machined micro-tensile specimens, demonstrating that the fs-laser is a reliable machining route for the micro-tensile specimens.

X-ray computed tomography was used to validate the correct geometry of the machined gauge section produced from an innovative gauge thinning method adopted from IREQ's research collaborator, Dr. Robert Wheeler. As well, finite-element analysis (FEA) was performed to determine the deformation behaviour under both linear-elastic and non-linear elastoplastic conditions of (100) copper and 415 steel models simulated in pure tension, prior to the fabrication of the micro-tensile specimens, respectively.

Furthermore, significant progress has been made towards targeting martensite grains in the 415-steel microstructure using electron backscattered diffraction (EBSD) analysis to produce single crystal and interphase interface micro-tensile specimens. A workflow towards grain targeting using EBSD analysis has been developed, as well as for the relocation of grains using reference fiducial marks for future fabrication of the single crystal and interphase interface 415 micro-tensile specimens.

III. Acknowledgements

There are many people that I would like to thank for their support and contributions to my research work during my time as a master's student. First off, I would like to give a big thank you to Nabil Bassim as my supervising professor for reaching out to me during my 4th year as an undergraduate student during my capstone course with the opportunity to fulfill a graduate degree working in microscopy and metallurgy. In addition, he has helped me to overcome obstacles and provided insightful solutions and ideas to my research.

I would like to thank David Wilkinson as my committee member, who provided me the tools and knowledge on the mechanical behaviour of materials (through his MATLS 751 course) that allowed me to analyze the results of the mechanical tests.

I would like to give great appreciation to my PHD candidate colleague, Mehdi Mosayehbi for his ongoing support and help on many aspects of the project. We both started our degrees at the same time with both of our degree projects being complimentary to one another. We worked together with our research collaborators at IREQ on a larger-scale metallurgy project. The characterization of turbine steels from Mehdi's 3D reconstruction work using FIB and x-ray tomography provided me with the knowledge I needed to understand the microstructure of the steels at hand for the mechanical analysis of the micro-tensile specimens.

I would like to give thanks to the researchers at IREQ including Daniel Paquet, Pierre-Antony Deschênes, Laurent Tôn-Thât for allowing me to visit IREQ and perform micro-tensile tests in their lab space. As well, they provided time outside of their busy work schedules to discuss project updates and to conduct the mechanical tests, as well as train me to use their custom-built micro-tensile bench.

I would like to thank the staff and the people at the Canadian Centre for Electron Microscopy (CCEM) for their kind presence and allowing me to use their facility and microscopes. Specifically, I would like to thank Hui Yuan for his patience, technical support, and training on the Helios 5 UXe G4 Dual Beam Plasma FIB SEM microscope. As well, I would like to thank

Travis Casagrande for producing the fs-laser-machined micro-tensile specimens for my work on the Zeiss Crossbeam 350 and for providing solutions with the help of Sabaa Rashid on the quality of the specimens. I would also like to thank Brian Langelier, Chris Butcher, and Jhoynner Martinez for access to the CCEM, training on sample preparation, EBSD analysis, and operation of the SEM microscopes.

I would like to also thank everyone from the Bassim Research Group for their companionship, ongoing support, and encouragement throughout the duration of my masters.

As well, I would like to thank everyone from the Faculty of Engineering for allowing me to be part of the innovative research and McMaster University for the letting me grow in my academic career as a graduate student.

IV. Table of Figures

V. Table of Tables

VI. List of Abbreviations and Symbols

Focused ion beam (FIB)

Plasma-focused ion beam (PFIB)

Femtosecond laser (fs-laser)

Electrical discharge machining (EDM)

Liquid metal ion source (LMIS)

Secondary ion mass spectroscopy (SIMS)

Integrated computational material engineering (ICME)

Micro-electronic mechanical system (MEMS)

Single crystal (SC)

Bicrystal (BC)

Secondary-electron-microscopy (SEM)

Grain boundary (GB)

Electron backscatter diffraction (EBSD)

Region of interest (ROI)

Energy-dispersive X-ray spectroscopy (EDS)

Laser-induced periodic surface structures (LIPSS)

Heat-affected zone (HAZ)

Material removal rate (MRR)

Transmission electron microscope (TEM)

Crystal plasticity finite element modelling (CPFEM)

Finite-element analysis (FEA)

Inverse pole figure (IPF)

X-ray computed tomography (x-ray CT)

Ultimate tensile strength (UTS)

Yield Stress (YS)

Bright-field imaging (BF)

Dark-field imaging (DF)

Equation Terms:

Equation 1: $\tau_{CRRS} = \sigma_y cos\varphi cos\lambda$

Yield strength, σ_y

Angle between the loading axis and normal direction to the slip, φ

Angle between the loading axis and slip direction, λ

Critically resolved shear stress, T_{CRSS}

Equation 2: $\sigma_y = \sigma_0 + \frac{k_y}{\sqrt{d}}$

Stress in the material prior to dislocation motion, σ_0

Grain size diameter, d

Material strengthening coefficient, k_y

Equation 3: $f_{Ga} = \frac{1}{\propto \mu}$

Fraction of implanted gallium ions in the material for every number of incoming ions, f_{Ga}

Fraction of ions that remain in the material after sputtering, α

Ion sputter yield, μ

Equation 4: $\Delta T = \frac{P}{\pi a k}$

Ion beam power, P

Material thermal conductivity, k

Ion beam diameter, a

Temperature rise, ΔT

Equation 5: $\beta_r = \frac{n_i}{E_\perp}$

Effective beam brightness β_r

Ion plasma density, n_i

Mean thermal ion energy, $E_\perp$

Equation 6: $\frac{P_{Xe^2}}{2m_{Xe}} = \frac{P_{Ga^2}}{2m_{Ga}}$

Mass of xenon ions, m_{Xe}

Mass of gallium ions, m_{Ga}

Momentum of xenon ions, P_{Xe}

Momentum of gallium ions, P_{Ga}

Equation 7:
$$\begin{bmatrix}\sigma_1\\ \sigma_2\\ \sigma_3\\ \sigma_4\\ \sigma_5\\ \sigma_6\end{bmatrix} = \begin{bmatrix}c_{11} & c_{12} & c_{12} & 0 & 0 & 0\\ c_{12} & c_{11} & c_{12} & 0 & 0 & 0\\ c_{12} & c_{12} & c_{11} & 0 & 0 & 0\\ 0 & 0 & 0 & c_{44} & 0 & 0\\ 0 & 0 & 0 & 0 & c_{44} & 0\\ 0 & 0 & 0 & 0 & 0 & c_{44}\end{bmatrix}\begin{bmatrix}\varepsilon_1\\ \varepsilon_2\\ \varepsilon_3\\ \varepsilon_4\\ \varepsilon_5\\ \varepsilon_6\end{bmatrix}$$

c_{11}, c_{12}, and c_{44} are the stiffness constants for an anisotropic material.

Equation 8:
$$\begin{bmatrix}\sigma_1\\ \sigma_2\\ \sigma_3\\ \sigma_4\\ \sigma_5\\ \sigma_6\end{bmatrix} = \begin{bmatrix}168.4 & 121.4 & 121.4 & 0 & 0 & 0\\ 121.4 & 168.4 & 121.4 & 0 & 0 & 0\\ 121.4 & 121.4 & 168.4 & 0 & 0 & 0\\ 0 & 0 & 0 & 75.4 & 0 & 0\\ 0 & 0 & 0 & 0 & 75.4 & 0\\ 0 & 0 & 0 & 0 & 0 & 75.4\end{bmatrix}\begin{bmatrix}\varepsilon_1\\ \varepsilon_2\\ \varepsilon_3\\ \varepsilon_4\\ \varepsilon_5\\ \varepsilon_6\end{bmatrix}$$

$c_{11} = 168.4., c_{12} = 121.4$, and $c_{44} = 75.4$ are the stiffness constants for (100) copper.

Equation 9: $\sigma = E\varepsilon$ (Hooke's Law)

Strain, ε

Stress, σ

Young's Modulus, E

Equation 10: $\sigma_{true} = \sigma_{eng}(1 + \varepsilon_{eng})$

True stress, σ_{true}

Engineering stress, σ_{eng}

Engineering strain, ε_{eng}

Equation 11: $\varepsilon_{true} = ln\ (1 + \varepsilon_{eng})$

True strain, ε_{true}

Engineering strain, ε_{eng}

Equation 12: $\varepsilon_{elastic} = \frac{\sigma_{true}}{E}$

True elastic strain, $\varepsilon_{elastic}$

True stress, σ_{true}

Young's Modulus, E

Equation 13: $\varepsilon_{plastic} = \epsilon_{total} - \varepsilon_{elastic}$

True plastic strain, $\varepsilon_{plastic}$

Total strain, ϵ_{total}

True elastic strain, $\varepsilon_{elastic}$

Equation 14: $Head\ displacement\ \left(\frac{\mu m}{s}\right) = l_0\dot{\gamma}$

Initial gauge length, l_0

Strain rate, $\dot{\gamma}$

Equation 15: $True\ gauge\ width = \frac{Measured\ Gauge\ Width}{Cos(\theta)}$

θ is the degrees is the tilt off-set from the 52-degrees milling configuration of the PFIB stage used during the gauge thinning process

Equation 16: $m = cos\phi cos\lambda$

The angle between the loading direction and the slip direction, ϕ

The angle between the loading direction and slip plane normal, λ

Equation 17: $T_{CRSS} = m\sigma_Y$

Schmid factor, m

Critically resolved shear stress, T_{CRSS}

Yield stress, σ_Y

Equation 18: $d_0 = \sqrt{(Y_{0,2} - Y_{0,1})^2 + (X_{0,2} - X_{0,1})^2}$

$Y_{0,1}$, $Y_{0,2}$, $X_{0,1}$ and $X_{0,2}$ represents the initial X and Y positions of the two points on the fiducial marks, respectively.

Initial distance between two reference fiducial marks on the gauge surface, d_o

Equation 19: $\varepsilon = \frac{\Delta d}{d_0} = \frac{d - d_0}{d_0} = \frac{\sqrt{(Y_2 - Y_1)^2 + (X_2 - X_1)^2} - d_0}{d_0}$

X_1 and X_2 represents the X-positions of two points taken at the fiducial marks

Y_1 and Y_2 represents the Y-positions of the two points taken at the fiducial marks

Elongation of the gauge length, Δd

Instantaneous distance between the two points at the fiducial marks, d

VII. Declaration of Academic Achievement

I declare that the research discussed this thesis is of my own authentic work. The contributions from individuals to the research project are listed below:

Travis Casagrande who operated the Zeiss Crossbeam 350 to produce the fs-laser-machined copper and 415 martensitic stainless steel micro- tensile specimen cutouts.

Mehdi Mosayehbi who operated the Nikon M2 225 KV CT Scanner to produce X-ray computer tomography scans of the fs-laser-machined 415 micro-tensile specimens. In addition, Mehdi also performed image processing of the specimens using Dragonfly software.

Pierre-Antony Deschênes and Laurent Tôn-Thât who performed the micro-tension tests on the fabricated copper and 415 micro-tensile specimens using the custom-built micro-tensile bench at the Hydro-Quebec Research Center (IREQ). In addition, Pierre-Antony and Laurent trained me to use the MD software and micro-tensile bench to perform mechanical testing of the tensile specimens.

Daniel Paquet who gave a crash course on finite-element analysis (FEA) during my summer 2022 off-campus research period at IREQ.

David Wilkinson who provided me with the course knowledge on the mechanical behaviour of material from my enrollment in the MATLS 751 course.

Table of Contents

VIII. Chapter 1: Literature Review: The Size Effect in Miniature-Sized Mechanical Test Specimens

1.1. Introduction: What is the Size Effect Phenomena?

When the dimensions of material specimens enter the micro-scale and nanoscale regime, the mechanical behaviour of the specimens differ from that of the bulk material. A size effect is exhibited by the dimensional limits imposed on the material specimen during plastic deformation. The internal dislocation structure of the size-limited specimen possesses a size dependency that changes the specimen's deformation process due to the discretization of the failure mechanism based on pre-existing defects, as opposed to mechanical behaviour for an ensemble of defects at the macro-scale. For micro-electronic mechanical system (MEMS) applications, the structures of the miniature electronic circuit components are susceptible to defects and fractures as much as macro-scale structures do such as turbines and aircrafts [[*1*]. Therefore, it is important to study the deformation of material specimens at the nano and micro-size regime. In addition, the extrapolation of miniature-scale specimens' mechanical properties can be used to develop integrated computational material engineering (ICME) models of bulk scale materials, which can be used to predict the behaviour of fatigue crack growth and initiation in bulk structures before they occur [2]. In literature, mechanical testing of miniature specimens through experimental and computational methods have been performed to determine the existence of size dependent deformation processes. When specimen dimensions reach the size of dislocations sources (such as Frank-Read sources) in the sub-micron regime, a shortage of dislocations are contained within the volume size, and the deformation processes becomes dependent on the size and the number of dislocations. The starvation of dislocations in the internal structure causes nucleation events and multiplication of dislocations to occur [3].

Size effect experiments have been typically performed in singe crystal (SC) materials in literature, due to the periodic nature of having a single-orientated lattice structure. Single crystal materials are free from grain boundaries. Therefore, dislocations motion is only hindered by point, line, and planar defects that exist in the crystal lattice. In addition, bicrystal (BC) material specimens have also been fabricated to determine the mechanical size effects of the specimens. BC materials consist of only two grains in the material structure, where a single GB separates two differently orientated grains. Grains in the microstructure are often targeted to seek out the two grains of interest for machining the BC specimens for mechanical testing. In addition, due to the high fraction o the GB within the BC specimen, the GB plays an important role in the mediation of dislocation processes.

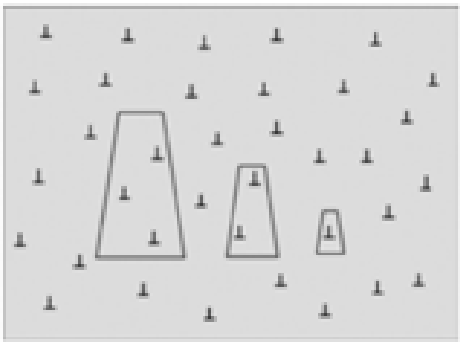

Figure 1: Schematic showing the influence of dimensional limitations of single crystal material specimens on the number of dislocations contained inside the internal structure. The diagram exhibits a decreasing dislocation density with decreasing specimen dimensions [[*4*].

As the dimensions of micro and nano-sized material specimens decreases, the number of dislocations contained within the specimen volumes also decreases, as depicted by the schematic in Figure 1 [[4]. The limited number of dislocations and dislocation interactions causes negligible work-hardening behaviour exhibited by miniature-scale material specimens. The evolution from bulk mechanical behaviour to size-limited deformation behaviour could be seen through short strain bursts resulting from the pile-up of dislocations near the free-surface [3]. With the help of secondary-electron-microscopy (SEM), in-situ micro and nano mechanical testing can be performed. The presence of parallel slip glides can be observed and analyzed during micro-compression and micro-tensile testing of the material specimens, as seen in Figure 2 and Figure 3, by *Uchic et al. (2004)* and *Kihara et al., (2015)*, respectively [3] [5].

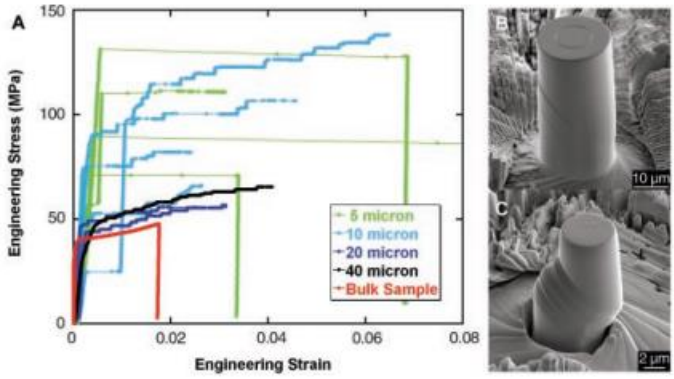

Figure 2: SEM image of compressed deformed pure <134> Ni micro-pillars of diameters 10 µm and 2 µm (right image) and the corresponding stress-strain curves for all deformed pillars of various diameter sizes and of bulk <134> Ni [3].

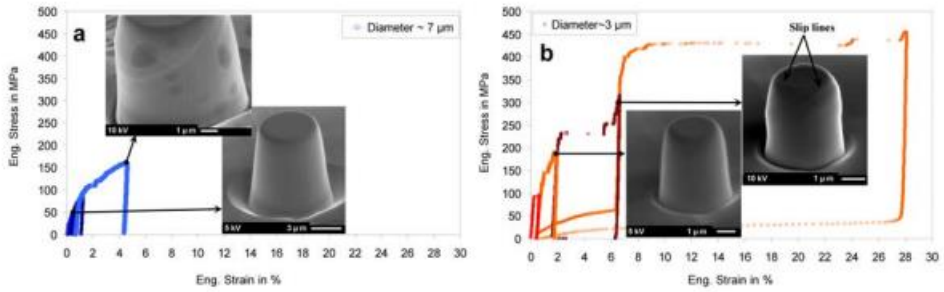

Figure 3: Corresponding stress-strain curves showing plastic deformation behavior of SC Ni micro-compression pillars of diameters (a) 7-µm and (b) 3-µm [16].

1.2. Different Mechanical Testing Methods

Each type of micro-mechanical test method has their benefits and drawbacks for investigating the size effect in materials. When fabricating micro-mechanical test specimens, it is important to have accurate alignment and quality-machined specimens for mechanical testing [5] [6]. When the dimensions of material specimens reach the micro and nanoscale regime, mechanical test specimens become significantly more sensitive to stress concentrations, mechanical deflection, and misalignments during testing. For example, micro-compression pillars with high aspect ratios (gauge length to side length) are prone to buckling failures under compression loading [5]. In addition, misalignments of micro-tensile specimens to the tensile axis during testing can cause bending stresses at certain areas of the gauge length, inducing strain gradients composed of geometrically necessary dislocations (GNDs), seen through computational modelling of SCs by *Deshpande et al. (2005)* [6]. GND strain gradient can also be induced in micro and nano-indentation testing, resulting to a higher measured hardness than that of bulk-scale indentation sizes [7][8][[9]. Therefore, it is important to have a reliable fabrication route for producing miniature-scale mechanical test specimens for investigating the size effect. Common fabrication routes include ion milling performed using the FIB, electro-chemical etching, photolithography, and femto-second laser machining [5] [10] [11]. In this report, different micro-mechanical test methods performed in literature to determine the existence of the size effect phenomenon in miniature SC and BC material specimens will be discussed.

As will be mentioned in Chapter 3 on fs-laser applications for machining micro-mechanical test specimens, micro-tensile testing is a common mechanical test method used to obtain direct stress-strain data from uniaxial tensile loading. The testing method is suitable for over a wide range of materials including metals, ceramics, and polymers. Tensile testing provides the ability to observe the fracture behaviour of materials through observation of the fracture surface, while other mechanical testing methods cannot [12]. Although, drawbacks to performing micro-tensile testing include high sensitivity to misalignment of the specimen when material specimens are pulled in the tensile direction. Even very small misalignment angles (from a few to less than 1 degrees) during tensile loading can cause bending and shearing stresses imposed on the specimen, resulting in the development of strain gradients and high stresses exhibited by the specimen than expected from pure uniaxial tensile testing [13].In

addition, there can also be challenges to machining high-quality miniature-sized tensile specimens (that are free from machining artifacts such as curtaining) when using conventional machining methods such as the FIB. In addition, complications that can also arise from the machining process is possible tapering of the gauge section, stress concentrations originating from reduced sections of the tensile specimens, ion damage from FIB machining, and heat-effect zones from thermal processes such as electrical discharge machining (EDM) and laser-machining [14]. Although, one of the benefits to the testing method is that there is versatility in the tensile geometries that can be produced. In size effect experiments seen in literature using micro-tensile testing, researchers have developed micro-tensile geometries from dog-bone shaped tensile specimens to needle-shaped tensile specimens, where each geometry that cater to the specific deformation mechanism that is being studied. [[5] [10] [13].

1.3. Strain Gradients

During micro-tensile testing, off-axis rotation and displacement away from the tensile loading axis is often constrained to perform pure one-dimensional uniaxial straining of micro-tensile specimens. To investigate the effects of constraining rotation at the ends of micro-tensile specimens, finite-strain dislocation simulations of SCs of various width sizes were performed by Deshpande *et al., (2005)* [6]. The crystals were strained in pure uniaxial tension under constrained and unconstrained conditions of rotational movement in the tensile axis. The models were developed to mimic tensile grips used to pull miniature SC tensile specimens. From the simulation results, the constrained specimens of various widths exhibited a strong Bauschinger Effect, as seen by the stress-strain curves in Figure 4. When the specimens were loaded and then unloaded, a hysteretic shape for was observed in the stress-strain curves of crystals of various width sizes. Plastic yielding and high flow stresses were seen in the reverse direction, resulting in a linear decrease in stress against the corresponding strain. Upon loading, elastic stress is built up at the ends of the constrained SCs. This Bauschinger effect was due to the release of stored elastic energy during unloading of the crystal. For the unconstrained specimens, a weak Bauschinger effect was observed, where no significant release of elastic energy was present, and approximately the same stress magnitude was observed during reverse loading of specimen (no hysteresis was present in the stress-strain curves for the SCs of the same width sizes as the constrained SCs).

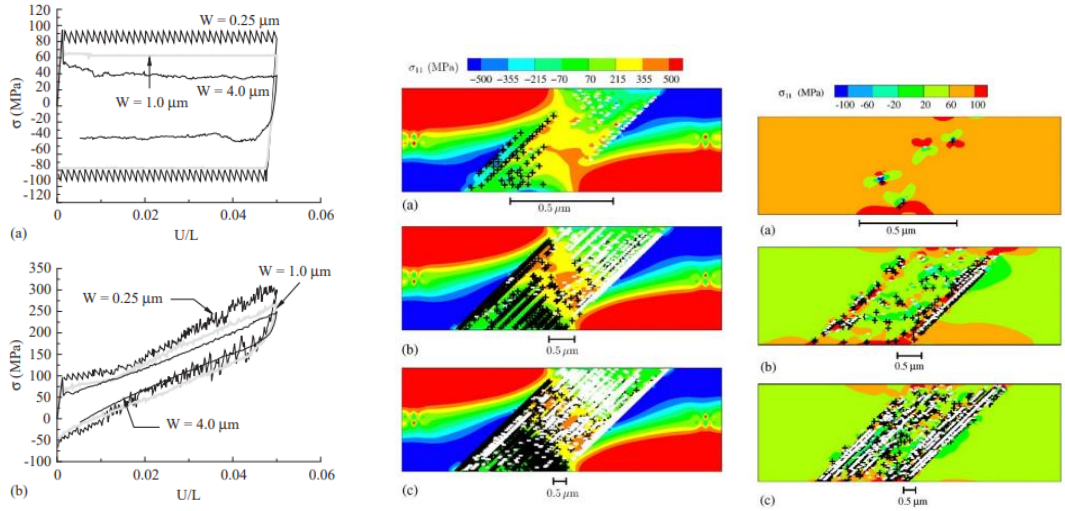

Figure 4: Stress-strain curves of a single crystal modelled under constrained and unconstrained conditions for rotation of the tensile axis. Under uniaxial tensile loading, a strong Bauschinger effect is exhibited by the constrained single crystal (top left image). Model of constrained single crystal showed pileup of GNDs in distinct slips bands (middle image). Dislocations are more uniformly distributed in the unconstrained SC model of the same corresponding width size as the constrained SC model (left image) [12].

In addition, a weak size dependence was seen for the constrained specimens, as the average dislocation density is significantly higher (due to the strain gradient caused by the constrained ends) compared to that of the unconstrained specimens. For the unconstrained specimens, the dislocation density is seen to decrease with decreasing specimen size, due to the increase dislocation-escapes at the free surface. The dislocation density was also seen to increase with decreasing specimen width size for the constrained specimens, and this was suggested to be the result of bending stresses induced when rotation of tensile axis is constrained. The bending stresses cause a build-up of GNDs. The dislocation density of GNDs increased with decreasing specimen width. The GND strain gradient was visible in the constrained SC models in the shape of kink-like-bands, as seen in the top right image of Figure 4 [12].

1.4. Effect of Anisotropy

The effect of crystal anisotropy on the deformation behavior of miniature SC specimens becomes more significant as the size of the specimens decreases. When the dimensions of SC material specimens decrease, dislocation motion becomes more directionally dependent. In a size effect study performed by *Kihara et al., (2015),* the effect of anisotropy on the deformation process of SC nickel micro-tensile specimens was investigated [13]. In the study, the dog bone-shaped nickel micro-tensile specimens were fabricated and mechanically tested from two different crystallographic directions of nickel (<111> and <223>, respectively). For the study, the specimens had a square gauge cross-section of 7.5 µm x7.5 µm and a gauge length of 40 µm respectively. The specimens were fabricated using a Ga+ FIB and pulled using tensile grippers made from a diamond indenter, as seen in Figure 5. Specimens were tested under a constant displacement rate of 0.1 µm/s. From the mechanical testing, all specimens exhibited load drops prior to 5% strain, due to the initiation of slip glides.

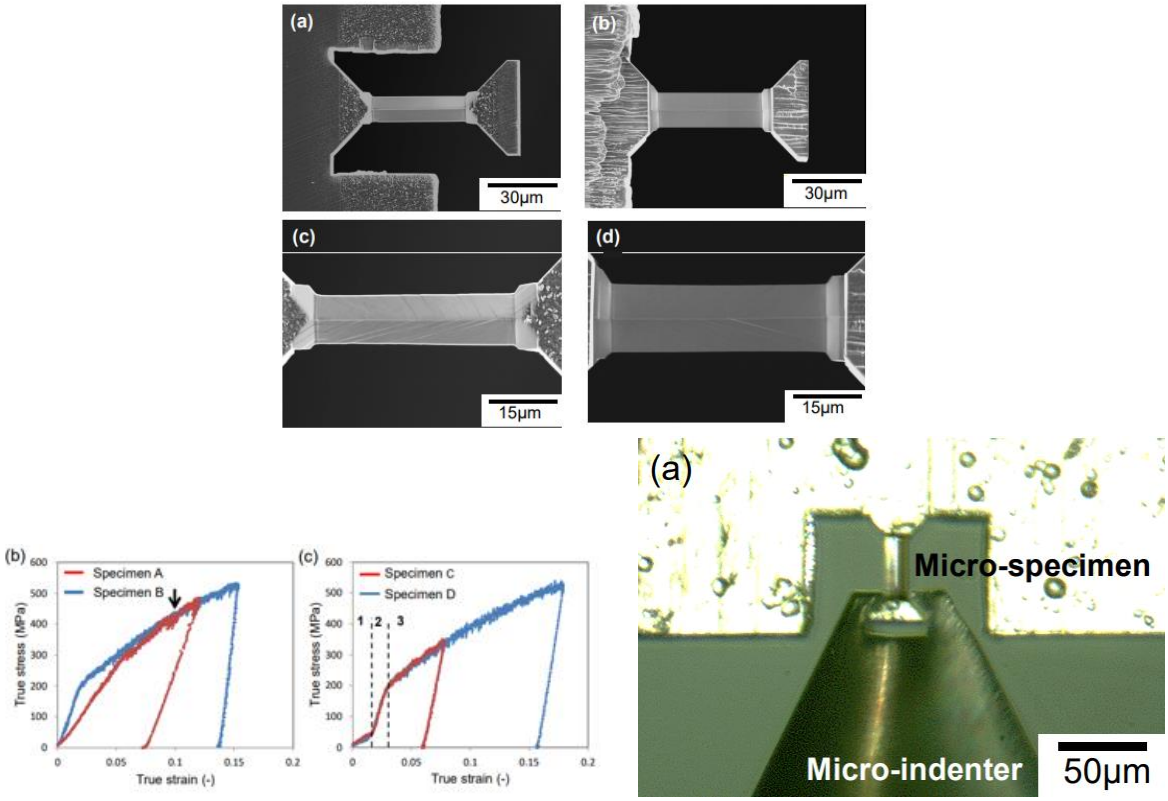

Figure 5: Tensile testing of bone shaped single crystal Ni micro-tensile specimens with crystal orientation of (111) as specimens a and b and crystal orientation of (223) as specimens c and d tested at different elongations, and images (b) and (c) shows their corresponding true stress-strain curves. Bottom right image shows tungsten gripper used to pull the corresponding tensile specimens [13].

The yield strength and Schmid factor for each specimen were calculated using the critical resolve stress equation shown in Equation 1, where τ_{CRRS} is the critically resolved shear stress, σ_y is the yield strength, φ is the angle between the loading axis and normal direction to the slip plane, and λ is the angle between the loading axis and slip direction [13]. From the results of the stress-strain curves for the (223) Ni tensile specimen (seen in the bottom-left image in Figure 5), three stages of plastic deformation were identified. In the first stage, initiation of single slip glide occurred at a high Schmid factor value, resulting to a low tensile strength at the beginning of source activation. In stage two, strain hardening is initiated as multiple slip events occur at the same plane, as slip systems at lower Schmid factors are activated. In stage three, cross-slip occurs as multiple slip from other slip planes combine with one another, (resulting to a lower work hardening rate at stage three). The results of the stress-strain curves for the (111) Ni tensile specimens exhibited only two stages of plastic deformation. Multiple slip glide deformation occurred in the initial stage of loading, due to similar Schmid factor values for slip systems (having a narrow distribution in the Schmid factor). In the second stage, cross-slip from multiple slip planes occurred, (similar to the stage three deformation process of the (223) Ni tensile specimens). Therefore, from the study by *Kihara et al., (2015),* the deformed SC nickel micro-tensile specimens strained having different crystallographic orientations, respectively, showed

that crystal anisotropy has an effect on number of activated slip planes for miniature-scale SC material specimens.

$$\tau_{CRRS} = \sigma_y cos\varphi cos\lambda \qquad \text{Equation 1}$$

1.5. Effect of Specimen Geometry

Kiener et al., (2008) developed an innovative machining method for fabricating micro-tensile specimens that allowed for precise alignment of the specimen along the tensile loading axis during mechanical testing [[5]. To study the effects of specimen aspect ratio on the deformation mechanism of size-limited material specimens, needle-shaped SC copper micro-tensile specimens were produced using the FIB [5]. The micro- tensile specimens were also developed to remove the limitations of high-aspect ratio testing of specimens that existed with micro-compression testing. The specimens were machined with aspect ratios (gauge length to side length) ranging from 1:1 to 13.5:1, respectively. Custom-machined tungsten grippers were used to pull the specimens for different sized tensile specimens. Each tensile gripper fit the head of each tensile specimen with precise accuracy consisting of a ±1 μm offset from tensile axis, as seen in image (b) of Figure 6. The head of each specimen also had a shoulder flank angle ranging from 45 degrees to 90 degrees. The SC copper specimens were machined in the <-234> direction (direction parallel to the tensile loading axis).

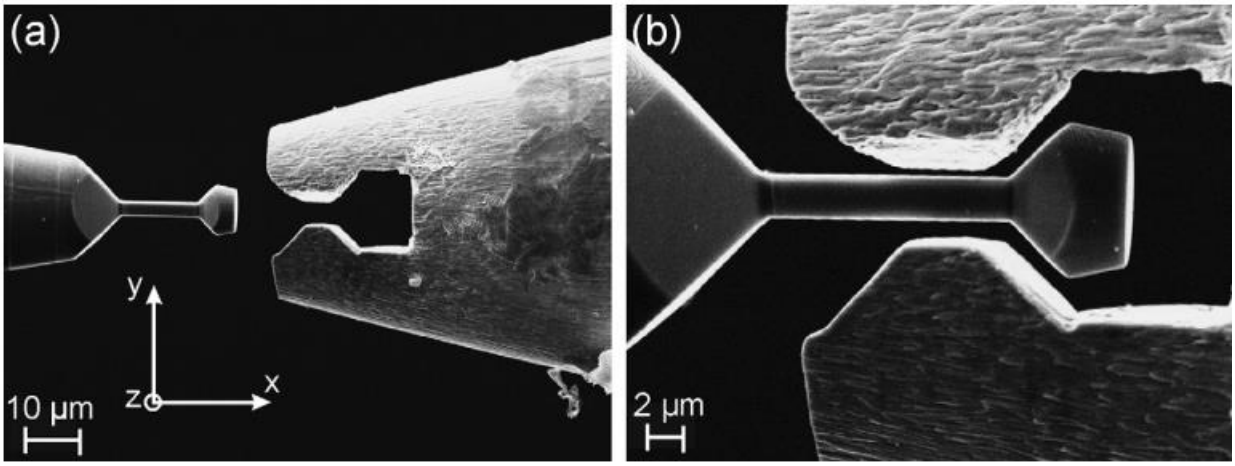

Figure 6: In-situ SEM images featuring micro-tensile testing of needle-shaped single crystal Cu tensile specimens using custom-machined tungsten grips for specimens of various aspect ratios [5].

Specimens with aspect ratios of 5:1 and higher showed low hardening rates. The 5:1 aspect ratio-specimens exhibited pure single slip deformation, which was observed and validated through SEM observations and 2D-EBSD scans of the gauge surface, respectively, as seen in Figure 7. In addition, no evident necking was observed on the specimen, validating the existence of pure single slip glide deformation. For single slip deformation to occur, a redistribution of local stress developed from a number of single slip sources must be activated. In addition, the flow stress in the single slip deformed specimen has a dependence on the Frank Read source size. The size of Frank Read sources can be split into two geometry types: a single-ended L-

ended dislocation and a full U-ended dislocation, as seen in the schematic of image (b) in Figure 8. Larger source sizes were seen for larger side length specimens. The initial U-mill dislocation will eventually become an L-mill dislocation through contact with the free surface. In addition, L-mills can also be introduced in the specimen initially from FIB milling. In addition, the Frank-Read sources can be characterized as screw or edge dislocations (each having different energies).

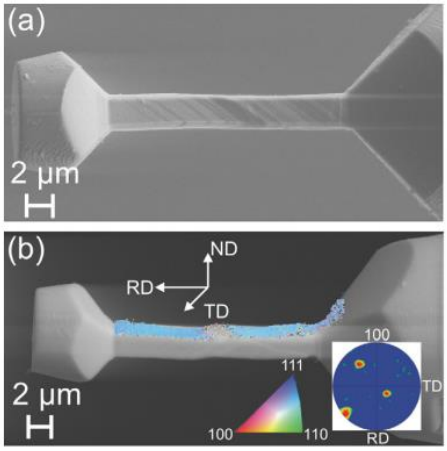

Figure 7: Pure single slip deformation seen in high aspect ratio- machined SC Cu micro-tensile specimens through SEM imaging (a) and EBSD mapping of gauge surface (b) [5].

For specimens with a low aspect ratio of 1:1, dislocation pileups occurred at the ends of the specimens. Higher flow stresses and significant hardening rates were observed for the low aspect ratio specimens compared to that of the high aspect ratio specimens due to the accumulation of dislocations at the ends of the tensile specimens. This is due to shear stresses imposed on the gauge section of the specimens. The short length of the gauge section confines the motion of free slip glide. Therefore, dislocations tend to enter the head of the specimens at a 45-degree angle (causing a build-up of dislocations at the ends of the specimens), as seen in Figure 8. In addition, depending on the angle of the inclined shoulder of the tensile specimen head, a higher number of dislocations in the dislocation pile up can lead to a higher shear stress for the specimen. For example, the 1:1 aspect ratio specimen machined with a 90 degrees flank end exhibited a higher flow stress and a larger number of dislocations of 85 MPa and 30 dislocations respectively, compared to that of the 45 degrees flank end specimen with a shear stress of 160 MPa and 15 dislocations in the pile up. Therefore, different deformation processes occur between specimens with low and high aspect ratios, respectively. Single slip deformation occurs in high aspect ratio specimens, causing pure single glides to exit the free surface and exhibit low flow stresses and no significant work-hardening, while in low aspect ratio specimens, the motion for slip glide is confined by the short gauge length of the tensile specimen, resulting to the build-up of dislocations at the ends of the specimens and high flow stresses and significant work-hardening of the tensile specimen [5].

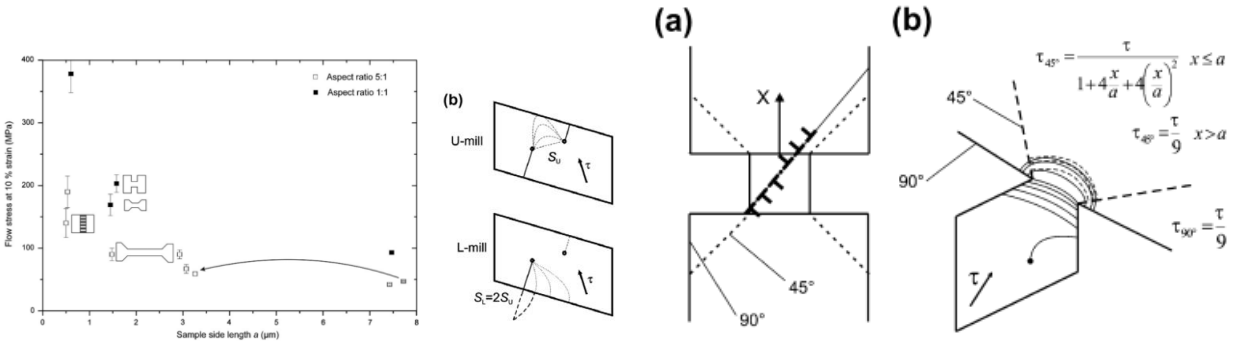

Figure 8: Scale chart showing the increase of flow stress at 10% strain with decreasing aspect ratio (left image). Generation of U-mill and L-milled structures of Frank Read sources in pure single slip deformation (middle image). Schematic of dislocation slip glide through tensile specimen with low 1:1 aspect ratio (right image) [5].

1.6. Role of the Grain Boundary in Miniature Bicrystal (BC) Specimens

Miniature bicrystal (BC) micro- compression pillars experiments have also been performed to determine the role of the GB on the size effect of two different orientated adjacent SCs. In theory, GBs create barriers for dislocation motion. According to the Hall-Petch theory, the strength of polycrystalline materials increases with decreasing grain size up to a certain extent. The yield strength σ_y, of a polycrystalline material can be calculated using the Hall-Petch equation, as seen in Equation *2*, where σ_0 is the stress in the material prior to dislocation motion, d is the grain size diameter, and k_y is the material's strengthening coefficient [15]. From the equation, the strength of the material can be described as inversely dependent on the square of the average grain size of the material. The Hall-Petch theory is valid for describing polycrystalline materials of the bulk scale, and it can also be used to describe the significant work hardening behaviour seen in micro-BC specimens [16]. In micro-BC specimens, additional deformation processes occur at the vicinity of the GB. As the dimensions of the specimen reaches the micron and nanoscale regime, the GB fraction is high in BC specimens. The GB has a size effect on the deformation process of the BC pillars when the GB fraction is high in the specimen. On the other hand, when the GB fraction is low in bulk BC specimens, the GB has a negligible size effect of the plastic deformation [17][18].

$$\sigma_y = \sigma_0 + \frac{k_y}{\sqrt{d}} \qquad \text{Equation 2}$$

Through recent years, a large scatter of experimental conclusions on the effects of the GB were reported in nano-indentation testing and micro and nano- compression testing of BC specimens [16]. For instance, the GB has the ability to strengthen the BC specimen by the impedance of dislocations near a twin grain boundary. On the other hand, the GB can also lower the strength of the specimen through GB mediated plasticity processes such as GB rotation and GB sliding, when the GB fraction is high in sub-micron and nanoscale-sized BC specimens. In addition, the misorientation angle along the loading axis between the two adjacent grains can

also determine the fatigue strength of the BC specimen. It has been reported by *Zhang et al., (2008) and Li et al., (2014)* that the resistance to fatigue crack growth is low in for high-angle GB BC specimens [19][20]. Also, twin boundaries can also affect the fatigue behaviour of the specimens as well, depending on their misorientation angles [17]. In this report, case studies of micro-BC compression experiments have neglected or minimized the GB effect in studying the size-dependent deformation mechanisms.

For the process of developing digital twin models through crystal plasticity finite element modelling (CPFEM) (discussed more in detail in Chapter 7) of the microstructure of polycrystalline materials, it is important to incorporate the role of the GB on the deformation behviour of the local microstructure. This can be done through the reapeatable process of fabricating and mechanically deforming bicrystal micro-mechanical test specimens. at the sub-micron level, the strength of the bicrystal specimens can be dependent on the angle of the GB and the fraction of GB contained within microstructure. The experimental data extracted from the bicrystal experiments can be used to validate the mechanical response of the digital twin models.

To machine bicrystal micro-mechanical test specimens, the process can be quite complex. The specimen containing only two grains of interest and one GB must be completely isolated from the rest of the microstructure. The application of electron backscattered diffraction (EBSD) analysis is a valuable tool for determining the grain orientation and providing an overview map of the grain size and grain morphology for targeting two adjacent grains for machining bicystal specimens. An efficient and repeatable sample preparation protocal of creating the bicrystal specimens can provide sufficient statistics on how the GB effects the deformation behaviour of sub-micron scale specimens. An recipe developed for targeting grains of interest (using EBSD and ion milling and deposition with the PFIB) for producing BC micro-tensile specimens out of the 415 maternsitic stainless steel (used for manufacturing hydro turbines at Hydro-Quebec) is discussed in Chapter 7.

IX. Chapter 2: Literature Review: Plasma-Focused Ion Beam

2.1. Introduction to Focused Ion Beam Microscopy

Focused ion beam microscopy is a widely used microscopy technique for manipulating miniature structures and material specimens. Ion collisions with the surface of the sample material allows for various materials interactions to occur. Based on the ion-specimen interactions, FIB can lead to the generation of secondary ions/electrons for imaging, the implantation of ions in a specimen can produce doping for producing semiconducting properties, and the sputtering of materials associated with the collision cascade between the specimen material and the incoming ion can occur. Ions-sample collisions can also induce plastic deformation, heat formation, and a damage layer in the specimen material.

The FIB becomes a powerful tool for characterizing a sample when coupled with a secondary electron microscope (SEM) in a dual-beam set-up (called a dual beam or FIB-SEM). Typically, the electron and ion beams are located at a 50–55-degree angle from one another, so analysis with one beam is tilted relative to the other. The system of a dual-beam set-up allows for the manipulation of a specimen's region of interest (ROI) using an ion beam and piezoelectric manipulator while providing immediate analysis of the specimen with the electron beam. To expand the materials characterization capabilities of dual-beam, additional detectors for performing energy-dispersive X-ray spectroscopy (EDS) analysis and electron backscatter diffraction (EBSD) allow for elemental analysis and crystallographic orientation information, respectively, about the specimen [21].

The removal of targeted material in a specimen (via ion milling) is dependent on the interactions between the ions and matter. The momentum of ions allows different collision cascade events to occur underneath the specimen surface. The liquid metal ion source (LMIS) as a Ga+ ion source has been used widely for FIB application due to the high brightness of the source. Gallium is also stable and non-volatile, making it an ideal ion source candidate for specimen manipulation. Gallium has a low melting temperature of 30 degrees Celsius and a low vapour pressure, which provides phase stability in a high vacuum chamber of the dual beam [21].

A LMIS ion source is typically stored in a reservoir. Heat is applied to the reservoir and tip to melt the liquid metal and cause it to flow down to a tungsten filament. Extraction of ions from the tip of the tungsten filament is performed using a high voltage to ionize the liquid drops coming out of the needle tip. The ion source is concentrated at the tip of the tungsten filament through opposing forces of a generated electric field from an electrode and high surface tension of the liquid ion sources in contact with the tungsten. As a result, the ion source is emitted from the tungsten filament in the shape of a Taylor cone with a tip cone radius of approximately 2 nm (and varies between 2-5 nm for different ion emission sources). Wien filters are used to separate the different ion charges and ion masses. Once the ion masses and ion charges are separated, the ion source travels down towards beam defining apertures, in which different ion currents are available depending on the beam size of the selected ion current used. Afterwards, the ion beam travels down fib column through a condenser lens to concentrate the ion beam to smaller probe size and through an objective lens, where focusing of the ion beam is performed on the specimen. The ion beam is rastered across the specimen using scanning coils to control the movement of the beam in the X and Y directions. Due to the larger mass of ions, electrostatic lenses are used to guide the ions down the ion column and to focus the ion beam. Beam deflection during rastering of the ion beam across the specimen is performed by deflecting the ion beam off axis using electromagnetic field plates and ions are collected by a Faraday cup to measure ion current [21].

To maintain a spherical beam shape, stigmation correctors are used in coincidence with focusing of the ion beam on the specimen. This prevents the stretching effect of the secondary ion image in the X and Y direction during analysis of the specimen. The ion spot size decreases with decreasing ion current used in the FIB. Ultimately, the smaller the beam diameter, the higher the spatial resolution and precision for milling and deposition of precursor gases.

Although, the cost of having a smaller beam size is compromised by longer milling times at lower ion currents. A perfectly small spherical beam size cannot be practical, due to the existence of spherical aberrations from the lenses of the FIB column. In addition, the intrinsic ion interaction during collision cascade events with the specimen also causes different ion interaction to occur, including redeposition of specimen material, heat-induced phase transformations, and deposition of ions in the specimen.

The set-up of a dual beam FIB-SEM system consists of an electron column with an incident angle normal to the specimen surface and an ion beam at an incident angle of 52 degrees from the normal of the specimen surface. A specimen holder holds the specimen in place on to the stage of the dual-beam chamber. The stage has the ability to move in the X, Y, and Z directions in the chamber. The stage can also be tilted and rotated to obtain to 52-degree ion configuration for milling and deposition, as well as other tilt and rotation angles for accessing detectors for different analysis of the specimen, including EBSD and EDS and secondary ion mass spectroscopy (SIMS). Prior to performing the appropriate analysis on the material specimen using the ion beam, initial focusing of the specimen is done to determine the region of interest (ROI) using the SEM. After the specimen is focused, the eucentric height is set for the specimen. The eucentric height is obtained by tilting the stage of the specimen up to the tilt angle that is required for the performance of the ion beam. When the specimen does not move laterally over a specified tilt angle range, the eucentric height is reached. Focusing at a high magnification and keeping track of a feature that is part of the specimen helps to determine a constant specimen height is achieved during tilting of the stage [21].

Precursor gases are often deposited on the surface of a specimen's ROI using either tungsten, platinum, carbon, or a combination of two or more of the gases. Depositions using precursor gases have been typically used in FIB applications to create protective caps or markers that can be used as references for sites of interest.

2.2. Solid-Ion Interactions

The range in which ions travel inside the specimen is dominated by the nuclear and electronic stopping power of the ions. In a journal article on advanced FIB applications by *Bassim et al. (2014),* the stopping power and range for five major ion sources for FIB ranging from smallest to largest ion mass (He+, Ne+, Ag+, Ga+, and Xe+) were simulated using stopping and range of ions in matter (SRIM) Monte Carlo simulations at 30 keV in silicon at a zero-degree incident angle [22]. From the SRIM simulations, it was observed that for the lighter ions such as He+, electronic stopping is the most dominant stopping mechanism in the collision cascade. The lateral straggle and penetration depth along beneath the surface of the material is significantly higher for He+ in silicon, compared to the heavier ions. Ions slowly lose their kinetic energy through inelastic collisions as they travel deeper beneath the specimen surface. The sputter yield for He+ is <<1, due to the strong electronic stopping power. Although, the low lateral straggle makes He+ a good candidate for high spatial resolution imaging and nano-milling of thin films [22]. For the collision cascades of the heavier ions (particularly Ga+ and Xe+) simulated, the lateral straggle in much lower, and nuclear stopping becomes the dominant

stopping power for the ions. The strong interaction between the ion and the nuclei provides a great momentum transfer for the ion as it travels through the depth of the specimen. This produces elastic collisions with atoms in the specimen. In turn, a lower loss in kinetic energy by the heavier ion's path in the specimen produces a significantly higher sputter yield than that of He+ ions. In addition, a higher probability for reflection and backscattering of ions is generated for heavier ions, resulting in a lower chance for ion implantation, compared to lighter atoms.

2.3. Ion Sputtering

Ion sputtering is caused by the bombardment of ions on the specimen material. The contact of the ions travelling at high kinetic energies on the specimens causes the breakage of atomic bonds, allowing for material to be milled away. The sputter yield is dependent on many factors, such as the crystallographic texture of the specimen material, incidence angle of the ion beam, the amount of material redeposition and rastering method of the ion beam. The sputter rate differs intrinsically for different polycrystalline materials, due to the degree of ion channeling through the crystal lattice structure. In Figure 9, the channelling contrast between two adjacent copper grain describes the different sputter rates between the two grains. The darker grain exhibits a shallower depth and lower sputter yield compared to the deeper grain with a bright contrast. The difference in the texture of the sputtered area between the two grains can also be due to the difference in anisotropic properties of the two grains. The difference in the closed pack crystal structure of the two adjacent grains can have an impact on the sputter yield between the two grain surfaces. In addition, the routine in which the ion beam is rastered across the specimen's ROI (whether through a single pass or multi-pass ion milling) can also dictate the amount of redeposition and quality of the milled area [21].

For example, in Figure 9, the slow rastering of the ion beam through a single pass milling of the copper area in the top image produced a deeper and more concave area with higher amounts of redeposited material, than for the area rastered at higher speeds through multiple passes, causing a shallower milled area. In addition, the sidewalls are more vertical in the multi-pass ring, due to the negligible amounts of redeposition.

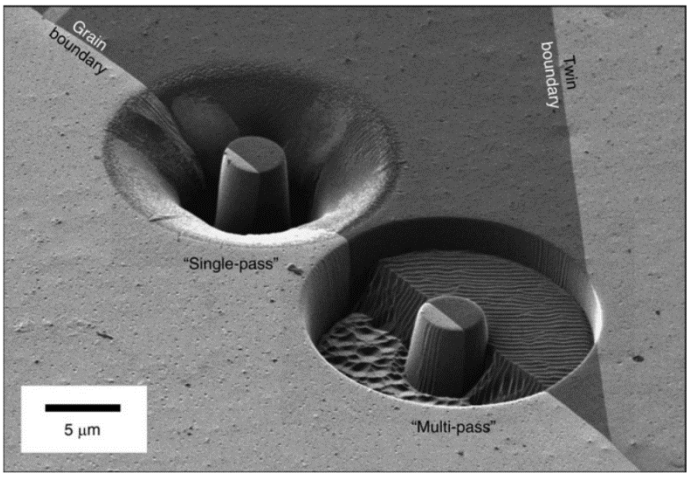

Figure 9: Rings milled using Ga+ FIB on the GB of copper. The ring milled using single pass tattering of ion beam is deeper with higher amounts of redepositions compared the shallower multi-pass-milled ring with lower amounts of redeposition [21].

2.4. Emission of Secondary Electrons from Collision Cascade

A collision cascade model is used to depict the solid-ion interactions occurring beneath the specimen surface, as shown by the schematic in Figure 10. When Ga+ ions are accelerated at a relatively high energy ranging from 5 kV to 30 kV and comes in contact with the specimen surface, the kinetic energy of the ions is decreased by the collision with atoms in the specimen. The distance that the ions travel inside the specimen is dependent on the specimen material, type of ion source, and the FIB process parameters used. There exists both elastic and inelastic collision cascade events. In an inelastic collision event, an ion travels a short distance inside the specimen near the surface. A transfer in energy occurs with the emission of a secondary electron from the specimen matter. The secondary electrons (SEs) are emitted from the interaction between the atoms and the ions, as the ions enter the specimen at high kinetic energies. The SEs (low energy valence electrons) are emitted from the first few atomic layers of the specimen, as atomic bonds get broken during the sputtering of the specimen. The ion-induced secondary electrons (ISEs) get collected by conventional secondary electron detectors (such as an Everhart Thornley detector).

The collision cascade model represents both inelastic and elastic collision events for the ion-specimen interactions during ion milling. In an elastic collision event, the ion travels deeper inside the specimen, causing displacement of atoms by the incident ion path through the specimen. The path created by the ions causes the sputtering of material away from the ion beam path. Ultimately, the Ga+ ions will lose all their kinetic energy and come to rest inside the specimen. The aftermath of elastic ion collisions inside the specimen are implantation of Ga+ ions, emission of secondary electrons and displacement of atoms (causing distortion in periodicity of the material's crystal lattice). In addition, heat is also produced from the breakage of atomic bonds during elastic collisions [21].

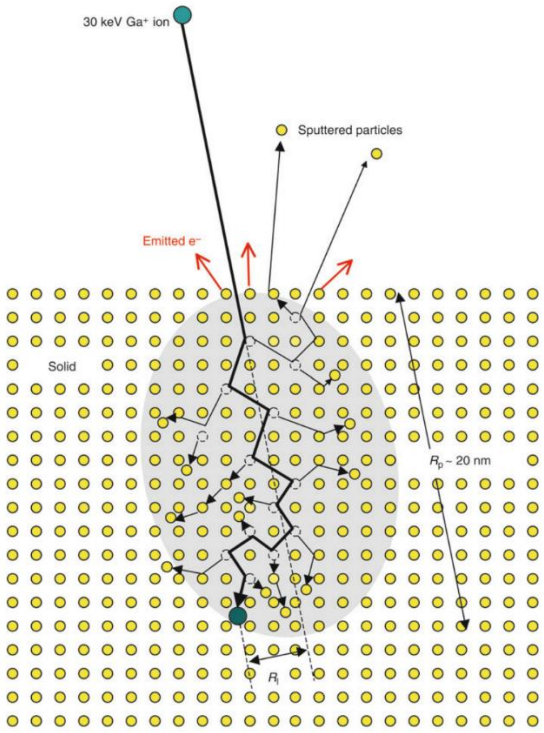

Figure 10: Collision cascade model of Ga+ ions showing different solid-ion interactions within the specimen [21].

During an inelastic collision event, energy of the sputter ion in the specimen gets lost to the electrons in the sample, resulting to both ionization of atoms and the emission of secondary electrons (in the form of radiation). Secondary electrons originating from the primary ion source are called ion-induced secondary electrons (ISEs). For Ga+ sourced FIBs, ISEs typically originate close from the surface, where approximately 1-10 electrons with energies less than 10 eV are emitted for ion voltages ranging from 5-20 kV [21]. ISEs provide contrast mechanisms and information about the specimen that differ from SE sources coming from a primary electron beam, as seen in the image contrasts between the two sources for polycrystalline copper in Figure 11 [21]. Secondary electrons coming from an ion beam provides material contrast describing the topology of the specimen can be obtaining during imaging, while an ion beam provides both material contrast and crystal contrast. ISEs produce channelling contrast during imaging the specimen. Channelling contrast is due to the ion beam hitting the specimens with grains having different crystallographic orientations. Therefore, SEs are also emitted from different trajectory angles. Crystal contrast is a beneficial imaging technique that can be used for obtaining information about the grain size and shape, and crystallographic texture of the microstructure. However, prolonged exposure of the ion beam on the specimen during imaging can cause ion beam damage such as Ga+ implantation and ion etching of the specimen.

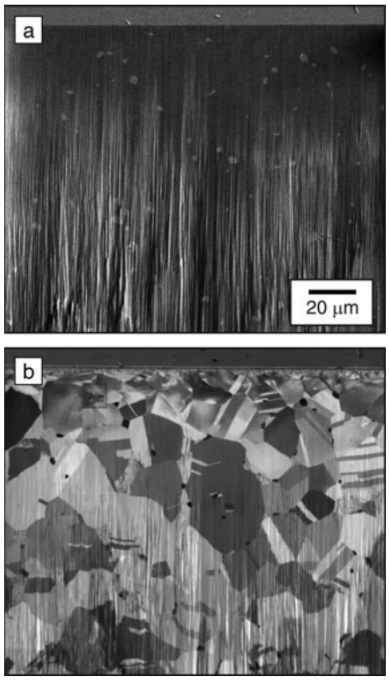

Figure 11: Shadow and curtaining effects seen for both secondary electron (top image) and ion-induced secondary electron (ISE) (bottom image) taken of polycrystalline copper, respectively [21].

Sputter redeposition often occurs as sputtered material gets redeposited into the region of interest. Therefore, the redeposited material must be removed by performing a seconding milling run of the ROI. Redeposition of material often causes non-vertical side walls to be cut. To obtain sharper cuts of the material, the specimen is often over-tilted to avoid redeposition.

The sputter yield is defined as the number of sputtered atoms per each incoming ion. Ways to increase sputter yield for the application of milling can include increasing the incidence angle of the ion beam. When the incident angle is increased, the number of sputtered atoms per collision cascade also increases. In addition, a larger number of reflected backscattered ions occur at increased incidence angles. It was shown through experimental and simulation work that a 75-80 degrees incidence angle gave the highest sputter yield for Ga+ ions in Si, SiO_2, W, and Au, respectively [23]. In addition, when the incidence angle increases, the ion range in the specimen also decreases. Although, the influence of the incidence angle on the ion range becomes less significant at lower ion energies.

2.5. Ga+ Ion Implantation

Ion implantation occurs during the sputter of material using Ga+ ion beams. When the ions travel inside the specimen, they lose kinetic energy as they travel deeper into the specimen. Thus, the ions come to rest in the specimen. The amount of ion implantation increases proportionally with ion flux (the number of ions per area per time) while limited by the removal of the top layer of material from sputtering. The maximum amount of Ga+ implantation is reached during steady

state of milling. Steady state occurs when the depth of the milled area is equal to the ion range of the given energy and incidence angle of the ion beam. At this point, the Ga+ concentration remains constant inside the specimen – i.e., the specimen mills as fast as it implants. However, this can be complicated by the presence of ion channeling - the steady state of Ga+ implantation can increase with increasing ion channelling in polycrystalline materials. Different analytical techniques have been used to quantify the amount of gallium inside the specimen. One of the best analysis techniques would be through chemical analysis using TEM Auger depth profiling of the targeted ion area of the specimen. The fraction of implanted gallium ions in the material for every number of incoming ions (f_{Ga}), can be determined using Equation 3, where α is the fraction of ions that remain in the material after sputtering, μ is the ion sputter yield, and αμ is the sputter yield per implanted ion. Gallium concentration in the material is expected to be lower when the sputter yield is higher during milling performed at glancing angles rather than at an angle normal to the sample surface. In some cases, implanted Ga+ ions can diffuse and react to the specimen, where both the material and gallium have the same crystal structure and similar channel effects [21].

$$f_{Ga} = \frac{1}{\propto \mu} \qquad \text{Equation 3}$$

To reduce surface damage due to ion implantation, it is best to mill using low ion energies with heavier ions such as Ga+, Ar+, and Xe+. When the ion energy is decreased, the ion interactions become more limited towards the specimen surface. Ion implantation can also be reduced by choosing a heavier ion source such as Xe+, due to the reduced ion range in the sample. Decreasing the ion voltage has a greater influence on reducing ion implantation than choosing a heavier ion source between Ga and Xe+ ion sources. In Figure 12, a non-linear decrease in ion range is observed with decreasing ion energy in Si for He+, Ne+, Ar+, Ga+, and Xe+ ion source with an 85 degrees incidence angle. This too is complicated by the fact that at low energies due to chromatic aberrations in the lensing system, it becomes difficult to produce a small beam diameter, and milling acquisition times become significant longer at lower ion energies [23].

The event of ion implantation can cause modification in the electronic properties of the material [24]. Therefore, the chemical and phase information about the specimen becomes misleading as it had been altered by the inclusion of Ga+ ions. For metals, the dislocation layer formed from the ion beam damage can induce localized residual stresses on the specimen surface such as the formation of high angle grain boundaries and twin structures [25].

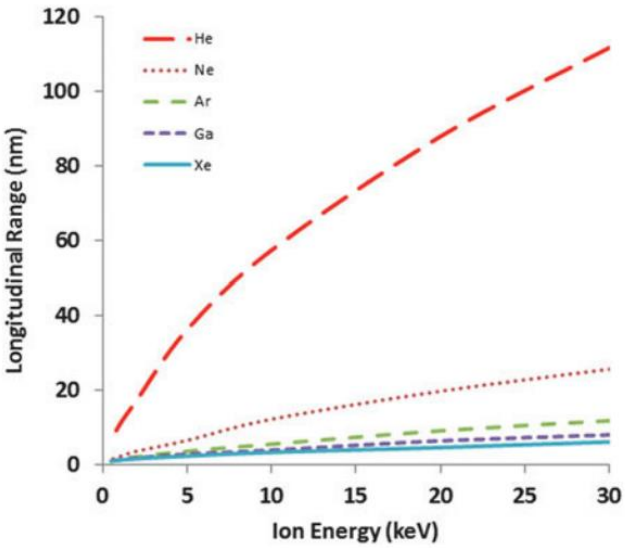

Figure 12: Depth of ions traveling beneath the surface of a silicon specimen at an incident angle of 85 degrees for different ion sources [23].

2.6. Ion Damage

Ion damage imposed on the material can be the result of ion sputtering at high ion doses and dose rates. When the ion dose is high, overlaps of collision cascades can occur, resulting to possible defect formation in the material. The type of ion damage varies with material and temperature. Amorphization is a common occurrence from ion damage. Covalently bonded materials such as Si, Ge, GaAs, and C (diamond) are especially susceptible to amorphization by ion exposure, due to the disorder imposed on highly directional bonded atoms. Although, for pure metals, amorphization does not occur as readily from high ion exposure, due to the non-directionality of the crystal bonds. Although, presumably, if there were contents of C, O, or Ga in the specimen, a thin amorphous layer would form on the surface. Other defects from ion exposure includes point defects, dislocation formation, grain recrystallization, morphology changes, and intermetallic phase formation. Copper is the most susceptible to point defects and dislocation loop formation during FIB milling (and this can be observed in copper TEM films) [26].

In some cases, temperature can also play a role on the ease of damage formation by ion exposure. At higher or lower temperatures, materials can decompose more readily, leading to the formation of amorphous layers and new phases. From ion sputtering, the kinetic energy of ions is almost entirely transferred as heat energy into the specimen, where a small fraction of the kinetic energy is dissipated as radiation or emitted to particles and defects in the specimen. The maximum temperature that the specimen can reach is dependent on the beam power P, specimen thermal conductivity, specimen geometry and contact to a heat reservoir. Without a reservoir, the temperature rise due to ion exposure can be approximated using Equation 4, where a is the ion beam diameter, k is the material's thermal conductivity, and P is the ion beam power. For poor thermal-conducting materials, the temperature rise can be significant (such as for polymers and

biological specimens of less than 0.3 W/mK), or it can be negligible for highly conductive materials (such as metals). In the case of high aspect ratio specimens (height-to-diameter), where the diameter of the specimen is approximately equal to that of the ion beam, the temperature rise given in Equation 4 is multiplied by the height-to-diameter ratio of the specimen. Therefore, it is important for specimens to be in good contact with a heat reservoir for dissipating away the heat induced by the ion beam, (especially for materials with low conductivity and high-aspect ratio geometries, such as a TEM lamella or nano-pillar sample).

$$\Delta T = \frac{P}{\pi a k} \qquad \text{Equation 4}$$

Curtaining is one of the most obvious FIB artifacts that occurs during ion milling. For example, curtaining commonly occurred from the fabrication process of the copper micro-tensile specimens as seen in Figure 68 under Chapter 5 of the freshly milled surface of the gauge section. Curtaining can also be seen obvious in both the SE and ISE images taken of the freshly milled surface of polycrystalline copper in Figure 11. Due to the influence of local topography of the specimen surface on the sputter yield, ripple patterns and shadow effects can be produced on the milled surface. Curtaining can occur when the specimen is made from more than one material, in which the sputter rate differs for each material. In addition, crystallographic orientation can also play a role on the milling rates for a polycrystalline material. *Qian et al., (2005)* determined that for micro-pillars milled out of two copper grains of differing orientation using Ga+ ions at 30 keV, the sputter yield and surface roughening between the grain boundary of the two grains was different due to the channelling effect of the two oriented grains [27]. Curtaining is commonly due to the quality of the prepared surface. Initial roughening or curvature from polishing procedures or from contamination and debris can cause different sputter yields during solid-ion interactions. This mechanism for curtaining is similar to that for different incident angles of the ion beam used to produce different sputter rates.

2.7. Plasma Ion Source

Other emerging FIB ion sources over the decades include inductively coupled plasma (ICP), laser-cooled low temperature ion sources (LoTIS) and gas field ionization sources (GFIS). ICP ion sources such as Xe+, Ar+, and O+ provide a wide range of currents available for milling. Thus, the plasma focused ion beam (PFIB) can be used to machine larger volume materials at a sufficiently more shorter milling time compared to that of the traditional gallium FIB. For ICP FIB microscopes, the plasma ion gas source is contained in a cylindrical dielectric plasma chamber, as seen in Figure 13. A radio frequency (RF) is fed to an antenna that is connected to both sides of the chamber. The RF is used to produce an induction field that accelerates electrons surrounding the plasma ion source. The electrons population becomes heated while the ion source remains at room temperature. In addition, a Faraday shield is placed around the antenna to reduce fluctuations in the electric field created by the voltage coming from the antenna, while maximizing the inductive coupling power of the antenna. Extraction electrodes located at the bottom of the cylindrical chamber are used to pull away the ions from the plasma. The large

extraction currents available for ICP chambers provide the ability to perform large volume material removals using milling currents that are 6-times higher than that of LMIS ion sources. For example, a relatively large difference in the top ion current available for milling is seen between LMIS-sourced Ga+ ions and ICP-sourced Xe+ ions of 60 nA and 2.5 µA, respectively. [22].

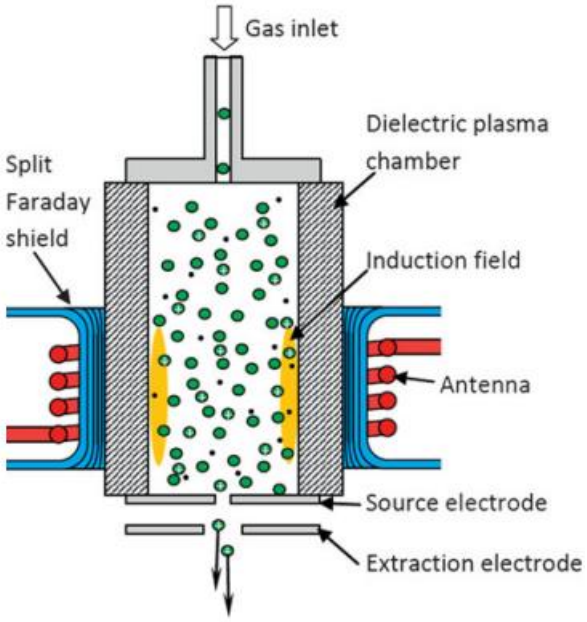

Figure 13: Schematic showing generation of ICP FIB source [22].

While the large density of the xenon plasma ion sources results in a lower brightness than that of light plasma ions such as helium, neon, and argon, the effective beam brightness of a xenon ion source is still higher than that of a Ga+ ion source when ion currents of 6nA and higher are used. The effective beam brightness β_r, can be defined by $\beta_r = \frac{n_i}{E_\perp}$ Equation 5, where n_i is the ion plasma density and $E_\perp$ is the mean thermal ion energy. From the proportionality statement, the objective of increasing the effective beam brightness of the ion source is to maximize the ion density and minimize the thermal energy of the ions. When the effective beam brightness is increased, the beam diameter of the xenon plasma source will be decreased. This increase in brightness can allow spatial resolution comparable to the Ga+ ion source at ion currents less than 6 nA. A typical xenon plasma ion source has an energy spread of 5eV. This energy spread originates from the distribution energy of ions in plasma source. It is assumed that 2eV of the total energy spread is contributed from the temporal modulations created by the plasma potential and the RF field. Advances in ICP FIB technology is aimed to reduce the energy spread of xenon ion sources to less than 3 eV by eliminating the temporal modulations in the plasma source.

$$\beta_r = \frac{n_i}{E_\perp} \qquad \text{Equation 5}$$

2.8. Advantages of Xe+ PFIB Over Ga+ FIB

One of the advantages of xenon-ion sourced FIBs is that the collision cascade is much shallower and narrower than that of Ga+ ion cascades. Therefore, the ion implantation yield for Xe+ ions is lower than that of Ga+ ions. In addition, it was seen by *Zhong et al., (2020*), in as prepared 99.9% pure Al TEM specimen through STEM BF and HAADF imaging of a grain boundary intersecting the surface of the Al foil, where an enrichment of Ga was seen on one side of the GB when prepared with a Ga+ FIB, while no detectable enrichment of Xe near the grain boundary of Al using Xe+ plasma-FIB milling. The segregation of Ga+ ions is due to the high concentration of vacancies formed from the energy exchange between Al atoms and Ga+ ions. Al atoms have the tendency to absorb the energy from ions, creating vacancy defects in the Al lattice during sputtering. Near the GB sites, the negative vacancy binding energy of Ga+ to Al is preferentially high, causing a large concentration of Ga+ ions to sit in the Al vacancy sites. In addition, as the incidence angle of the ion beam increases, a higher concentration of enriched Ga+ ions will be present near the surface of the Al specimen. The absence of Xe+ enriched ions near the GB for the PFIB-machined Al specimen, can be due to the inert nature of the noble gas, resulting too little to no obstruction of the Al crystal lattice [28].

In addition, it was seen by *Zhong et al. (2020)*, that the Xe+ amorphous layer formed on the Al specimen was slightly thinner than that of Ga+ amorphous layer when machined at 0.23 nA current and 30 keV voltage, correspondingly. *Kelley et al., (2013)*, observed a more distinctly larger amorphous layer formed by Ga+ ions than by Xe+ ions on silicon, in which the material amorphize much more easily than polycrystalline Al (due to the strong covalent binding of Si). In addition, it was observed through TEM BF imaging in Figure 14, that the Xe+ plasma-FIB machined Al specimen exhibited the lower amount of redeposition of sputtered material compared to the Ga+ FIB-machined Al specimen. From the TEM BF images, there was a negligible speckle contrast of the Xe+ ions in Al. In contrast, the speckle contrast appeared distinctively for Ga+ FIB-machined Al specimen as a result of Ga+ segregation and redeposition. This difference in redeposition for the two ion sources is due to the fact that Xe+ ions travel with a higher momentum than Ga+ ions. At the same voltage and charge dose of Ga+ and Xe+ ions respectively, the kinetic energy can be described using Equation *6*, where m_{Xe} and m_{Ga} are the momentums and P_{Xe} and P_{Ga} are the mass and momentum of the xenon and gallium ions, respectively. From Equation *6*, the difference in the ion momentums is determined to be $P_{Xe} = 1.37P_{Ga}$. The larger momentum of Xe+ ions help prevent the redeposition of sputtered material from coming in contact with the milled surface by pushing the milled material away from the milled surface [28].

$$\frac{P_{Xe^2}}{2m_{Xe}} = \frac{P_{Ga^2}}{2m_{Ga}} \qquad \text{Equation 6}$$

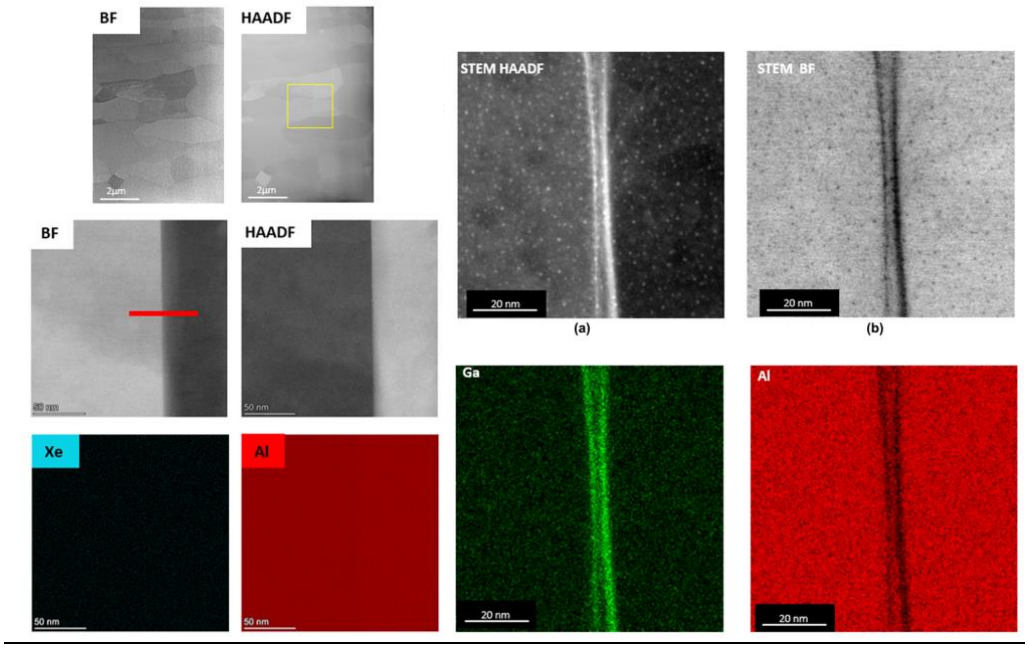

Figure 14: Bright field (BF) TEM imaging of a Al grain boundary showing speckle patterns of agglomeration and redeposition for gallium ion-sourced milled surface (on the right) and negligible agglomeration and redeposition for a xenon ion-source milled surface (on the left) [28].

2.9. Large Volume Material Removal Using PFIB

Xenon ions can mill larger volumes at six times the speed that of Ga+ ions [29]. As well, ion implantation can be significantly reduced using Xe+ ions due to the inert nature of the noble gas [25]. The dual beam plasma FIB/SEM (PFIB) can also mill at higher currents while reducing the thickness of an amorphous layer formed on the specimen surface. Although, the ion beam is only feasible for milling away the first few hundred of micron of material, before having to compensate long acquisition times to material removal. Therefore, the PFIB is a much more attractive choice to the conventional gallium FIB as the dual-beam component of the laser-FIB system.

X. Chapter 3: Literature Review: Femtosecond Laser-Machining

3.1. Introduction to Femtosecond Laser FIB-SEM System

The design of the femtosecond laser FIB/SEM (also know as the Tribeam by Thermo Fisher Scientific and the Crossbeam LaserFIB by ZEISS) has helped to eliminate the long machining times that exists with the dual beam plasma-FIB. The coupling of the femtosecond (f-laser) to a dual beam FIB-SEM microscope allows for high ablation rates and large volumes of material to be removed. The nature of the fs-laser's nonlinear optics (provided by its ultra-short pulse duration) mitigates the formation of a heat-affected zone (HAZ) on the surface of the laser-ablated material [29]. Therefore, miniature fabrication processes such as for large volume EBSD serial cross-sectioning, specimen preparation of micro and nano mechanical test specimens, TEM lamella lift out, integrated circuit defect analysis, and the manipulation of living cell substructures can be performed at a rapid rate with high quality precision. A schematic of the femtosecond laser (fs-laser) ablation of a material's cross-section using the ZEISS Crossbeam LaserFIB is shown in Figure 15.

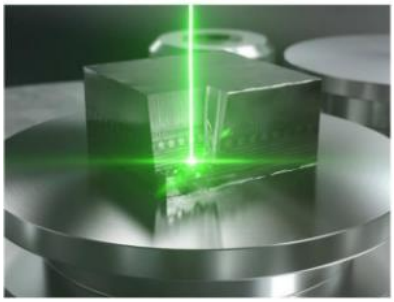

Figure 15: Femtosecond laser ablation of a metal specimen using the Zeiss LaserFIB *[29]*.

In Figure 17, a 3D chart shows the multi-modal capabilities of the triple beam system to fabricate large scale specimen volume sizes, high resolution imaging, and allow large areas of interest to be analyzed. Even for hard metals such as tungsten carbide, which would take around 86 days to mill a 100 μm^3 volume using a Ga+ FIB, the fs-laser can fabricate the same material volume in under a few hours [29]. Although, the benefits of the ion beam (in a separate dual beam chamber to the fs-laser chamber) in the triple beam set-up allows for low current ion milling of the roughly laser-machined surface by cleaning redeposited materials, surface roughness, and laser induced surface structures (LIPSS) from the laser-ablated surface. The quality of the milled surface can be dependent on the ion source, specimen material, and ion beam process parameters used, in terms of ion-induced damage, ion redeposition, ion implantation, and curtaining.

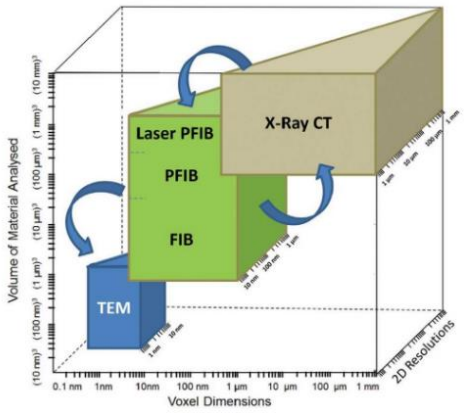

Figure 16: 3D chart of multimodal capabilities of combining different microscopy techniques together for high resolution imaging and large volume analysis [30].

As mentioned in the previous chapter, the dual beam FIB/SEM has been widely used for material analysis and applications such as energy dispersive spectroscopy (EDS) analysis, TEM specimen preparation of biological specimens, electron backscattered diffraction (EBSD) analysis, and atom probe tomography (APT) tip fabrication. Figure 17 shows a schematic of the dual beam set-up and milling in the bottom image, and the fs-laser's ablation process on the top image. In the dual beam chamber, the FIB column is oriented 52 degrees to the normal of the specimen surface and the SEM beam is located normal and directly below the specimen surface. In addition, the fs-laser is also positioned normal to the specimen surface in the laser's processing chamber. The dual beam chamber is often equipped with additional detectors that allow for complementary elemental and grain information about the specimen to be collected such as the Oxford EDS and EBSD detector. A gas injection system (GIS) is also added to the dual chamber, which allows for the deposition of certain platinum, tungsten, carbon, or a combination of gases onto the surface of the specimen for protection against the high current ion beam during milling or for the creation of fiducial marks to allow a reference position for the ion beam during milling. The SEM can be used to take immediate images of the specimen and analyze the current state of the specimen after deposition and removal of material by the FIB. For most commercially developed triple beam systems, a Ga+ FIB is equipped for the dual beam system.

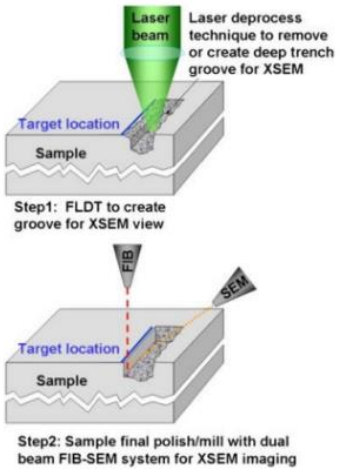

Figure 17: Schematic of the femtosecond laser ablation of a specimen cross-section (top image) and the final milling/polishing performed by the FIB and high-resolution analysis of the machined cross-section performed by the SEM (bottom image) [31].

3.2. Advantages of Fs-Laser FIB-SEM Setup

The set-up of the Laser-FIB-SEM system by Zeiss is accomplished by having two separate chambers for the operation of the fs-laser ablation process and the FIB-SEM system [29]. There are several benefits to isolating the laser ablation process from the high-resolution analysis performed by electron and ion beam columns. Firstly, more movement of the stage is available in both chambers of the laser and the FIB-SEM. There is less danger for the collision of beam columns, detectors, and lenses; large volume specimens can be inserted in the laser chamber and larger number of detectors can be placed in the dual beam chamber. Furthermore, the separation of the two units prevents ablated material from the laser process to encounter the components of the FIB-SEM and disrupt the high-resolution microscopy of the SEM and FIB columns. After the specimen has been machined by the fs-laser, it is transported from the laser chamber to the dual beam chamber via airlock under high vacuum. The dual chamber airlock system is shown in Figure 18 for the Zeiss LaserFIB.

Although the dual chamber has its advantages for liberating specimen size restrictions, there are still some downsides to the double chamber set-up. One of its disadvantages is the repetitive transport time of the specimen back to the laser chamber from the FIB-SEM chamber, which can cause an error of approximately 2µm when realigning the laser beam. Another disadvantage is that's the material debris from laser ablation accumulates near the beam's exit window before the laser gets focused and diverted through a series of mirrors. The accumulation of material can prevent the laser from working properly. Therefore, the ablated material must be periodically cleaned out of the laser chamber to prevent the build up of material debris, thus, effecting the operation of the components in the fs-laser unit [29].

Figure 18: Photo of the ZEISS Crossbeam [32].

3.3. Two-Phonon Phenomenon in Fs-Laser Machining

The fs- laser typically uses photons as its source of irradiation. The photon intensity for the fs-laser is typically $10^{13}\,\frac{W}{cm^2}$ to allow penetration of the laser beam through matter [33]. The photons are initially accelerated through a series of energy pulses (packets of photon energy). When the laser interacts with the specimen, an event of multiphoton ionization occurs where the energy of the photons gets absorbed by ionized electrons from the specimen. Afterwards, a plasma of high potential energy is created from the ionization of electrons, where the energy of from the laser is stored by the positively and negatively charged ions. The transfer of energy between an ionized electron and an unionized electron occurs at non-equilibrium conditions [33]. Afterwards, the broad beam of high energy gets attenuated to its preferred Gaussian beam spot size. The fs-laser's spot size diameter has a direct relation on the laser's ablation rate, which is dependent on multiple laser process parameters such as the laser's peak fluence, number of laser pulses per pass, and the pulse duration [34]. Peak fluence is described as the laser's highest flux value (the highest energy density through the laser beam's cross-sectional diameter) that can be obtained [35]. Fluence is usually expressed in units of $\frac{Joules}{cm^2}$. For example, in an experiment performed by *Chaja et al., (2016*), the fs-laser's ability to remove material was tested at different Gaussian beam spot sizes. It was discovered from the experiment that there is an optimal spot size for the highest material removal rate (MRR) exhibited by the fs-laser. Afterwards, the MRR starts to decrease with increasing spot size. A plot showing the relationship between the laser's ablation rate and peak fluence for different laser beam spot sizes can be seen in Figure 19 [36]. In addition, fs-laser ablation can be performed in the atmosphere of air because of the zero-charge photon laser source. Therefore, high-vacuum settings can be neglected in the fs-laser's processing chamber [29].

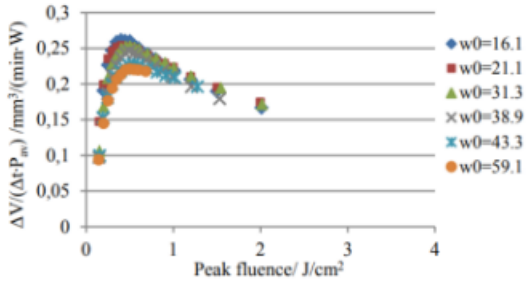

Figure 19: The effect of peak fluence on the material removal rate at different beam spot sizes (w0) (indicated by the different colours and shape data points) [36].

3.4. Laser-Induced Periodic Surface Structures (LIPSS)

The fs-laser still provides some limitations in creating an artifact-free laser-ablated surfaces. When the specimen is irradiated by the fs-laser, the formation of a laser-induced periodic surface structures (LIPSS) layer occurs on the freshly laser-machined surface. The development of LIPSS is due to the interaction of laser beam's polarized energy with the electronic properties of the specimen. On the specimen surface, there exists the oscillation movement of plasmons induced by the electric field of the incident laser beam when the beam's polarization is perpendicular the specimen surface. The constructive and destructive interference caused by the energy waves of the plasmons creates the LIPSS structure of a ripple pattern on the specimen surface with a depth ranging from tens to hundreds of nanometers depth beneath the surface [37]. The LIPSS structure becomes more distinct as the number of laser passes increases. The depth and structure morphology of the LIPSS layer can be controlled by the fs-laser's processing parameters such as spatial frequency, scanning direction, number of laser passes, and the thermal and vibrational frequencies of the environment in which the laser machining is performed in [38].

Figure 20 shows the structure of low spatial frequency LIPSS (LSFL) and high spatial frequency LIPSS (HSFL) formed on a titanium alloy. The structure of the HSFL is finer than that of the LSFL because of the short wavelength of the laser's light used for the ablation process [31]. Beneath the LIPSS layer, there can also exist other modified microstructure layers of the material induced by the fs-laser's irradiation. Firstly, right beneath the LIPSS layer can exist a layer of increased dislocation density in the microstructure. The thickness of dislocation layer is governed by the beam angle to the specimen surface and the Gaussian intensity distribution of the beam. The dislocation layer can be minimized by having the laser beam parallel to the specimen surface and using a low fluence configuration of the beam. At high fluence rates, the laser beam damage can cause the crystalline structure of certain polymers and metals to recrystallize. The heat dissipated onto the surface from the laser's long exposure time at high fluence can cause thermal deformation of the crystal lattice, resulting to an amorphous layer formed beneath the LIPSS layer. The amorphous layer can be minimized by using a low fluence laser beam at parallel configuration to the surface, as demonstrated on tungsten carbide by *Straw et al., (2014),* where the absence of an amorphous layer was observed by TEM diffraction

analysis [31]. The direction of the laser's polarized light source should be parallel to the surface of the specimen in order to have minimal surface substructures. This configuration allows for the laser beam to meet Gaussian intensity distribution where the laser can operate at its low fluence ablation threshold rate [39]. Figure 20 shows an SE image of the polarization of a laser beam parallel to the plane of incidence (specimen surface) compared to the polarization of a laser beam perpendicular to the specimen surface. When the beam's polarization deviates at angles away from the parallel configuration, the formation of the LIPSS structure becomes more pronounced.

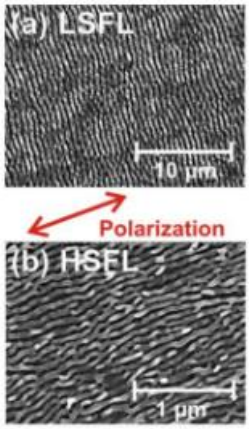

Figure 20: SEM image of the low spatial frequency LIPSS (LSFL) and high spatial frequency LIPSS structures of a titanium alloy [31].

3.5. Laser-Induced Heat-Affected Zone

The switch to laser machining has allowed for high material ablation rates for large volume material up to a few centimetres in dimensions. Therefore, for specimens that would take a few days, months, or even years to machine using FIB can be done in a span of few hours or minutes with the use of lasers. Laser beams travel through the material in a series of pulses and scans the region of interest using a line pattern through a series of laser passes until the section of the specimen has been machined through its desired depth. The nanosecond (ns)-laser, although possessing higher laser speeds than the fs-laser, causes an unavoidable heat-affected zone (HAZ) layer ion the subsurface during ablation [39]. To recover the original microstructure surface, the HAZ layer must be removed. This removal step can be time consuming and costly.

The formation of the HAZ layer is due to the long pulse duration (high fluence) of the ns-laser, which allows time for heat to transfer into the specimen during ablation. In contrast, the fs-laser has an ultra-short pulse duration threshold and a high peak power that prevents heat from the laser to dissipate into the specimen. The fs-laser consists of a low-fluence ablation threshold rate of approximately 1-2 $\frac{Joules}{cm^2}$ compared to the high fluence of 5-6 $\frac{Joules}{cm^2}$ of a ns-laser [39]. In turn, the formation of the HAZ layer can be mitigated by the athermal ablation behaviour of the fs-laser. In addition, high ablation rates can still be achieved using the fs-laser, leaving specimens with a smooth quality surface finish, and may not require further surface cleaning using the FIB [39]

3.6. Fs-Laser Applications to Machining Micro-Tensile Specimens

A current developing application using the fs-laser FIB-SEM system is the fabrication of specimens for micro-mechanical testing. One of the tasks for material researchers is to try to understand the root cause of micro-defects in a material that would potentially grow into large cracks visible to the naked eye. Information about the bulk mechanical behavior of materials is not enough to understand the cause of material defects without information on the localized intrinsic behaviour of the material at the microstructure level. Therefore, to understand the geometric size effects of a material under straining conditions, micromechanical tests such as tensile, compression, bending, and indentation testing need to be performed.

The measurement of strain for micro-mechanical specimens fabricated with the FIB is often constrained to studying only a few nanoscales to sub-micron sized grains at the local microstructure [40]. This is due to size limitations of fabricating mechanical test specimens using ion milling of either Ga+ or Xe+ ions. Acquisition time can be very long for milling out large specimens of more than a few hundred microns in dimensions. In addition, milling at high ion currents has its limitations as it can cause smoothed side edges, redeposition of ablated material, and an ion-induced damage layer on the milled specimen surface.

With the use of the fs-laser, it is possible to produce micromechanical test specimens with relatively large sizes (from a few microns to over 500 microns in dimensions) and with a significantly low acquisition time compared to the FIB [34]. An example of a fs-laser fabricated René 88DT steel specimen by Eastman et al. is shown in Figure 21 [41].

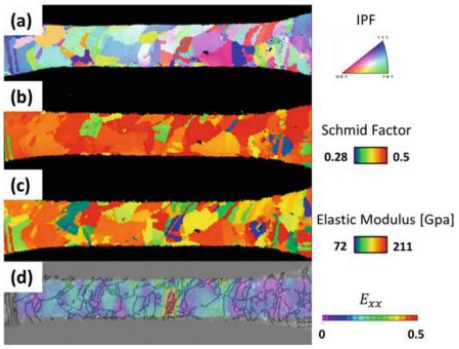

Figure 21: Digital image correlation (DIC) and overlay of EBSD orientation maps performed on FIB fabricated micro-tensile specimens of René 88DT steel [41].

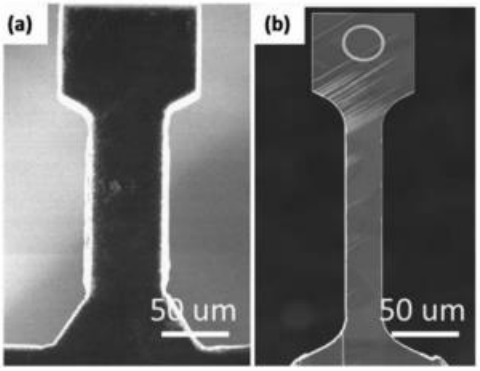

Figure 22: SEM images of fs-laser fabricated micro-tensile specimens for René 88DT [41].

Uniaxial micro-tensile specimens are one of the most versatile ways to study the strain behaviour of the local microstructure due to the direct information obtained about the specimen's mechanical behaviour from stress-strain curves. Micro-tensile testing also allows for the *mapping of localized strain along rectangular gauge length of the specimen using digital image* correlation (DIC) as shown in Figure 22 for the FIB fabricated René 88DT steel specimen [41].

In an experiment performed by *Voisin et al.*, (2017), the mass production of micro-tensile specimens from 15 µm aluminum and 10 µm thick copper foils were performed using a Clark MXR CPA fs-laser for in-situ TEM uniaxial tensile testing. The fs-laser process route of the micro-tensile specimen was compared with that using electropolishing. The length of the specimens needed to be short enough to fit in the TEM chamber, but also thick enough to allow for handling of the specimen during the in-situ micro-tensile testing procedure. In addition, a fast and repeatable fabrication process was desired to make multiple identical specimens in a reasonably short amount of time. Electropolishing being a reasonably cost-effective fabrication route than the FIB and avoids the consequences of ion implantation in the material, was chosen as one of the fabrication routes for creating the geometry of the micro-tensile specimens from the Al and Cu foils. Although, from the experiment, the electropolishing process created an uneven surface thickness of the specimens, resulting in the formation of cracks during straining at areas having a more transparent thickness, which would interfere with the study of twinning and high angle grain boundaries during EBSD analysis.

The alternative route uses the fs-laser to cut out the specimen geometry and the dual beam Ga+ ion FIB/SEM to clean the specimen at low ion currents. When laser-machining a 25 µm gauge groove in the micro-tensile specimen using the femtosecond laser, there existed the formation of substructures in nanoscale sized grains, which led to the observation of twin boundaries from the EBSD analysis conducted on the ablated specimen surface shown in Figure 23. *Voisin et al., (2017),* experimented in varying the process parameters of laser's energy and the number of laser passes to find the optimal configurations of the beam to prevent the formation of the substructures. The final specimen geometry consisting of a 2 mm length x 0.3 mm width x 75 µm gauge length is shown in Figure 24. The final geometry was created with a pulse energy of 4 µJ and a reduced number of laser passes from 12 to 6-10 using a copper foil thickness of 10 µm. From the chosen laser process parameters, no twinning in the local microstructure of the specimen was seen in the EBSD grain maps. Although, after laser

machining, transparent holes were formed in the gauge groove. Low current ion milling using a Ga+ FIB helped to increase the opening of the groove by milling away the uneven transparency. Because the specimen was machined with the fs-laser beam's polarization being perpendicular to the specimen surface, a 1 µm LIPSS layer that was formed. FIB ion milling was performed on the top and bottom surfaces of the specimen to remove the LIPSS layer.

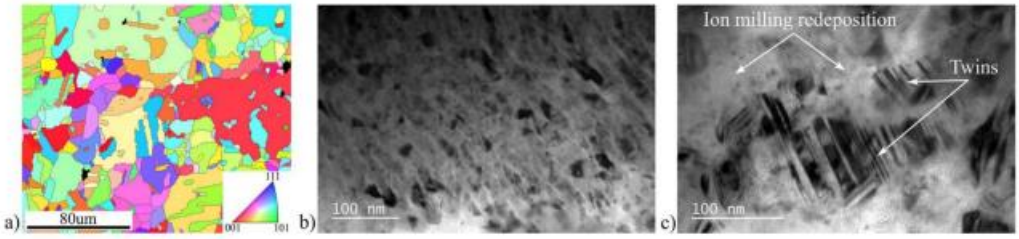

Figure 23: (a) EBSD map of a copper micro-tensile specimen exhibiting fs-laser-induced twinning in the microstructure, (b) and (c) TEM images showing ion milling redeposition of surrounding material and twin structures for the copper specimen fabricated at high laser pulse energies [40].

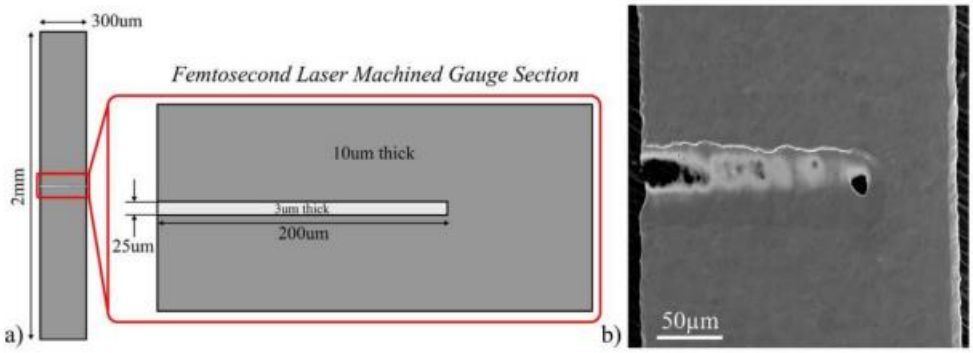

Figure 24: (a) dimensions of the final fs-laser fabricated copper micro-tensile TEM specimen, (b) SEM image of the copper micro-tensile specimen's gauge groove before FIB clean-up [40].

XI. Chapter 4: Finite-Element Modelling

4.1. Introduction to Finite-Element Analysis (FEA)

Finite-element (FE) models were created prior to the machining of the copper and 415 martensitic stainless steel micro-tensile specimens, respectively. The objective of performing finite element analysis (FEA) was to predict the behaviour of materials assigned to the micro-tensile specimen structure under various physical conditions. A gradual progression of developing simple 2D one-element models to complex 2D and 3D tensile specimen models is outlined in this section of the thesis. The overlying purpose of creating various structural models simulated under pure tension leading up to the final true-scale 3D micro-tensile specimen model is to minimize errors when choosing and applying the appropriate boundary conditions for the 3D tensile specimen model. The final 3D micro-tensile specimen model is used to predict the deformation behaviour during micro-tension testing of the specimen and to validate whether the appropriate tensile specimen geometry is chosen for the fabrication process of the copper micro-tensile specimens (discussed in Chapter 5). The FEA modelling of the tensile structures also helps to determine whether the specimens are able to meet the loading conditions of the micro-tensile bench. After desired mechanical results are achieved through the simulation of the FEA models, a mass production of micro-tensile specimens can be machined by the fabrication methods using the plasma-FIB and fs-laser discussed later in Chapter 5.

In addition, different notch geometries (consisting of cicular and elliptical fillets at the reduced section of the wedge connection) were investigated to determine the optimal fillet shape that would minimize the localized stress concentration located along the gauge section.

FEA is often performed by manufacturers and engineers to gain insight on how material products would deform under different stress conditions (such as vibrational, incremental, and constant stress loading). Different types of FEA modelling can include thermal, fluid flow, dynamic, and static analysis. FEA can be used to replicate rapid changes in the deformation such as drop tests, impact and collision tests or failure response of the materials through explicit dynamic simulations. It can also be used to simulate quasi-static stress-strain responses of materials under static or dynamic conditions.

FEA models are comprised of either 1D or 2D shapes called elements connected by nodes at their corresponding vertices. Elements are individual building blocks that make up the mesh of an FEA model. A fine mesh allows for the output of a more accurate model solution, in comparison to a coarser applied mesh applied to the material structure. For the FEA models discussed in this section of the thesis, ANSYS Workbench 2023 software (Student License) was used to develop and simulate the models. The model geometries were created using the ANSYS SpaceClaim Module. Afterward the 2D and 3D geometries were produced in SpaceClaim, the structures were exported to the ANSYS Mechanical module, correspondingly. In ANSYS

Mechanical, the model mesh, boundary constraints, applied external loads, and static structural analysis of the respected model was produced. Model results (such as the normal stress and strain in the X, Y, and Z directions) were computed after the simulation was completed.

FEA models were simulated under both linear-elastic and elastoplastic deformation conditions, respectively. Linear-elastic deformation only produces reversible strain to the model, in which the deformed body returns back to it's original shape after unloading. Non-linear elastoplastic deformation is a combination of both elastic and plastic strain induced to the model, in which during the initial stage of straining, the model behaves only elastically, and after the transition to from the linear to the non-linear regime of the stress-strain curve, the material deforms both elastically and plastically with a combination of both reversible and irreversible strain induced to the model during uniaxial ensile loading. Empirical laws derived from Hooke's law were used to develop the linear-elastic models simulated under uniaxial tensile loading. For the non-linear elastoplastic models discussed in this section, experimental stress-strain data extracted from micro-tension tests of (100) copper and 415 steel (respectively), were fed into an isotropic hardening tool in ANSYS to describe the plastic stress-strain behaviour of the specimen material.

The FEA models simulated under uniaxial tensile loading were assigned to the material properties of (100) copper and 415 martensitic stainless steel. The model simulations were used to determine whether the appropriate tensile specimen geometry was chosen for machining the micro-tensile specimens. Prior to creating 3D model of the chosen ASTM-standard tensile specimen geometry, two-dimensional models were created to validate whether the appropriate boundary constrains were imposed on the models for simulating uniaxial tensile loading. The 2D FEA models include one 1-element model and three different tensile specimen geometry half models. The first tensile specimen half model was simulated without the wedge component and consists of symmetry along the Y axis, as seen in Figure 29.

Afterwards, two tensile half models with the wedge component were produced to add the corporation of the wedge component on the specimen's mechanical response. The symmetry of the 2D tensile specimen models (with the wedge component) is along the X-axis. The difference between the two 2D tensile specimen half models (with the wedge component) is the notches used for the connection between the grip and the gauge section. One of the 2D tensile specimen half models consists of only circular notch connections at both the reduced section between the grip and the gauge section and between the wedge connection and the gauge section (as seen in Figure 32), while the other half tensile geometry consists circular notch connections between the grip and the gauge section and elliptical notch connections at the wedge connection (as seen in Figure 34). To determine the appropriate notch shape and size at the reduced section of the wedge connection, both elliptical and circular notches were applied to the tensie specimen half model, respectively. The objective is to reduce the localized stress concentration at the gauge by choosing the optimal notch geometry and size.

4.2. Material Assignments

The FE-models were assigned to the material properties of anisotropic single crystal copper orientated in the (100) plane and 415 martensitic stainless steel, correspondingly. Initially, the material properties of (100) copper and 415 steel were added into the ANSYS materials library. The materials were exported into ANSYS mechanical to assign the structure the required material properties (e.g. Poisson's ratio, Young's modulus, experimental tensile stress-strain data for non-linear elastiplastic models, etc.,) during the material selection process of simulating the models under uniaxial tensile loading. Table 1 lists the mechanical properties inputted in ANSYS materials library for single crystal copper and 415 steel, respectively. The Young's Modulus and Poisson's ratio for the AISI standard 415 (S41500) stainless steel was determined from [61].

Table 1: Buk Material Properties of (100) Copper and 415 Martensitic Stainless Steel

Material	**Young's Modulus (GPa)**	**Poisson's Ratio**
(100) Copper	66.7	0.42
415 Martensitic Stainless Steel	200	0.28

For the material assignment of (100) copper to the FEA models, the anisotropic stiffness matrix was produced using the elastic stiffness constants for single crystal copper orientated in the (100) plane. The elastic stiffness constants for (100) copper are $c_{11} = 168.4\ GPa$, $c_{12} = 121.4\ GPa$, and $c_{44} = 75.4\ GPa$ and are determined from [62]. Equation *8* shows the stiffness matrix for (100) copper with the inputted elastic stiffness constant following the matrix structure of Equation 7. Due to the symmetry exhibited by the copper FCC cubic lattice, it is expected that the tensile modulus for (100) copper would be 66.7 GPa in all (001), (010), and (100) symmetry planes. On the other hand, 415 steel is a polycrystalline material that consists of number small grains oriented in different crystallographic orientations. Therefore, an isotropic value of the Young's modulus of 200 GPa was used to describe the linear-elastic behaviour of the steel at the bulk scale.

$$\begin{bmatrix}\sigma_1\\ \sigma_2\\ \sigma_3\\ \sigma_4\\ \sigma_5\\ \sigma_6\end{bmatrix} = \begin{bmatrix}c_{11} & c_{12} & c_{12} & 0 & 0 & 0\\ c_{12} & c_{11} & c_{12} & 0 & 0 & 0\\ c_{12} & c_{12} & c_{11} & 0 & 0 & 0\\ 0 & 0 & 0 & c_{44} & 0 & 0\\ 0 & 0 & 0 & 0 & c_{44} & 0\\ 0 & 0 & 0 & 0 & 0 & c_{44}\end{bmatrix}\begin{bmatrix}\varepsilon_1\\ \varepsilon_2\\ \varepsilon_3\\ \varepsilon_4\\ \varepsilon_5\\ \varepsilon_6\end{bmatrix} \qquad \text{Equation 7}$$

$$\begin{bmatrix}\sigma_1\\ \sigma_2\\ \sigma_3\\ \sigma_4\\ \sigma_5\\ \sigma_6\end{bmatrix} = \begin{bmatrix}168.4 & 168.4 & 168.4 & 0 & 0 & 0\\ 121.4 & 168.4 & 168.4 & 0 & 0 & 0\\ 121.4 & 121.4 & 168.4 & 0 & 0 & 0\\ 0 & 0 & 0 & 75.4 & 0 & 0\\ 0 & 0 & 0 & 0 & 75.4 & 0\\ 0 & 0 & 0 & 0 & 0 & 75.4\end{bmatrix}\begin{bmatrix}\varepsilon_1\\ \varepsilon_2\\ \varepsilon_3\\ \varepsilon_4\\ \varepsilon_5\\ \varepsilon_6\end{bmatrix} \qquad \text{Equation 8}$$

To model the non-linear elastoplastic behaviour of the two materials (respectively), experimental plastic stress and strain data were inputted into the multi-linear plasticity hardening tool in ANSYS to define the plastic region of the tensile stress-strain curve up to the ultimate yield strength. The experimental data was extracted from micro-tensile experiments performed previously on 415 martensitic stainless steel and single crystal copper micro-tensile specimens, respectively. The 415 micro-tensile specimen was machined by one of Hydro-Quebec's metallurgist research collaborators, Robert Wheeler. Robert Wheeler machined the 415 micro-tensile specimen using using a Ga^+ sourced FIB, while the copper micro-tensile specimen was machined using a Xe+ sourced PFIB and the fs-laser at the Canadian Centre for Electron Microscopy (CCEM). Note that the simulation of the copper tensile specimen models under non-linear elastoplastic deformation behaviour was performed after the fabrication of the copper micro-tensile specimens. The plastic strain data was extracted from the stress-strain curve of the fs-laser-machined micro-tensile specimen 4 from wedge 3 (with fabrication details discussed in Chapter 5). All FEA models discussed in this thesis were simulated in ANSYS Mechanical at a room temperature of 25 degrees Celsius to avoid thermal effects on the mechanical deformation of the models.

4.3. Plane Strain Versus Plane Stress

Plane stress is a geometric condition used in FEA to approximate the stress-state of a 2D structure, where the stress in the out-of-plane direction approaches zero. By setting the parameter for the models to planar stress conditions in ANSYS, it is assumed that the models are very thin and do not experience stress in the out-of-plane direction. Therefore, the models deform according to the Poisson's ratio. The deformation of the models in the out-of-plane direction is unhindered by stresses induced by the surrounding material in the third dimension. Therefore, under plane stress conditions, the models can be considered an infinitely thin plate, where no interior stresses are generated in the out-of-plane direction [42]. In ANSYS, the results of the 2D tensile specimen models are generated using planar stress approximations to allow for the structures to exhibit strain in all three directions. To define plane stress conditions, a thickness value is specified for the 2D FEA models, correspondingly.

If the geometric condition for the models was set under planar strain conditions, it would be assumed that stress was induced in the out-of-planes direction by the surrounding material of a finite thick model structure. The surrounding material would cause a compressional stress in the out-of-plane direction when the structures are simulated in tension, correspondingly [42]. By doing so, this would modify the normal stresses in the two in-plane directions by introducing a third stress in the out-of-plane direction. The third stress would affect the accuracy of measuring the experimental value of the Poisson's ratio and Young's modulus of the specific material assigned to the FEA models.

4.4. Linear Elastic FEA Model Geometries

Linear-elastic models were produced to validate the mechanical response of the tensile structures under the chosen boundary constraints and external loads for simulating uniaxial micro-tensile testing and prior to the simulation of the plastic strain region of the materials. The linear-elastic model solutions were validated through the comparison of numerical solutions calculated using Hooke's Law. For all linear-elastic models produced and assigned to the specific material properties of 415 and (100) copper (respectively), the Young's Modulus, Poisson's ratio, and the normal stress distribution along the gauge section were plotted in Excel using the normal elastic stress (in the tensile loading direction) and total strain data obtained from the model solutions.

The geometry of the micro-tensile specimen follows the ASTM standard testing methods for a pin-loaded tensile test specimen outlined in [43]. The benefit of using a pin-loaded tensile specimen geometry is the ease of aligning the specimen parallel to the loading-direction in the micro-tensile bench. For mechanical test specimens at the micro-scale level, aligning the specimen parallel to the loading direction is extremely important to obtain mechanical results of the specimen strained in pure tension. In comparison with a clamped-loaded micro-tensile specimen, slippage can occur at the grip during the tensile test if the specimen is not properly secured in the load train. When slippage occurs, it can cause shearing and bending of the specimen during the tensile test when the specimen is not perfectly aligned parallel to the tensile load axis.

For the machining process of the micro-tensile specimens, a pinhole with a diameter of 150 µm was fabricated at the free-end grip. The 150 µm pin diameter was chosen for the machining of the tensile specimens because it has enough clearance for the tungsten pinhole with a 145 µm diameter to be inserted in the pinhole. In addition, a gauge width of 100 µm was chosen for machining of all the tensile specimens. The dimension of the specimens that should only vary between each specimen for the size effect-study is the gauge thickness.

4.4. 2D One-Element Model

The one-element model was the first 2D linear-elastic FE-model to be produced and simulated under uniaxial tensile loading. The one-element model was used to determine the appropriate boundary conditions to be applied for performing uniaxial tensile loading on the simplest structure produced in FEA. The model consists of one element, which represents a single building block to a finite-element mesh. The element consists of a linear (first order) 1 mm x 1 mm square-shaped element with nodes at each corner of the element, as seen in Figure 25. By using the first-order one-element model, the effects of mesh convergence issues and long computational times can be neglected. The one-element model was simulated under uniaxial tensile loading in the X-direction using a force load and a displacement load, correspondingly. As seen by the schematic in Figure 26 of the structural analysis of the one-element model performed in ANSYS mechanical, the boundary constraints were assigned at the corner nodes of the square structure. Two nodal displacement constraints were placed at the left corners of the square, with node A creating a fixed displacement of zero in the X and Y direction, and node B representing a roller support, providing free motion in the Y-direction and a fixed displacement

of zero in the X-direction. In addition, a roller support was placed at node D to allow for the structure to deform in the X-direction. These boundary conditions allow for the model to maintain a static structure under an applied external load, while still able to deform elastically under the assigned Poisson's ratio value of the specimen material. On the right side of the one-element model shown in Figure 25, node C and D are assigned to either a load force or displacement load value.

In Figure 25, the one-element model was assigned to the material properties of 415 steel, where the nodal forces applied to the model was determined using Hooke's Law (in Equation 9) to meet the highest true stress value of 827.46 MPa in the experimental micro-tensile data obtained from Bob Wheeler's mechanical testing of the 415 micro-tensile specimen. The force of 41.37 N was distributed evenly by the two right nodes (labelled C and D in Figure 25), with each node carrying a force of 20.69 N in the X-direction. Under plane stress conditions, the one-element model was assigned to a thickness value of 50 μm, (which corresponds to the initial thickness value of the copper foil used to machine the micro-tensile specimens). The one-element model was also assigned to a thickness value of 12.33 μm (which corresponds to the thickness value of the thinned gauge section of the fs-laser-machined copper tensile specimen 4 from wedge 3). After validating the correct normal stress and normal elastic strain responses of the one-element model assigned to 415 steel using numerical calculations (listed in Appendix A1 of this thesis document), the model was simulated again in pure tension under the assigned material properties of (100) copper and linear-elastic conditions.

The stress-strain results were probed at the bottom-left node of the square structure, where a named selection tool was used to identify the nodal position in which the stress-strain results were computed. The highest stress value of 244.28 MPa from the experimental micro-tensile data of the fs-laser-machined copper micro-tensile specimen 4 from wedge 3 was used to compute the corresponding force value of 3.01 Newtons using Hooke's Law. Figure 27 shows the contour diagram for the total deformation response of the body of the (100) copper one-element model in the X and Y directions, respectively, and its undeformed wireframe (with the true scale of the deformation multiplied by 20).

$$\sigma = E\varepsilon$$ Equation 9 (Hooke's Law)

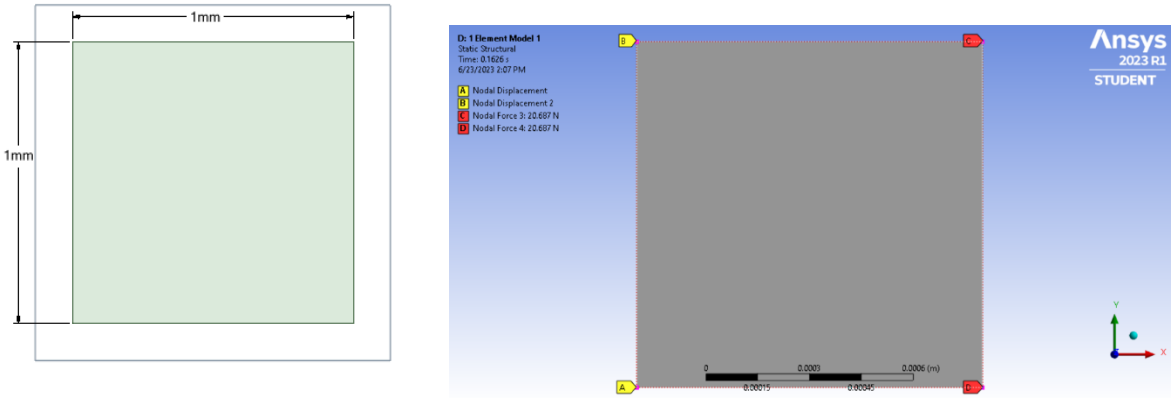

Figure 25: Images showing dimensions and boundary conditions applied for the 2D one-element model created in ANSYS Workbench 2023 under uniaxial tensile stress with an applied load force at the right-hand nodes of the model.

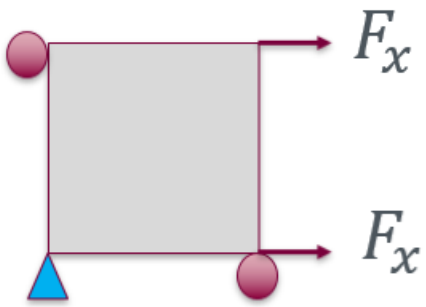

Figure 26: Schematic of boundary conditions imposed on the one-element model simulated under uniaxial tensile loading.

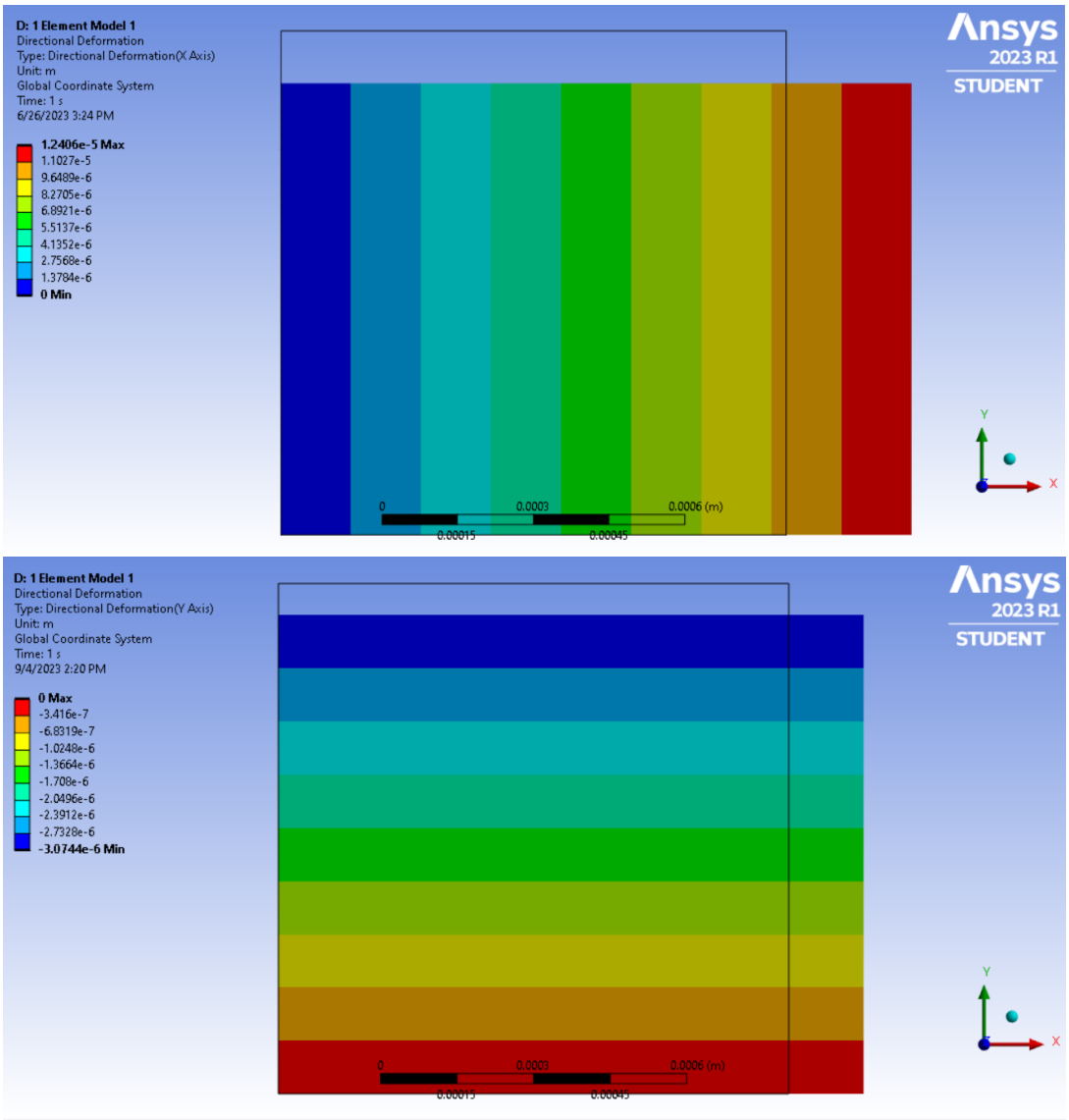

Figure 27: Contour diagram produced in ANSYS Mechanical for the total deformation of single crystl copper one-element model in the X-direction (top-image) and in the Y-direction (bottom-image) (exhibiting 20 times the true deformation) and its undeformed wireframe.

The alternative approach taken to simulate uniaxial tension on the 1-element model was to use an applied displacement load instead of a force load on the right-side nodes of the one-element model (as seen in Figure 28). Applying a displacement load on the 2D element provides a more realistic model of the copper micro-tensile experiments, since the micro-tensile tests are strain-rate dependent. For the one-element model assigned to the material properties of 415 steel and a thickness value of 12.33 µm, a displacement of $5.346x10^{-3}\ mm$ in the X-direction was applied to the top-right node and the bottom-right node, respectively. Also, it is important to keep in mind, that the motion of the displacement-loaded node in the Y-direction should be kept free to allow for deformation of the structure in the X-direction (thus, satisfying the Poisson's ratio effect). A static free body diagram of the displacement-loaded model with its corresponding

applied boundary conditions can be seen in Figure 28. Following the same procedure for the one-element model under an applied force load, the mechanical stress-strain response was analyzed at the top-right node of the element. In addition, the model provided the mechanical results for stress and strain at each corner of the one-element model.

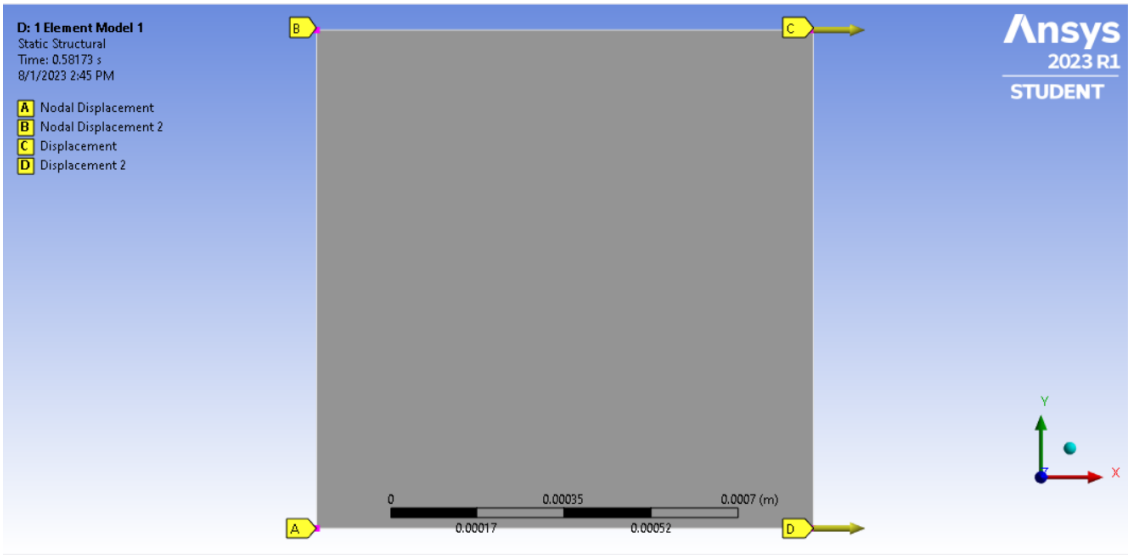

Figure 28: Diagram of the 2D 1-element model created in ANSYS Workbench 2023 under uniaxial tensile stress with an applied displacement load at the right-hand nodes of the model.

4.5. 2D Half-Model of Micro-Tensile Specimen (with Free-End)

After validating the mechanical behaviour of the one-element model under linear-elastic conditions using the appropriate boundary conditions for uniaxial tensile loading, the first 2D tensile specimen model was produced. To reduce the complexity of the model geometry and reduce the computational time, the first tensile specimen model produced was a symmetrical tensile specimen half model with the absence of the wedge connection. The geometry and dimensions of the tensile geometry with the free grip end can be seen in the SpaceClaim diagram in Figure 29. The design of the tensile specimen model conforms to the true scale of the geometry and dimensions of the copper specimens (excluding the notch connections to the wedge component) expected to be machined using the PFIB and fs-laser, respectively. Similar boundary conditions from the one-element model were imposed on the tensile specimen model, as seen by the schematic in Figure 29. The model was pulled in pure tension in the Y-direction. The load force was only applied to the upper-half edge of the pinhole, in order to represent the tension on the pinhole induced by the pin when the specimen is loaded in the micro-tensile bench. A fixed support is applied to the vertex of the gauge section to prevent movement of the model in the Y-direction. In addition, a roller support was applied at the symmetry line of the half model to prevent pivot errors during the simulation. With the applied boundary conditions, the model is able to deform freely in the X and Y directions.

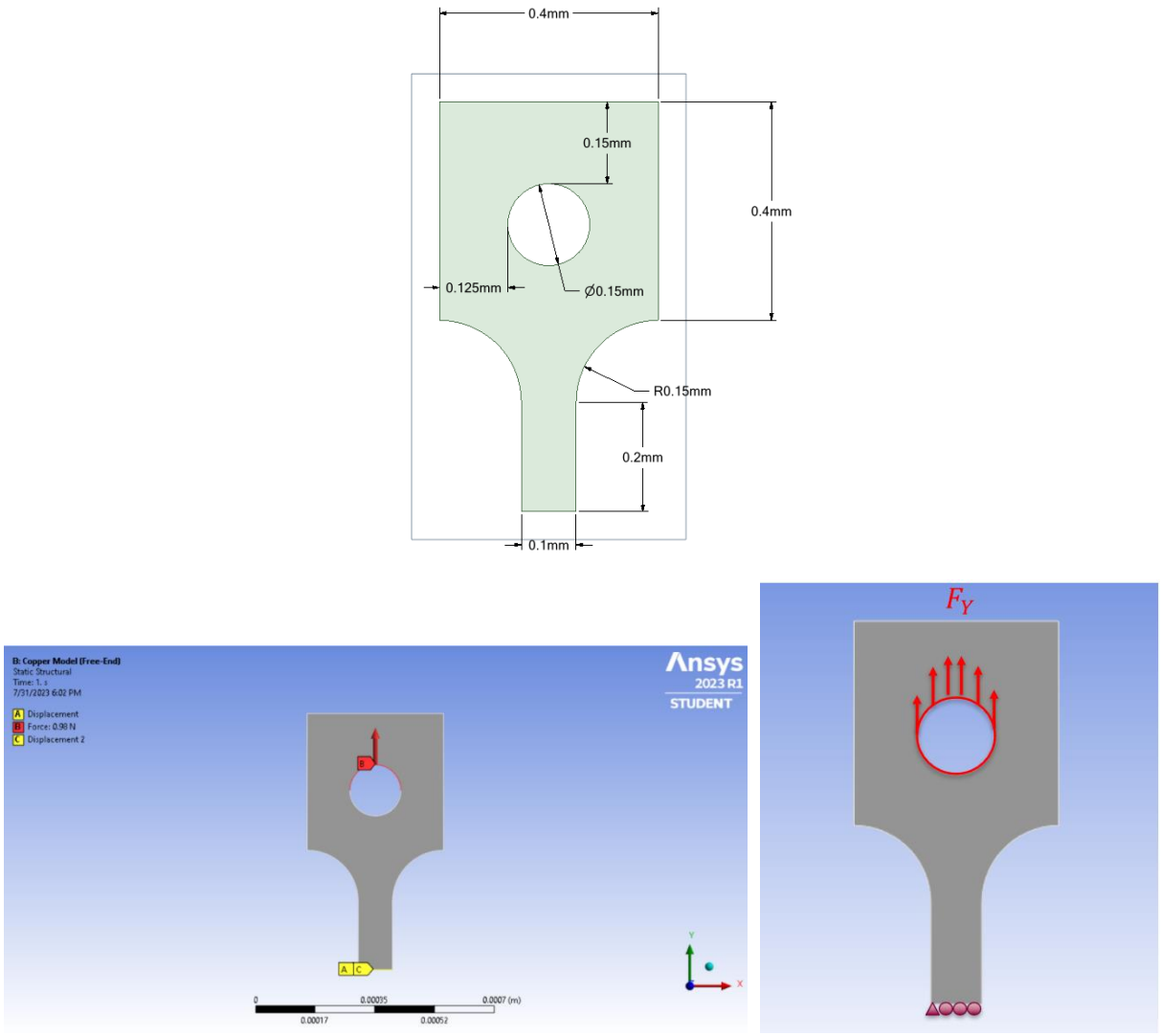

Figure 29: Geometry and boundary conditions applied for 2D tensile specimen half model with free-end simulated in pure tension.

The tensile specimen model was meshed using 2D quadratic elements with an elemental size of $2x10^{-6}m$. This value was chosen to be the smallest possible mesh fize for all three 2D tensile specimen structures prior to encountering numerical limitation errors of the ANSYS Student Licensing software. Linear-elastic conditions were initially imposed on the model to obtain the stress and strain results at a nodal point located at the gauge section of the tensile specimen. The tensile model was initially assigned to the material properties of 415 steel with a specimen thickness of 50 µm. Large circular fillets were used to reduce the localized stress concentration at the reduced section between the grip and the gauge. From the linear-elastic model, the normal stress in the Y-direction, and normal elastic strain in both the X and Y directions (correspondingly) were obtain from the result of the simulation. The Young's Modulus and Poisson's ratio for 415 were validated by plotting the model results in Excel (as seen in Figure 131 and Figure 132 under Appendix A2, respectively).

After validating the correct stress and strain responses of the model with its corresponding analytical solutions for (100) copper and 415 steel, the normal stress distribution was determined along the gauge length of the specimen using the construction path tool in ANSYS Mechanical, as seen in Figure 30. The normal stress distribution in the Y-direction from the free-end to the symmetry end was computed and plotted in Excel with respect to the length of the gauge, as seen in Figure 31 for (100) copper. The normal stress distribution along the gauge length is approximately constant until it reaches the free end with the circular notch connections, where the normal stress increases exponentially. After determining the stress distribution along the gauge length, the tensile model was assigned to a thickness value of 12.33 µm and to the material properties of (100) copper, respectively. The stress and strain response of the model was then re-evaluated for the new thickness value and material.

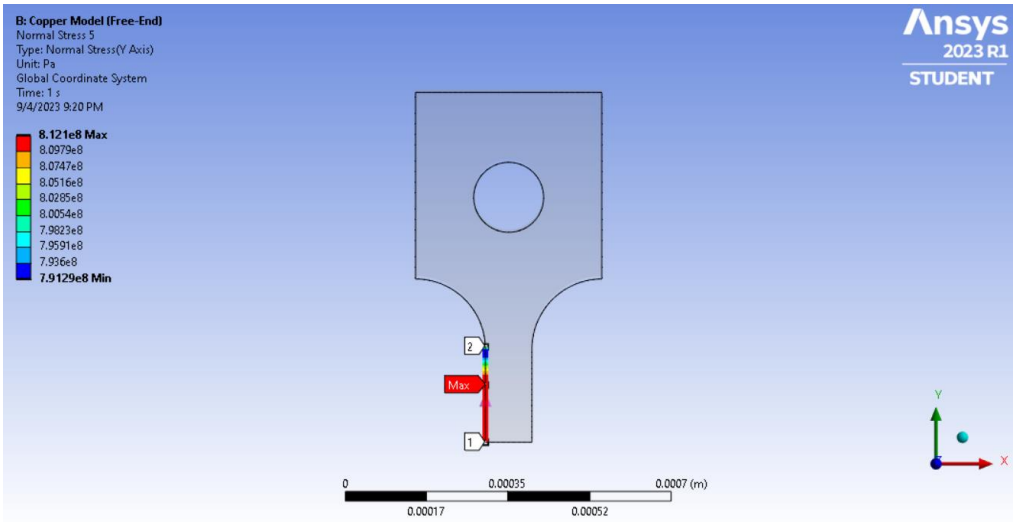

Figure 30: Contruction path along the gauge length edge for probing the normal stress distrubtion on the Y-direction for the 2D tensile specimen half model (without the wedge connection).

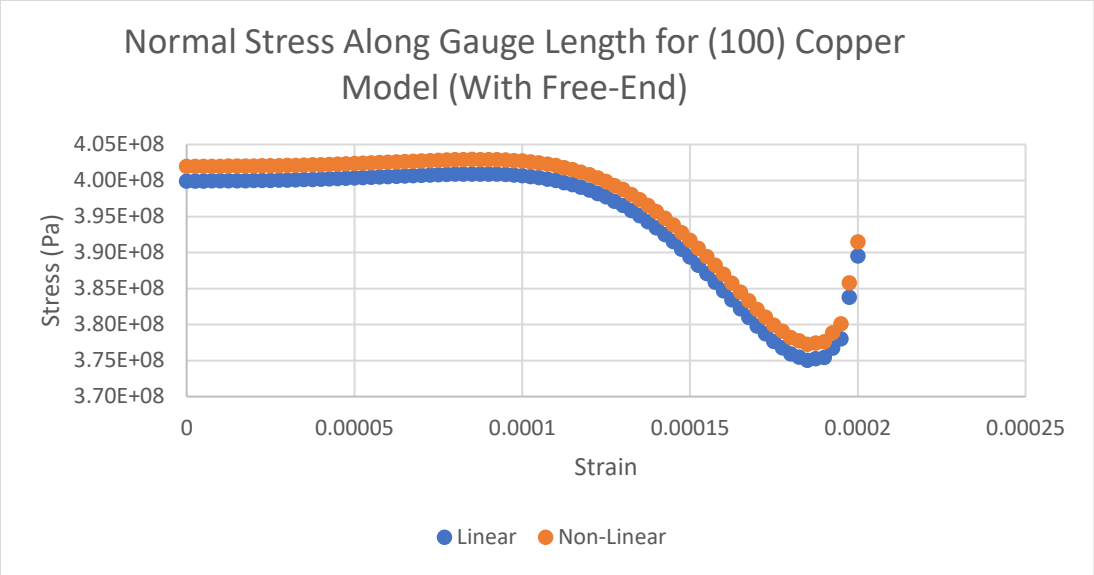

Figure 31: Plot of normal stress distribution along the gauge length edge of 2D tensile specimen half model (without the wedge connection) assigned to (100) copper under linear-elastic and elastoplastic conditions, respectively

4.6. 2D Half-Model of Micro-Tensile Specimen with Circular Notch Connections

The next 2D FEA tensile specimen model produced in ANSYS was a half tensile specimen model consisting of the wedge component and only circular notch connections at the reduced sections. The model was produced to incorporate the effect of the wedge component on the mechanical behaviour of the tensile specimen and to simulate a more realistic model of the specimens when it comes to machining the micro-tensile specimens attached to the wedge material. A schematic of the model's geometry and dimensions can be seen in Figure 32. A global mesh size of $2x10^{-6}$m was applied to the tensile specimen model. For the boundary conditions (depicted in Figure 32) of the model under uniaxial tensile loading, a load force was applied to upper half region of semi-circular edge of the pinhole. The half model has a symmetry region along the Y-axis, which cuts the specimen in half along the centerline of the gauge length. Roller supports were placed at the edges of the specimen, where the symmetry region is present (excluding the perimeter of the pinhole). A fixed support is placed on the bottom edge of the wedge to simulate a static structural analysis of the tensile specimen model.

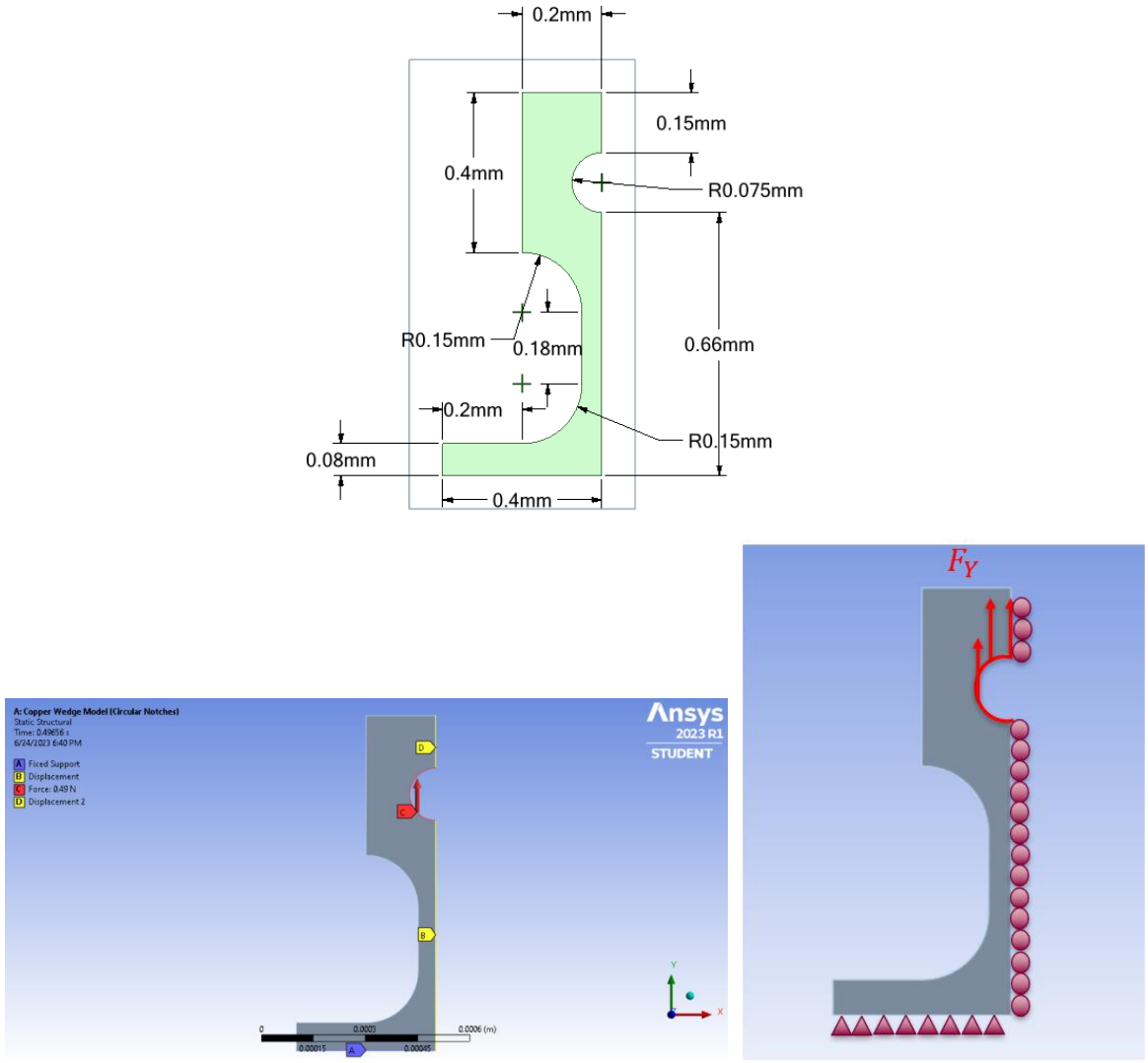

Figure 32: Dimensions and boundary condition for 2D micro-tensile specimen half model with a 180 µm x 50 µm (length to width) gauge and circular notch connections.

To calculate the normal elastic stress and strain induced at the gauge section during uniaxial tensile loading in the Y-direction, a named selection was assigned to a nodal point on the gauge section. The model results of the normal elastic stress and strain correlates well with the analytical results of the model. Therefore, the boundary conditions were well defined for modelling the half tensile geometry with the wedge component under pure uniaxial tensile loading. In addition, the normal stress distribution along the gauge edge is probed using a constructed path from the grip end to the wedge connection. The distribution of normal stress along the gauge edge was plotted in Excel to see the variation in the nominal stress of the gauge section, as seen in Figure 33 for (100) copper. From the linear and non-linear model curves, it was observed that the normal stress was the highest at the ends of the gauge length (due to the presence of the circular notches) and plateaus to a nominal stress value away from the notches. The gauge length has a symmetrical normal stress distribution, due to the identical circular fillets

at both ends at the gauge with the same notch radius value of 150 µm. The symmetry of the stress distribution with the circular notches minimizes the stress-concntration at the reduced sections at the grip and wedge ends.

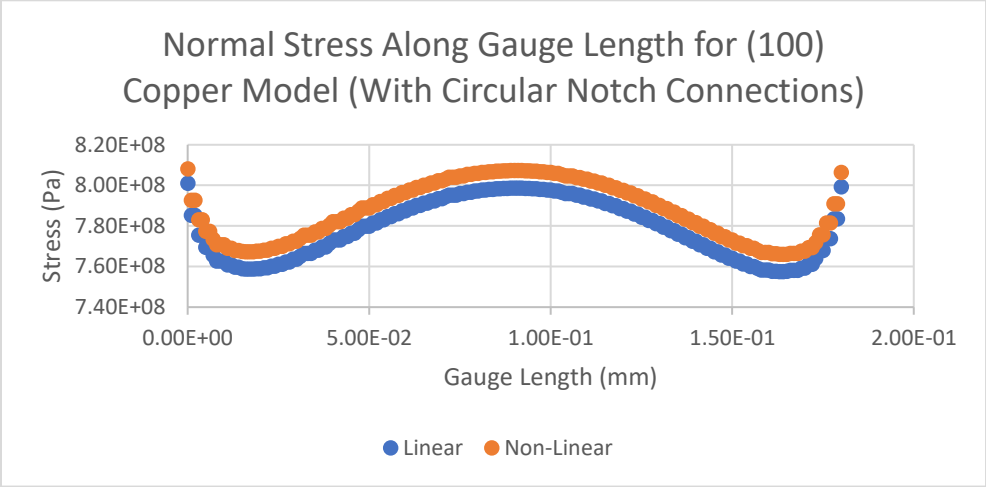

Figure 33: Plot of normal stress distribution along the gauge length edge of 2D tensile specimen half model (with circular notches) assigned to (100) copper under linear-elastic and elastoplastic conditions, respectively.

4.7. 2D Half-Model of Micro-Tensile Specimen with Elliptical Notch Connections

Another FE-model was created to incorporate the wedge component of the tensile specimens, with elliptical notches at the wedge connection. The elliptical fillet had a minor radius of 40 µm and a major radius of 100 µm. At the grip end of the gauge section, circular notches with a radius of 150 µm remained in place. The model's geometry and dimensions can be seen in Figure 34. A fine global mesh size of $2x10^{-6}$m was applied to the 2D face of the model. Similar to the first wedge component model, the half model exhibits symmetry along the X-axis. The boundary constraints applied to the model (depicted in Figure 34) are roller supports at the symmetry line of specimen and a fixed support is placed at the bottom edge of the wedge. A uniform load force was applied to the semicircular pinhole. The model was assigned to material properties of 415 and (100) copper, correspondingly. For each assigned material to the model, the normal elastic stress and strain results were probed from a single nodal point located at the gauge section using the named selection tool in ANSYS. The experimental results of the model for both materials correlated well with the model's numerical solution. Experimental results for the stress and strain response of the three tensile specimen half models simulated under linear-elastic conditions are listed in Table 2 and Table 3 (under the assigned material properties of (100) single crystal copper and 415 steel, respectively).

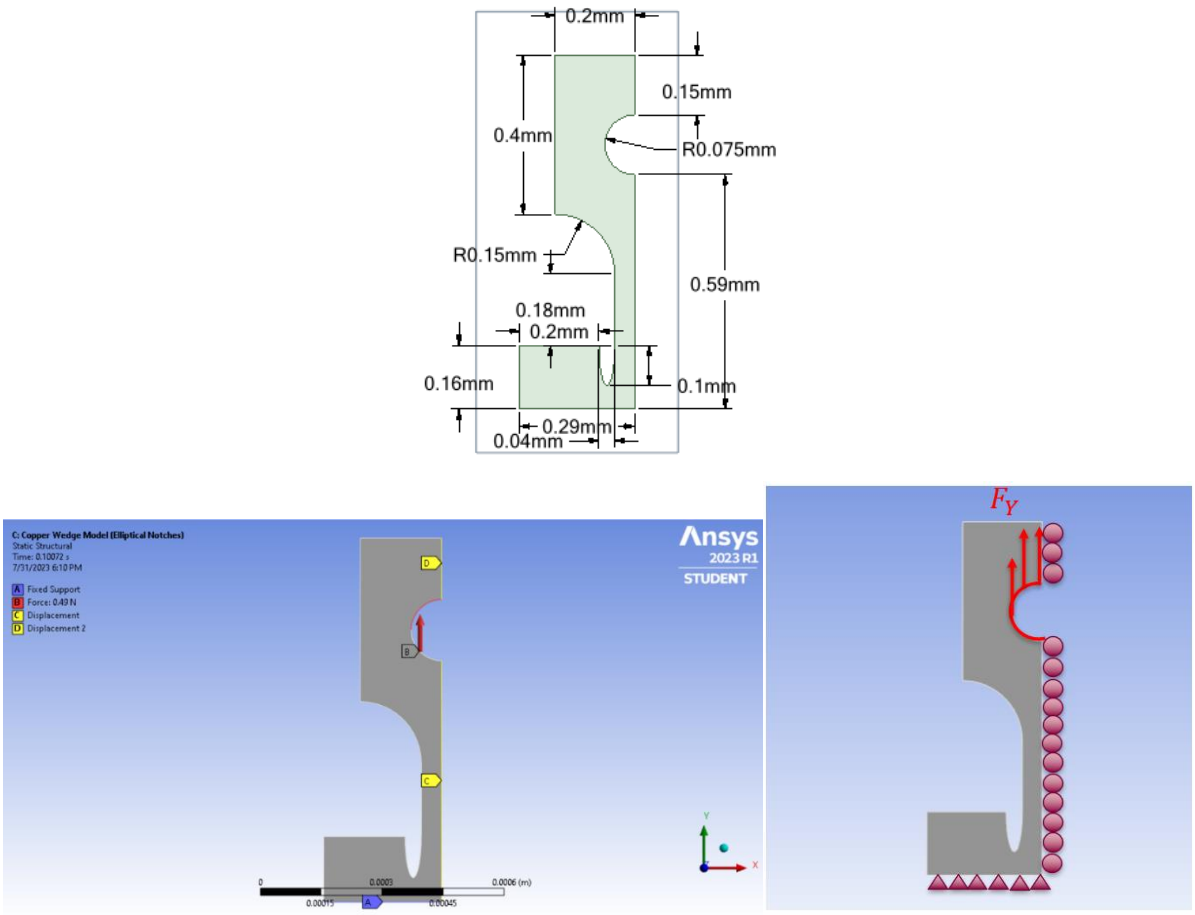

Figure 34: Dimensions and boundary condition for 2D micro-tensile specimen half model with a 180 µm x 50 µm (length to width) gauge and elliptical notch connections.

The elliptical notches provide a more asymmetrical stress distribution along the gauge length and a narrorower stress distribution between the gauge section and the wedge component compared to that of circular notches, as shown in the norml stress distribution plot in Figure 35 for (100) copper. Although, the geometry would allow for more time efficient machining of the specimens, since less surrounding material is being removed via milling to create the elliptical notch connections than for circular fillets.

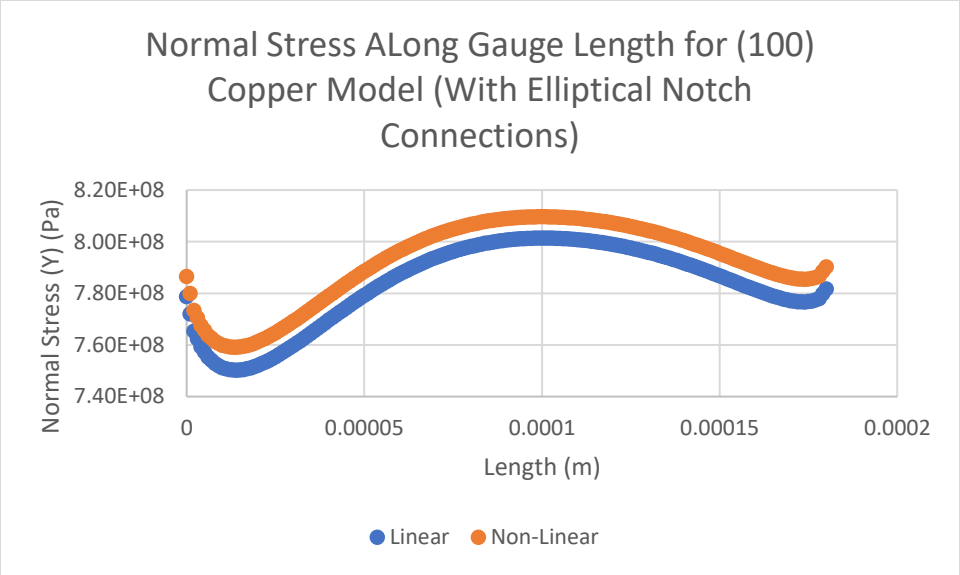

Figure 35: Plot of normal stress distribution along the gauge length edge of 2D tensile specimen half model (with circular and elliptical notches) assigned to (100) copper under linear-elastic and elastoplastic conditions, respectively.

Table 2: FEA Model Results for (100) Single Crystal Copper Under Linear-Elastic Conditions

Mechanical Property	Exp. Results (Without Wedge Connection)	Exp. Results (Circular Fillets)	Exp. Results (Elliptical Fillets)
ϵ_x	$-4.99x10^{-3}$	$-5.0x10^{-3}$	$-5.01x10^{-3}$
ϵ_y	$1.12x10^{-2}$	$1.12x10^{-2}$	$1.12x10^{-2}$
$\sigma_y\ (MPa)$	$7.9489x10^{8}$	$7.9685x10^{8}$	$7.9526x10^{8}$

Table 3: FEA Model Results for 415 Martensitic Stainless Steel Under Linear-Elastic Conditions

Mechanical Property	Exp. Results) (Without Wedge Connection)	Exp. Results (Circular Fillets)	Exp. Results (Elliptical Fillets)
ϵ_x	$-1.44x10^{-3}$	$-1.42x10^{-3}$	$-1.44x10^{-3}$
ϵ_y	$5.13x10^{-3}$	$5.14x10^{-3}$	$5.13x10^{-3}$
σ_y	$7.95x10^{8}$	$7.96x10^{8}$	$7.94x10^{8}$

4.8.Force Convergence and Defining a Multilinear Plasticity Hardening Model

After the models were validated under linear-elastic conditions, stress and strain data from the non-linear plastic strain region was inputted into the one-element model and the three 2D tensile specimen models for the respected materials of 415 and (100) copper. The Multilinear Isotropic Hardening Tool in ANSYS was used to define the plastic region of the experimental

stress-strain curve of the respected material. With this tool, only the non-linear region of plastic strain was used to model the mechanical behaviour of the models simulated in pure tension. Therefore, the data from the non-linear plastic deformation region of the stress-strain curves was isolated and inputted into the hardening tool for the respected materials of 415 steel and (100) copper. Using the raw data from the micro-tensile tests of (100) copper and 415, the large deformation behaviour of the materials upon yielding can be modelled under uniaxial tensile loading. The tool uses a piecewise linear function and linear interpolation of the experimental stress and strain data to model the plastic behaviour of the assigned material in tension. Although, the limitation of the tool is that it can only be used to define the plastic hardening region of the curve (from the yield point up to the ultimate tensile strength of the material). In addition, isotropic elasticity must be defined in the material's library for both (100) copper and 415 steel (respectively), such as the Young's Modulus and the Poisson's ratio. Therefore, the stiffness matrix was replaced with the tensile modulus of 66.7 GPa and Poisson's ratio of 0.28 for (100) single crysal copper.

The Young's Modulus of 415 steel was determined from the experimental data of the single 415 micro-tensile specimen produced by Robert Wheeler (Engineering Technician at Motherson Sumi Systems Limited (MTSL)) for the research work on the micro-tensile testing of low carbon martensitic stainless steels conducted by PhD Candidate Peirre-Antony Deschênes [63]. The slope value of linear portion of the stress-stain curve was taken from two points on the true stress-strain curve (from the initial point of zero strain up to prior to the yield point of the curve). The measured value of the Young's Modulus of 415 was approximately $154.782\ GPa$, which is significantly lower than the theoretical value of $200\ GPa$. This difference in the Young's Modulus values can be due to the finite number of martensitic grains constrained at the gauge section, which makes up the average stiffness for the tensile specimen. The difference can also be due to the experimental inaccuracy of measuring the tensile modulus from the positive slope of the linear-elastic region of the curve .

In the micrometer-scale of machining the gauge length of the micro-tensile specimen, martensitic grains were targeted using a 2D-EBSD scan of the material surface and the coordinates of the grains in the EBSD map are saved in order to machine the micro-tensile specimens containing the grains of interest. Therefore, it is possible that only one or two grains are contained at the gauge section of the micro-tensile specimen. For the (100) copper model, the theoretical value of the Young's Modulus was used, due to the large scatter of data in the linear portion of the experimental data from the micro-tension test.

When defining the non-linear elastoplastic hardening behaviour of a material specimen in ANSYS, experimental engineering stress strain data must be converted to true stress and strain data. The conversion of engineering stress and strain to true stress and strain data can be computed using Equation 10 and Equation *11*, respectively. This conversion to true stress and strain data was performed to consider the plastic deformation of the specimen that occurs without the change in specimen volume. Under pure tensile loading, the cross-section of the material reduces due to elongated straining of the specimen. The stress increases

instantaneously to compensate for the reduced area during testing. Therefore, the hardening model must be able to capture the effects of the increased stress at the gauge.

$$\sigma_{\text{true}} = \sigma_{\text{eng}}(1 + \varepsilon_{\text{eng}}) \quad \text{Equation 10}$$

$$\varepsilon_{true} = ln\,(1 + \varepsilon_{eng}) \quad \text{Equation 11}$$

After the data has been converted to true stress and strain data, plastic strain was separated from the elastic strain of the total strain of the material using Equation 12 and Equation 13. It is important to keep in mind, that under plastic deformation of the material, the material continues to deform elasticity up to the ultimate tensile strength of the material. After the plastic strain was separated from the total strain of the true stress and strain curve, the region of the negative stress (in which necking of the material occurs) was excluded from the plastic hardening model. This is due to the limitations of the tool, in which it only supports the positive non-linear hardening behaviour from the yield point and up to the ultimate tensile strength. Although there are damage initiation and failure analysis models that exist in the ANSYS software, the models in this project only deals with the deformation accumulated up to the positive strain hardening portion of the stress-strain curves [64].

$$\varepsilon_{elastic} = \frac{\sigma_{true}}{E} \quad \text{Equation 12}$$

$$\varepsilon_{plastic} = \epsilon_{total} - \varepsilon_{elastic} \quad \text{Equation 13}$$

When inputting the plastic strain data with its correspond stress value into the hardening tool, the yield point is set to zero for both stress and strain values to indicate the start of plastic deformation of the material. Experimental data for the plastic strain and corresponding stress values inputted into the hardening tool can be seen in Table 13 and Table 14 under Appendix A3 for 415 and (100) copper, respectively. To simulate the non-linear effects elastoplastic behaviour of the materials, non-linear effect and large deformation settings were turned on in the models' analysis parameters. In addition, the force was applied to the non-linear models gradually through the use incremental load steps (specified under the analysis settings in ANSYS Mechanical) with a defined minimum number of 20 sub-steps, an initial number of 200 sub-steps, and a maximum number of 10,000 sub-steps for the model solution to converge.

For the non-linear elastoplastic models, the boundary conditions imposed on the structures remained the same as the linear-elastic simulations. The load force applied to the

models reflects the highest stress value inputted into the multilinear isotropic hardening tool. Although, due to the large deformation imposed by the non-linear deformation of the models, the force value must be decreased to a value that meets the criteria defined by the plastic strain data. If the model exceeds the highest stress values defined by the model, the model solution will not converge under the user-defined force convergence criteria in ANSYS, as seen in Figure 36 for the one-element model assigned to the material properties of the 415 steel. Therefore, the force value that was used for the corresponding 2D linear-elastic model was reduced for the non-linear models to meet the force criteria for the multilinear hardening model. Another solution to overcome the convergence issue is to add more data points to the positive slope of the curve prior to necking of the gauge section. Although, for the experimental data of the 415 steel and (100) copper specimens, all data points were defined up to the UTS prior to the negative non-linear slope of the true stress and strain curves. When a large load displacement was applied to the non-linear models beyond the defined plastic strain region of the curve, the models will behave perfectly plastic, in which the stress values beyond the last defined data point in the multi-linear hardening tool remains constant under increasing strain of the structures [64].

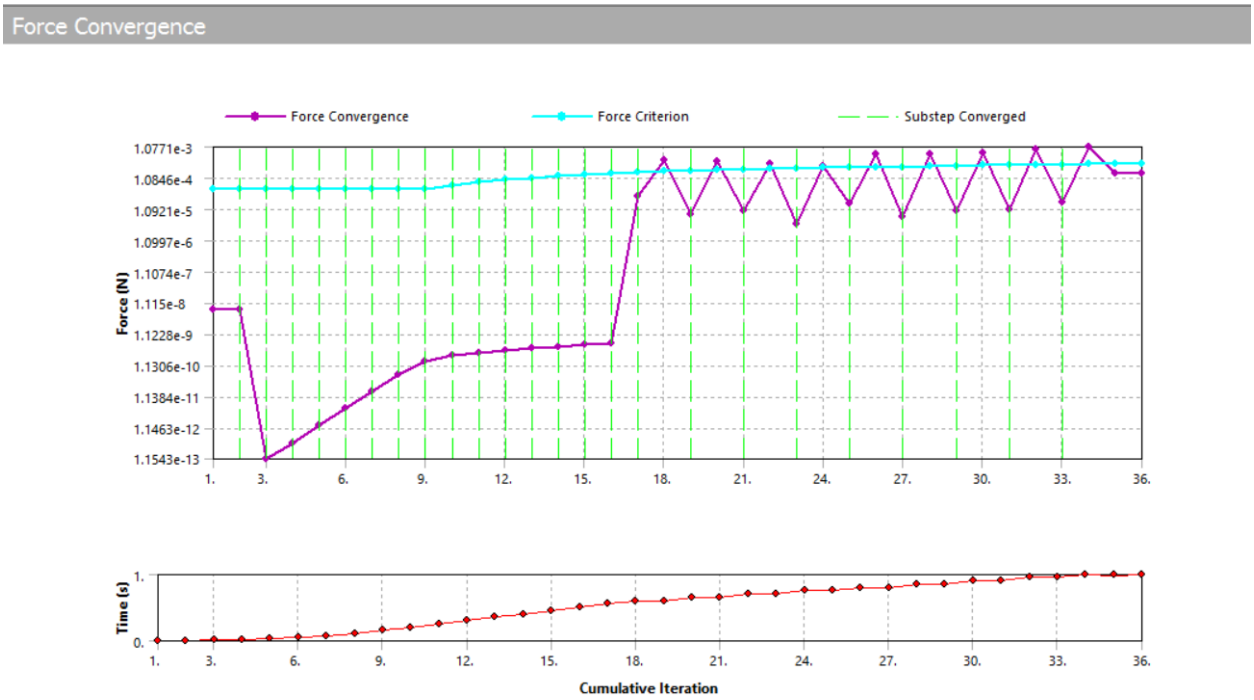

Figure 36: Force convergence-versus sub-steps plot for 415-assigned one-element model simulated in pure tension. Blue line indicates force criterion with a reference value of 0.02 Newtons.

The stress and strain results for the non-linear models were probed at the same nodal point positions as the linear-elastic models. To obtain only the plastic strain results exhibited by the model solutions under uniaxial tensile loading, a user defined result was produced to probe plastic strain in the direction of the uniaxial tensile loading at the defined nodal point of the model. For the one-element model, the user-defined code, EPPLX was used to define the plastic strain in the X-direction and EEPLY was used to define the plastic strain in the Y-direction for all three 2D tensile specimen half models. To probe only the linear elastic strain of the one-

element model and 2D tensile specimen models, EPELX and EPELY were specified in the user defined solutions, respectively. The total strain from the entire deformation of the models can be determined using the EPTOX and EPTOY user defined solutions, which include the sum of both the elastic and plastic strains of the models. To obtain the entire true stress-strain curve (containing both the linear-elastic and non-linear elastoplastic deformation behaviour of the material) from the simulated tensile models, the normal stress in the tensile pulling direction can be plotted against the total normal strain (using the user defined solutions of EPTOX and EPTOY for the one-element model and 2D tensile specimen models, respectively). Contour models exhibiting the non-linear elastoplastic normal stress distribution throughout the structures of the 2D tensile specimen half models can be seen in Figure 37, Figure 39 and Figure 38, respectively for the 2D tensile specimen model with the free-end, with circular notches only, and with both circular and elliptical notches, repectively. The maximum stress distribution (represented in red contour) is located at the gauge sections for all three models.

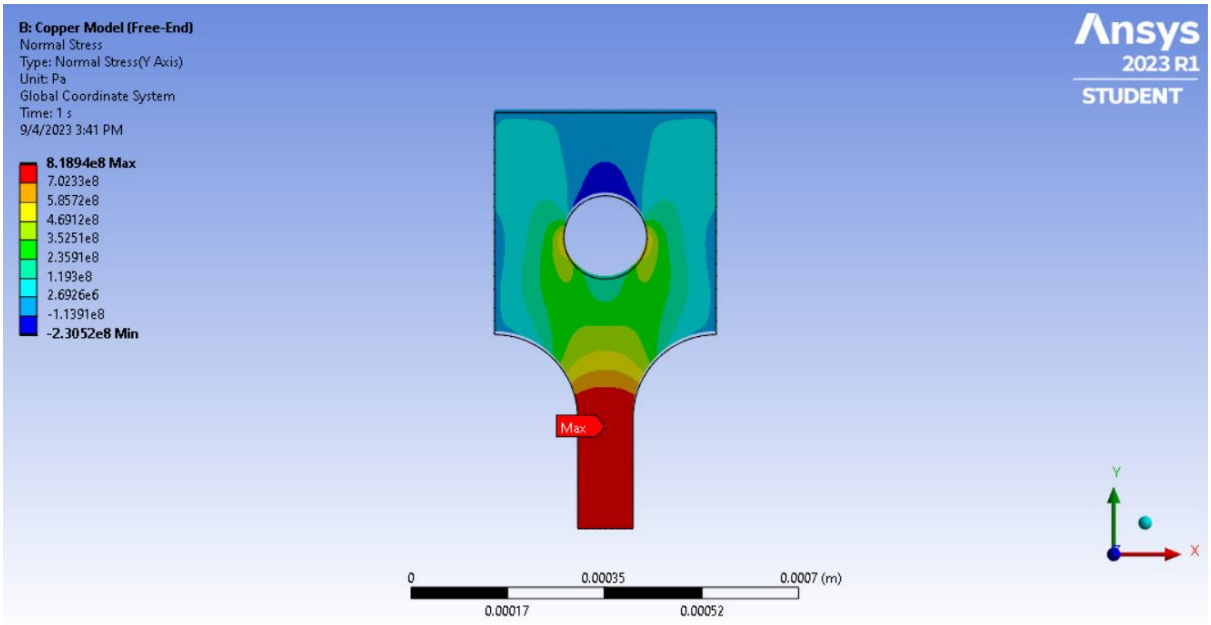

Figure 37: Contour plot of the normal stress distribution of the 2D tensile specimen half model witout the wedge connection under non-linear conditions.

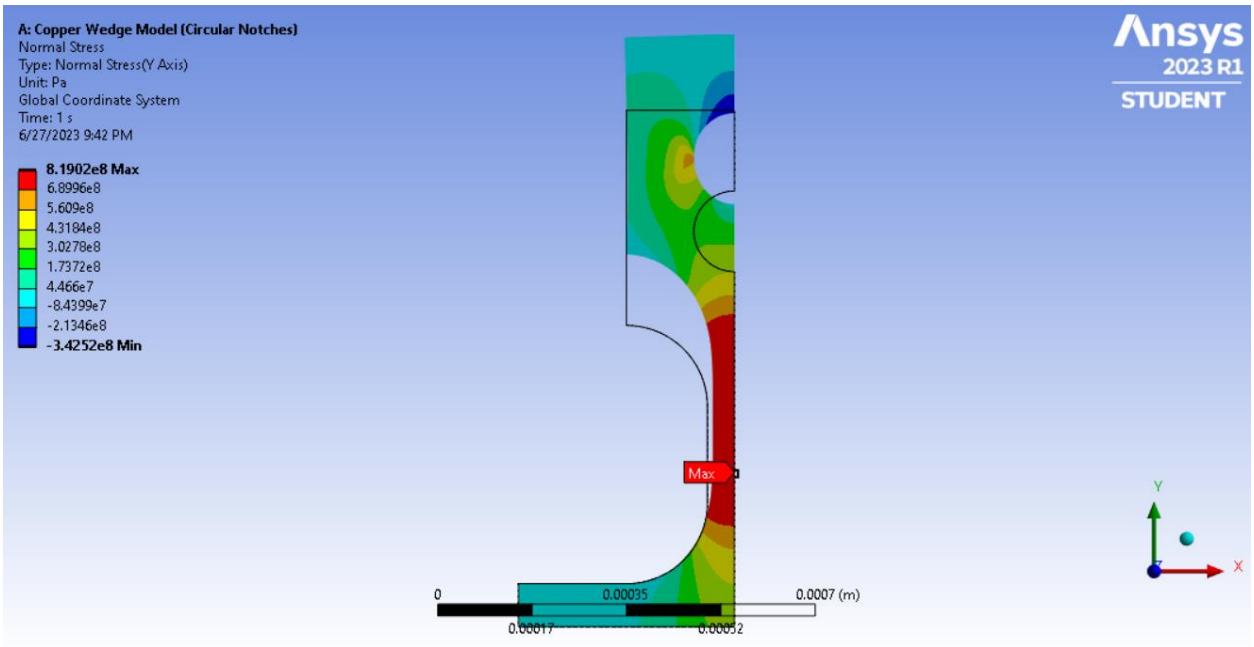

Figure 38: Contour plot of the normal stress distribution of the 2D tensile specimen half model with circular notches at the wedge connection under non-linear conditions.

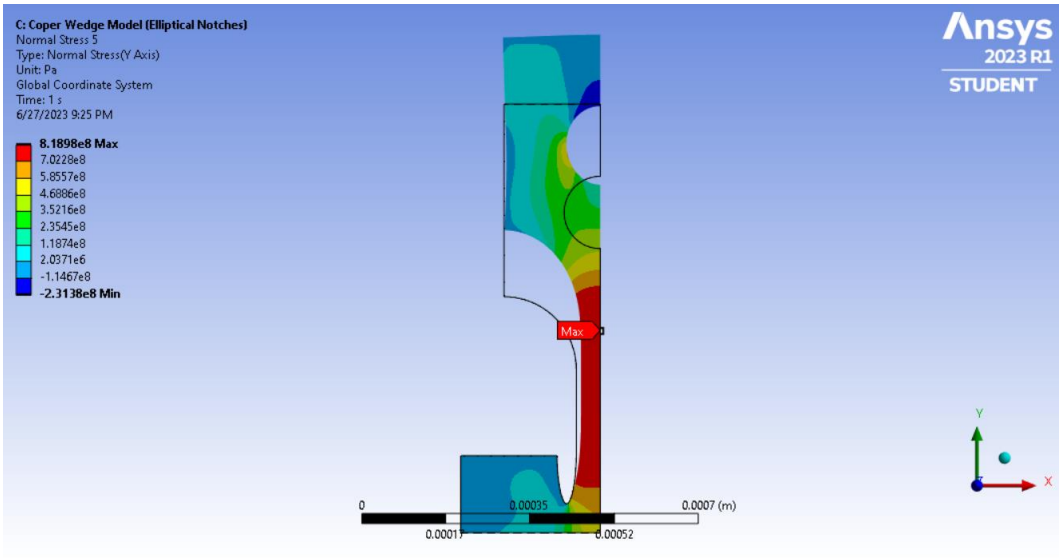

Figure 39: Contour plot of the normal stress distribution of the 2D tensile specimen half model with circular and elliptical notches at the wedge connection under non-linear conditions.

4.9.3D Model Micro-Tensile Specimen Geometry

After validating the linear-elastic behaviour of the 2D tensile specimen half models, a 3D model was produced to represent a more practical geometry of the final machined micro-tensile specimen using fabrication methods performed with the PFIB and fs-laser. The geometry of the 3D model was developed in ANSYS SpaceClaim (as seen in Figure 40) and simulated under uniaxial tensile lodaing in ANSYS Mechanical. The geometry consists of a single tensile-dog

bone-shaped structure with a pin-loaded grip and the wedge component as the fixed end. During the mechanical testing of the micro-tensile specimens, the wedge would be held in place by the specimen holder in the micro-tensile bench by grips to prevent the sliding of the wedge during tensile testing. In particular, the 3D model was produced to represent the tilted gauge section of the tensile specimen produced by the thinning method adopted from the fabrication work of micro-tensile specimens by Robert Wheeler. The tilted gauge is developed during the thinning process of the gauge cross-section with milling performed using the PFIB (discussed in detail later Chapter 5). In the PFIB chamber, the wedge containing all the tensile specimen geometry cutouts (attached to a cross-holder on the stage) was tilted a few degrees away from the normal of the ion beam in order to provide a line-of-sight for thinning the gauge sections of tensile specimens lined up beside one another As a result, a tilted gauge was produced off-axis from the surface of the tensile specimen grip and wedge component. Therefore, a 3D model was necessary to model the effects of the tilted gauge section on the stress and strain response of the structure under pure tensile loading. In addition, the rectangular gauge section (represented in the 2D models) becomes a parallelogram-shape (seen in the 3D model) from the gauge thinning process.

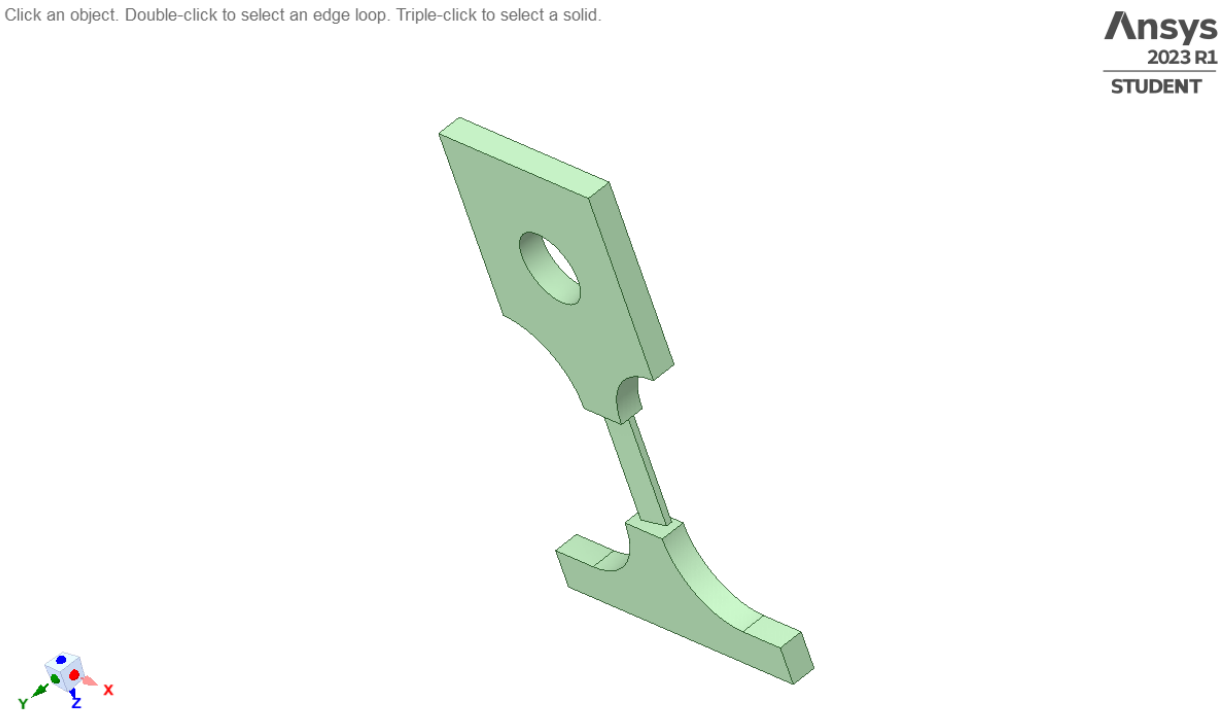

Figure 40: 3D geometry of a single micro-tensile specimen model produced in ANSYS SpaceClaim.

For the tilted gauge section of the 3D model, a thickness value of 12.33 µm was chosen to present the final thinned gauge section of the fs-laser-machined copper micro-tensile specimen 4 from wedge 3. The length and width of the gauge section is 251 µm and 58.3 µm, respectively. The grip and wedge connection have a thickness value of 50 µm to represent the non-thinned copper wedge sections. Dimensions for the length and width of the grip section and pinhole diameter were of the values as the 2D tensile specimen half models. In addition, due to the more gradual and symmetrical normal stress distribution along the gauge length of the tensile

specimen half model with only circular notch connections at the reduced sections, the 3D model adapted the specimen circular notches for connections at the wedge and grip section.

The model was meshed using trapezoidal elements using a global mesh size of $5.9x10^{-5}\ m$. To conform to the numerical limitations of the ANSYS Student License and reduced computational time of the model simulations, the mesh was refined only at the faces of the gauge section, leaving the grip and wedge sections with a much coarser mesh size. A refined mesh size of $2x10^{-6}m$ at the gauge section was used to obtain a more accurate and precise solution from the simulation.

The boundary conditions imposed on the 3D model can be seen in Figure 41. The 3D model was constrained differently from the 2D tensile specimen half model with circular notches. Because the 3D model represents the full geometry of the single tensile specimen, no roller supports were needed to indicate symmetry regions. Instead, a fixed support was assigned to the bottom face of the wedge component to prevent the model from moving freely under an applied tensile load. A uniform force was applied to the interior face of the pinhole to pull the specimen in tension in the Z-direction. In addition, to prevent the bending motion of the model in the Y and X directions, roller supports were applied to the front faces of grip and wedge component. The roller supports allows the model to be deform in the X and Y-directions (to satisfy the lateral deformation of the assigned material to the model).

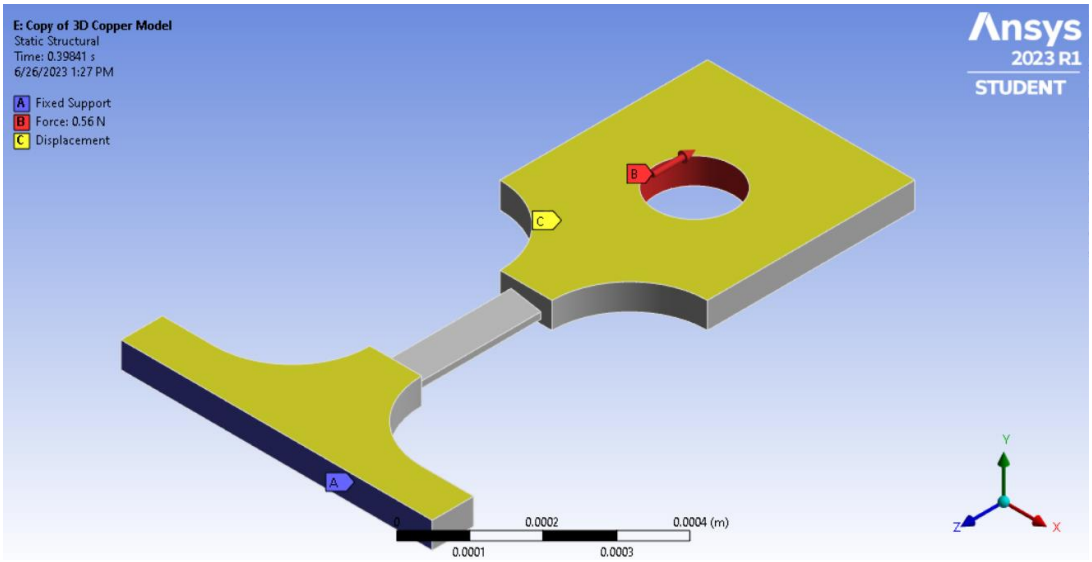

Figure 41: Boundary conditions applied to 3D tensile specimen model in ANSYS Mechanical.

After the model was applied with the appropriate boundary conditions and mesh criteria, the model was initially simulated under linear-elastic conditions. The model solutions for normal stresses and strains were extracted at a single nodal point on the gauge section by assigning a named selection to the nodal point. When the model was assigned to the material properties of 415 and (100) copper, correspondingly, the model solutions for the normal elastic strain in the Z-direction and X-direction, and normal stress in the Z-direction were obtained and compared with analytical solutions. The difference between the experimental model results and the numerical

results were less than 1%, as seen in the Table 4 and Table 5 of the summarized results for (100) copper and 415 stainless steel models, respectively. Figure 42 shows a plot of the normal stress distribution along the gauge length edge of the 3D model assigned to the material properties of (100) copper. In the plot, it is seen that the stress is maximized at the center of the gauge length (away from the reduced sections) under elastoplastic conditions. This is due to the plastic strain induced at the gauge section, where the cross-sectional area of the gauge reduces under increasing strain of the specimen, causing an increased in stress at the gauge section. The normal stress distribution in the Z-direction for the 3D model can be seen in Figure 43. In the figure, the model was simulated under non-linear elastoplastic condition and assigned to the material properties of (100) copper. Note, that, the maximum stress is located at the corner of the gauge section instead of the center of gauge surface, due to the stress concentration accumated at the sharp corner.

Table 4: FE Model Results: For 3D Tensile Specimen Model Assigned to (100) Copper

Mechanical Property	(100) Copper (Numerical Slution)	(100) Copper (ANSYS Result) Linear-Elastic	% Difference
ϵ_x	$-1.31x10^{-3}$	$-1.31x10^{-3}$	0.28
ϵ_z	$3.11x10^{-3}$	$3.12x10^{-3}$	0.28
$\sigma_z\ (MPa)$	$2.08\ x10^{8}$	$2.08x10^{8}$	0.28

Table 5: FE Model Results: For 3D Tensile Specimen Model Assigned to 415 Stainless Steel

Mechanical Property	415 Martensitic Stainless Steel (Numerical Solution)	415 Martensitic Stainless Steel (ANSYS Result) Linear Elastic	% Difference
ϵ_x	$-1.43x10^{-3}$	$-1.43x10^{-3}$	0.23
ϵ_z	$5.11x10^{-3}$	$5.12x10^{-3}$	0.23
$\sigma_z\ (MPa)$	$7.91x10^{8}$	$7.93x10^{8}$	0.23

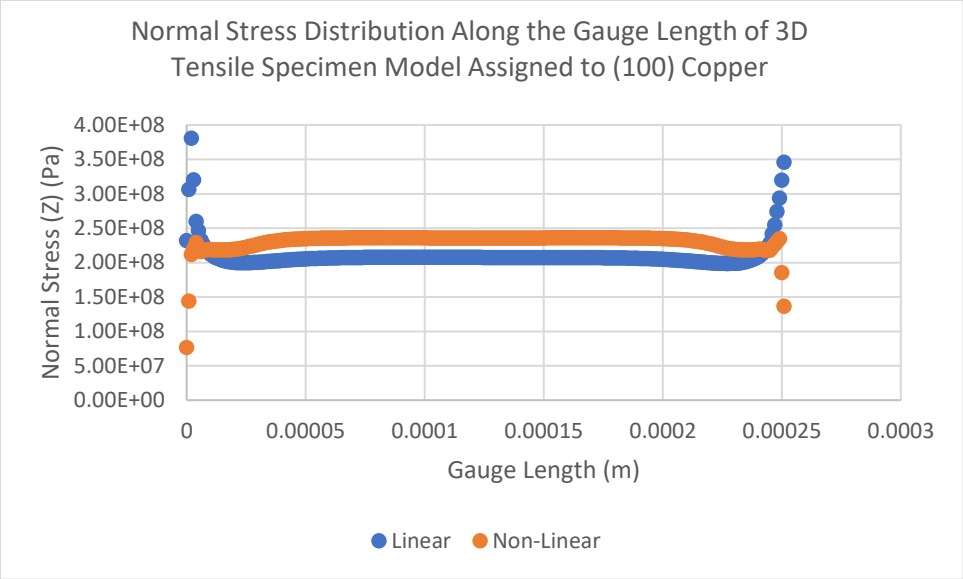

Figure 42: Plot of normal stress distribution along the gauge length edge of 3D tensile specimen model assigned to (100) copper under linear-elastic and elastoplastic conditions, respectively.

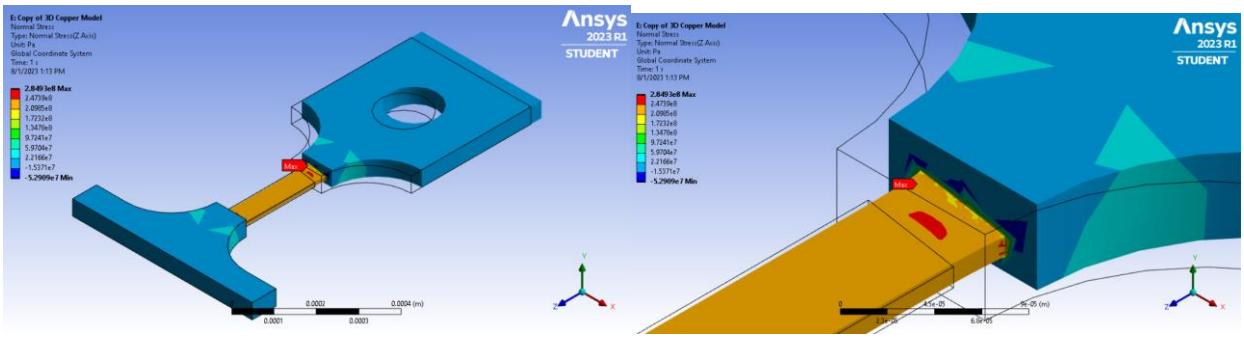

Figure 43: Normal stress distribution in the Z-direction (tensile direction) for 3D micro-tensile specimen assigned to (100) copper. Maxiumum stress localized t the corner of the gauge section (left image).

4.10. Comparison of Plasticity Models to Experimental Data

For each 2D model simulated under uniaxial tensile loading, both linear-elastic and non-linear elastoplastic deformation behaviour of the structures under the assigned material properties of 415 and (100) copper was represented through true stress and curves extracted from the model solutions. The total strain and normal stress were extracted at the nodal points located on the bottom left vertex of the one-element model and at the center of the gauge section of the tensile specimen models, respectively. Figure 44 and Figure 45 shows the stress-strain curves for all models simulated under uniaxial tensile loading assigned to the material properties of (100) copper and 415 stainless steel, respectively. The plots also include true stress-strain curves for the one-element model undergoing both a constant load force and a displacement load force (respectively).

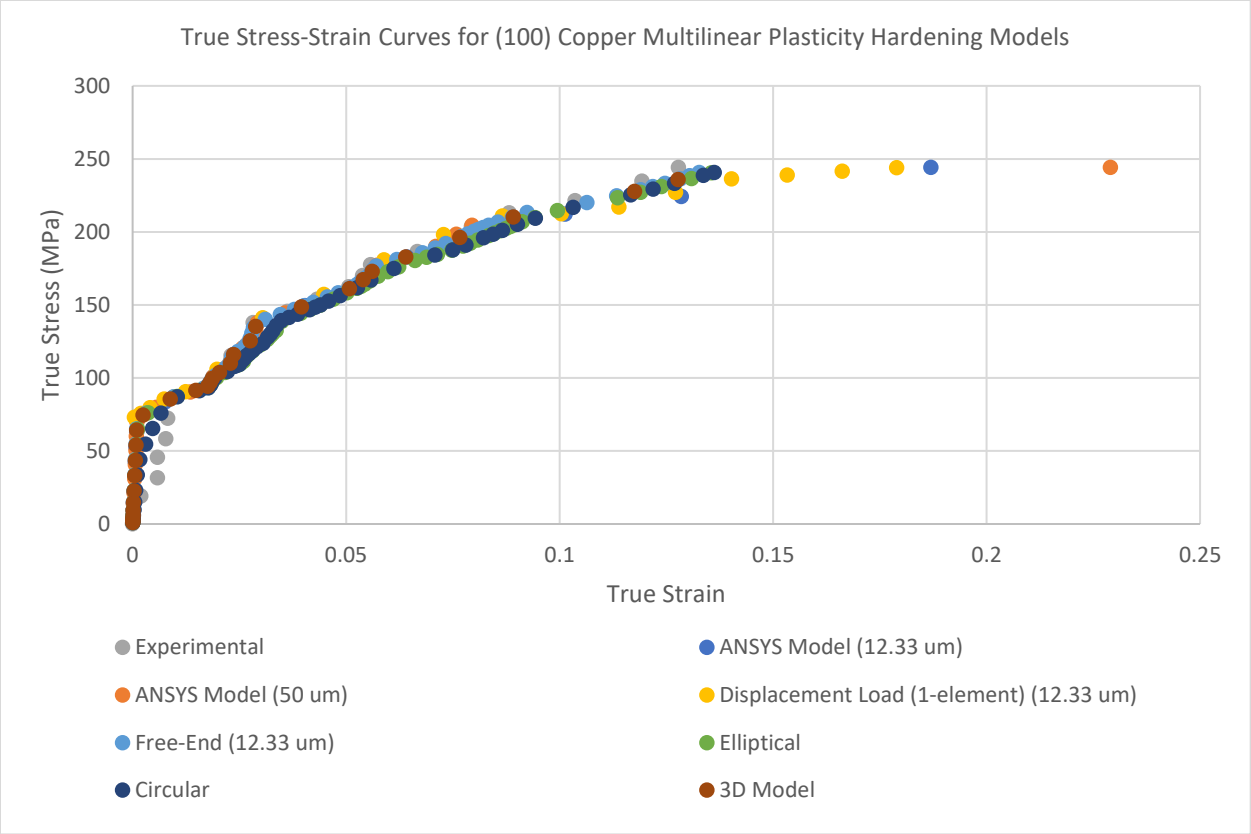

Figure 44: (100) copper models simulated under pure tension and elastoplastic deformation conditions using multilinear hardening took in ANSYS. Model results are compared to that of experimental tensile data.

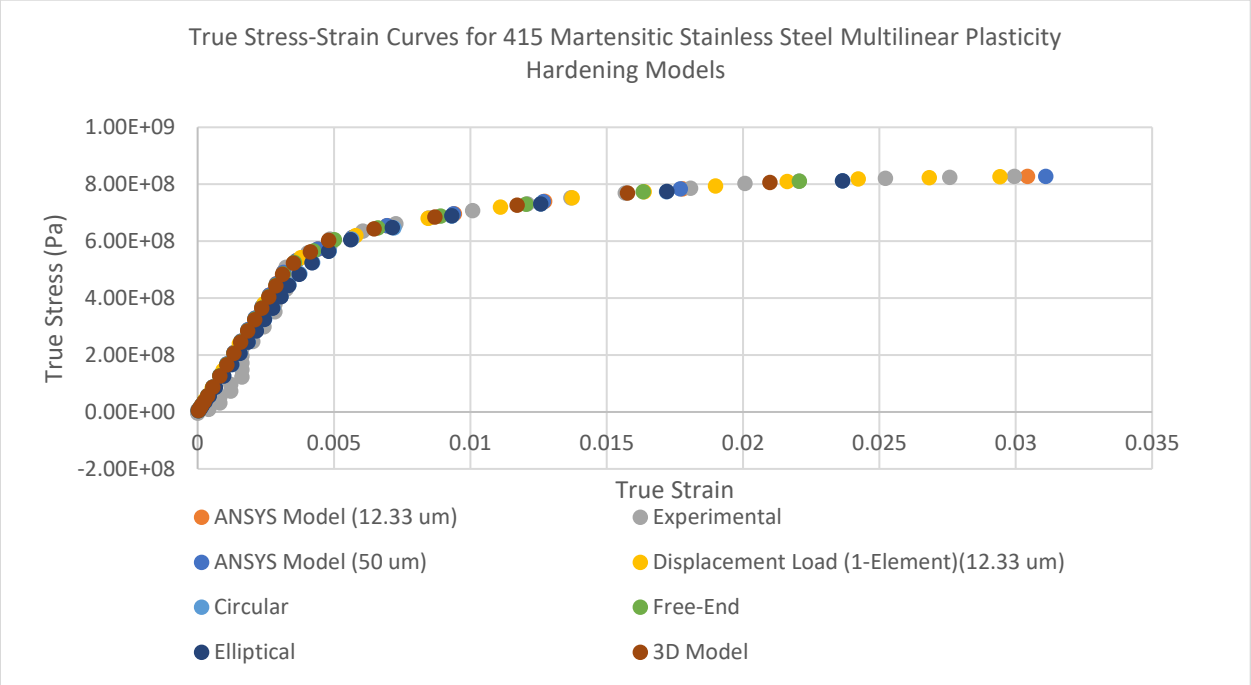

Figure 45: 415 stainless steel models simulated under pure tension and elastoplastic deformation conditions using multilinear hardening took in ANSYS. Model results are compared to that of experimental tensile data.

There were no differences seen in the mechanical behaviour of the models simulated under two different cross-sectional thicknesses of 12.33 µm and 50 µm. All stress-strain curves for the models of different tensile geometries, cross-sectional thicknesses, and load type showed a good fit to the experimental true stress and strain data of 415 and (100) copper, respectively. Although, a small deviation from the experimental data was seen for the 2D tensile specimen half models with an applied load force on only the upper half of the semicircular pinhole, as seen from the plot in Figure 46 for the material assignment of 415 steel. Since the specimens were only pulled partially on the pinhole (with the lower half of the pinhole unhindered by the tensile load, the specimens exhibit a slightly lower tensile stress at the gauge section (as seen by the lower stress distribution at the non-linear plastic hardening region of the true stress-strain curve). Therefore, when the load was applied to the full circular edge of the half pinhole, the stress evaluated at the gauge section fits more accurately to the experimental data. The difference in the tensile stress by which the load force was applied on the whole pinhole and partially at the pinhole is about 18.6% for the circular notch specimen and 75.6% for the elliptical notch specimen.

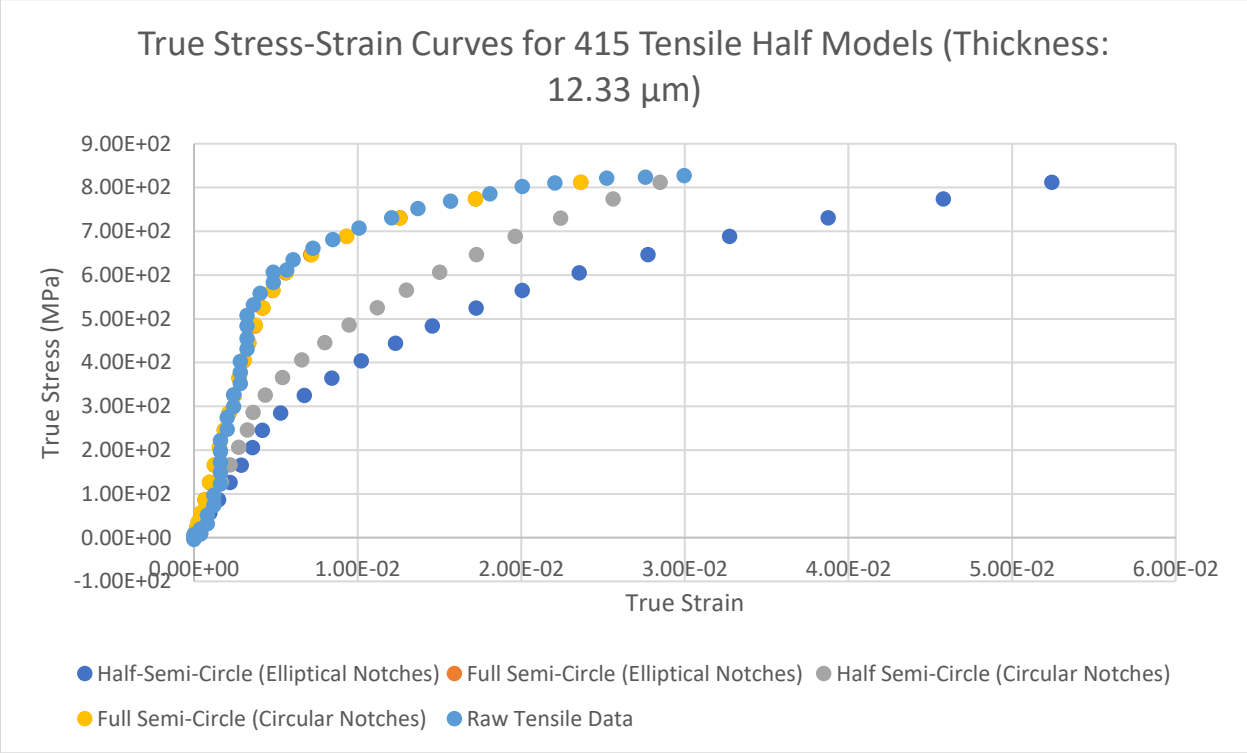

Figure 46: Difference between true stress-strain results of 2D tensile specimen half models (under elastoplastic conditions) when uniform force is applied to the half the semi-circular pinhole edge as opposed to the whole edge of the semi-circular pinhole.

4.11. Summary and Conclusions on the FEA Models

From the FEA models developed in ANSYS, it was concluded that the correct mechanical behaviours were used for the four tensile specimen models in tension, including the linear-elastic response of reversible deformation and non-linear elastoplastic deformation regions of the

model's stress-strain curves for the material assignments of (100) copper and 415 steel, respectively). Through the gradual transition of simple to complex modelling of static structural models simulated under uniaxial tensile loading, appropriate boundary conditions were chosen, and the mechanical response validated using numerical solutions. In addition, it was seen through the normal stress distribution along the gauge length that elliptical notches provide a sharper transition of stress between wedge component and the gauge section, while the circular notches provide a more gradual transition of stress distributed between the reduced sections of the gauge. It was observed from the 2D ad 3D tensile specimen models that the normal stress distribution along the edge of the gauge length was the highest near the reduced sections of the wedge and grip connections under linear-elastic deformation. However, when tensile specimens were deformed under non-linear elastoplastic conditions, the maximum normal stress was located near the middle of the gauge section. The model's stress-strain results indicate that the tensile specimens would likely fracture at the middle of the gauge section if the tensile specimens were constrained and aligned well in the sample holder and micro-tensile bench during micro-tension testing.

The 3D model was able to incorporate a more realistic geometry of the micro-tensile specimens by including the tilted gauge section produced from the thinning method using the PFIB and adopted from Robert Wheeler. To improve on the geometry condition of the 3D model, it is recommended that additional circular notches would be assigned to corners of the thinned gauge section (to represent the curvature induced from ion milling). After thinning of the gauge section in the PFIB via milling, it is seen that the sputtering of ions in the materials created curved edges along the gauge width due to the mechanisms of ion sputtering. Therefore, it would be important to incorporate curvature at the gauge width edges to match a realistic model of the fabricated micro-tensile specimens.Without the fillets at the gauge corners, the maximum normal stress in the tensile load direction would be located at one of the corners of the tilted gauge section. The addition of the fillets would help to eliminate the stress concentration near the edge of the gauge width and allow for the stress to be distributed symmetrically along the gauge section.

XII. Chapter 5: Fabrication Process of Copper Micro-Tensile Specimens

5.1. Introduction

In this chapter, the fabrication process and methods for producing the copper micro-tensile specimens used for studying the size effect phenomenon are discussed. After simulating the mechanical response of the 2D and 3D FEA models of the micro-tensile specimens assigned to the material properties of (100) copper, the micro-tensile specimens were ready to be fabricated. A copper foil with a 99.998% purity orientated in the <001> direction was used as the base

material to fabricate the micro-tensile specimens out of. In addition, for the size effect study, single crystal copper was chosen for its well-known mechanical studies performed through miniature-scale mechanical tests on its anisotropic mechanical properties in literature [15]. Specifically, micro-tensile specimens and micro-compression pillars have been fabricated to perform mechanical testing for the study of distinct dislocation mechanisms that occur in the substructure of size-limited specimens, as discussed in Chapter 1 of this thesis document. As mentioned in literature, the change in specimen size for observing size-limited deformation behaviour is often done by varying the pillar diameter or pillar side length for micro-compression pillars and varying the aspect ratio (side length to width) of the gauge section for micro-tensile specimens. For this project of studying the size effect in the copper micro-tensile specimens, the gauge cross-section is varied throughout a range of thickness values from 4 µm to 32 µm. 2-3 micro-tensile specimens of similar gauge cross-sectional thickness were produced to add reproducibility and to define standard deviations in the mechanical behaviour in the stress-strain curves of the corresponding specimens.

Two innovative machining methods for the micro-tensile specimen fabrication are investigated. The first machining method uses only the Helios 5 UXe Dual Beam Plasma FIB-SEM to fabricate the specimens out of individually prepared (100) copper foil wedges, including the specimen geometry cutout, thinning process, cleaning of rough edges on the gauge section, and tungsten precursor-deposited reference fiducial marks. The fiducial marks are used to track the strain accumulated during in-situ mechanical tensile-testing of the specimens. The term used to reference the first fabrication method is PFIB-machined micro-tensile specimens throughout the context of this thesis.

The second fabrication method studied consists of both machining routes of the PFIB and the fs-laser from a ZEISS 350 Crossbeam to prepare the same geometry as the first fabricated machining method of PFIB- machined copper micro-tensile specimens. Due to the significantly high material ablation rate of the fs-laser, the fs-laser is used to cut out the tensile specimen geometry, while the PFIB is used to thin the gage section of the specimens, clean up rough edges, and to deposit the reference fiducial marks in the second fabrication method studied. The second fabrication method is termed as fs-laser-machined micro-tensile specimens. From both fabrication methods for producing the micro-tensile specimens, the machining time, cleaning-up process from the rough machining steps, machining quality, and differences in mechanical behaviour between specimens of different machining methods are examined.

The micro-tensile specimens were also used to test the accuracy of a newly custom-built micro-tensile bench and to see whether the geometry of the fabricated micro-tensile specimens (with the adopted thinning method from Robert Wheeler) would provide accurate results that display a mechanical size effect from the post-mechanical test data, as seen for copper micro-mechanical test specimens observed in literature.

5.2. Materials and Apparatus

A 50 mm x 5 mm x 0.050 mm thick 99.998% pure (100) copper foil (non-annealed) was commercially purchased from Thermo-Fisher Scientific to be used as the base wedge for machining out the micro-tensile specimens. Small rectangular wedges with dimensions of 15 mm x 10 mm x 0.05 mm were cut out of the bulk copper foil, in order to meet the specimen geometry constraints for placing the base wedge containing the micro-tensile specimens inside the PFIB chamber and the custom-built micro-tensile bench. For the PFIB chamber, the height of the copper wedge is limited when the wedge is flipped 90 degrees on the specimen wafer holder for performing the gauge thinning process (where the cross-section of the wedge faces normal to the ion beam). The height of the wedge must be between the minimum and maximum clearance of a 4mm working distance, (which is measured prior to pumping the PFIB chamber). In addition, the wedge must also fit on the specimen holder of the micro-tensile bench to secure the specimen in place with screwed grips, as seen in Figure 47. The individual wedges were cut out using a carbon steel blade and two glass sliders to hold in the foil flat between the incision line. Four wedges were prepared for the fs-laser-machined specimens, while three wedges were prepared for the PFIB-machined specimens of the same dimensions. The targeted number for micro-tensile specimens machined were 24, with 6 on each of the 4 individual wedges of the fs-laser-machined specimens, and 8, 10, and 3 for the three individual wedges of the PFIB-machined specimens, correspondingly.

Figure 47:Copper wedge placed on the specimen holder prior to insertion into the custom-built micro-tensile bench.

5.3. First Fabrication Process: PFIB-Machined Copper Micro-Tensile Specimens

For the initial batch of copper micro-tensile specimens, the order of the fabrication steps is as followed; tensile specimen geometry cutout, thinning of the gauge section, cleaning of rough edges, and deposition of reference fiducial marks. As mentioned in Chapter 2, the capabilities of the PFIB for using high ion currents for milling, high special resolution, and non-reactive nature of Xe atoms allows the PFIB to be a preferential machining method for fabricating the copper micro-tensile specimens.

5.3.1. Tensile Specimen Geometry Cutout

The first step of the fabrication process is creating the geometry of the micro-tensile specimen out of the copper wedge prior to the thinning process of the gauge section. The geometry cutout follows the same dimensions for a full-scale model of the 2D tensile specimen model with elliptical notches, as shown in Figure 32. To produce the tensile specimen cutout for PFIB-machined micro-tensile specimens, surrounding material of the tensile geometry is removed using milling patterns arranged in an outline of the specimen geometry. The milling patterns are provided by the FEI (Field Electron and Ion Company) software of the PFIB's user interface. The tensile specimens are machined one wedge at a time. Therefore, after each process is finished for each wedge, the pervious wedge is taken out the PFIB chamber and replaced with the next wedge to be machined. The wedge of interest was initially secured onto a custom-built wafer holder using a bolt and allene key. On the wafer holder, the cross-section of the wedge faces upwards. A stub holder is then used to hold the wafer holder containing the wedge in place onto the stage PFIB chamber. When the wafer holder is placed onto the stub holder, the cross-section of the wedge is flipped 90 degrees to allow the surface of the wedge to face upwards. At this configuration, the ion beam is expected to sputter away material at an incident angle of normal to the wedge surface, which is seen in Figure 48 for one of the copper wedge during the geometry cutout process. In addition, prior to pumping the chamber of the PFIB, the height of wedge on the stage is measured to make sure the clearance between the 4 mm working distance from the SEM polepiece and the height of the specimen is met.

After the chamber is pumped to a high vacuum environment, the eucentric height of the specimen is set. The eucentric height is the point in which the position of the specimen does not change in the Z-direction (direction towards the polepiece) when the tilt of the stage is changed. The eucentric height is set by focusing on a feature on the surface of the copper wedge at a high magnification of 10 µm or higher. Once the height of specimen remains constant at a tilt range from 0 to 52 degrees, the stage can be tilted to the 52-degrees configuration for performing ion milling (as seen in Figure 48). The surface of the wedge is also focused and aligned horizontal to the ion window's field-of-view at the edge of the wedge. Alignment of the edge allows for the tensile specimens to be lined up at the edge at approximately the same height as one another. Once the specimen is aligned and focused, milling boxes (consisting of circles and rectangles are used to create the outline of the tensile specimen geometry cut out. Tensile specimens are cut out one-by-one due conform to the size limitation of the ion beam's field-of-view size (of 500 µm x 700 µm for milling using an ion current of 2.5 µA). The tensile specimens are lined up beside one another along the edge of the wedge, as seen in Figure 49. The clearance between each specimen grip is approximately 20 µm.

Figure 48: Specimen and stage configuration in Helios Plasma-FIB chamber for cutting out tensile specimen geometries, cleaning of gauge edges, and deposition of fiducial marks.

To machine of the micro-tensile specimen cutouts, the highest ion current of 2.5 µA provided by the PFIB and an ion voltage of 30 keV were used for the fabrication step. The depth in which the ions penetrate through the top surface and through the bottom surface of the wedge was set to 70 µm in the Z-direction to ensure the tensile specimen geometry was fully milled-out. For each tensile specimen cutout, the milling process was performed in parallel. The parallel milling configuration offered by the PFIB allows for all the milling shapes in the tensile specimen pattern to be milled out at the same time with consistently the same penetration depth, as opposed milling in series configuration, where each milling box is milled one-by-one in the pattern.

The relatively high ion current and voltage used allows for the tensile specimen cutouts to be milled out quickly, while still maintaining a high-quality machining of the freshly milled edges of the specimen cutout. Each tensile specimen cutout took approximately 40 minutes. The total machining time for 24 specimens took approximately 16 hours (excluding the alignment time, construction of tensile specimen milling pattern, and transferring of wedges in and out of the PFIB chamber). For the three wedges, 10 specimen cutouts were machined on the first wedge (labelled PFIB-machined copper wedge 1), 8 on the second wedge (labelled PFIB-machined copper wedge 2), and 6 on the third wedge (labelled PFIB-machined copper wedge 3). SEM images of the final tensile specimen cutouts for wedge 2 can be seen in Figure 49.

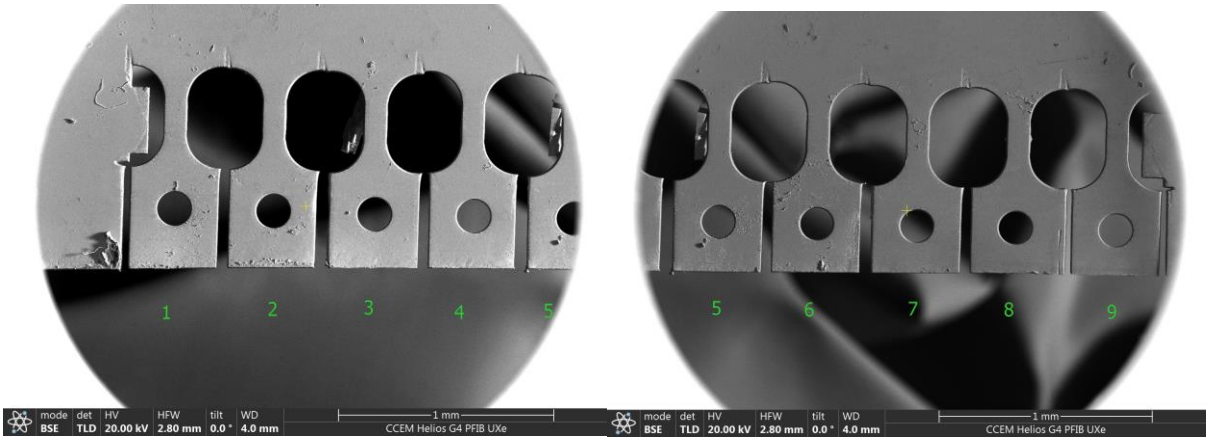

Figure 49: Final PFIB-machined copper micro-tensile specimen cutouts on wedge 2.

5.3.2. Thinning of the Gauge Section

The thinning process of the gauge section was the second fabrication step performed after tensile specimen cutouts were completed. For the thinning process, only the gauge cross-section is reduced in thickness, while the remainder of the tensile specimen region is kept to an initial thickness value of 50 µm. The thinning method used for the copper specimens was developed by Robert Wheeler. A schematic showing the thinning method of the tensile specimens with the ion beam of the PFIB is shown in Figure 50. The thinning method allows for a thinned parallel gauge section to be produced, while adding a tilt to the section in conjunction to the surface of the grip and wedge connection. The tilt is produced by tilting the stage and specimen a few degrees away the 52-degrees milling configuration.

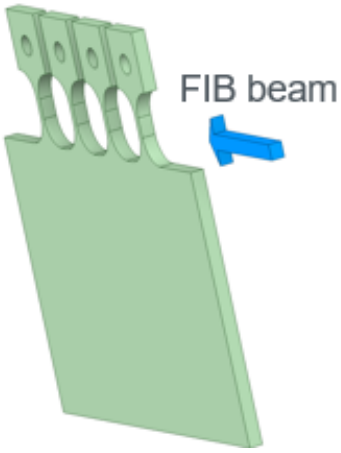

Figure 50: Schematic of tensile gauge thinning method developed by Robert Wheeler.

After the tensile specimen cutouts were produced, the wedge was taken out of the PFIB chamber in order to reorientate the position of the wedge on the stage for performing the thinning process in the PFIB. When the wedge was taken out of the chamber, the stub holder was detached from the wafter holder. For performing the thinning process, only the wafer holder is

attached to the cross-holder on the stage in order to position the copper wedge with the cross-section facing normal to the ion beam at the 52-degrees milling configuration, as seen in Figure 51. In addition, due to the height limitation of the PFIB chamber, the dimension of the wedge becomes significant. From the initial fabrication step of the milling out the tensile specimen cutouts, the specimens were cut out on the shorter edge of the wedge (of 10 mm) in order for the wafer holder to clamp the longer edge (of 15 mm) when performing the thinning process. In addition, the position allows for the gauge cross-section of each specimen to be seen in the line-up of the tensile specimens with the few degrees stage tilt away from the 52-degrees milling configuration.

Figure 51: Specimen and stage configuration in Helios 5 Plasma-FIB chamber for thinning gauge sections of copper micro-tensile specimens.

After the specimen was loaded into the chamber, focusing, alignment, and the specimen's eucentric height was performed on the cross-section of the copper wedge. A feature on the cross-section is used to set the eucentric height. Due to roughness of the copper edges, the highest point on the cross-section must be located as the eucentric point in order to meet the 4 mm working distance requirement of the PFIB. To create the line-of-sight for observing the surfaces of the tensile specimens during thinning of the gauge sections, the stage was under-tilted from the 52-degree milling configuration by 3-10 degrees. The under-tilt allows for the top surface of specimens to be seen, rather than the cross-section of the wedge. The degree of the under-tilt of the specimen depends on the flatness of the copper wedge and the clearance of negative space between each gauge section of the tensile specimen. The clearance must be large enough to place rectangular milling boxes at the top and bottom edges of the gauge section for performing the thinning process. The copper wedges are easily malleable and can bend during handling with tweezers and preparation of cutting the individual wedges with the carbon steel blade. Therefore, there isa slight curvature for some of the copper wedges. To compensate for the curvature, the PFIB stage is tilted with a higher under-tilt angle than compared to a flat wedge, in order to see the clearance of negative space between the top and bottom edges of the gauge section. For flat

wedges, the under-tilt ranged from 3 to 4 degrees (with stage tilts of 49 to 48 degrees, respectively). For wedges exhibiting curvature, an under-tilt of 12 to 14 degrees (with stage tilts of 40 to 38 degrees, respectively) was used to observe the specimens on the top surface of the wedge.

During the geometry cutout process, large circle-shaped milling patterns of 150 µm in diameter were used to create the circular notches of the wedge and grip connections. When the circle patterns overlap with one another, a large clearance of surrounding material was be removed during milling of the tensile specimen cutout. Figure 52 and Figure 53 show the clearance between each gauge section, allowing for milling boxes to be placed at the top and bottom of the gauge length edges for thinning the gauge section without milling through the neighbor specimens. After the specimens were located on the top surface, the ion beam was refocused at a low ion current of 10 nA (to prevent ion-induced damage to the specimens). A focused ion beam allows for a high-quality milled surface to be produced.

Prior to placing two rectangular cleaning-cross-sectional milling boxes on the top and bottom edges of the gauge section length edges, the initial thickness of the gauge cross-section was measured. In addition, rectangular measurement boxes were used to center the milling boxes at the gauge section. The reduced section containing the notches were not thinned. Therefore, the length of the milling boxes was only extended out to the gauge section. The length of the milling boxes had a consistent value for all PFIB and laser-machined specimens during the thinning process to establish a consistent length of the gauges for all specimens fabricated for the size-effect study of (100) copper. Therefore, the length of the top and bottom milling boxes had a fixed value of 244.4 µm. In addition, the top and bottom milling boxes were centered by keeping the X-position of the two milling boxes the same. For the size effect study, the target thickness of the gauge sections are 5 µm, 10 µm, 20 µm, and 30 µm.

Figure 52 and Figure 53 show ISE images taken before and after the thinning of the gauge section for specimen 5 from wedge 1. The final thickness values for each PFIB-machined copper tensile specimen are listed in Table 6. The target thickness value is the space produced between the top and bottom milling boxes. The gauge sections of each specimen were thinned with an ion voltage of 30 keV and an ion current of 0.2 µA. Due to the beam tails (causing broadening of the ion beam) at the ion current of 0.2 µA, an extra clearance of 5µm was added between the target thickness of the top and bottom milling boxes.

Cleaning cross-sectional rectangular milling boxes were used for thinning the gauge sections. Cleaning cross-sectional milling boxes allows for directional milling to be performed in series configuration. A Z-depth of 70 µm was used for thinning the cross-section of the gauge for both the top and bottom milling boxes. The milling direction for the bottom rectangular cleaning cross-sectional milling box was set to mill from the bottom to the top of the milling box. And for the top milling box, the milling direction was set to start from the top of the milling box to the bottom of the milling box. This configuration for the milling process allows for material to be completely removed to the specified Z-depth in a controlled timely manner. When the Z-depth increases for the rectangular cleaning cross-sectional milling boxes, the milling time also increases. In addition, decreasing the ion current also increases the milling time.

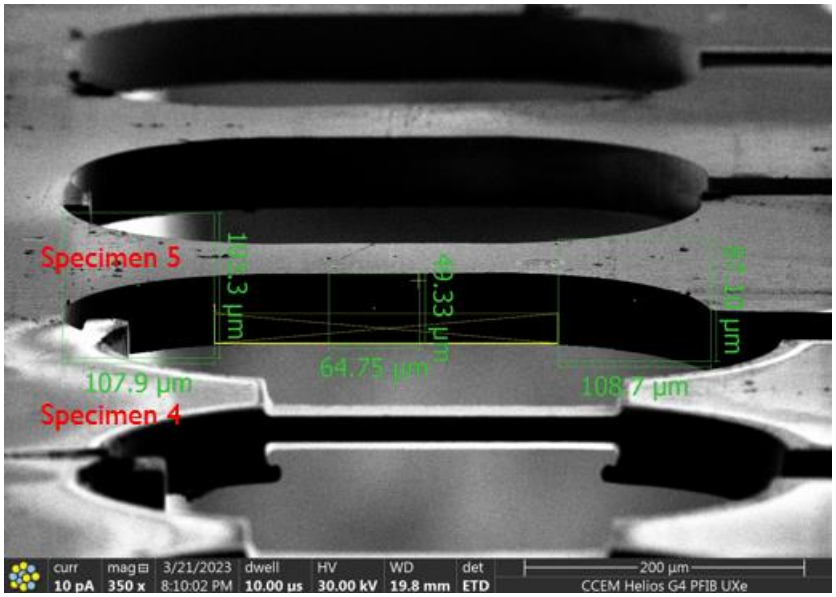

Figure 52: ISE image showing placement of the measurement boxes and bottom milling box on the gauge section prior to performing the thinning process of the gauge section for PFIB- machined specimen 5 on wedge 1.

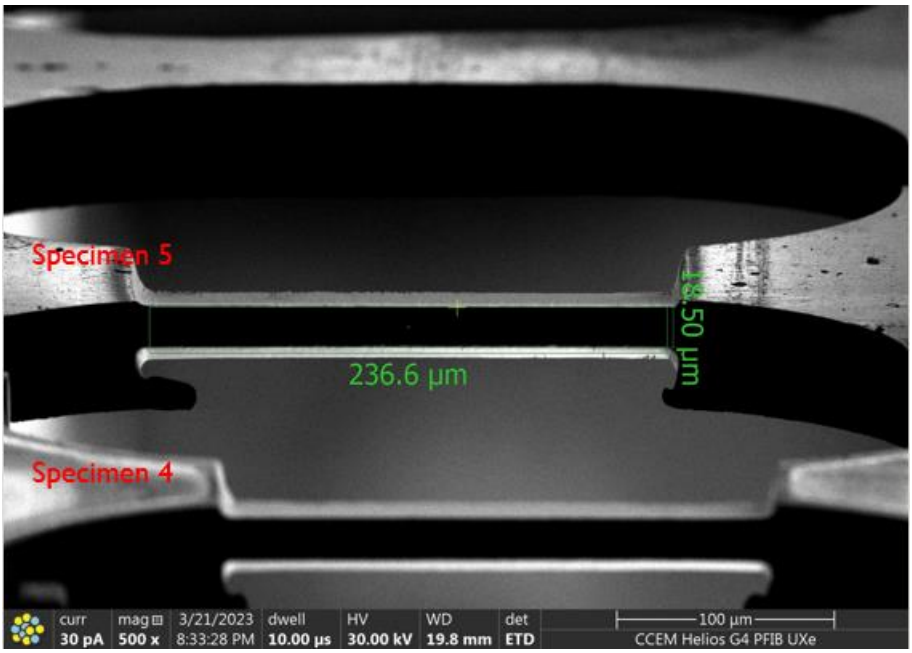

Figure 53: ISE image showing the true thickness of the PFIB-machined specimen 5 on wedge 1at a stage tilt of 42 degrees.

Table 6: Final Gauge Thickness Values for PFIB-Machined Copper Micro-Tensile Specimens.

Specimen	Gauge Thickness (µm)
Wedge 1- Specimen 1	19.1
Wedge 1- Specimen 2	20.0

Wedge 1- Specimen 3	13.5
Wedge 1- Specimen 4	18.5
Wedge 1- Specimen 5	18.5
Wedge 1- Specimen 6	14.1
Wedge 1- Specimen 7	15.4
Wedge 1- Specimen 8	18.1
Wedge 1- Specimen 9	12.3
Wedge 1- Specimen 10	20.8
Wedge 2- Specimen 1	11.2
Wedge 2- Specimen 2	10.0
Wedge 2- Specimen 3	12.3
Wedge 2- Specimen 4	11.6
Wedge 2- Specimen 5	12.3
Wedge 2- Specimen 6	6.0
Wedge 2- Specimen 7	5.7
Wedge 2- Specimen 8	5.0
Wedge 3- Specimen 1	26.2
Wedge 3- Specimen 2	25.4
Wedge 3- Specimen 3	31.6
Wedge 3- Specimen 4	31.6
Wedge 3- Specimen 5	28.8
Wedge 3- Specimen 6	31.4

The thinning process begins with the specimen near the edge of the wedge (closest specimen in the ion beam's field-of-view). After the first specimen was thinned, the final thickness and gauge length was measured using a measurement box over the gauge section. Afterwards, the wedge was moved in the Z-direction to bring the next specimen in the line-up to be thinned. Focusing of the ion beam is performed at 10 nA when a new specimen in-line is brought closer to the field -of-view for thinning. The process of thinning was repeated until all gauge sections of the specimens on the wedge were thinned to their targeted thickness value. Approximately 4-6 copies of each corresponding thickness value were produced for repeatability during mechanical testing. The milling time for each gauge section that is thinned is dependent on the target thickness of the gauge section and the ion current used. For the 30 μm thick gauge section produced, the milling time took approximately 7-11 minutes while the most thinned gauge sections with thickness values of 4-6 μm took approximately 20-23 minutes with an ion current of 0.2 μA, respectively. As well, all 24 specimens across the three wedges were thinned with the same method adopted from Bob Wheeler.

After the gauge section was thinned for each specimen on the wedge, an ISE image was taken to measure the final thickness of the thinned gauge. The edges of the thinned gauge section produced an edge effect, in which a thin white layer is observed on the top and bottom edge of the gauge lengths, as seen in Figure 52 for specimen 5 of PFIB-machined copper wedge 1. The white layer is an accumulation of ion-induced secondary electrons at the edges. The edge effect is caused by the difference in the topology of the specimen, in which more secondary electrons

are emitted from the subsurface of the specimen at elevated surfaces compared to that of flat surfaces. In addition, a small curvature of the gauge edge was produced after thinning the gauge section. The curvature of the edges is due to ion interactions with the material during ion sputtering.

5.3.3. Cleaning of Gauge Section Rough Edges

After thinning the gauge sections of each PFIB-machined copper tensile specimen, surface roughness along the right and left-hand edges long the gauge length removed using low ion current milling performed with the PFIB. The surface roughness comes from curtaining produced during the tensile specimen geometry cutout process. Curtaining is unavoidable in the milling process due to the difference in surface topology from rolling deformation induced during the material processing of the copper wedge. Rocking polish is way to eliminate curtaining. Although, rocking polish is difficult to perform for a thin wafer attached to a cross-holder on the PFIB stage. Therefore, the additional step of cleaning the edges by removing the layer of surface roughness is performed for all copper tensile specimens (including both PFIB and fs-laser-machined specimens).

The copper wedge was taken out of the PFIB chamber after the gauge sections of all the specimens on the wedge were thinned. The wafer holder containing the wedge is reattached to the stub holder that was used during the specimen geometry cutout process. The height of the specimen is remeasured and reintroduced into the PFIB chamber. The eucentric height was set by focusing on a feature on the surface near the edge of the wedge. After setting the eucentric height, the tensile specimens were located on the wedge. The SE beam is used to observe the roughness of the gauge length edges at a 0-degree stage tilt. From analyzing the surface of the wedge using the SE beam, curtaining was seen on the surface of the gauge section from the thinning process. Alignments were performed in the ion beam window by aligning the gauge length edge of one of the specimens vertically (90 degrees from the width of ion beam's field-of-view).

The removal of the edge roughness along the gauge length was performed by introducing two milling boxes at the right and left gauge length edge, respectively, as seen in right SEM image of Figure 54. The cleaning of the edges was performed on the specimens on the wedge one-by-one. The length of the milling boxes was kept at a constant value of 248.2 μm for all the specimens cleaned in this milling process. The initial set width of the milling boxes was 5 μm. The width of the milling boxes was extended to account of the curvature of the rough edges near the reduced section of the wedge and grip connections. Prior to applying the milling boxes, the initial width of the gauge section was measured in order to center the milling boxes horizontally across the gauge width, as seen in left SEM image in Figure 54. In addition, the two milling boxes placed at the left and right gauge length edges have the same X-position to maintain symmetry of the gauge length after the edge roughness was removed.

Rectangular cleaning cross-sectional milling boxes were used to clean the edges. The milling was performed from left to right for the left milling box and right to left for the right

milling box with an indicated Z-depth (being approximately the size of the gauge thickness). For all of the tensile specimens, the removal of the rough edges was performed at an ion current of 0.2 µm and an ion voltage of 30 keV. Figure 55 shows an SEM image of specimen 3 from wedge 2 of the cleaned edges of the gauge section. From the milling process, the removal of the edge roughness reduces the width of the gauge section. After the edges of each specimen was cleaned, the final width and length of the gauge section was measured.

Figure 54: ISE images of gauge section of copper tensile specimen 3 from wedge 2 prior to cleaning of the edges. Left image shows centering of milling boxes using measurement boxes and right image shows final position of milling boxes prior to initiation of ion milling.

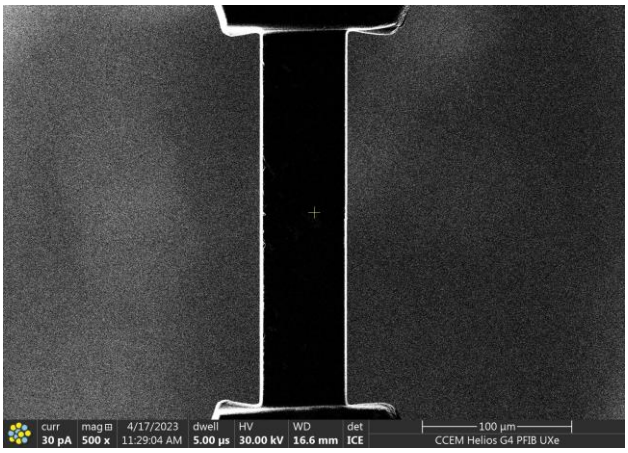

Figure 55: ISE image of the cleaned gauge section from copper tensile specimen 3 from wedge 2.

5.3.4. Fiducial Marks

The final step in the fabrication process for the PFIB-machined copper micro-tensile specimens is the deposition of reference fiducial marks on the gauge section. The reference fiducial marks were used to track the elongation of the gauge. During the mechanical testing of the copper tensile specimen, the specimen is strained at increasing load intervals induced by the micro-tensile bench. Between each load interval, the load is kept constant to take an SEM image of the elongated specimen with the deposited fiducial marks on the gauge surface. The fiducial

marks were created using a tungsten deposited precursor gas in the PFIB. The pattern of the fiducial marks are two X shapes deposited near each end of the gauge section. Each X-shaped fiducial mark was created with two 10 µm x 2 µm rectangular deposition boxes rotated 45 degrees in the ion beam's field-of-view. The fiducial marks were only deposited on one side of the gauge surface of each tensile specimen. Only two fiducial marks were needed to measure the strain from one end of the gauge (near the wedge) to the other of the gauge (near the free-end grip). During the data analysis of the post-mechanical testing of the copper tensile specimens, the X and Y coordinates at a point location on each fiducial mark was measured using ImageJ software. A more detailed explanation of the calculation for the strain of the copper tensile specimens can be found in Chapter 6 on the mechanical testing and results of the copper tensile specimens.

After the edges were cleaned for all the tensile specimens on the wedge, the deposition of the fiducial marks was performed with the same stage position of the wedge. Therefore, the wedge did not need to reorientate or taken out of the PFIB chamber to deposit the fiducial marks. The deposition of the tungsten precursor gas was performed with the wedge surface facing normal to the ion beam at the 52-degrees milling configuration. The multi-chem injector for the precursor gas was inserted into the chamber view at the set working distance of 4 mm and at the ion default configuration of the 52-degrees stage tilt. Compared to other precursor gases such as carbon and platinum available on the Helios 5 UXe Dual Beam Plasma-FIB, tungsten is the hardest material and must be deposited at a controlled rate. For producing the fiducial marks on the gauge surface, tungsten was deposited at an ion voltage of 12 keV as opposed to a very high ion voltage of 30 keV to prevent the formation of gas bubbles in the tungsten deposition. In addition, due to the dimensions and target depth of the fiducial marks, the highest ion current that can be used to deposit the fiducial marks is 0.33 nA for a 10 µm x 2 µm rectangular milling box with a 2 µm target depth. Therefore, the readily available current in the PFIB used for the deposition was 0.1 nA. Prior to the insertion of the multi-chem injector, the gauge section is moved into the left-side of the field-of-view of the ion beam to ensure the multi-chem would not over-shadow the gauge -section. When the multi-chem comes in front and covers the view of the specimen, the deposition of the fiducial marks will not be deposited onto the gauge section of the tensile specimen. Focusing, image brightness, and contrast were adjusted prior to deposition of the fiducial marks. The deposition pattern of the two fiducial marks was deposited in parallel configuration for each tensile specimen on the wedge. The deposition took approximately 2-3 minutes for each specimen. Figure 56 shows an SEM image of the deposited fiducial marks on specimen 4 of PFIB-machined copper wedge 1. After the deposition for specimen on the wedge, the multi-chem was retracted from the chamber to allow for analysis of the specimen using the SE beam at the 0-degree stage tilt configuration. Afterwards, the wedge was moved in the X-direction to repeat the deposition process for the next specimen in line by focusing the ion beam at 10 nA prior to insertion of the multi-chem. Figure 57 shows the final PFIB-fabricated micro-tensile specimens for wedge 3.

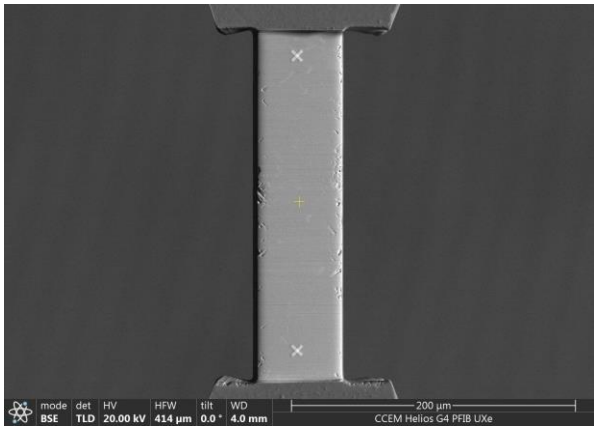

Figure 56: Final fabrication stage of PFIB-machined copper micro-tensile specimen 4 from wedge 1.

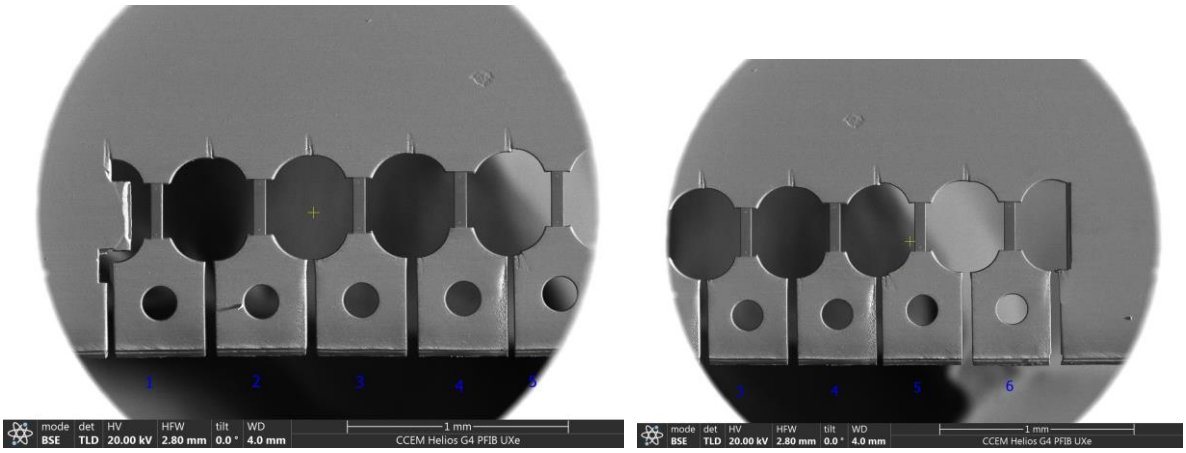

Figure 57: Line up of PFIB- machined copper micro-tensile specimens after fabrication process for wedge 3.

5.4. Second Fabrication Route: Fs-Laser and PFIB -Machined Copper Micro-Tensile Specimens

In the second fabrication method, the fs-laser and PFIB were both used to machine the copper micro-tensile specimens. The role of the fs-laser from the Zeiss Crossbeam 350 was to make the tensile specimen geometry cutouts out of each individual copper wedge (as opposed to using the PFIB, which was done for first fabrication method). The process parameters of the fs-laser can be optimized to provide a high resolution and material ablation rate for machining the cutouts of the tensile specimen geometry with dimensions ranging from tens to hundreds microns. The optimal laser parameters chosen to machine high quality surfaces and edges is material dependent. For example, some materials are softer, while some are harder than others. The type of material can determine the material removal rate, laser fluency, laser velocity, and

laser power. While the fs-laser-ablation process of the tensile specimen cutouts can be relatively quick, the laser can leave a layer of laser debris on top of the specimen surface from the ablation process. Therefore, sonication-cleaning with alcohol solution was used to remove the laser debris laser on tensile specimen surfaces. In addition, the fs-laser follows a Gaussian beam distribution, in which the laser beam's spot size broadens when it penetrates deeper into the material. The broadening of the beam can lead to a tapering of the edges of the newly laser-ablated material surface.

The PFIB was used to thin the gauge sections after creating the tensile specimen geometry cutouts using the fs-laser. The thinning process follows the identical thinning method used for PFIB-machined copper micro-tensile specimens. In addition, the PFIB was also used to clean the edges of the gauges section from the tapering caused by the Gaussian beam distribution of the fs-laser. At the same time of removing the tapers, the PFIB also removes rough edges developed from curtaining by the fs-laser during the specimen geometry cutout process.

The fabrication processes were compared between each other for the PFIB-machined micro-tensile specimens and the fs-laser-machined micro-tensile specimens. Similarly, 24 tensile specimens were machined and distributed on four 15 mm x 10 mm x 0.050 mm (100) copper wedges, with each wedge contained 6 fabricated tensile specimens. The wedges labelled wedge 1, wedge 2, wedge 3, and wedge 4. The same target gauge thickness values of 5 µm, 10 µm, 20 µm, and 30 µm for the tensile specimens were prepared.

5.4.1. Tensile Specimen Geometry Cutout with Fs-Laser

The fs-laser from the Zeiss Crossbeam 350 was used to make laser cutouts of the tensile specimen geometry on each of the four copper wedges. This step of the fabrication process was performed by *Travis Casagrande* (research associate and technician at the CCEM), who operated the Zeiss Crossbeam 350 to create the specimen cutouts with the fs-laser and prepared the CAD drawings of the tensile specimens. According to Travis Casagrande, the fs-laser's process parameters were optimized for a quick ablation process using the laser process parameters listed in Table 7. To make the tensile cutouts, the maximum power of the fs-laser was used. Due the existence of large gaps between each laser pulse, the maximum laser power of 29 MV was reduced to 10 MV. In addition, a pulse duration of 350 fs, a laser wavelength of 515 nm, and a laser pulse energy of 10 µJ were used to machine the copper tensile specimen cutouts.

The laser fluence is defined as the laser's energy per unit area of the laser's spot size on the specimen. Since the beam diameter of the fs-laser was not well-defined, the laser fluence was approximated to be 11 $\frac{J}{cm^2}$.

The number of passes used to make the tensile cutouts with the laser was dependent on the thickness of the specimen. Therefore, a larger number of passes were used for the wedge of the 415-steel with a thickness of approximately 100 µm, while a smaller number of passes were used to make the tensile cutouts out of the 50 µm copper wedge. Therefore, this resulted in a

slightly longer machining time of the 415 micro-tensile specimens for the same number of specimen cutouts produced (by a few minutes).

The laser frequency defines the rate of the laser pulses used for machining. A laser frequency of 120 kHz per packet containing 4 laser bursts was used to machine the tensile cutouts. Each burst contains 4 pulses, with each pulse having a time spacing of 4 ns between each other. Each packet of the 4 laser bursts occurs 120, 000 times per second, (resulting to a spacing of a few micro-seconds between each 4 bursts). The laser's scanning velocity that was used is 400 $\frac{mm}{s}$. The laser beam's diameter was roughly estimated to 14 μm by the combination of the laser's frequency and velocity, since the two parameters dictate the amount of overlap that occurs between each laser pulse. Although, this is a rough estimate of the laser's beam diameter, and other ways to calculate the beam diameter have been determined by Zeiss and Trumpf.

The ablation rate is the sum of all processing effects, including beam focus and the intrinsic properties of the material (such as material hardness and existence of various microstructural phases). In addition, the tracking focus of the laser on the specimen was not always precise. Therefore, the ablation rate was not constant over the duration of the laser machining. A way to get a rough estimate of the ablation rate can be from calculating the amount of volume material removed from the starting and finishing time of the machining the tensile cutouts. However, the number of laser passes that were used to remove the material can still occur even after all the surrounding material of the tensile cutouts have been cleared (to ensure that all material is removed with the extra passes). Therefore, a more realistic way to determine the machining time for the tensile specimens was determining the time it took to machine a set of 6 tensile specimens per copper wedge. And for the machining of 6 copper tensile specimen cutouts with the fs-laser, it took approximately 5 minutes.

Table 7: Fs-Laser Parameters Used for Machining 415 Steel and (100) Copper Micro-Tensile Specimens

Process Parameter	
Pulse duration (fs)	350
Laser frequency per 4 bursts (kHz)	120
Laser Pulse Energy (μJ)	10
Average Laser Power (MW)	10
Scanning Velocity $\frac{mm}{s}$	400
Laser Fluence $\frac{J}{cm^2}$	~11
Laser Wavelength nm	515

To create the laser-cutouts of the tensile specimens, a CAD drawing of the tensile specimen geometries was developed in the Zeiss program for the fs-laser prior to the laser-machining of the tensile specimens. The geometry and dimensions of the tensile specimens were identical to that of the PFIB-machined copper micro-tensile specimens shown in Figure 40. The CAD drawing consists of a 6x1 row of the tensile specimen geometries (with the hatched areas of the pattern being target ablation sites of the fs-laser, as seen in Figure 58). The pattern is

positioned on the edge of the copper wedge. Each specimen on each wedge gets machined one at a time. Figure 60 shows two SEM images of the laser-machined tensile specimen cutouts on an individual wedge. Figure 59 shows an image of the laser cutting process of the tensile specimens inside the laser chamber of the Zeiss Crossbeam 350 microscope.

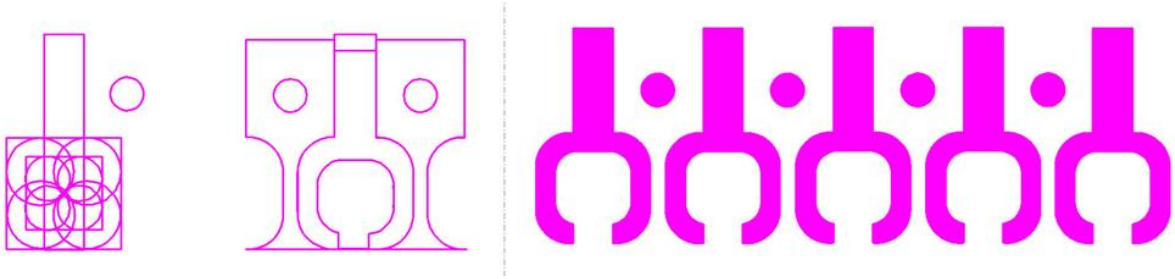

Figure 58: Copper micro-tensile specimen geometry cutouts developed using Zeiss CAD software of the Crossbeam 350. Image taken by *Travis Casagrande, CCEM (2023).*

Figure 59: Image of laser cutting process for the copper micro-tensile specimens in the fs-laser chamber of the Zeiss Crossbeam 350 microscope.

5.4.2. Nail Polish Experiment

An experiment was created to determine whether the removal rate of the laser debris on the copper surfaces can be accelerated. Two of the four wedges were applied with nail polish on both surfaces of the copper wedge prior to the cutting the tensile specimen geometries out with the fs-laser. It was hypothesized that the laser debris will sit on the nail polish layer instead of the copper wedge. The other two wedges had no nail polish applied to the surfaces when machining

the tensile specimen cutouts. It was assumed that when the nail polish and laser debris layers would be immediately dispersed in an acetone solution. In addition, the wedges with applied nail polish would take less time to remove the debris layers compared to the bare wedges.

Two of the four wedges were placed into the chamber of the fs-laser at a time. Each of the two wedges were placed on a stub holder, respectively, using carbon tape. Afterwards, the wedges were placed on the center of the fs-laser stage. The specimen is surrounded by 4 apertures of the stage. Prior to machining the specimens, the position of the wedges was detected by the fs-laser by calibrating the position of the specimens on the stage in reference to the position of the apertures. Once the calibration is complete, the laser-machining was begun. The laser-machining of the 12 specimens took under 6 minutes to complete. Figure 61 shows the final laser-machined tensile specimen geometries for one of the nail-polish applied wedges.

From the final laser-cut-out, both sides of the tensile specimens (extending into the wedge component) had a layer of laser debris (of a few tens of microns thick) accumulated from the laser-ablation process. The laser debris is ablated copper material that sits on the surface during the high-power ablation process. In addition, a thin bridge connecting each specimen at the edge of the wedge and blocks of surrounding material between each specimen was produced from the lay-over of the CAD drawing on top of the wedge surface. The blocks of surrounding material were poked out of each wedge using tweezers to allow for a line-of-sight of the gauge sections to be produced for performing the thinning process in the PFIB. The bridge was produced to protect the specimens from breaking off the edge during the sonication process of removing the laser debris from the wedge surfaces in the next fabrication step. The laser-machined tensile specimens produced precise dimensions in the X and Y-axis of the geometry, as measured in the SEM image shown in Figure 63.

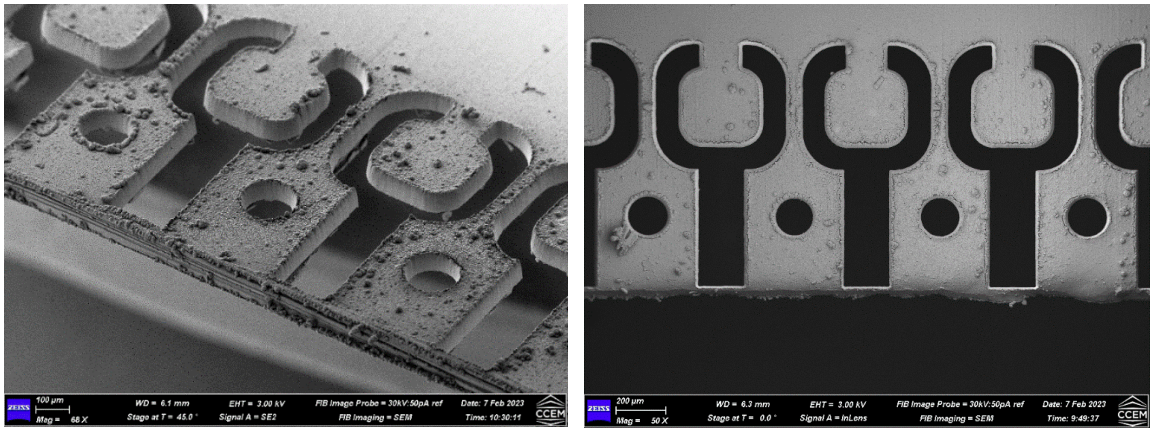

Figure 60: SEM images of tensile specimen geometry cut-out pattern of copper micro-tensile specimens lined up at the edge of a copper wedge performed using fs-laser ablation from the Zeiss Crossbeam 350 microscope. SEM images taken by *Travis Casagrande, CCEM (2023).*

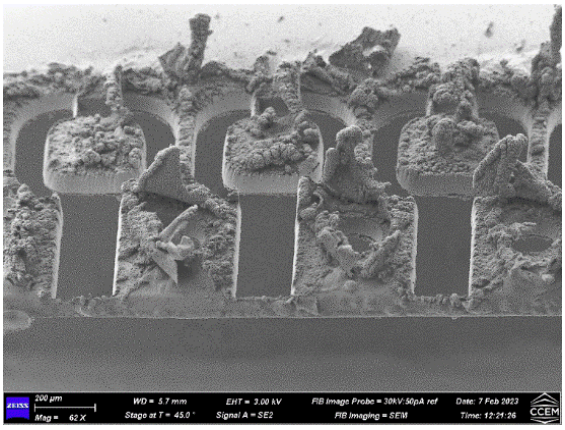

Figure 61: SEM image of copper tensile specimen cut-outs with the fs-laser. Layers of both nail polish and laser debris sits on the bottom of the tensile specimen surfaces after laser machining. SEM image taken by *Travis Casagrande, CCEM (2023).*

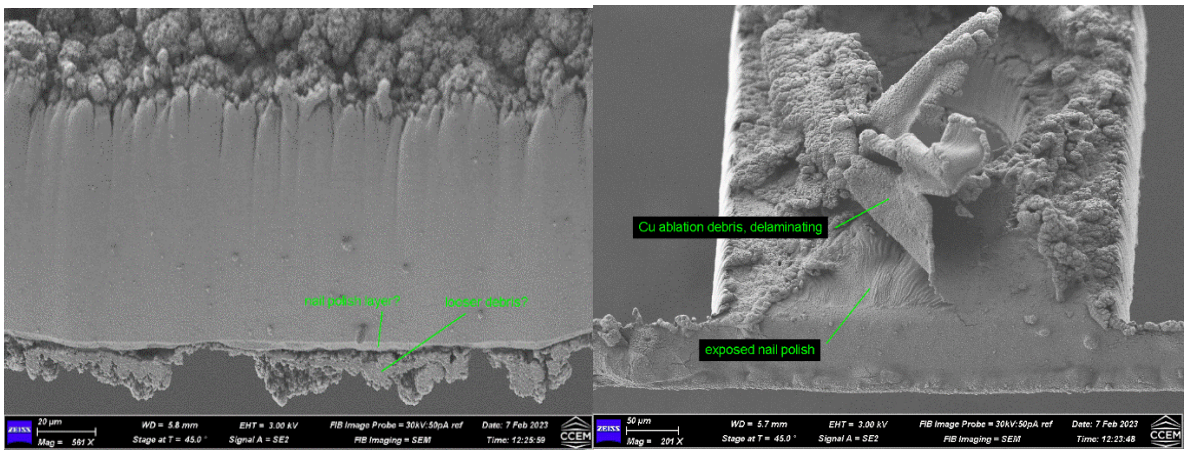

Figure 62: Magnified view of the nail polish and laser debris layers on the grip surface of a fs-laser-machined copper micro-tensile specimen. SEM images taken by *Travis Casagrande, CCEM (2023).*

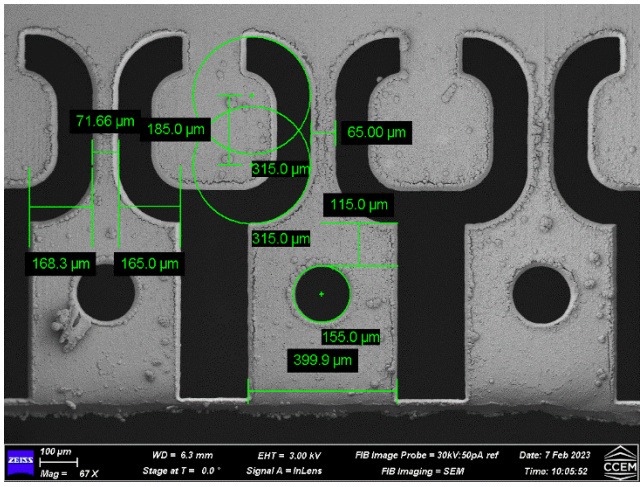

Figure 63: Measured dimensions of tensile specimen geometry cutouts by the fs-laser. SEM image and measurements by *Travis Casagrande, CCEM (2023).*

5.4.3. Laser Debris Removal Using Ultra-Sonic Bath

A cleaning procedure was developed to remove the laser-debris on the surfaces of the wedge from the fs-laser-machined tensile specimen cutout process. Once the newly prepared laser-ablated copper tensile specimen cutouts were taken out of the fs-laser chamber of the Zeiss Crossbeam 350, the wedge were individually transported into a beaker of alcohol solution. For the two wedges without applied nail polish on the surfaces, ethanol was used as the cleaning solution. For the two wedges with applied nail polish, acetone was used instead. Both the temperature of the alcohol solutions and the atmosphere of the fume hood in which the sonication took place, was at a room temperature of 25 degrees Celsius. Each wedge was placed in a 500 ml beaker containing 50 ml of alcohol solution, as seen in right image in Figure 64. Afterwards, the beaker containing the alcohol solution and wedge were transferred to a transmission electron microscope (TEM) sonicator. Ultra-sonication cleaning was performed to remove the laser-debris layer and other contaminants on the surfaces of the wedge using high frequency sound waves, as seen in left image of Figure 64. The sonicator helps to loosen the adhesion of the debris on the wedge surfaces. In addition, heat is also produced from the vibration sound waves, which aides the contact removal of the contaminants on the surfaces [44].

The sonication process for the two bare wedges without the applied nail polish was done for 20 minutes on each side of each wedge. After sonication was done on one side, the wedge was flipped using tweezers to begin sonication cleaning on the other side. A light microscope was used to observe the quality of the surfaces of the wedge after each sonication of each side of the wedges. For the two wedges with applied nail polish, the laser debris was immediately dispersed into the acetone solution when it was placed into the beaker. Sonication took 5-7 minutes on each side of the nail polish wedges. Figure 65 and Figure 66 shows SEM images of the surface quality of a nail polish wedge and a bare wedge after sonication cleaning, respectively. The sonication cleaning for all four wedges took approximately 2 hours to complete.

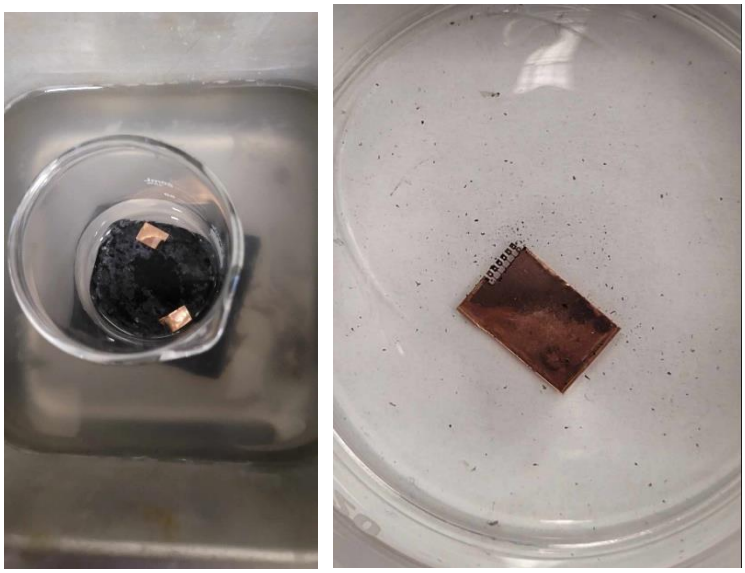

Figure 64: Sonification cleaning of fs-laser machined copper micro-tensile specimens.

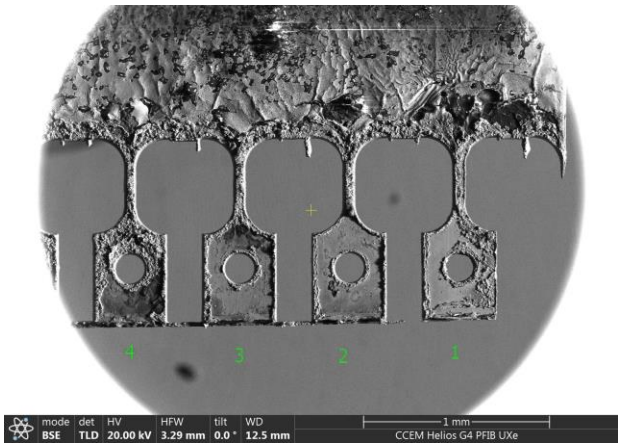

Figure 65: Final geometry cutouts of the fs-laser-machined micro-tensile specimens on wedge 1 (with applied nail polish on the surface).

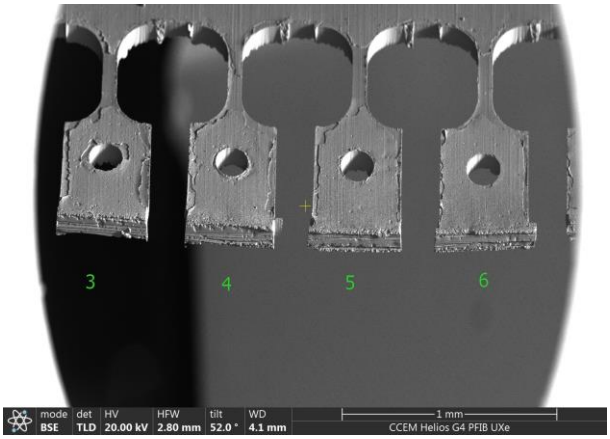

Figure 66: Final geometry cutouts of the fs-laser-machined micro-tensile specimens on wedge 3 (without nail polish applied to the surface).

From the sonication cleaning process, the tensile specimens remained unhindered by the force of the high frequency sound waves. Although, some components of the thin bridge holding the specimens together and blocks of surrounding material between each tensile specimen got broken off during sonication, as seen in Figure 65. For all four wedges, a remaining amount of laser debris stayed on the surfaces of the wedges. For the bare specimens, the laser debris was removed almost entirely from the gauge section of the tensile specimen cutouts but remained on the wedge component and the grip section of each specimen. For the nail polish-applied wedges, the laser debris was mainly removed on the wedge connection and grip sections but remain adhesive on the edges of all the tensile specimen cut-outs (including the edges of the gauge section), as seen in Figure 65. The most important section of the tensile specimen cut-outs that needs to be free of laser-debris is the surfaces of the gauge section. The removal of the laser debris on the gauge section allows for a better observation of the true initial thickness of gauge section. With the laser debris layer on the gauge sections, the milling time for the thinning process can be reduced. In addition, the amount of curtaining from the surface topology (influenced by the surface roughness of the laser debris layers) would also be reduced. Therefore, the bare specimens represented a better result of the surface quality of the wedges after sonication cleaning with alcohol solution. Even though the removal of the laser debris on the gauge sections took a longer time for the bare wedges, there was no adhesion of the laser debris on the gauge length edges.

For future improvements on the nail polish experiment, it would be beneficial to heat up the acetone solution to a temperature of 40-50 degrees Celsius, in order to induce thermal energy to remove the adhesion of the laser debris on the gauge length edges. In addition, it is recommended that the nail polish wedges should be immediately sonicated right after laser-ablation of the tensile specimen geometry cut-outs to prevent time for the chemical bonds of the nail polish with the laser debris to be formed. The formation of the chemical bonds can be due to the heat dissipated by the high-power laser ablation process.

5.4.4. Removal of Bridge Connections

After the fs-laser-machined tensile specimens had undergone the sonication cleaning process, the remaining bridge connections were removed between each tensile specimen using ion milling performed by the Helios 5 G4 UXe Dual Beam Plasma FIB-SEM. Initially, each individual wedge was loaded onto a wafer holder and connected to a stub holder to perform ion milling at a 52-degrees stage tilt with the wedge surface facing normal to the ion beam. After alignments and the eucentric point was set for the working distance of 4 mm between the wedge surface and pole-piece, rectangular cleaning cross-sectional milling boxes were placed on top of the thin bridge connections. The removal of the bridge connections was performed at a high ion current of 2.5 µA. The Z-depth of the milling boxes was 70 µm to ensure that the bridge connections were completely milled through. The removal of all the bridge connections took approximately 15 minutes for each wedge. The direction of milling for the cleaning-cross-sectional milling boxes varied left-to-right and right-to-left-right for each bridge section removed.

5.4.5. Thinning of Gauge Section

After the bridge connections between the tensile specimens were removed, the thinning process of the gauges was performed. The wedge was transferred out of the PFIB chamber and then repositioned on the PFIB stage (with only the wafer holder) to perform the thinning process. The same thinning method adopted from Bob Wheeler used for the PFIB-machined micro-tensile specimens was used for the fs-laser machined copper micro-tensile specimens. Initially, alignments and set-up of the eucentric point was performed on the surface of the cross-section of the wedge at the highest point of the wedge. Afterwards, the wedge was positioned on the PFIB stage with the cross-section of the tensile gauge lengths facing normal to the ion beam at the 52-degrees-milling configuration. The plane of the wedge was tilted a few degrees from the normal of the ion beam to create the line-of-sight for locating the tensile specimens on the wedge surface. Two rectangular cleaning cross-sections were centered on the edges of the gauge length of each specimen with milling direction moving from top to bottom and bottom to top, respectively, for the top and bottom milling boxes.

The gauge sections of the nail-polish applied tensile specimens had a thin layer of laser debris (of less than 10 µm) to be removed by milling. Therefore, the length of the milling boxing was extended outwards to accommodate the extra thickness of the gauge section. For the bare specimens, the true thickness of the gauge section was thinned to the target thickness for each tensile specimen. Table 8 lists the thickness of each fs-laser-machined copper micro-tensile specimen of their corresponding wedge number. Note, specimen 1 from wedge 1 was not thinned due to lack of clearance space between the gauge length and the base material for placing the milling boxes.

Table 8: Final Gauge Thickness Values for Fs-Laser-Machined Copper Micro-Tensile Specimens.

Specimen	Gauge Thickness (µm)
Wedge 1- Specimen 2	4.4
Wedge 1- Specimen 3	6.2
Wedge 1- Specimen 4	3.7
Wedge 1- Specimen 5	5.4
Wedge 1- Specimen 6	5.8
Wedge 2- Specimen 1	10.4
Wedge 2- Specimen 2	10.0
Wedge 2- Specimen 3	9.1
Wedge 2- Specimen 4	12.9
Wedge 2- Specimen 5	12.9
Wedge 2- Specimen 6	9.6
Wedge 3- Specimen 1	33.9
Wedge 3- Specimen 2	32.3
Wedge 3- Specimen 3	30.0
Wedge 3- Specimen 4	29.3

Wedge 3- Specimen 5	29.7
Wedge 3- Specimen 6	26.6
Wedge 4- Specimen 1	18.3
Wedge 4- Specimen 2	20.3
Wedge 4- Specimen 3	19.5
Wedge 4- Specimen 4	18.7
Wedge 4- Specimen 5	16.5
Wedge 4- Specimen 6	19.4

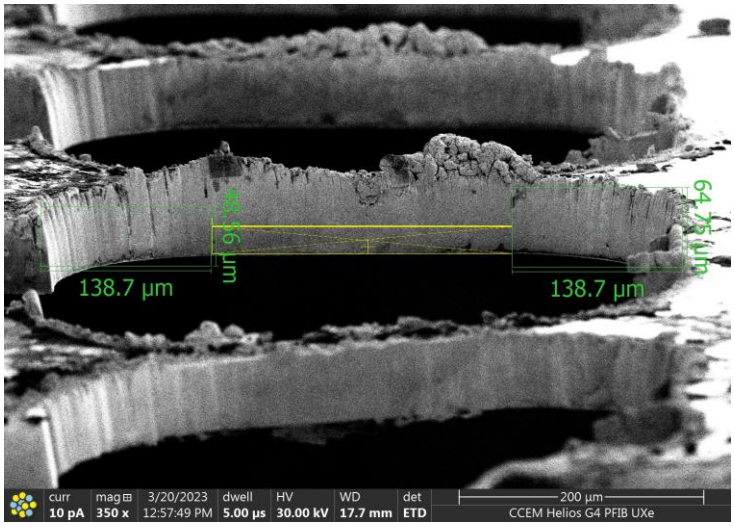

Figure 67: Centering of milling boxes using measurement boxes prior to thinning of the gauges of the fs-laser-machined copper micro-tensile specimens.

5.4.6. Cleaning Of Gauge Section Rough Edges

After the gauge sections were thinned to the targeted thickness values for the fs-laser-machined copper micro-tensile specimens, the rough edges along the gauge length were removed using ion milling performed with the PFIB. The procedure is identical to that performed for the PFIB-machined copper micro-tensile specimens. Two rectangular cleaning cross-sectional milling boxes of 248.2 µm x 5 µm were centered and placed onto the right and left edges of the gauge length. After centering the milling boxes, the width of the milling boxes was extended to cover any curvature along the length of the gauge section. Compared the PFIB-machined tensile specimens, the roughness along the gauge edges of the fs-laser-machined specimens is more rigorous due to the curtaining caused by debris accumulation during laser-ablation by the fs-laser. The accumulation of the laser debris causes changes in the surface topology, thus causing changes in the laser-material interactions during ablation. Therefore, the roughness on the edges of the tensile specimen cutout is produced by laser debris curtaining from the fs-laser. Figure 68 and Figure 69 shows an SEM image a fs-laser-machined specimens of the before and after cleaning state of the gauge length edges, respectively. The presence of ion-induced curtaining

(on the gauge surface) and laser-induced curtaining (on the gauge edges) is indicated with red arrows.

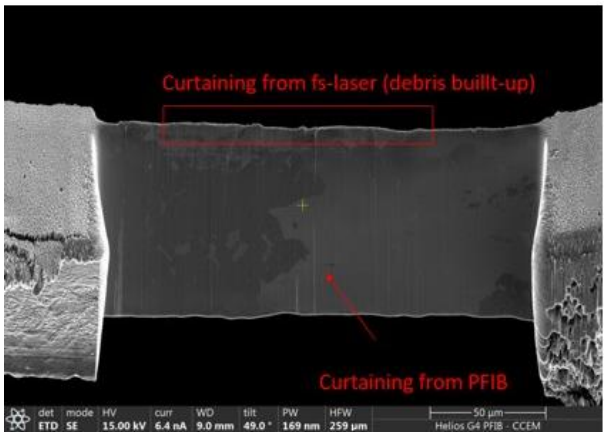

Figure 68: Curtaining from ion milling and fs-laser machining exhibited on the gauge section of one of the fs-laser-machined copper micro-tensile specimens.

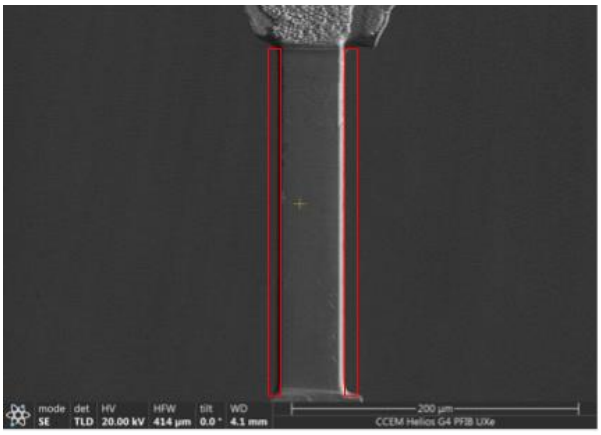

Figure 69: Position of milling boxes (shown as red boxes) and final state of the cleaned gauge edges.

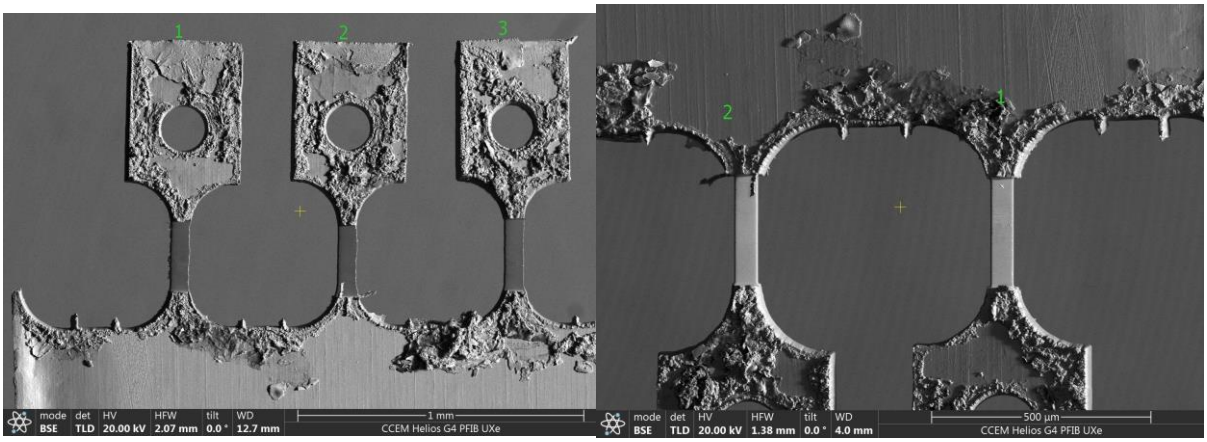

Figure 70: SEM images of fs-laser-machined specimens wedge 4 specimens before and after cleaning of gauge edges.

5.4.7. Fiducial Marks

After the gauge edges were cleaned for each fs-laser-machined micro-tensile specimen using the PFIB, reference fiducial marks were directly deposited on the ends of the gauge surface. The same X-shaped fiducial mark geometry (of 10 µm x 2 µm in dimensions) that was used for the PFIB-machined specimens was used for the fs-laser-machined specimens. The fiducial marks were produced using a tungsten gas precursor deposition from the multi-chem of the Helios 5 PFIB UXe DualBeam Plasma-FIB. The deposited tungsten fiducial marks for fs-laser-machined copper micro-tensile specimen 3 from wedge 4 can be seen in Figure 71.

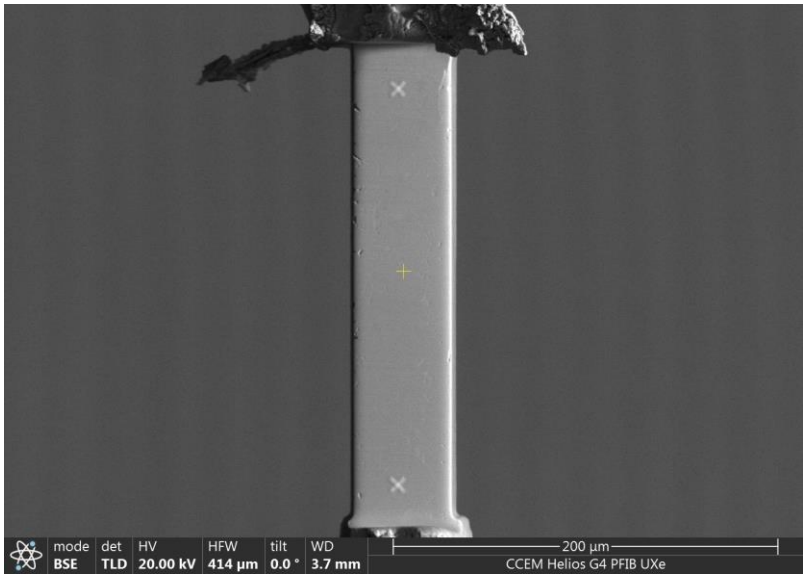

Figure 71: Deposited reference fiducial marks on the gauge surface of a fs-laser-machined copper-micro-tensile specimen.

5.4.8. Remarks on the Fabricated Fs-Laser Copper Micro-Tensile Specimens

In comparison to the PFIB-machined specimens, the grip and wedge component have a lower surface quality than the PFIB specimens, due to the adhesion of remaining laser debris on the surfaces. Although, the gauge sections from both fabrication methods were of similar quality, as observed through SEM imaging of the final-machined specimens. In addition, the spacing between each specimen grip on the wedge edge is wider than that of the PFIB specimens. The larger spacing causes a higher probability of bending of the specimens (in-plane and out-of-plane of the wedge surface) when the laser wedges are transferred in and out of the PFIB chamber and during repositioning of wedge on the wafer holder. Thinner gauges are more prone to bending during the transfer process. The bending occurred for a few of the specimens on wedge 1, wedge 2, and wedge 4 of the fs-laser specimens. For example, the right SEM image in Figure 72 shows fs-laser-machined specimen 4 of wedge 1 bent sideways after the wedge was transferred out of the PFIB chamber and reposition on the wafer holder prior to performing the removal process of the rough edges on the gauge. Since the specimens in wedge 1 were very thin (with gauge thicknesses ranging 3.7-6.2 µm), the sample were more prone to bending due to the thinner and smaller gauge structure compared to the significantly larger and heavier mass of the grip section. In addition, the weight of the laser-debris on the specimen grips can also contribute to the bending of the specimens. One improvement to the fabrication process of the fs-laser-machined specimens is to keep the bridge connections intact with the specimens until the final step of depositing the fiducial marks was completed to prevent specimen from moving out of plane.

One way to reduce the thickness of the grip section is to thin the wedge (via ion milling with the PFIB) prior to the fabrication process of the micro-tensile specimens. The wedge with the initial thickness of 50 µm would be positioned onto a wafer holder and then inserted into the PFIB chamber. In the chamber, the cross-section of the wedge would face normal to the ion beam at the 52-degrees milling configuration for thinning the cross-section. The wedge would be thinned to a thickness value of 15-20 µm and to a depth of approximately 400 µm (to account for the full length of the grip section). Afterwards, the wedge is partially thinned, it will be taken out of the PFIB chamber for the process of the fabricating the micro-tensile specimens to begin (starting with the tensile specimen cutouts). This additional step in the fabrication process will be used to towards developing future micro-tensile specimens (outside of the specimens mentioned in this thesis document).

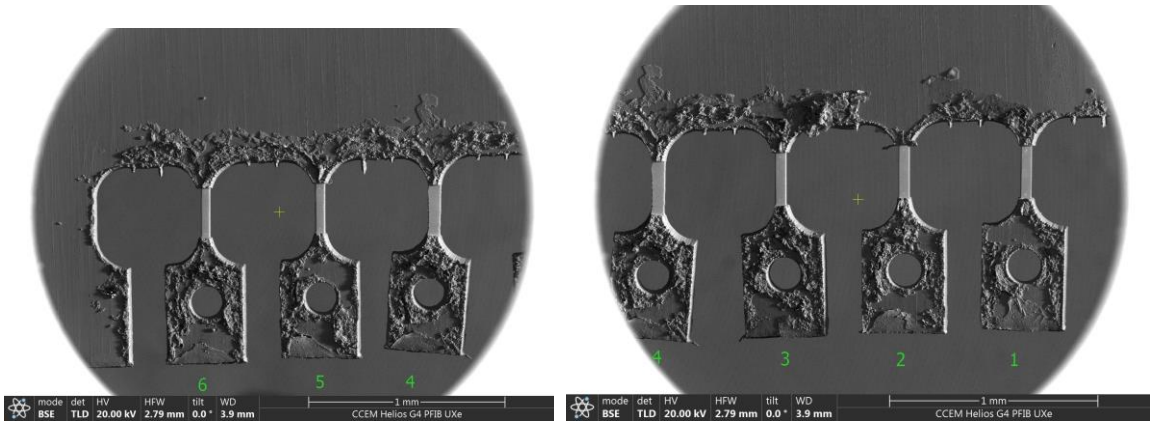

Figure 72: Final fabrication state of fs-laser-machined copper micro-tensile specimens from wedge 1.

Table 9: Machining Times for Each Fabrication Process of the Different Machining Routes

Fabrication Step	Fabrication Time	
	Fs-Laser and PFIB Machined (Per 6 Specimens a Wedge)	PFIB-Machined Only (Per 6 Specimens a Wedge)
Geometry Cut-Outs	~5 minutes	~5 hours
Ultra-Sonic Cleaning	~30 minutes	N/A
Removal of Blocks and Bridge Material	~30 minutes	N/A
Thinning of the Gauge Section (0.2 µA Ion Current Used)	~36 minutes to 3 hours (dependent on amount of material removed)	~36 minutes to 3 hours (dependent on amount of material removed
Cleaning of Gauge Edges (0.2 µA Ion Current Used)	~3-10 minutes (dependent on amount of material removed)	~3-10 minutes (dependent on amount of material removed)
Fiducial Marks Deposition (0.33 nA Ion Current Used)	~18 minutes	~18 minutes
Total Fabrication Time:	**~ 2-4.5 hours**	**~ 6-8.5 hours**

5.5. Validation of Single Crystal Copper Using Electron Backscattered Diffraction (EBSD) Analysis

To validate that the copper foil was indeed a single crystal grown in the <100> direction by the manufacturer company, 2D EBSD analysis was performed on gauge surface of one of the fs-laser-machined copper tensile specimens in the dual beam chamber of the Helios G4 UXe Plasma-FIB-SEM microscope, as shown by the post EBSD acquisition maps in Figure 73. The description of the EBSD analysis set-up and process can be found in Chapter 7 for EBSD analysis performed on the 415-micro-tensile specimens. From the post-EBSD acquisition maps obtained from the 2D scan of the gauge surface, the inverse pole figure (IPF) maps in the X, Y, and Z directions were used to determine the crystal orientations of the copper microstructure. As seen in Figure 73, the results show that the copper material is indeed a single crystal orientated in

the (001) plane in all three directions, (aside from small amount of contamination picked by the EBSD scans).

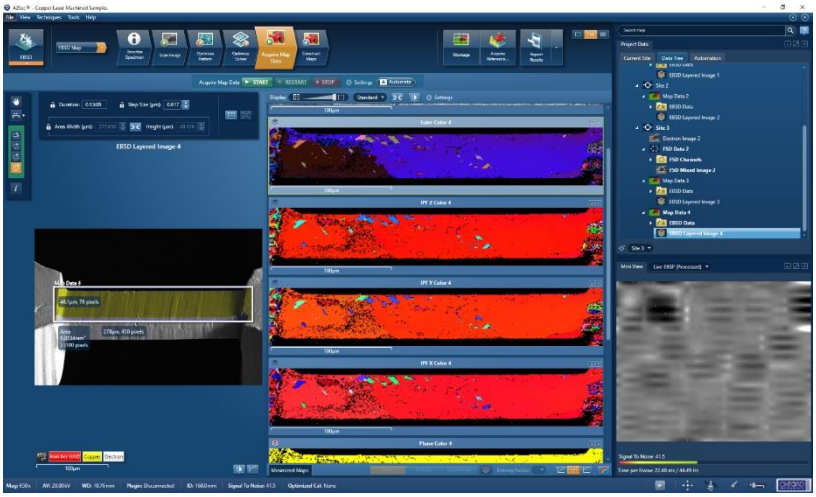

Figure 73: 2D EBSD scan of the gauge surface of a fs-laser-machined copper tensile specimen.

5.6. Validation of Geometry for Thinned Gauge Cross-Sectional Area

The shape of the gauge cross-section of the fabricated tensile specimens using the thinning method adopted from Robert Wheeler was validated using the application of X-ray computed tomography (x-ray CT) and image processing performed with Dragonfly software. From the gauge thinning process of the micro-tensile specimens, it was desirable to produce a parallelogram-shaped gauge cross-section with fixed dimensions (of gauge width and thickness) throughout the gauge length. The under-tilt applied to the stage during thinning creates the parallelogram-shaped gauge cross-section during the thinning process as the ion beam removes material at a small angle away from the wedge surface on both the bottom and top surfaces of the gauge. A poor milling application would cause a non-uniform parallelogram-shaped gauge or a trapezoidal-shaped gauge to be produced, which would be undesirable as it would affect the mechanical behaviour of the specimen during micro-tension testing.

Analysis using ISE and SE imaging from the ion beam and the secondary electron beam (respectively), provides separate views of the gauge thickness and gauge width. Therefore, a full view of the gauge cross-section of the width and thickness is not possible with the PFIB, (unless destructive methods were taken into consideration by cutting the gauge perpendicular to it surface to view the gauge cross-section). Instead, the non-destructive method of x-ray CT was used to generate a 3D scan of a wedge containing fabricated 415 micro-tensile specimens. The x-ray CT scans of the 415 tensile specimens was performed by *PhD Candidate, Mehdi Mosayehbi of McMaster University*, who is specialized in operating the Nikon M2 225 KV CT at the Centre for Electron Microscopy. The Nikon M2 225 KV CT is a high-performance X-ray CT scanner

with a tungsten X-ray source. Through the bombardment of electrons at the tungsten target, x-rays are emitted. The x-ray CT scanner provides 3D imaging of the material by scanning the material at different angles. The scanner compiles the 2D scans taken from the various angles into a 3D representation of the material. The scanner also provides a spatial resolution of up to 3 µm and a field-of-view limitation of approximately 280 µm x 280 µm in width and length. In addition, internal features of the material specimen can also be imaged through x-ray CT. The ability to view the internal structure of the tensile specimens was significantly important to determine the shape of the gauge cross-section. The view of the cross-section shape along the gauge length can be observed through the 2D-to-3D image reconstruction of the gauge section using Dragonfly from the internal 2D x-ray CT scans taken of the specimens.

The 415 micro-tensile specimens used for the x-ray CT scans were fabricated with a prepared 415 wedge through the sample preparation method outlined in Chapter 7. Along one edge of the 415-prepared wedge, 4 specimens with a tensile geometry consisting of a 50 µm x 50 µm (length to width) gauge section were produced. Along the adjacent edge of the smaller gauge section specimens, 4 other tensile specimens with a larger gauge section of 180 µm x 100 µm (length to width) gauge section were fabricated. The two different tensile geometry patterns consisting of the small and large gauge section can be seen in Figure 74.

The purpose of fabricating two 415 steel specimen geometries with different gauge widths and lengths (for this Chapter of the thesis) is to determine the effect of the gauge dimensions on the uniformity of the gauge cross-section after the thinning process. Initially, the plan for producing this specific batch of 415 micro-tensile specimens was to study the deformation mechanisms occurring under different gauge sizes of the steel specimens and determine whether there exist size-limiting mechanical behaviours (similar to the single crystal copper micro-tensile specimens). However, due to the bending of the gauges, the tensile specimens would not give accurate results of the strength and deformation behaviour of the specimens (due to existing strain gradients and negative strain that would be calculated during post-data acquisition).

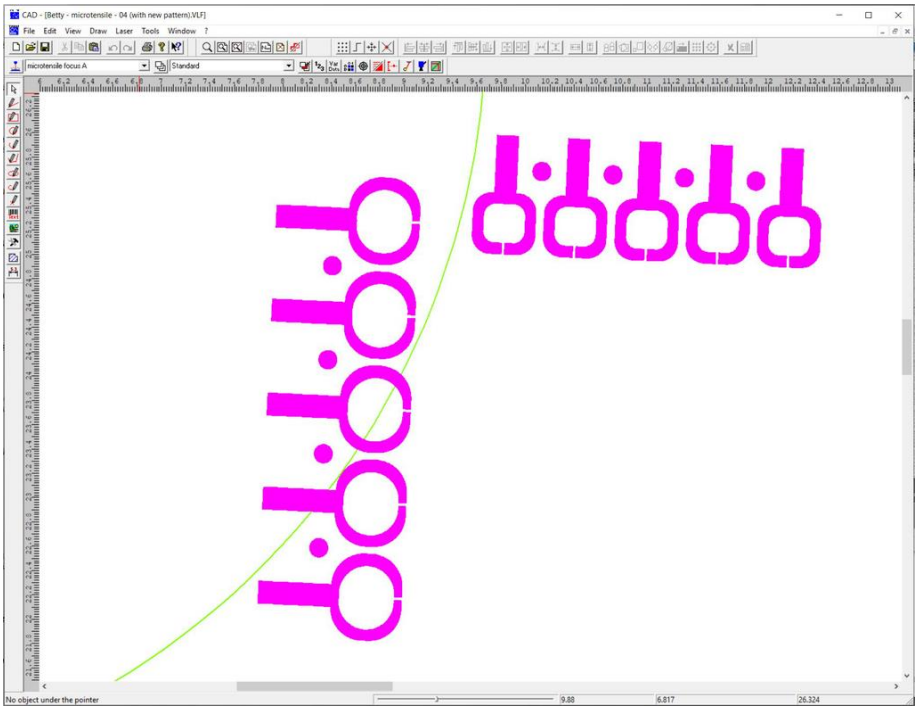

Figure 74: CAD drawing for fs-laser-machined 415 micro-tensile specimen cutouts of small gauge (left side) and large gauge (top side) tensile geometries. Image taken by *Travis Casagrande, CCEM (2023).*

The fabrication process for the 415 micro-tensile specimens follows the same procedure steps as for the fabrication of the laser-machined copper micro-tensile specimens used to study the size effect phenomenon, (including geometry cutout, gauge thinning, removal of the rough gauge edges, and deposition of reference fiducial marks processes). Initially, the tensile specimen geometries were cut out using the fs-laser with the laser parameters outlined in Table 7. Afterwards, sonification cleaning was performed (using ethanol solution) to remove the laser debris layer that sits onto of the tensile specimen surfaces from the laser-ablation process. Once the specimens are cleaned from the laser-debris, the gauge sections of each tensile specimen were thinned to arbitrary thickness values using ion milling performed by the Helios 5 PFIB UXe DualBeam Plasma FIB-SEM microscope. Afterwards, the rough edges of the gauge length were removed with low ion milling performed with the PFIB. The roughness along the gauge edges originates from laser-curtaining during the tensile cutout process with the fs-laser. After the edges were cleaned, a tungsten deposition of two X-shaped reference fiducial marks were deposited on the ends of the gauge surface. The final state of the fabricated 415 micro-tensile specimens can be in the SEM images of Figure 75. After the fabrication process was complete, the 415 specimens were mechanically strained using the custom-built micro-tensile bench at IREQ. Partial straining of the specimens was performed to prevent the specimen from reaching the fracture point, but also strained to surpass the yield point of the material. Partial straining was performed to observe the deformed necking region of the gauge section from the internal scans by the x-ray CT, as seen for specimen 2 of the large gauge section tensile geometry in Figure 80 of the Dragonfly image reconstruction of the gauge cross-section. Only specimens 1, 2, and 3 of the larger gauge section and specimen 2 of the smaller gauge section geometries were strained. Two of the gauge sections of specimen 4 from the large gauge section and specimen 4 from the

small gauge section geometries were too thin to withhold the weight of the non-thinned grip, causing bending of the gauge section. Therefore, those specimens could not be used for x-ray scanning or mechanical testing.

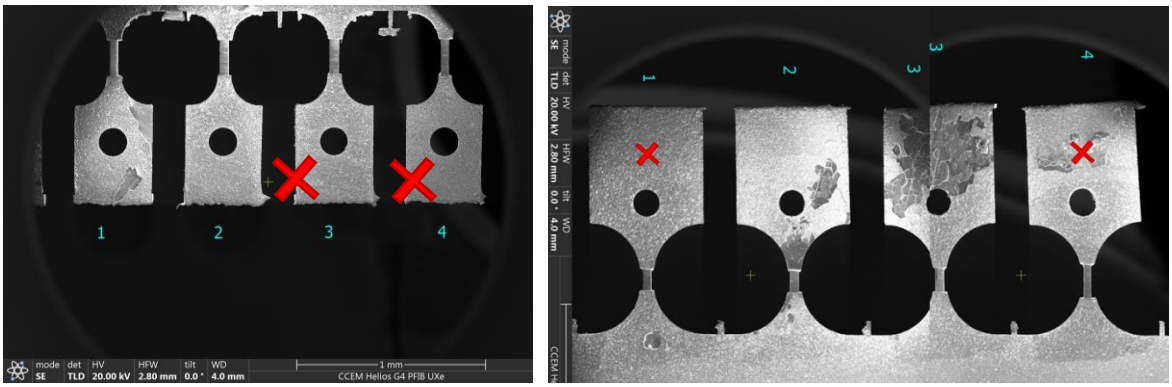

Figure 75: SEM images showing the final fabrication state of 415 micro-tensile specimens (with 100 µm x 50 µm gauge section geometries (right image) and 50 µm x 50 µm gauge section geometries (left image)). Red X marks indicate the samples that were used for x-ray CT.

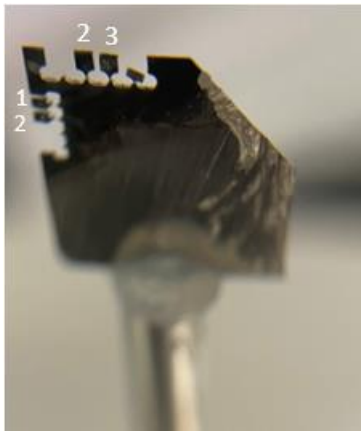

Figure 76: 415 steel wedge containing fs-laser-machined micro-tensile specimens. Wedge is placed specimen holder of the Nikon M2 225 KV CT scanner. Numbers indicate specimens that were scanned using x-ray CT. Image taken by *Mehdi Mosayehbi, McMaster University (2023)*.

Out of the eight fabricated 415 micro-tensile specimens, four specimens were scanned using the Nikon M2 225 KV CT. Specimens 2 and 3 with the small gauge section geometry and specimens 1 and 2 with the large gauge section geometry were scanned, as indicated by the photos of the wedge attached by the specimen holder of the scanner in Figure 76. The scans took approximately 1 hours and 23 minutes to scan two of the specimens at a time. Figure 77 and Figure 78 show the x-ray CT scan for specimens with the large and small gauge sections and their magnified views, correspondingly. From the scans, roughness on the grip and wedge surfaces from remaining laser debris and contaminants that sits on top of the surfaces is exhibited. For the specimen 2 and 3 with the smaller gauge section, the scans show a poor-quality finish for the thinning of specimen 2's gauge section, while the edges of the gauge section for specimen 3 looks uniform throughout the gauge length. For specimens 1 and 2 with

the larger gauge section geometry, the gauge section of both specimens looks uniform from the side view x-ray CT scans.

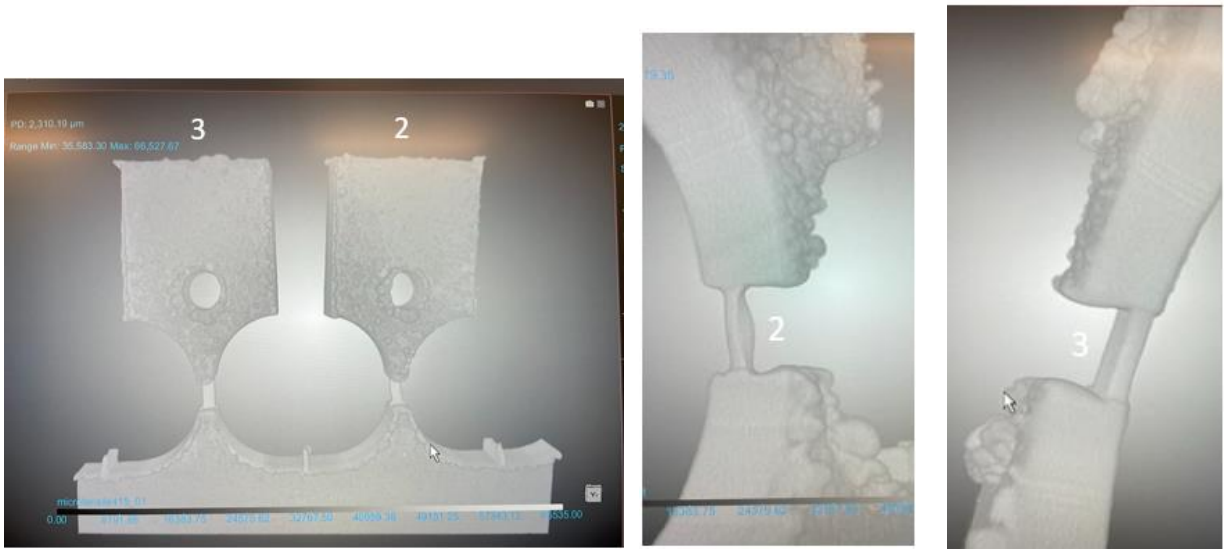

Figure 77: 3D X-ray computed tomography scans of fabricated 415 micro-tensile specimens (with a 50 µm x 50 µm gauge section geometry) by *Mehdi Mosayehbi, McMaster University (2023).*

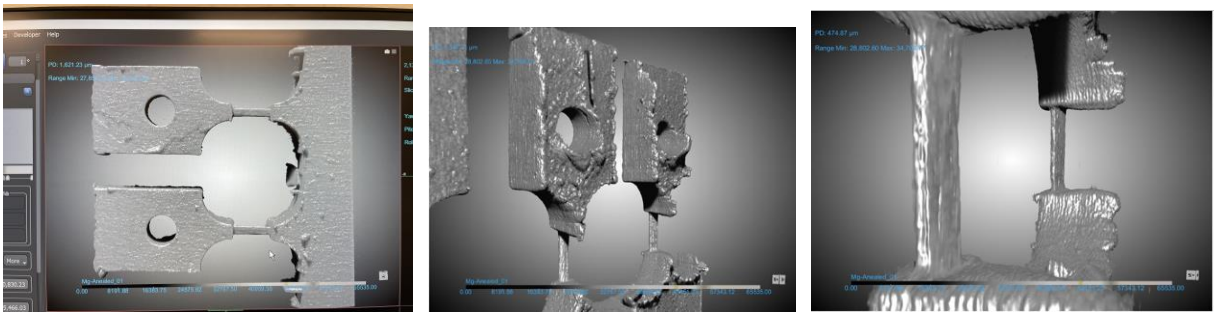

Figure 78: 3D X-ray computed tomography scans of fabricated 415 micro-tensile specimens (with a 50 µm x 50 µm gauge section geometry) by *Mehdi Mosayehbi, McMaster University (2023).*

The 2D-to-3D image reconstruction of the gauge cross-section for each of the 4 specimens scanned using x-ray CT was performed using Dragonfly by *Mehdi Mosayehbi* of *McMaster University (2023*). The gauge sections of the tensile specimens were reconstructed by exposing the internal view of the cross-section along the gauge length. 2500 2D projection images with a pixel size of 1.46 µm were taken of each specimen gauge section, starting from the grip-end of the gauge length towards the wedge connection. The reconstructions of the gauge section using Dragonfly software can be seen in Figure 79 for the specimens with the larger gauge section geometry and in Figure 80 for the specimens with the smaller gauge section geometry.

For specimen 2 with the smaller gauge section, the reconstruction of the gauge section shows non-uniformity of the cross-section throughout the gauge length. The shape of the cross-section changes from a parallelogram to a trapezoidal shape. It was more difficult to machine a thin gauge (to a thickness of 10 µm or less) for the samples with a smaller gauge section, due to

the shadowing from the thick grip and wedge sections. In addition, due to the remaining laser debris that sits on the surfaces, the debris interferes with the sputtering mechanisms of the ion beam during the thinning process. However, the 3D image reconstruction of the gauge cross-section for specimen 1 of the two smaller gauge section specimens exhibited a uniform parallelogram-shaped cross-section throughout the gauge length. From the 3D image reconstruction performed with Dragonfly of the gauge cross-section of specimen 1 and 2 with the larger gauge section, the cross-sections of both specimens also had a uniform parallelogram-shaped cross-section through the gauge lengths, correspondingly.

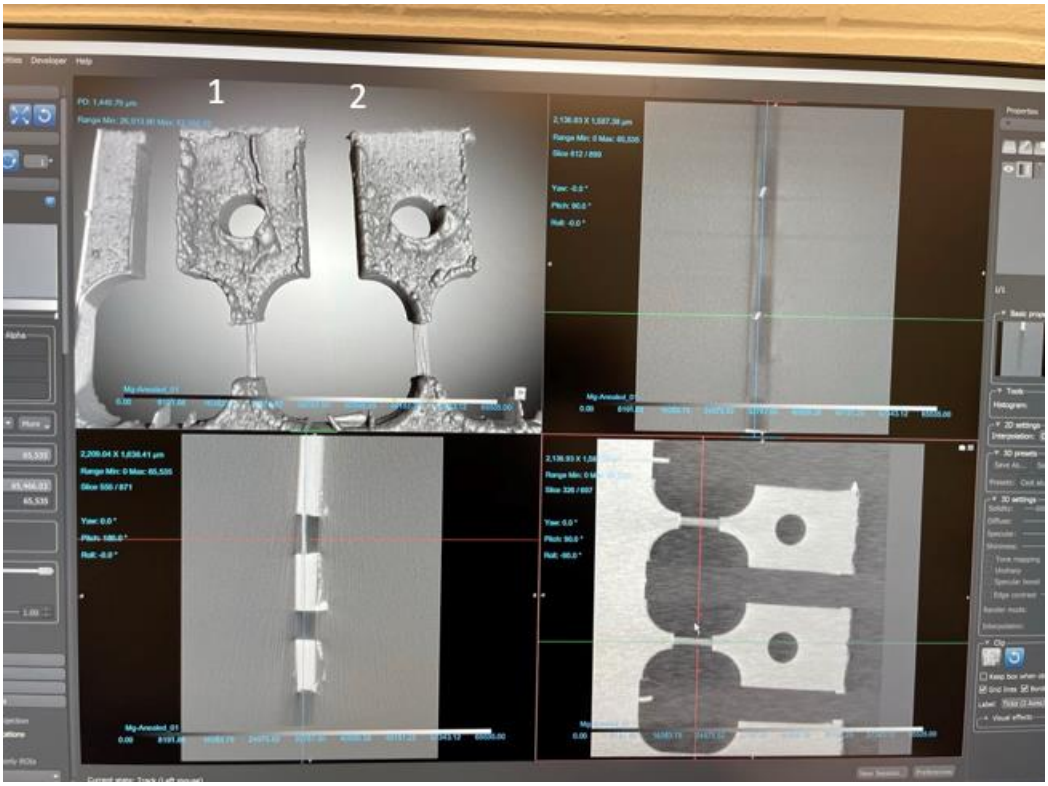

Figure 79: Image reconstruction of the gauge cross-sections for 415 tensile specimens 2 and 3 with a **180 µm x 100 µm** gauge, respectively, using Dragonfly image processing software performed *by Mehdi Mosayehbi, McMaster University (2023).*

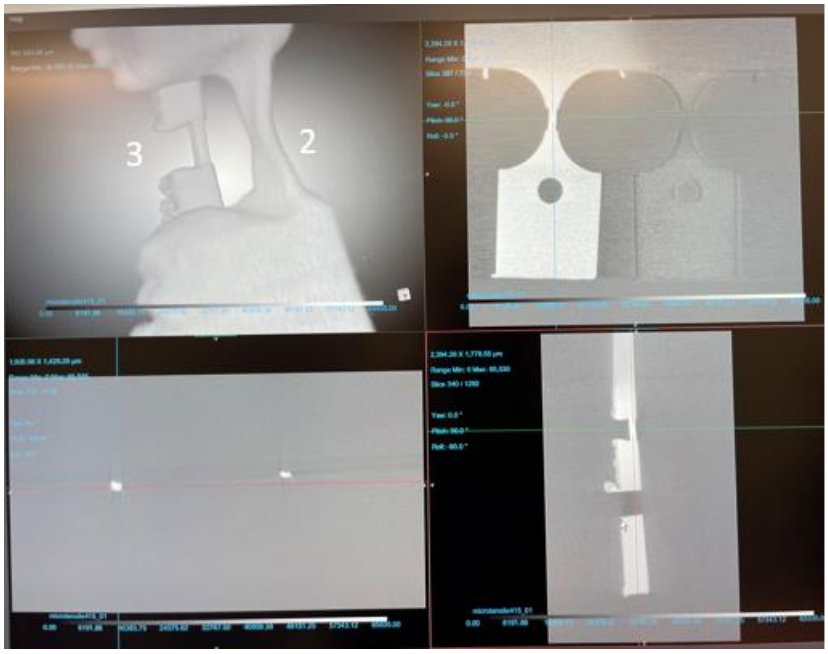

Figure 80: Image reconstruction of the gauge cross-sections for 415 tensile specimens 2 and 3 with a **50 µm x 50 µm** gauge, respectively, using Dragonfly image processing software performed by *Mehdi Mosayehbi, McMaster University (2023).*

XIII. Chapter 6: Mechanical Testing of Copper Micro-Tensile Specimens

After the fabrication process for the copper micro-tensile specimens was completed, the specimens were strained in tension to extract their mechanical properties. The purpose of conducting micro-tensile testing of the specimens is to determine whether a size effect exists for the specimens with various gauge thicknesses. Changes in the mechanical properties observed in the plastic region of the stress-strain curves were obtained during post-mechanical data analysis (such as the tensile yield stress, strain at yield, and the ultimate tensile strength) of the specimens with a gradual decrease in the gauge size (and vice versa) is an indication of size-limited dislocation events occurring during plastic deformation of the specimens. As mentioned in literature on the size effect of miniature-scale mechanical test specimens, the deformation behaviour becomes dependent on the dimensions of the specimen in the sub-micron regime as the dimensions get close to the size of dislocations. Nucleation events occur in the internal structure of size-limited single crystal specimens containing a limited number of dislocations. Higher flow stresses have been exhibited by the specimens from micro-tension testing.

In literature, *Kiener et al., (2008)* had determined the existence of the size effect by varying the aspect ratio by keep the gauge width of the needle shaped (122) copper micro-tensile specimens fixed for all specimens fabricated using a Ga+ FIB [5]. In addition, size-limiting mechanical behaviours have been seen through compression testing of SC micro-pillars fabricated out of nickel and copper *by Zhang et al., (2015)* and *Kheradmand et al., (2010),* respectively, where the size of the pillar diameters ranged from 1-10 µm and 3-7 µm, correspondingly [17] [16]. Therefore, for the copper micro-tensile specimens fabricated and discussed in Chapter 6, it is expected that a size effect from the mechanical testing for the range of tensile specimen thickness values of the gauge section (of 4.6 µm to 31.3 µm) will be observed from the post analysis of the stress-strain curves.

The micro-tensile testing of the copper specimens was conducted at the Hydro-Quebec Research Institute (IREQ) using their custom-built micro-tensile bench developed by Kammarth & Weiss. In the past, micro-tensile benches developed by Kammarth & Weiss have been designed to test the strength of reinforced fiber materials. Although, the custom-built micro-tensile bench was built to test and withstand the high strength of turbine steels. To determine whether the micro-tensile bench provided reliable and accurate results from the mechanical tests, the calibration of the newly developed equipment was performed by testing the fabricated copper micro-tensile specimens.

A size effect can be determined from the micro-tension tests of the copper specimens by determining the onset of plasticity (yield stress) from the post-data analysis of the stress-strain curves and comparing the experimental results with the bulk or milli-scale yield stress value of (100) copper found in literature. In addition, the mechanical testing of (100) copper will also help to validate whether the appropriate tensile specimen geometry was used to fabricate the

micro-tensile specimens, (in accordance with the E8/E8M ASTM standard for a pin-loaded tensile specimen) [43]. Afterwards the accuracy of the micro-tensile bench has been validated for performing micro-tension testing on single crystal copper, it can be used towards conducting mechanical testing on the turbine steels at IREQ, such as the 415 martensitic stainless steel (base material) and 309L austenitic stainless steel (wedge material).

6.1. Materials and Apparatus

The main components of the micro-tensile bench consist of a specimen stage, tungsten pin, and a tungsten carbide wire pulled in tension, a seen in Figure 82. The specimen stage holds the specimen holder in place using two screws, while the specimen holder holds a single wedge in place using screwed clamps, as seen in Figure 47. Silver paste is applied to the fixed edge on the specimen holder in order to create a conduction path for the wedge material in the high-vacuum SEM chamber. The tensile specimens are centered on the specimen holder in order for the pin to access the pinhole of each specimen grip. The importance of centering the tensile specimens on the holder is to prevent tension on one side of the wedge when the specimens are being pulled and to create space for the specimen holder to be screwed onto the micro-tensile bench.

After careful attachment of the wedge onto the specimen holder, the micro-tensile bench was loaded onto the chamber stage of the Hitachi S-3700N SEM microscope for conducting in-situ mechanical testing and analysis of the tensile specimens, as seen in Figure 81. An electric-driven motor was used to move the tensile stage with a resolution of 1 nm. While the tensile stage can be moved in the X, Y, and Z directions, the position of tungsten pin on the micro-tensile bench remained fixed in place. Therefore, the wedge can be moved in reference to the pin during loading and unloading the tensile specimen into the pin and while performing alignments of the gauge section to keep the specimen parallel and flat to the tensile loading direction. A controller was used to operate quasi-static movements of the tensile specimen stage such as tilt, rotation, and translation in the X, Y, and Z directions. In addition, the speed of each movement can be adjusted using the controller.

The micro-tensile specimen was pulled using a vibrating tungsten carbide wire. The wire was calibrated in tension to withstand a load of 2 Newtons or higher. The tensile tests were controlled using a MDS tensile module. The software provides measurements of instantaneous time, load, and elongation of each single micro-tensile test. The load was on the tensile specimen was tracked through a load-versus-time curve provided by the tensile module. The software can show the load on the tensile specimen in the forward direction (in tension) or in the reverse direction (in compression). In addition, the strain rate of the specimen dictated by the electric motor is specified in the MDS tensile module for each tensile test performed. A low strain rate of $5x10^{-4}\ s^{-1}$ was chosen for all tensile tests on the copper specimens. A low strain rate allows for ease of controlling the test and performing immediate analysis of the specimen when the load is paused during the mechanical testing. In addition, SEM imaging of the strain-state of the gauge surface can be taken at load intervals of 10 mN for calculation of strain during the post-data analysis. During micro-tension testing of a specimen, the tensile stage was moved with the pin-

loaded tensile specimen in the forward direction. Both the tensile specimen and the tungsten wire gets pulled in tension.

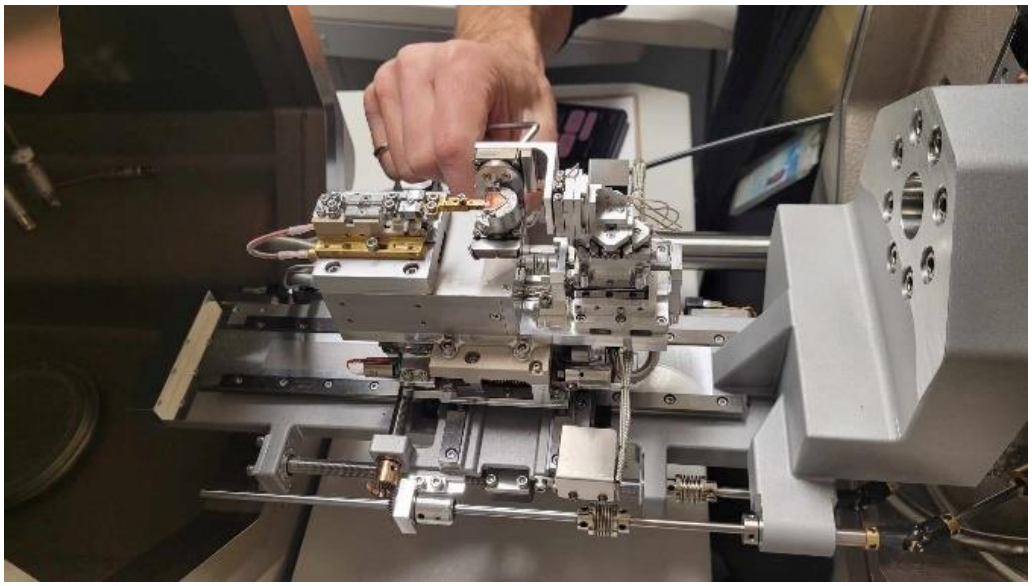

Figure 81: Insertion of the custom-built micro-tensile bench into the chamber of the Hitachi S-3700N SEM microscope.

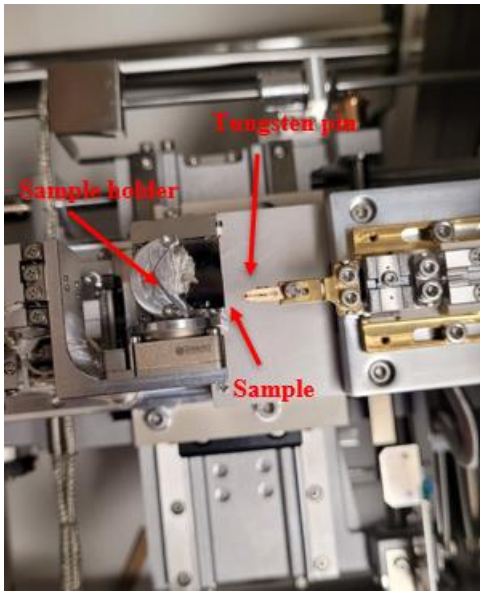

Figure 82: Main components of the custom-built micro-tensile bench consisting of the tungsten pin, specimen holder, and copper wedge.

6.2. Alignment of Copper Tensile Specimen for Mechanical Testing

Alignments of the copper micro-tensile specimens on the micro-tensile bench were made prior to the mechanical testing. It is important to make sure the specimen are well aligned in the tensile direction avoid bending and shearing stresses induced from off-axis alignment of the gauge section. After the micro-tensile bench was connected and loaded inside the chamber of the Hitachi S-3700N SEM microscope, the working distance of specimen holder height (of the tensile bench) was set to 15 mm prior to pumping the chamber. After the chamber is pumped to a high-vacuum atmosphere, the SE beam was turned on. The copper wedge containing the tensile specimens was brought into proximity of the tungsten pin by moving the tensile stage in the X and Y directions using the MDS (larger software package) controller. Prior to loading the tensile specimen into the tungsten pin, focusing and stigmation was performed to determine the working distances for the surfaces of the tensile grip and the pin, correspondingly at identical high magnification views. The working distances were measured to ensure that the copper wedge was higher (closer to the polepiece) than the pin. This prevents the pin from coming into contact with the grip section of the tensile specimen when the sample was moved above the pin, prior to inserting the grip into the pinhole.

Once the pinhole of the grip was moved above the pin, the field-of-view of the SEM is moved towards the gauge section to align the gauge length parallel to the tensile pulling direction. If the alignment was initially off by a few degrees from the tensile axis, the tensile stage can be rotated to realign the sample back in-axis to the pulling direction. After the gauge section was aligned to the tensile loading axis, the pinhole of the grip was centered and moved into the pin using the MDS controller. Initially, the tungsten pin was not manufactured perfectly straight (the pin was slightly bent). Therefore, movement in the and X and Y directions of the tensile stage during insertion of the sample was performed to compensate for the pin curvature. At the same time, the load-versus-time curve of the MDS software module was continuously checked to see whether the specimen comes in contact with the pin during insertion. In addition, the flatness of the copper wedge was checked by measuring the working distance of the specimen grip surface and the surface of the wedge component, corresponding at the same high magnification view. Changes in the two working distances can be adjusted by tilting the tensile stage until the two working distances match the same value.

Once the grip was loaded into the pin by a quarter distance deep from the bottom of the pin, the stage of the SEM was tilted to 15-2- degrees to observe the bottom of the pin. Afterwards, the loading of the specimen onto the pin continues until the bottom of the pin is reached. Full insertion of the specimen onto the pin is important to prevent bending of the pin during the tensile test. When the pin specimen was loaded to the bottom end of the pin (without the surface of the grip touching the bottom of the pin surface), the tensile specimen was pulled in tension by a few millinewtons to introduce a small tension in the specimen prior to beginning the mechanical test. The small tension prevents the specimen from moving during analysis of the specimen in the SEM prior to starting the mechanical test.

Initial measurements of the gauge length and width taken in the SEM using measurement boxes before beginning the test, as shown in Figure 84. The measurement of the gauge width accounts for the white layer on the gauge edge from the edge effect. The measured gauge length

is used to calculate the head displacement rate of the tensile specimen specified in the MDS module, which is the initial gauge length l_0 multiplied by the strain rate $\dot{\gamma}$ as shown in Equation 14. Also, it was noted that the measured gauge width in the SEM is not the true gauge width value. The true gauge value is larger than the measured gauge width in the SEM and is calculated by considering the tilt of the gauge section from the thinning process. Therefore, $True\ gauge\ width = \frac{Measured\ Gauge\ Width}{Cos(\theta)}$ Equation 15 was used to calculate the true gauge width value, where θ is the degrees off-set from the tensile axis (or the tilt off-set from the 52-degrees milling configuration of the PFIB stage used during the gauge thinning process).

$$Head\ displacement\ \left(\frac{\mu m}{s}\right) = l_0\dot{\gamma} \qquad \text{Equation 14}$$

$$True\ gauge\ width = \frac{Measured\ Gauge\ Width}{Cos(\theta)} \qquad \text{Equation 15}$$

After the gauge width and gauge length were measured, focus, brightness, and contrast in the SEM were adjusted for the field-of-view of the gauge surface. In addition, one of the reference fiducial marks at the ends of the gauge section was focused at high magnification views of 5-10 µm. It is important that the fiducial marks were highly focused to ensure the tracking of the strain using the fiducial marks can be done accurately from the SEM images taken at each 10 mN load intervals. After the fiducial mark were focused with good brightness and contrast, the gauge surface was centered in the SEM field-of-view at a magnification of 100 µm as seen in Figure 84.

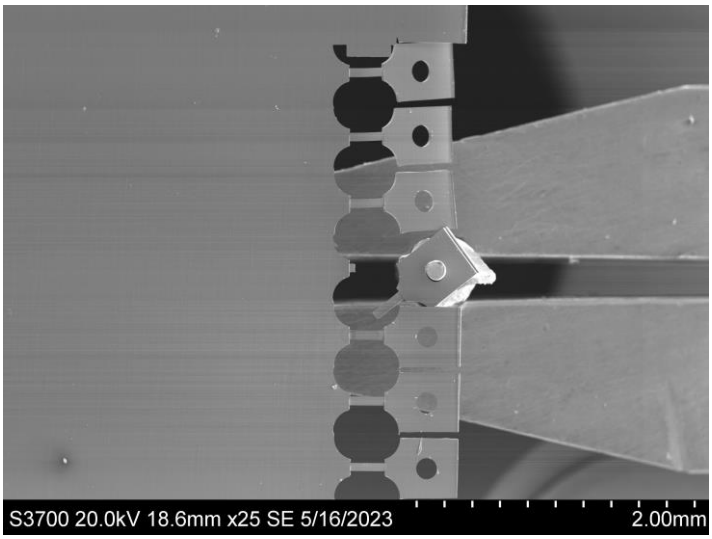

Figure 83: Low magnification SEM image exhibiting the mechanical testing of PFIB-machined tensile specimen 6 from wedge 2. Right side of the image shows the static clamp holding the tungsten pin of the micro-tensile bench used to pull the moving specimens in tension.

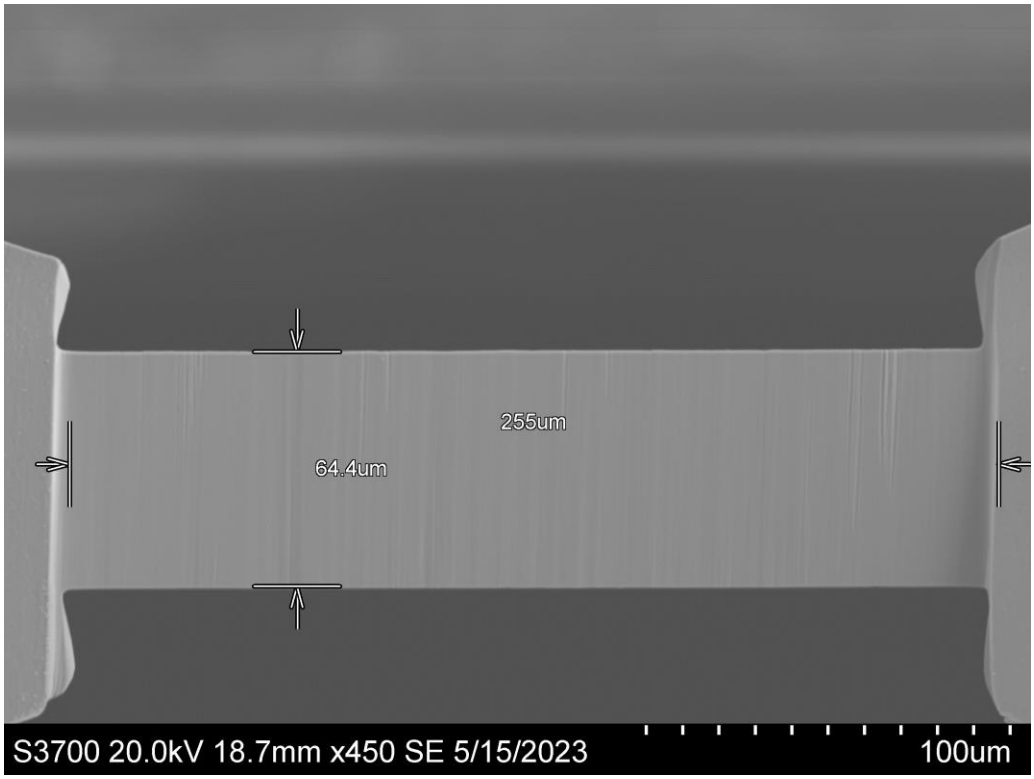

Figure 84: Measurements of the initial gauge length and width for PFIB-machined tensile specimen 6 wedge 2 prior to micro-tensile testing in the SEM.

6.3. Onset of Plasticity

After the gauge section was focused and aligned in the SEM field-of-view, the load and elongation on the MDS module was set to zero. A new tensile test was initiated for the tensile specimen. A SEM image was taken (prior to beginning the tensile test) as a reference image for measuring the initial distance between the two reference fiducial marks. The tensile specimen was moved in uniaxial tension with the indicated head displacement and strain rate of $5\ x10^{-4}\ s^{-1}$ in the MDS module. The test was stopped at every 10 mN to take an SEM image. After the SEM image was taken, the test was continued with a gradual increase in load until the next 10 mN load interval was reached. The number of images taken correlates to the number of data points used for plotting the stress-strain curve from each tensile test. Therefore, if the SEM images were taken at shorter load intervals, more data points would be acquired. Although, the number of images acquired up to the ultimate tensile strength (UTS) of the tensile specimen was also dependent on the size of the initial area of the gauge cross-section. A specimen with a smaller area (or smaller gauge thickness value) exhibits larger stress intervals (and less data points acquired) than that of thicker specimens. The resultant load-versus-time plot from the MDS module is a staircase curve with the horizonal sections of the curve representing periods of image acquisition. The load-versus-time curve was converted into a stress-versus time curve for all the tensile specimens tested, as shown in Figure 85 for fs-laser-machined tensile specimen 5 from wedge 3.

During the early stages of the mechanical test, the tensile specimen is elastically deformed. Indication of elastic behaviour can be seen from the staircase curve, where to load continues to increase when the test is paused during image acquisition. The load continues to increase due to the atomic bonds being stretched. Once the deformation of the tensile specimen reached the transition from elastic to plastic behaviour, an initial dip was seen in the horizontal section of the staircase-shaped curve. Th dip is an indication of the specimen's tensile yield stress (also known as the onset of plasticity). The load (or stress) was lowered to compensate for the initiation of slip between the atomic planes in the internal structure of the specimen. As the test continues with increasing load intervals, the dip during the relaxation periods become larger. The time is takes for the load to increase becomes longer during each load interval, due to the effects of strain hardening when multiple slip planes are activated. The tensile test continues pass the UTS point of the staircase curve until the load starts to drop as the tensile specimen continues to be strained. The drop in stress as the specimen continues to be pulled at an increasing load is an indication of damage accumulation (necking) of the tensile specimen. This method of determining the yield point of the copper tensile specimens was adopted from Wheeler *et al. (2016)*'s work on the micro-tensile testing of polycrystalline copper and magnesium micro-tensile specimens [10].

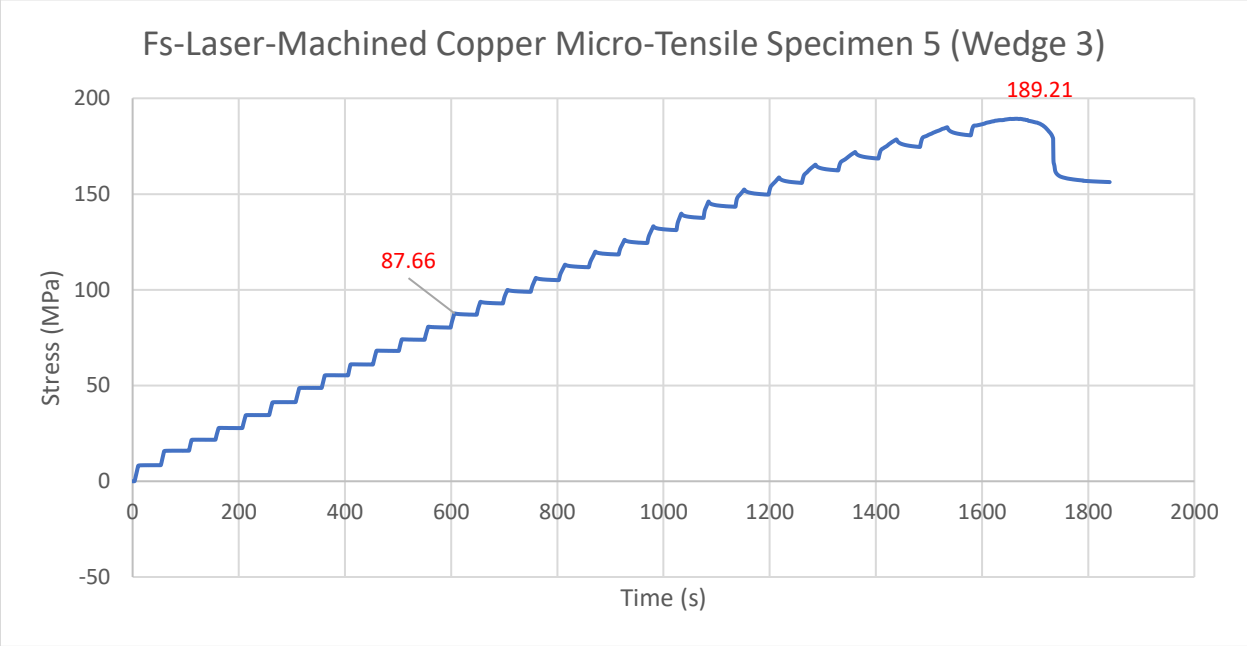

Figure 85: Stepwise stress-versus-time curve for fs-laser-machined copper micro-tensile specimen 5 from wedge 3. The onset of plasticity (yield stress) is indicated by initial dip in stress of the staircase curve. A yield stress of 87.66 MPa and an ultimate tensile strength of 189.21 MPa was measured for the tensile specimen.

6.4. Complications Encountered During Mechanical Testing of Copper Micro-Tensile Specimens

During the mechanical testing of both the PFIB and fs-laser-machined micro-tensile specimens, several complications occurred. For three tensile specimens, a harmonic occurred

during testing of each individual specimen, respectively. The harmonic was due to the vibration of the tungsten wire. This usually occurs when the wire has been strained over time during repetitive testing of specimens, resulting in a decrease in tension on the wire. Therefore, it is important to replace the tungsten wire on the tensile bench overtime from repeated mechanical testing of specimens.

When a harmonic was reached, the test was continued by increasing the tensile load until the harmonic was surpassed. The increase load required to surpass the harmonic is dependent on how the large the harmonic is. For the PFIB-machined tensile specimen 1 from wedge 1, a 30 mN load increase was required to surpass the harmonic, while a 50 mN was required to surpass the harmonic for the PFIB-machined tensile specimen 1 from wedge 1 and fs-laser-machined tensile specimen 5 from wedge 2. For the fs-laser-machined tensile specimen 4 from wedge 4, the harmonic was too large that the test had to be terminated since the yield point from the load-versus-time curve was indistinguishable.

Another complication that occurred for approximately half the number of tensile specimens that were tested was the rotation of the gauge section when the tensile specimens were strained in tension. The rotation of the tensile specimen caused the gauge section to be misaligned from the tensile loading axis. The misalignment caused the concentration of slip bands to form near the free end or fixed end of the tensile specimen's gauge section, as seen in Figure 86. Misalignment during testing was mainly due to the difference between the diameter of the pinhole and the tungsten pin. The tungsten pin had a diameter of 145 μm, while the pinhole of the PFIB-machined tensile specimens and the fs-laser-machined specimens had a diameter of approximately 155 μm, respectively. Therefore, the tensile specimen was able to rotate with the clearance space between the pinhole and the pin. Tensile specimens with a thinner gauge section (under 20 μm in thickness) are more sensitive to the misalignment, due to the lower stiffness of the gauge section compared to that of thicker tensile specimens (of 20-30 μm in thickness). This complication can be seen from the SEM images taken for both thin and thick tensile specimens, where most of the misaligned gauge sections occurred for the thinner tensile specimens. In most cases, when the specimens were aligned well to the tensile loading axis, the stress was concentrated at the middle of the gage section, which slip bands were seen originating from the middle of the gauge length, as seen in Figure 87.

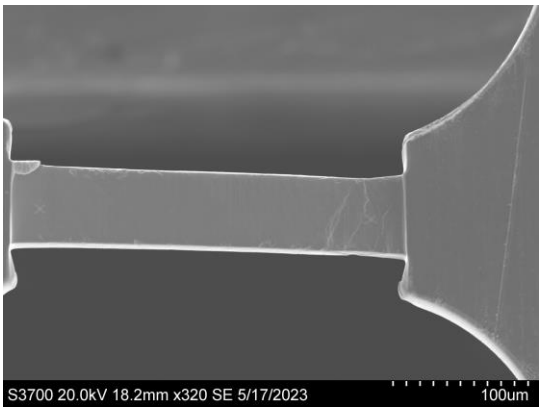

Figure 86: Misaligned tensile specimen (PFIB-machined tensile specimen 5 from wedge 1).

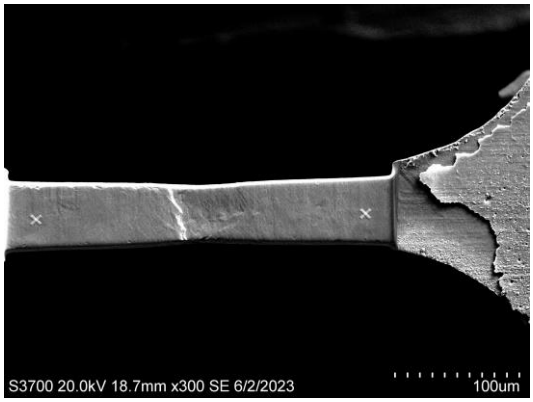

Figure 87: Aligned tensile specimen (fs-laser-machined tensile specimen 5 from wedge 3).

In addition, another complication encountered during mechanical testing of a few tensile specimens was the occurrence of drift of the tensile bench. The drift came from taking the tensile bench out of the SEM chamber and placing it back into the chamber when the old copper wedge was switched with a new copper wedge after testing all the tensile specimen on the old wedge. When the tensile bench was placed back into the chamber, the change in environment caused the tungsten wire to fluctuate. Therefore, drift from the tensile bench was observed through the load-versus-time graph, in which the load increases at a very small rate even though there was no tension on the specimen. Typically, the drift settles down within 1-2 hours after placing the tensile bench into the SEM chamber. When some of the tensile specimens were tested during the drift period, the yield point on the staircase curve was difficult to determine, due to the increasing load at each relaxation period. Therefore, for fs-laser tensile specimens 1 and 2 from wedge 3 and fs-laser-machined tensile specimen 3 from wedge 2, the drift of the vibrating wire produced a significantly higher yield stress value detected on the staircase curve compared to the yield stress of tensile specimens with similar gauge thicknesses. Therefore, the data from the mechanical testing of the three tensile specimens during drift were excluded from the size-effect study on (100) copper.

Although, 48 copper tensile specimens were fabricated (including both PFIB-machined and fs-laser-machined tensile specimens), only 32 specimens were tested. A larger number of the specimens were bent during handling of the fabrication process and mechanical testing stage. Table 15 under Appendix A4 lists all the PFIB-machined and fs-laser-machined tensile specimens that were mechanically strained using the custom-built micro-tensile bench and their corresponding yield stress values measured from the stress-versus-time curves.

6.5. Mechanical Test Results

6.5.1. Slip Behaviour

The mechanical testing of the copper tensile specimens showed a variety of deformation behaviours for specimens with various gauge thickness values. From the final SEM images taken of each strained tensile specimen, slip bands were present at the at the surface of the gauge section. After the onset of plastic yielding, the number of slip events between the atomic planes of copper increased under continuous incremental loading. For all strained tensile specimens, slip bands travelled up to the surface (from the interior of the specimen) prior to reaching the UTS.

Copper has 12 slip systems for an FCC material. Due to the anisotropic nature of the (100) copper, the material deforms in a more orderly fashion compared to polycrystalline copper (where the microstructure is composed of grains orientated in different directions). The deformation process of single crystal materials typically develops through four stages, as depicted in Figure 88 [45].

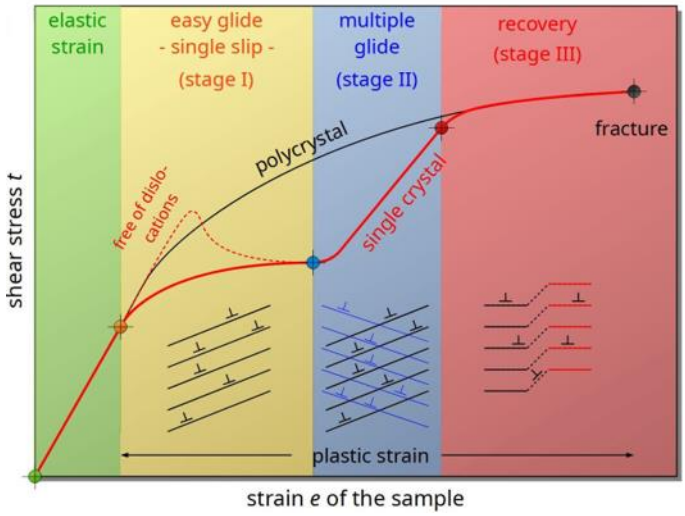

Figure 88: Stages of deformation depicted from a single crystal material's stress-strain curve [45].

In the first stage of deformation, the tensile specimen undergoes linear-elastic strain, as exhibited by the linear positive slope in Figure 88. During this stage, deformation induced on the tensile specimen is reversible. If the specimen was to be unloaded, the specimen would return to its original shape. During this stage, the atoms are displaced slightly in their atomic planes due to interatomic forces formed from the initial loading stage [46]. At this stage of deformation, there is no presence of slip between the atomic planes. The Young's Modulus which defines the stiffness of the material specimen (resistance to slip) can be extracted from the linear- positive slope. In addition, the elastic behaviour can be described using Hooke's laws, where the tensile stress is proportional to the amount of material displaced in tension [47].

In the second stage, single slip is the predominant deformation mechanism. Single slip presents itself as parallel slip bands formed across the body of the single crystal specimen, as shown by the schematic in Figure 89. At this stage of deformation, there is negligible work hardening involved since dislocations do not collide with another from different slip systems. Single slip typically originates from the primary slip plane of the crystal exhibiting the highest (or maximum) Schmid factor value. The Schmid factor, m, is a geometric quantity that describes

the slip plane and slip direction for a slip band formed when a specimen is under an applied external load. The Schmid factor can be calculated using Equation 16, where ϕ is the angle between the loading direction and the slip direction, and λ is the angle between the loading direction and slip plane normal, as depicted in Figure 90 [48]. In addition, the critically resolved shear stress, T_{CRSS} (shear stress required to initiate slip) in a single crystal material is also related to the maximum value of the Schmid factor and the yield stress of the materials, as seen by the relation in Equation 17. To acquire the Schmid factor for each single slip band formed on the gauge section of each strained tensile specimen, both ϕ and λ must be measured. To determine the slip plane normal, the angle in which the slip plane runs across the gauge cross-section must be measured, as well as the angle in which the slip plane runs along both sides of the gauge surface. Therefore, the slip band must be measured in 3D to obtain an accurate calculation of the Schmid factor value. For the purpose of defining only the types of slip bands formed on the gauge section for the copper specimens, the Schmid factors for the slip bands formed on the gauge surfaces were not calculated.

$$m = cos\phi cos\lambda \qquad \text{Equation 16}$$

$$T_{CRSS} = m\sigma_Y \qquad \text{Equation 17}$$

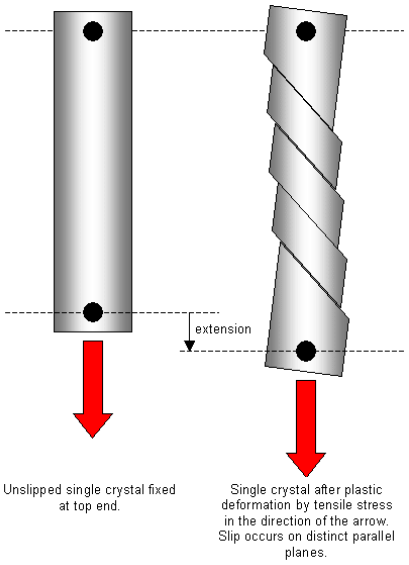

Figure 89: Schematic showing single slip behaviour under an applied tensile load [49].

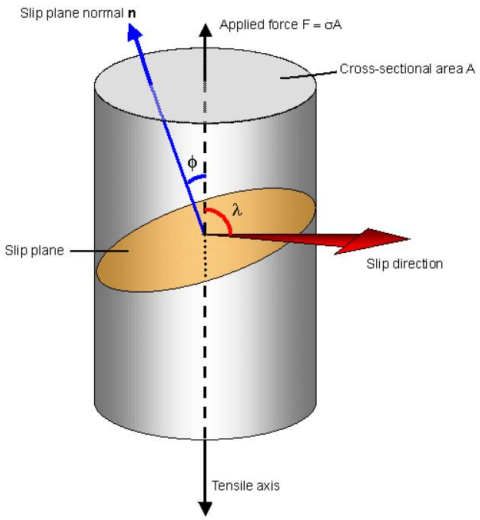

Figure 90: Schematic showing calculation for the resolved shear stress of a slip plane in a single crystal under an applied force of F=σA. [50].

Therefore, single slip deformation is the indication of initial yielding of the material. The yield point transition from elastic to plastic behaviour can be observed from the load-versus time curve. However, depending on how large the gauge cross-section is when converting the load intervals to stress intervals (from a load-versus-time curve to a stress-versus-load curve) the dip in the staircase curve can be difficult to spot for larger stress intervals used. For most strained specimens, single slip deformation could not be detected at the vicinity of the yield stress point from the image acquisition, due to the single slip originating from the subsurface of the gauge section. By the time the slip bands reach the surface, the activation of multiple slip bands in the third stage would have most likely occurred. This was seen for most gauge sections of the tensile specimens, where multiple slip events had occurred prior to necking. However, for a few tensile specimen, single slip was present at the gauge surface such as the fs-laser-machined tensile specimen 3 from wedge, as seen in Figure 91 of the consecutive SEM images taken (at 10 mN load intervals) prior to reaching the UTS point. As the tension test continued, stage three of deformation was introduced, where slip from different slip systems were activated through the presences of multi-slip from different planar directions. As well, single slip was seen for tensile specimens that had formation of slip bands in multiple areas of the gauges section. One example shows single slip formation happening for the fs-laser-machined tensile specimen 6 from wedge 2 in Figure 92, where single parallel slip bands were formed on the left end of the gauge section, while multiple slip systems were active on the right end of the gauge section. The rotation of the tensile specimen during the mechanical tests, may have caused localized bending stresses to occur at the right end of the gauge.

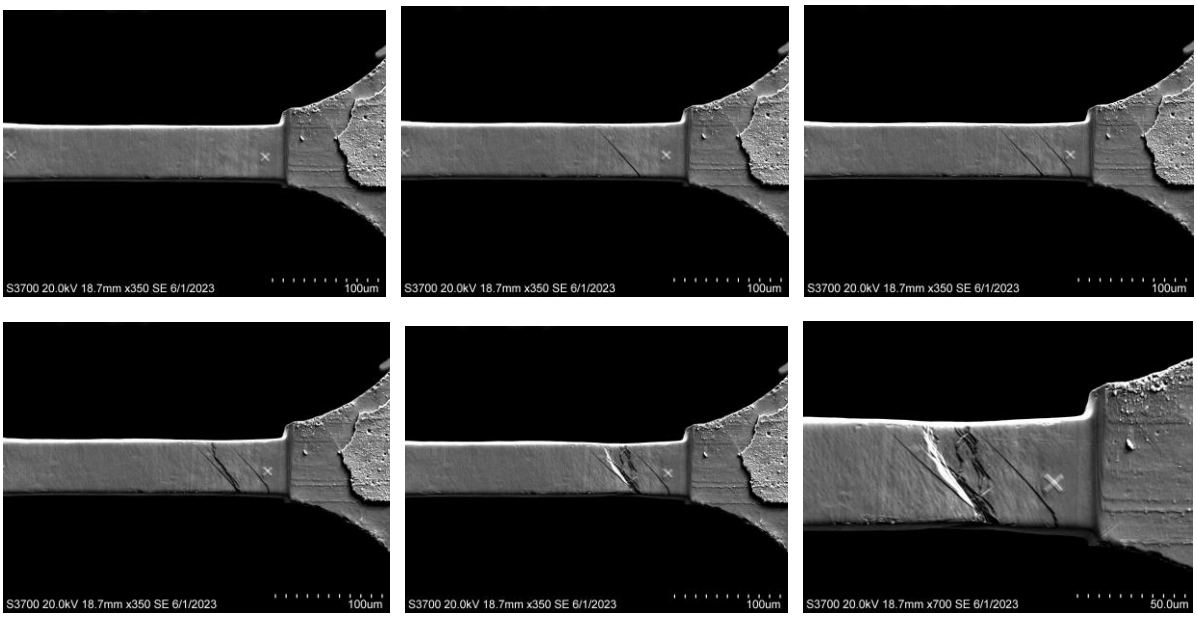

Figure 91: SEM image series of single slip formation and transition to multi-slip deformation behaviour of the gauge section for fs-laser machined tensile specimen 3 from wedge 3.

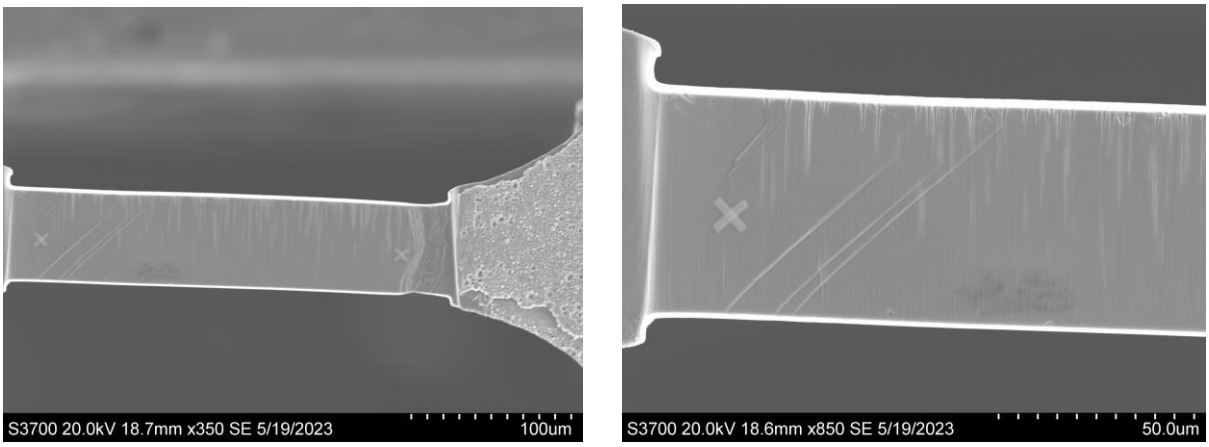

Figure 92: Single slip observed on left end of gauge section for fs-laser-machined tensile specimen 6 from wedge 2.

During the third stage of multi-slip deformation, slip bands from different slip systems of the crystal are activated. At this point, dislocations travelling at different planar directions intersect with one another and impede the motion of dislocations. Dislocations originate from different planar angles and directions. Sometimes, slip from different atomic planes occur at the same time, causing a traffic jam of dislocations. To overcome the dislocation impediment, a higher stress is required to drive the deformation process forward. In some cases, when two dislocations intersection with one another perpendicularly from different slip systems, a forest of dislocations is formed. Forest dislocations are static obstacles for dislocation motion. Therefore, when the tensile specimen is unloaded, the forest dislocations remain in the internal structure of the material. Mobile dislocations that originate from different slip systems tend to get stuck when they encounter forest dislocations. Due to the hindrance of plastic flow, work hardening is introduced at this stage of plastic deformation. In addition, during the intersection of

dislocations, jogs and kinks can also form and play a role in the work hardening behaviour of the material. A jog adds an addition line segment to the dislocation line, which requires addition energy to form. Dislocations also move less easily with the presence of jogs. A kink is a type of jog in which the line segment of the jog in formed in the slip plane (normal to the dislocation line). Multi-slip deformation can be seen in most of the strain copper tensile specimens, where multiple slip bands travel from the internal of the gauge up to the gauge surface at the same time. The locations of multi-slip were seen on the right and left ends of specimens, as well as in the middle of the gage section of other specimens, as shown in Figure 86, Figure 87, and Figure 92, respectively.

In the final stage of plastic deformation leading to the UTS of the tensile specimen, cross-slip and climb occurs to relieve the work hardening of the material produced in stage three. This is a stage of deformation is known as crystal recovery since dislocation are freed from blockage of other dislocations and are able to continue gliding through the material by taking another path in a different slip system. Under the elevated loading of the specimen in tension, dislocations cross over to different slip planes through dislocation climb for edge dislocations and cross slip for screw dislocations, as depicted by the schematics in Figure 93 and Figure 94, respectively. In the case of edge dislocations where the Burger's vector runs parallel to the edge dislocation, the dislocations are able to climb either negatively or positively over to another slip plane through the help of vacancy sources. Positive climb occurs when the dislocation is able to move and fill near by vacancy spot, while negative climb occurs when the dislocation acts as a vacancy source and is able to move to another slip plane when nearby atoms fill up the vacancy spot [51].

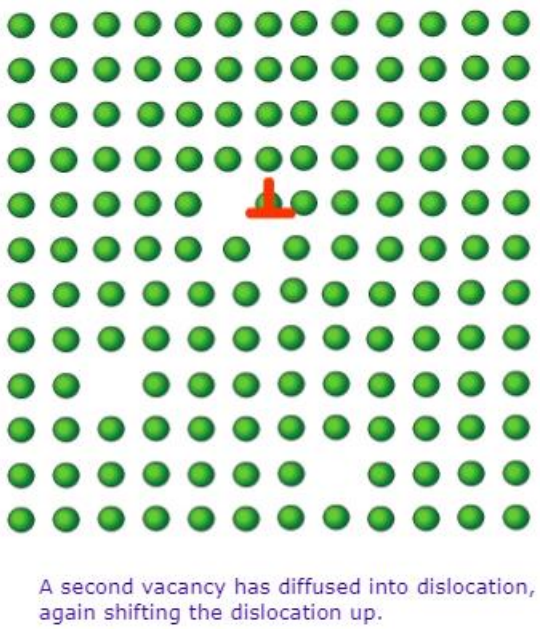

Figure 93: Schematic showing dislocation climb of an edge dislocation in a material lattice plane [51].

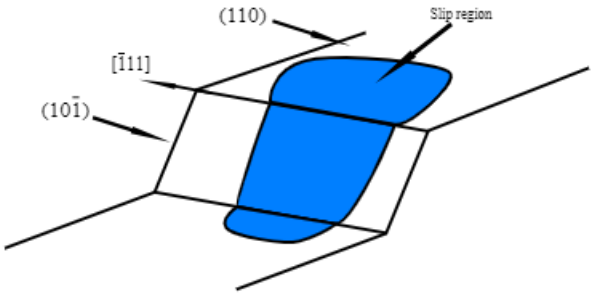

Figure 94: Schematic showing cross slip movement from one plane to another *[51]*.

Cross-slip occurs through the movement of screw dislocations from one slip plane to another. For cross-slip to occur, the Burger's vector must be perfectly parallel to the screw dislocation. The mechanism for cross-slip slip is more difficult to occur in FCC materials (such as copper) compared to BCC and HCP materials. The complexity is due to the ABCABC stacking sequence of atoms in the FCC lattice structure, as seen for the (111) plane for an FCC metal in Figure 95. In FCC materials, slip occurs through the formation of two partial dislocations from a full dislocation. The formation of the partial dislocation is more energetical favorable than producing cross slip in FCC materials. In addition, the partial dislocations formed produces a stacking fault sequence of ABC AC ABC in the lattice structure. The partials cannot cross slip since they can only move in the primary plane. Although, cross slip can occur only if the partials were to recombine (or combine with a different partial) to form a single screw dislocation again (also known as a constriction). After the cross-slip event, the dislocation splits again into two partial dislocations (different from that of the original pair), and the process of forming a constriction repeats again. The sequence of dislocation events is depicted by the schematic in Figure 96 [51].

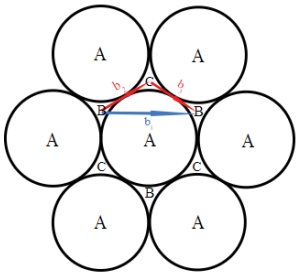

Figure 95: Two-step process of slip in the (111) plane of an FCC material with ABCABC stacking sequence [51].

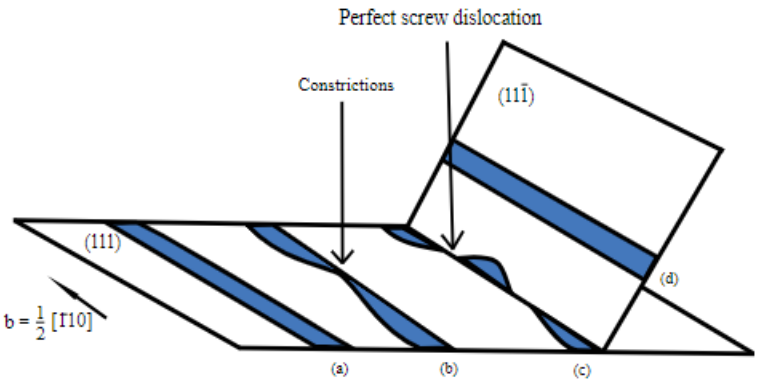

Figure 96: Schematic showing the consecutive development of constrictions and cross-slip for the (111) plane of an FCC material [51].

Distinct cross-slip formation was observed through SEM imaging for fs-laser-machined copper tensile specimen 1 from wedge 3, as seen in Figure 97. It can be observed through the hatching pattern on the surface of the gauge section that dislocations have crossed over to different slip systems when parallel slip bands formed perpendicular to other parallel slip bands. In addition, a zig-zag pattern was seen for some slip bands as they crossed from one plane to another, such as for specimen 1 from wedge 3. From the acquired SEM images of specimen 1 from wedge 3, it was observed that two parallel single slip bands were the first form of slip bands that surfaced to the gauge section. Afterwards, multiple slip formation was exhibited at the gauge surface. As the load increased, a large slip bands formed and ran across the gauge width. More single slip bands formed from the primary slip system and crossed the large slip band in a perpendicular fashion, as well as the formation of single slip bands from the slip system of the largest slip band seen in Figure 97. Cross-slip was also identified in PFIB-machined tensile specimen 6 from wedge 1 seen in Figure 98, where sharp staircase slip bands ran across the gauge width. The crossing of the dislocations can be distinctively identified by the angles that the screw dislocations make to cross from the initial slip band to another slip band from a different slip system.

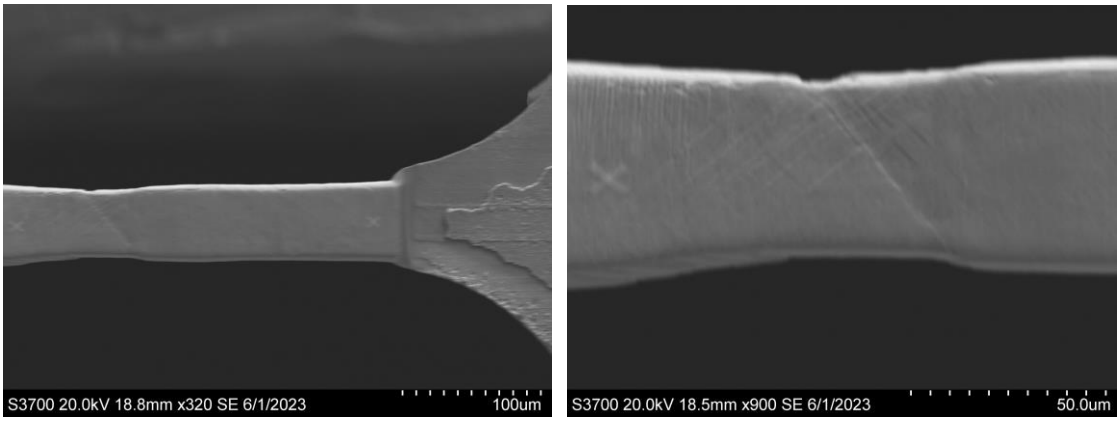

Figure 97: SEM image showing cross-slip from the mechanical deformation of fs-laser-machined tensile specimen 1 from wedge 3. Right image shows magnified view of the cross slip occurring at the center of the gauge surface.

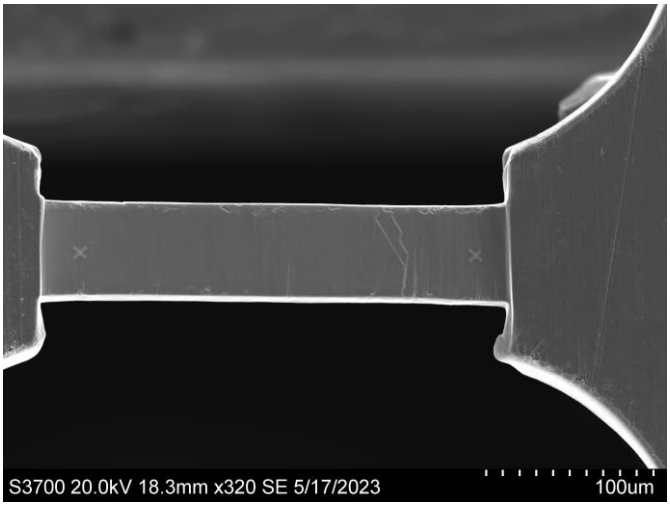

Figure 98: SEM image showing cross-slip in the plastically deformed PFIB-machined tensile specimen 6 from wedge 1.

For the misaligned tensile specimen, the formation of slip bands was more immediate. When the specimen was misaligned clockwise to the tensile loading axis, the stress was concentrated at the right end of the gauge section. When the specimen was rotated counterclockwise, the stress is concentrated on the left end of the gauge. Therefore, slip bands with surfaces of intrusion and extrusion were formed at the gauge ends due to induced shear forces from the misalignment, as seen in Figure 86. Therefore, a progressive development from the three stages of plastic deformation is not present for most of the misaligned specimens.

Figure 99 shows a plot of the measured yield stress values for all of the strain copper tensile specimens against their corresponding gauge thickness. The specimens were also categorized by the location and type of the slip bands formed on the gauge surfaces. From the plot, there are no significant trends that was seen for the effect of gauge thickness on the location and type of slip bands formed.

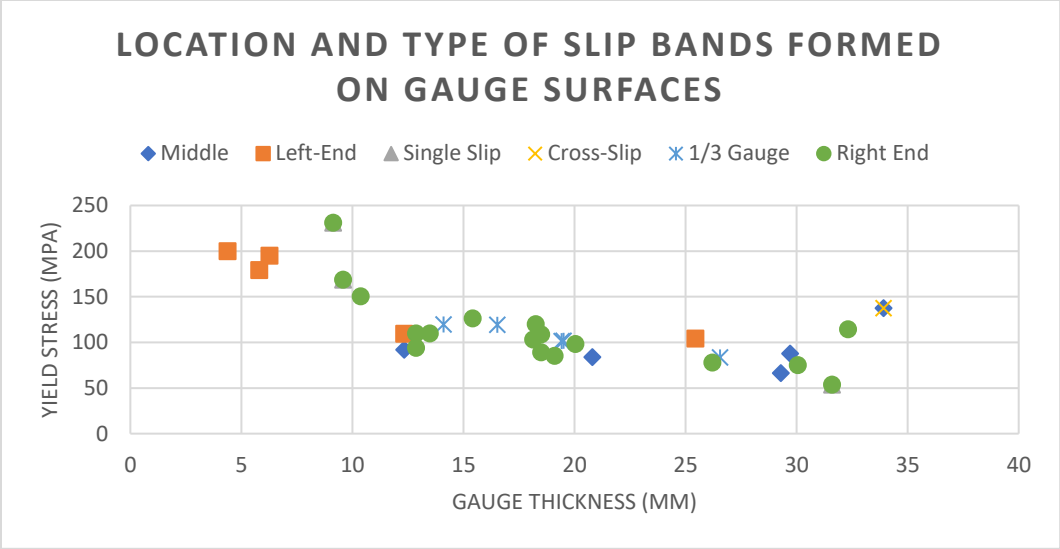

Figure 99: Tensile specimens of various gauge thicknesses exhibiting different slip behaviours.

6.5.2. Post Data Analysis: Strain Measurements

To develop a stress-strain curve for each tensile specimen tested, the SEM images taken at each load interval for each tensile specimens were processed using ImageJ software. The accumulated strain from each increasing load interval on the specimen was measured using the reference fiducial marks deposited on left and right ends of the gauge surface. The distance from one end of the fiducial to the other was measured from the point of the inner cross-section of the fiducials, as shown in Figure 100 by the red dot indicators.

The first image taken prior to the start of each mechanical test for the tensile specimens was used to measure the initial distance between the two fiducial marks. The initial distance d_o between the two fiducial marks was calculated using Equation 18 by taking the distance between two points of the fiducial marks using the X and Y coordinates of each point from the first SEM image taken prior to mechanical testing, where $Y_{0,1}$, $Y_{0,2}$, $X_{0,1}$ and, $X_{0,2}$ represents the initial X and Y positions of the two points on the fiducial marks, respectively. Therefore, the initial distance between the two fiducials prior to straining was used instead of the initial full length of the gauge section. The reason for not using the ends of the gauge section to make the strain measurements is that the corners of the edges have a slight curvature to them from the ion milling fabrication process, making more difficult to track the elongation using ImageJ.

Initially, when the SEM image of the gauge surface in loaded in the ImageJ softwaresoftware, a scale bar was set to a unit of 1 by measuring the length of the scale bar of the SEM image. Afterwards, the strain was measured along the distance between the two fiducial marks as they get further away from each other as the gauge section gets extended. The strain of the gauge was calculated using Equation *19* for each consecutive SEM images taken during the stepwise loading of the specimen, where X_1 and X_2 represents the X-positions of the two points taken at the fiducial marks, and Y_1 and Y_2 represents the Y-positions of the two points

taken at the fiducial marks, Δd represents the elongation of the gauge length, and d represents the instantaneous distance between the two points. The strain was measured for each SEM image taken at the relaxation periods of each tensile specimen tested. The corresponding stress values from the stress-versus was plotted the corresponding calculated strain values from the SEM images in an engineering stress-strain curve for each tensile specimen tested. Figure 101 shows the plotted stress-strain curve up to the UTS point for the fs-laser-machined tensile specimen 5 from wedge 3.

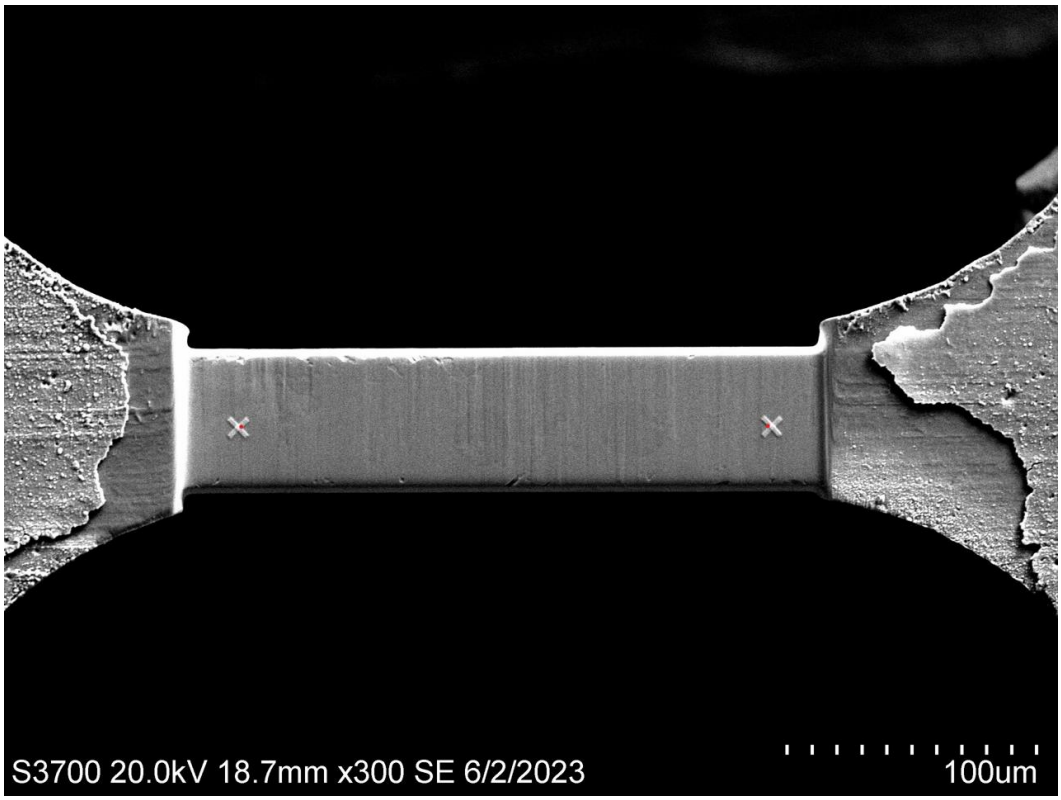

Figure 100: Location of reference points on the fiducial marks (indicated by red dots) for measuring strain using ImageJ software.

$$d_0 = \sqrt{(Y_{0,2} - Y_{0,1})^2 + (X_{0,2} - X_{0,1})^2} \qquad \text{Equation 18}$$

$$\varepsilon = \frac{\Delta d}{d_0} = \frac{d - d_0}{d_0} = \frac{\sqrt{(Y_2 - Y_1)^2 + (X_2 - X_1)^2} - d_0}{d_0} \qquad \text{Equation 19}$$

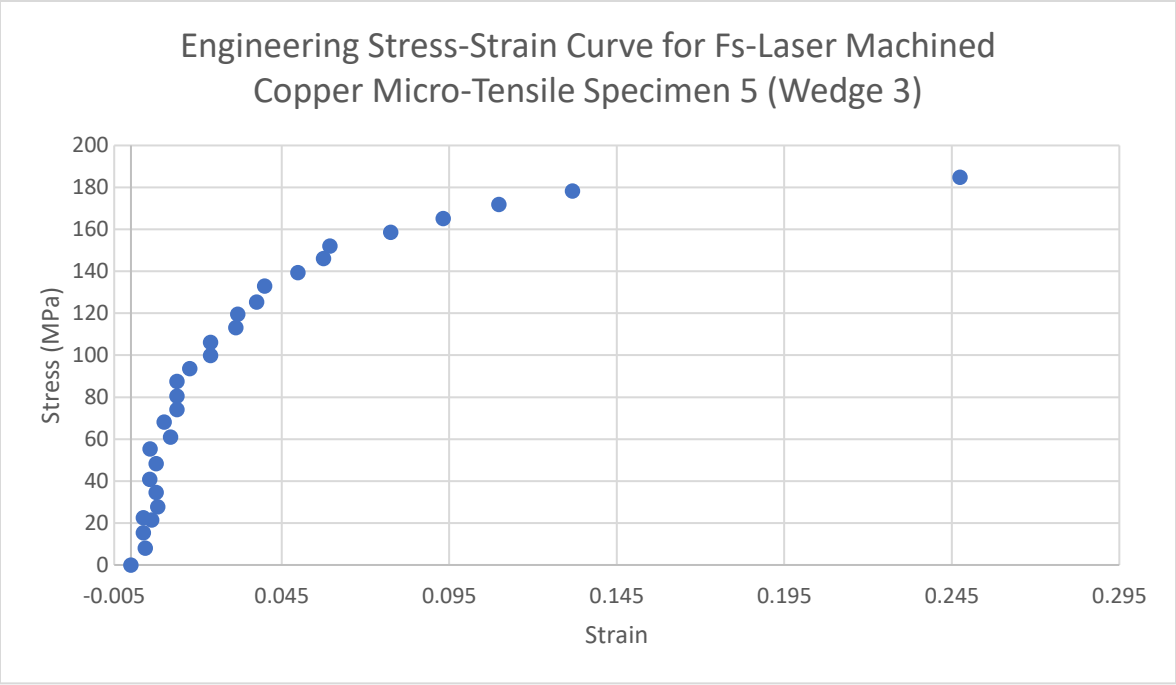

Figure 101: Engineering stress-strain curve for fs-laser-machined copper micro-tensile specimen 5 from wedge 3.

6.6. Validation of Size Effect Phenomenon

The object of fabricating and mechanically straining a large number of copper micro-tensile specimens was to determine whether there were existing size-limiting effects on the deformation behaviour of the tensile specimens, ranging from 31 µm to 4.6 µm. Size limiting effects were seen from copper micro-tension and micro-compression-tests in literature [5][17]. A decrease in the dislocation density occurs when the dimensions of the miniature test specimens is decreased. The reduced number of dislocation interactions prevents the progression of plastic flow from occurring as a number of dislocation escape from the specimen's free surface. Therefore, to continue the process of plastic deformation, dislocations nucleate at the surface of the specimen. The nucleation events cause an increase in the flow stress of the specimen. Eventually, (under an increasing applied load), an avalanche of dislocation erupts in motion to cause plastic yielding of the specimen.

As a result of the micro-tension testing on the copper specimens, it was observed that the size-limiting single crystal copper specimens have a significantly higher yield stress that that of the bulk value for anisotropic copper. Therefore, the (100) copper tensile specimens did indeed exhibit a size effect where the yield stress increased with decreasing gauge thickness.

It was hypothesized that due to the misalignment of almost half of the tensile specimens tested, it was expected that the yield stress would be effectively higher than it should be when bending stresses are induced on the gauge section. In addition, in was predicted that there would be no offsets in the size effect trend seen for the specimens of various sizes with the different

fabrication method taken (of either fs-laser-machined or PFIB-machined specimens). The samples from both machining processes would provide similar machining quality of the micro-tensile specimens.

From the stress-versus-time curves plotted for each copper micro-tensile specimen tested, the yield stress was determined by the initial dip the staircase curve. The yield stress for each tensile specimen was plotted against their corresponding gauge thickness, as shown in Figure 102. Due to the drift observed for the stress-versus-time curves for fs-laser specimens 1 and 2 from wedge 3 and fs-laser specimen 3 from wedge 2, the measured yield stress was significantly higher than that of the true value. Therefore, the three specimens were excluded from the size effect study. In addition, the size effect was also seen in plots shown in Figure 103 and Figure 104, which shows the influence of the size of the gauge cross-sectional area and gauge volume on the yield stress of the specimens, respectively.

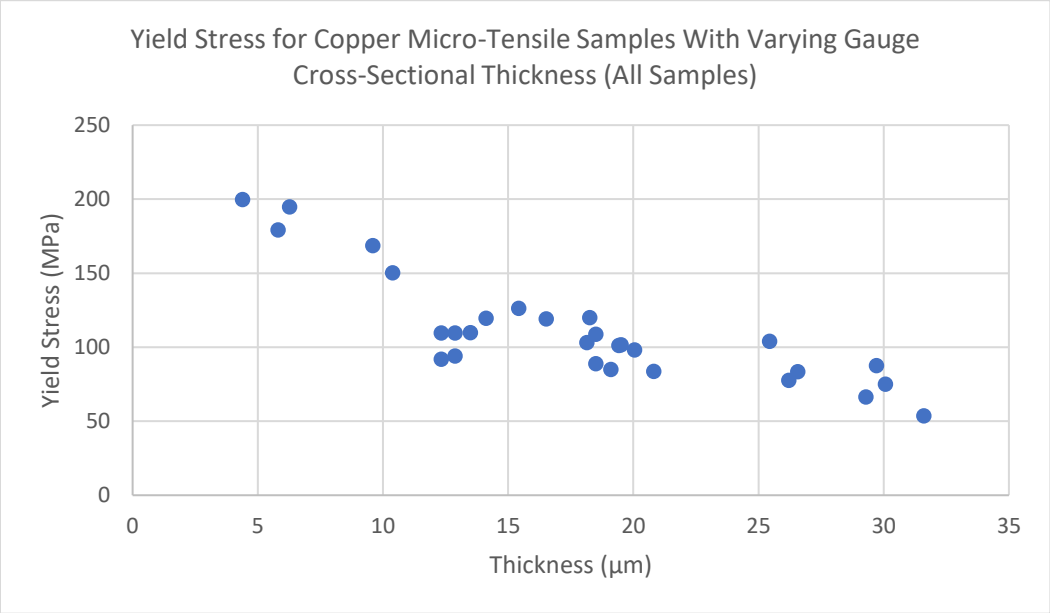

Figure 102: Plot of yield stress-versus gauge thickness exhibiting the size effect phenomenon for all tested copper micro-tensile specimens.

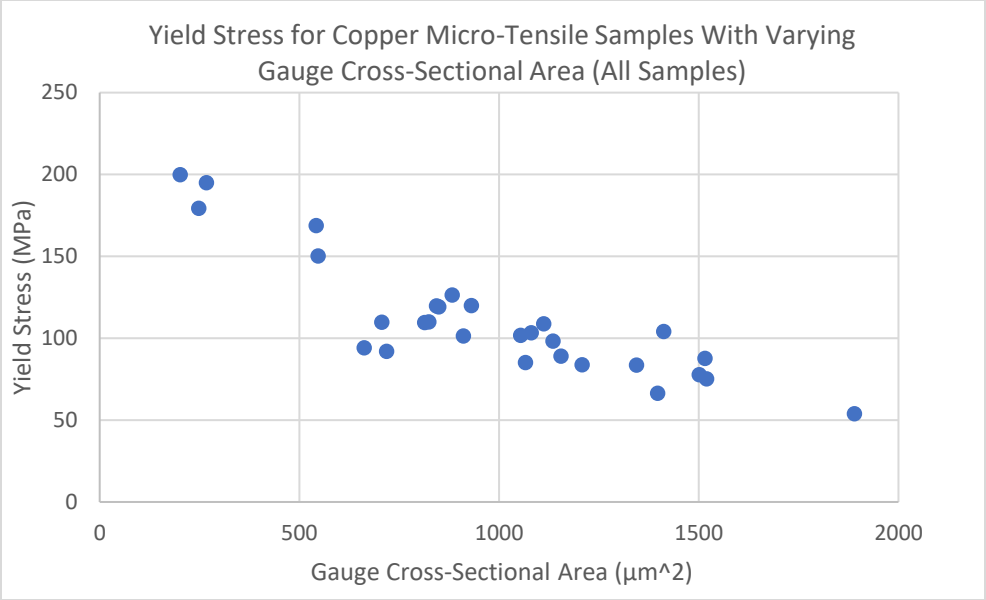

Figure 103: Plot of yield stress-versus gauge cross-sectional area exhibiting the size effect phenomenon for all tested copper micro-tensile specimens.

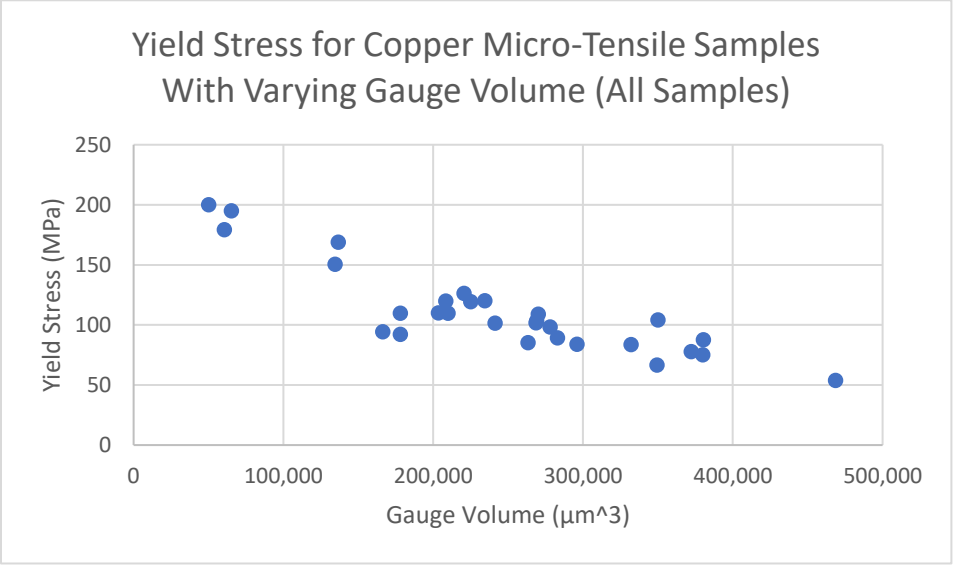

Figure 104: Plot of yield stress-versus gauge volume exhibiting the size effect phenomenon for all tested copper micro-tensile specimens.

In literature, the bulk yield stress was measured to be around 40-60 MPa. For example, *Tomoyuki Takeuchi, (1975)* performed milli-tension tests on single crystal copper by growing copper at various crystal orientations. The copper tensile specimens had a gauge volume of 2.1x 5.4 x 45mm^3, respectively. Then copper tensile specimen with a [001] growth direction exhibited a tensile yield stress of approximately 60 MPa in the corresponding stress-strain curve shown in Figure 105 [52]. Therefore, from comparing the bulk yield stress for [001] copper from Takeuchi's experiment to the yield stress values of the machined copper micro-tensile specimens, the largest specimens with gauge thicknesses of 31.6 µm and 29.29 µm exhibited

yield stress values closest to the literature bulk value. The transition point towards size-limited mechanical behaviour can be seen for specimens of 25-26 µm in gauge thickness, where the yield stress values began to deviate away from the bulk yield stress value. Afterwards, a gradual trend towards increasing yield stress was seen for specimens with increasing gauge thickness. Figure 106 shows the size effect of the copper specimens grouped together with similar gauge thickness values and with the addition of error bars representing the mean standard deviation of the yield stress and gauge thickness values of the copper specimens.

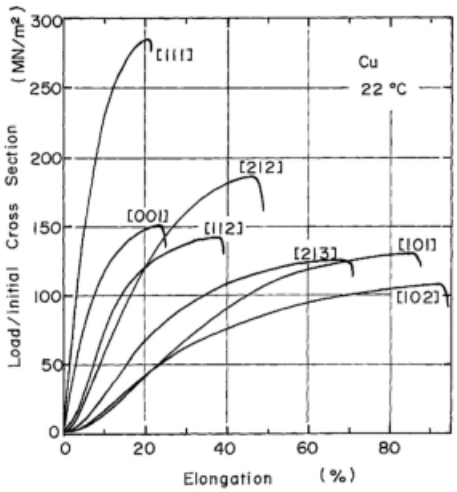

(b)

Figure 105: Milli-scale tensile experiments on copper single crystal orientated in various directions by Tomoyuki Takeuchi [52].

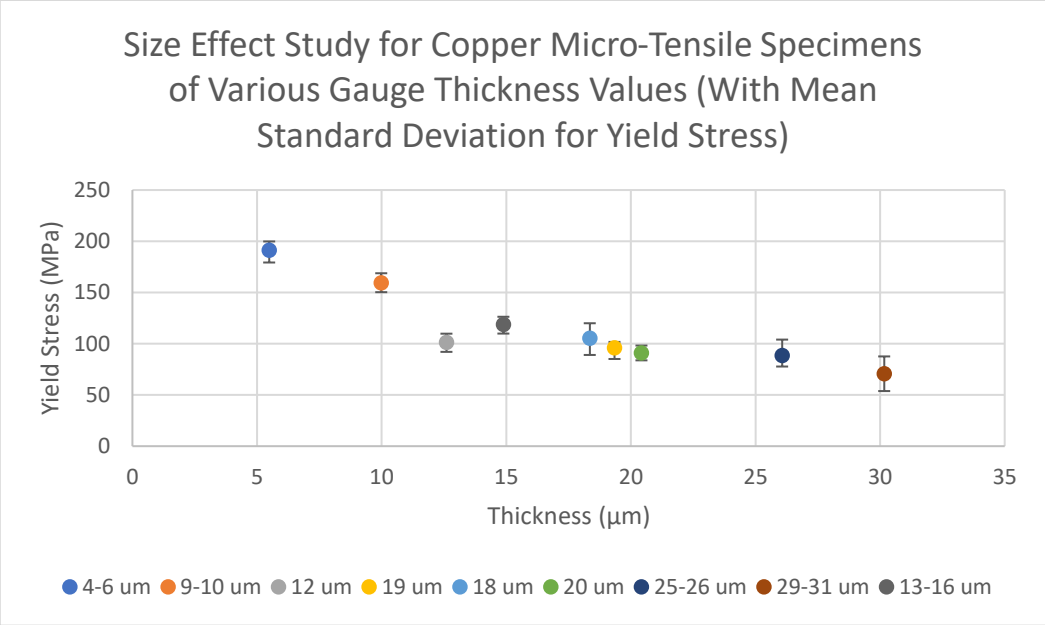

Figure 106: (100) copper micro-tensile specimens grouped by similar gauge thickness showing mean standard deviation for the average yield stress of each gauge thickness group.

6.7. Comparison of Mechanical Results Between PFIB and Fs-Laser-Machined Copper Micro-Tensile Specimens

The effect of the fs-laser and PFIB fabrication methods on the mechanical behaviour of the copper micro-tensile specimens is discussed in this section of the chapter. Samples were produced from two fabrication methods, with the first method consisting of only the PFIB to fabricate the specimens and the second method consisting of both the fs-laser and the PFIB to fabricate the tensile specimens. Both the machining routes produced specimens with different gauge cross-sectional thicknesses. The strained micro-tensile specimens were categorized by their machining routes and replotted in a yield stress-versus-gauge volume plot, as seen in Figure 107. From the plot, it is observed that tensile specimens fabricated from the two machining routes all follow similar trendlines of decreasing yield strength with increasing gauge thickness. Therefore, it can be concluded that the fs-laser can be a reliable fabrication route to machine the micro-tensile specimens. The results confirm that the new and innovative fabrication route of the fs-laser can save a significant amount of machining time to make the micro-tensile specimen geometry cut-outs. As shown in Table 9 under Chapter 5 of the summarized machining times for the two fabrication routes, the fs-laser would be 2-3 times faster to prepare the same amount of copper tensile specimens than if it were done with the only using the PFIB.

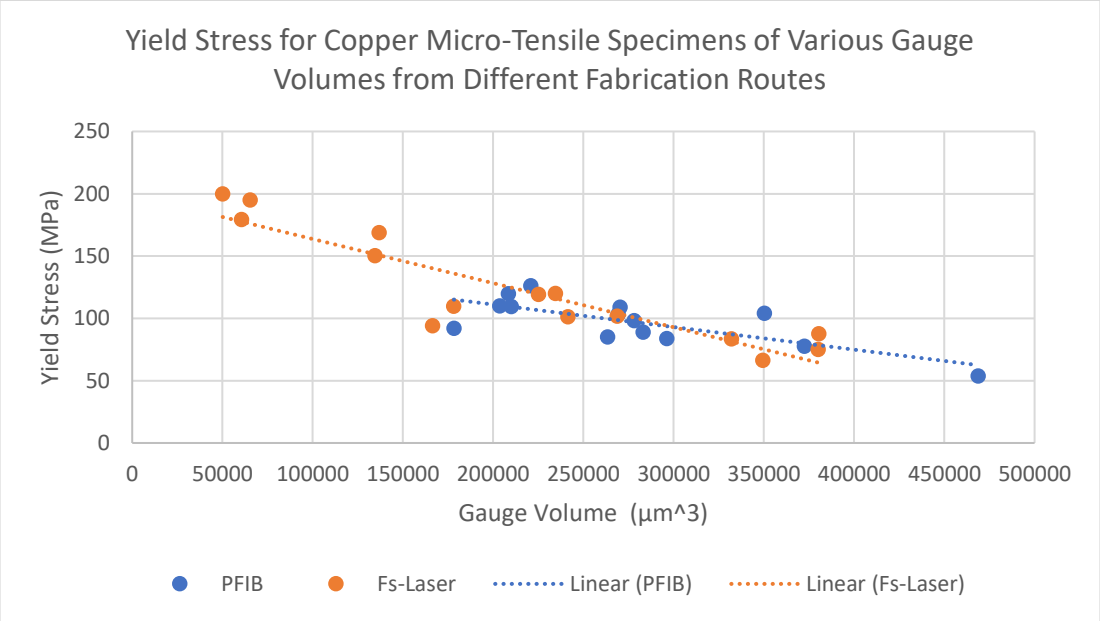

Figure 107: Effect of fabrication route taken on the yield stress of the copper micro-tensile specimens.

6.8. Effect of Gauge Misalignment on Size Effect Phenomenon

The effect of the misaligned tensile specimens on the size effect behaviour of copper was studied. The tensile specimens were categorized under two groups of specimens exhibiting either rotation (off-axis from the tensile pulling direction) and no rotation of the gauge section analyzed by the SEM images taken during periods of interval loading. The yield stress of each strained tensile specimen was replotted against their correspond gauge cross-sectional area, as seen in Figure 108. It can be observed from the grouping of the misaligned and aligned specimens that there is no significant offset from the size effect trend. Therefore, it was concluded that the misalignment of the specimens did not have a significant effect on the strength of the specimens. This can be due to the small rotation angle made by the misaligned tensile specimens with the largest misalignment angle of one the specimens being 2.6 degrees clockwise from the tensile axis. The bending stress maybe too small to cause a significant development of GNDs.

In addition, since the aspect ratio of gauge length to gauge width of the specimens are quite high (of approximately 5:1), the density of GNDs built up from the bending stresses at the ends of the gauge section is much lower than compared to that of a hypothetically low aspect ratio gauge section of 1:1, as seen in *Kiener et al, (2008)'s* work on dislocation mechanisms of miniature single crystal copper tensile specimens. The GNDs have room to glide across the gauge section in a high aspect ratio specimen. On the other hand, for a low aspect ratio specimen, the motion of dislocation is restricted by the specimen dimensions, causing GNDs to build up the surfaces, resulting to an increase in work hardening and flow stress of the specimen [5].

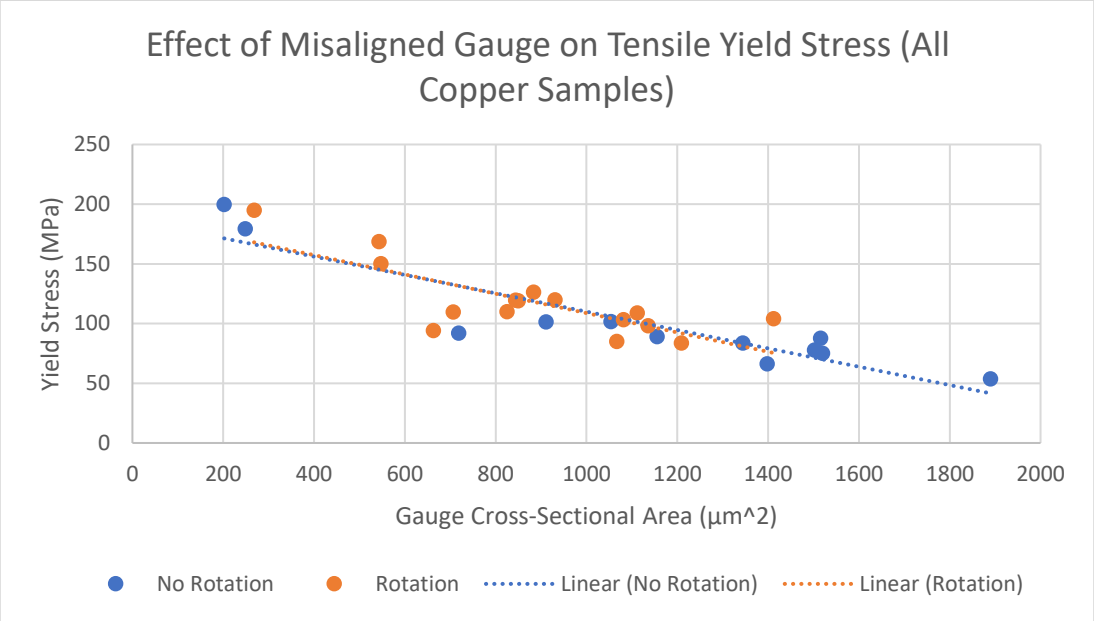

Figure 108: Effect of misalignment of the tensile gauge sections on the yield stress of the copper micro-tensile specimens.

When the tensile specimens were misaligned prior to straining in tension, a small bending moment can cause the tensile specimens to flex up or downwards during the initial start of the test. The flex causes the gauge section to compress at the initial stages of loading. The compression can be seen as negative strain calculated using Equation *19*. The negative strain was mainly seen in the elastic region of most of strained tensile specimens. When the specimens surpass the bending moment under increasing incremental load steps, positive strain is calculated for the gauge sections. Therefore, due to the large variation in data points of the elastic region from the negative strain accumulated from the initial bending moment, the Modulus of Elasticity could not be calculated accurately for the strained specimens. Figure 109 shows the negative strain region on the left-hand side of the stress-strain for PFIB-machined copper tensile specimen 3 from wedge 3.

To prevent the bending moment of the gauge section from occurring, it would be beneficial to reduce the clearance space between the pin and the pinhole by machining the diameter of the pinhole more closely to the diameter of the pin. This would prevent the pin from shifting out of alignment during testing. In addition, to reduce the sensitivity of the weight of the grip on the gauge section during loading of the pin in the pinhole and during testing, the grip should be thinned to a similar or identical thickness value as the gauge section.

Another possible cause of the negative strain can come from the initial bending of the gauge section prior to performing mechanical testing on the samples. Since single crystal copper is a very soft and ductile material, the thicker section of the grip can cause the thinner section of the gauge to bend after performing the thinning process in the PFIB. In addition, the transfer of the wedges in a non-vacuum environment can also increase the sensitivity of the specimens to bend as well. When the bent gauge sections are loaded in tension, the initial stage of the test of pulling the specimen in tension would cause a compressive force on the top surface of the gauge

(containing the fiducial marks). The compressive force would transition to a tensile force after the gauge section is straightened out from the tensile load.

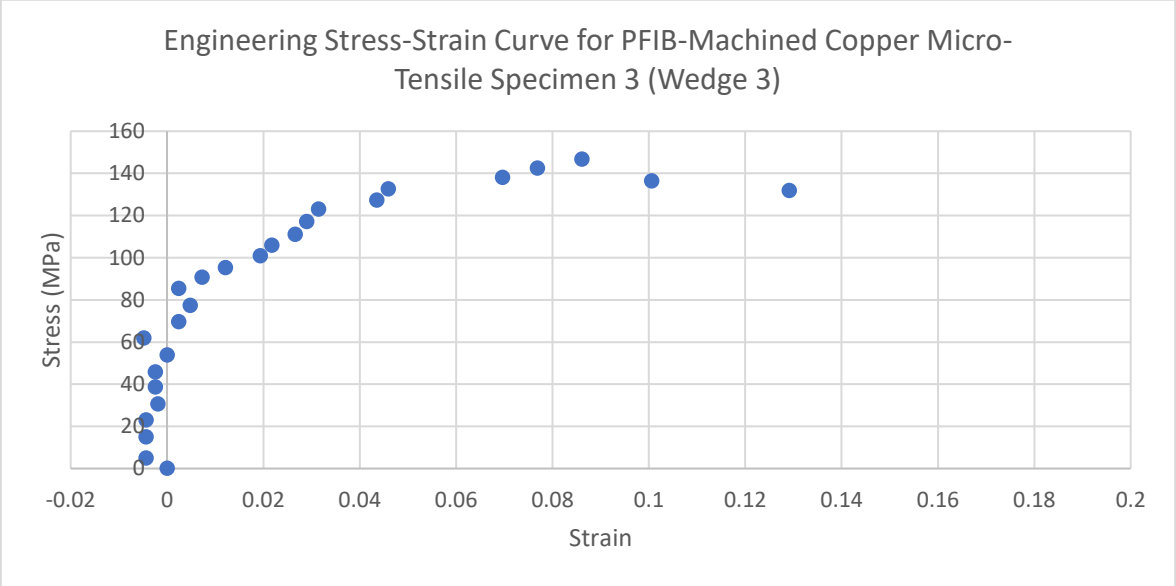

Figure 109: Stress-strain curve from the micro-tensile test of PFIB-machined copper tensile specimen 3 from wedge 3.

6.9. Measurement of Strain Using Gauge Edge

For the mechanical testing of two copper specimens, the edges of the gauge section were used to measure the strain the gauge sections, respectively. For the fs-laser machined tensile specimen 1 from wedge 4, the fiducial marks were deposited with a low resolution (due to unfocused ion beam during deposition). Therefore, the fiducial marks were too blurry to be used as reference markers to measure the strain in the ImageJ software. For the PFIB-machined tensile specimen 6 from wedge 2, the wedge was loaded on the specimen holder of the micro-tensile bench and into the PFIB chamber with the opposite side of the gauge section containing no fiducial marks. Therefore, the edges of the gauge were used as reference markers instead, as depicted by the red dots shown in Figure 110. As mentioned before, the issue with using the edges of the gauge section instead of fiducial marks for tracking strain is that the corners of the gauge exhibited curvature from the milling process of removing the rough gauge edges. The rounded corners made the tracking of the elongated gauge section less precise. Therefore, error in the total strain measured can be off by more than 5% from tracking the strain with fiducial marks. This difference was seen for the fs-laser machined-tensile specimen 4 from wedge 3, where an 8.08% total strain difference was exhibited between the two strain tracking methods.

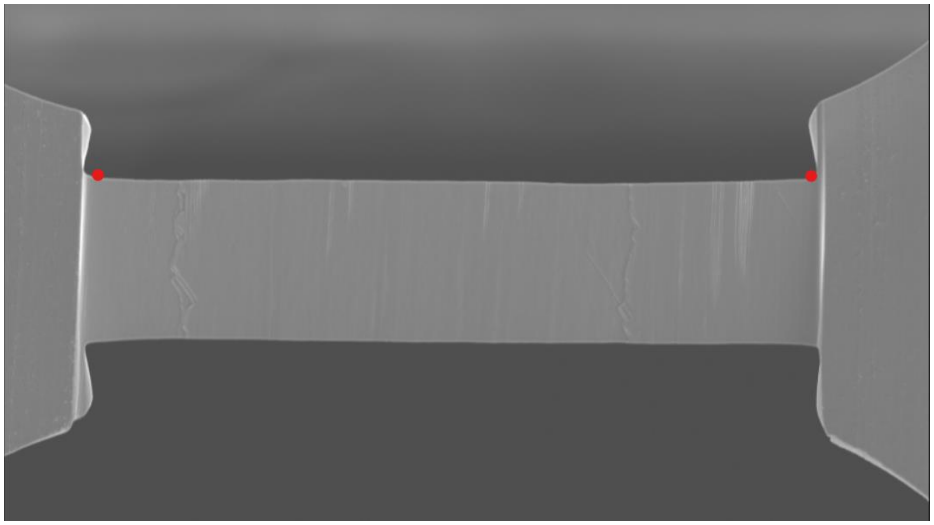

Figure 110: SEM image of PFIB-machined tensile specimen 6 from wedge 2 showing the tracking of elongation using the corners of the gauge section (indicated by the red dots).

6.10. Conclusions on Mechanical Testing and Size Effect Study on Copper Micro-Tensile Specimens

From the results of the mechanical testing of the single crystal copper micro-tensile specimens, it can be concluded the tensile specimen geometry, apparatus of the custom-built micro-tensile bench, and fabrication routes provided reliable mechanical results for the tensile specimens. From the SEM image acquisition, distinct slip bands can be observed from the deformation of the gauge section. In addition, the onset of plasticity can be identified from the stress-versus-load curve of each strained tensile specimen adopted from Robert Wheeler. A size-limiting behaviour was also observed for the specimen with the trend of increasing strength with decreasing gauge thickness. Some discretions in the calculated stress-strain curves are the negative strain values accumulated during the beginning of the tensile tests and instrumental errors consisting of harmonics and drift of the vibrating tungsten wire. Future improvements on the design of the tensile specimen geometry are to thin the grip section to a similar thickness as the gauge section to prevent bending moments on the gauge prior to mechanical testing. In addition, to prevent harmonics and drift from occurring during mechanical testing is to change the load wire regularly and wait for the micro-tensile bench to settle in the SEM chamber for a few hours prior to testing the specimens, respectively.

6.11. Future Work for Validating Size Effect in Micro-Tensile Specimens

To quantitively define the existence of the mechanical size effect that exists in the single crystal copper micro-tensile specimens, it would be a good idea to analyze the dislocation network that exists within the internal structure of the gauge section. A well-suited method for analyzing the dislocations network and dislocation density is through transmission electron microscopy (TEM) analysis. TEM produces both bright-field (BF) and dark-field (DF) imaging through the transmission of the electrons through a thinly prepared material specimen. BF imaging is formed through the collection of only the transmitted electrons through a well-defined aperture, while DF imaging only collects the scattered electrons from the sample through its own well-defined aperture. Both imaging modes of the TEM microscope provide different atomic (Z) contrast mechanisms. In BF imaging mode, lighter atoms show up brighter in images, while heavier atoms show up brighter in DF imaging mode, due to the tendency for heavier atoms to scattered easier than lighter atoms. The diffraction pattern produced from both respected imaging modes can provide imaging of microstructural features such as dislocations.

To prepare the strained copper micro-tensile specimen for TEM analysis, the gauge cross-section would have to be cut to a thickness of 100-200 μm and 3 mm in diameter to create a sample disk that would fit into the specimen holder of the TEM microscope. As seen by *Li et al., (2015)*'s work on the TEM analysis of the compressed copper BC micro-pillars, BF imaging of the surface of the specimen's cross-section along the longitudinal side length showed the pile up of dislocations along the GB [17]. The dislocation density was measured to be much higher near the GB compared to the rest of the surface area of the cross-section. If the dislocation network can be observed through TEM imaging of the strained copper micro-tensile specimens, it can help to validate the existence of the distinct dislocation mechanisms that come from the size-limiting effects of varying the gauge thickness on the mechanical strength of the specimens. The number of dislocations can also be determined as well through the BF and DF imaging of the surface of the gauge cross-section (either from cutting cross-section along the length or width of the gauge section). If the number of dislocations decreases with decreasing gauge thickness and increasing yield strength, it can be concluded that dislocation escape through the free surface and nucleation of dislocations occur to compensate for the limited dimensions of the specimens and dislocation movement.

XIV. Chapter 7: Future and Current Work on Turbine Steel Micro-Tensile Specimens

7.1. Introduction on Turbine Steel Micro-Tensile Specimens

One of the primary goals for developing the fast and reliable fabrication route of micro-tensile specimens using the combination of the fs-laser and the PFIB is to study the mechanical

behaviour of the local microstructure of 415 martensitic stainless steel. The composition of 415 is the wrought steel while CA6NM is the cast version of the turbine steel. The turbine steels are used to produce hydro-turbine components of Francis turbine at Hydro-Quebec, such as the turbine runner's head, crown, and blades. In addition, E309L austenitic stainless steel is the wedge material used to create connections between the welded bladed to the crown of the turbine runners and is the repair material for fixing existing cracks during maintenance periods of the turbines.

The base materials of the 415 and CA6NM steels have complex microstructures consisting of substructures of martensitic blocks and laths contained in the larger structures of prior austenite grains, as seen by the 2D EBSD scan of a 415-steel specimen surface in Figure 111. The base metals consist of both high strength and toughness properties while the weld material of E309L consist of moderate strength, ductility, and toughness properties. The two compositions of the ASTM standard and the composition developed and used by Hydro-Quebec of 415 martensitic stainless steel can be seen in Table 10.

The turbines at Hydro-Quebec get replaced by less than half the expected service life of 70 years. The early replacement is due to the failure of turbine components through macro-sized defects that grow overtime through cyclic stresses during turbine operations. The initiation of micro and nanoscale sized cracks are difficult to identify prior to the growth of the crack at larger length scales. In addition, the microstructure also plays a role in the initiation process of defects that begin through deformation mechanisms such as twinning, martensite formation, and high energy stacking faults. Extensive research has been conducted on the three turbine steels to better understand the role of local grain orientations, crystallographic texture, and grain morphology on the mechanical response of the steel under an applied external load. Research on the turbine steel through the development of crystal plasticity finite-element modelling (CPFEM) of the microstructure would help scientists better understand and predict the deformation behaviour of the steel at the intrinsic microstructure level.

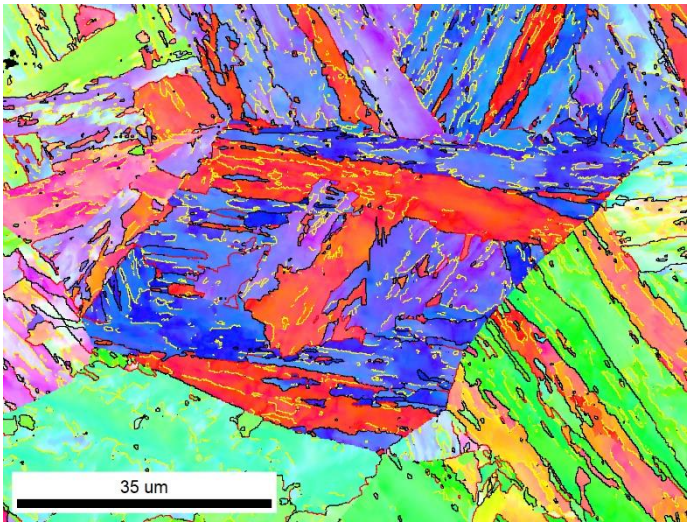

Figure 111: 2D EBSD scan of 415 martensitic stainless steel microstructure exhibiting martensite laths contained in prior austenite grains. Work by *Mehdi Mosayebi, McMaster University (2021).*

Table 10: Chemical Composition (%) for 415 Martensitic Stainless Steel

	Fe	C	Si	Mn	P	S	Cr	Mo	Ni
ASTM	Rest	<0.05	<0.6	0.5-1.0	<.03	<0.03	11.5	0.5-1.0	3.5-5.5
S41500	81.557	0.034	0.44	0.68	0.018	0.001	12.7	0.57	4.0

7.2. About Crystal Plasticity Finite-Element Modelling (CPFEM)

Digital twin models of the physical microstructure of the turbine steels are currently being developed by research scientists at IREQ using crystal plasticity finite element modelling (CPFEM). CPFEM uses concepts of traditional finite element meshing, external load simulations, and boundary conditions, with the addition of constitutive equations on stress-strain relationships in order to tell the model how the material would deform. But in order to verify whether theses models work, experimental data is needed to validate the mechanical response from the crystal plasticity models. Therefore, mechanical data is required to validate the CPFEM models, where the models behave under physical and kinetic constitutive stress and strain relationships. Therefore, micro-mechanical test specimens are a good way to target a finite number of grains to mechanically deform and obtain the yield strength of the local microstructure. This information can then be used to feed into the crystal plasticity models. Initially, a single or a few grains from the material's microstructure are represented by the CPFEM models as building blocks to the larger scale of a bulk model of the material's microstructure. Therefore, for the mechanical testing of miniature-scale specimens of the turbine steels, a minimum of 1-2 martensite grains are desired to be machined out of the local microstructure of the turbine steels. When only a few grains are isolated in a specimen, it allows for the observation of individual roles of single phase and interphase interface boundaries on the mechanical response of the specimen, which can differ from the bulk behaviour of the turbine steel.

7.3. Sample Preparation of 415 Steel Wedge

After the fs-laser was verified as a reliable fabrication route for machining the tensile specimen geometry cutouts using single crystal copper, micro-tensile specimens were fabricated out of the 415 martensitic stainless steel. The fs-laser was used to machine the tensile specimen geometry cutout for the 415 micro-tensile specimens. If the same task of the 415 cutouts were performed with the PFIB, it would take approximately 4-5 hours to mill out the exact tensile geometry and dimensions. A different micro-tensile specimen geometry for the 415 micro-tensile specimens was used instead of the geometry used to fabricated copper micro-tensile specimens. The new geometry consists of a larger grip and smaller gauge section of 50 µm x 50 µm, as seen in Figure 112. The smaller grip section allows for less grains to be contained in the reduced gauge section.

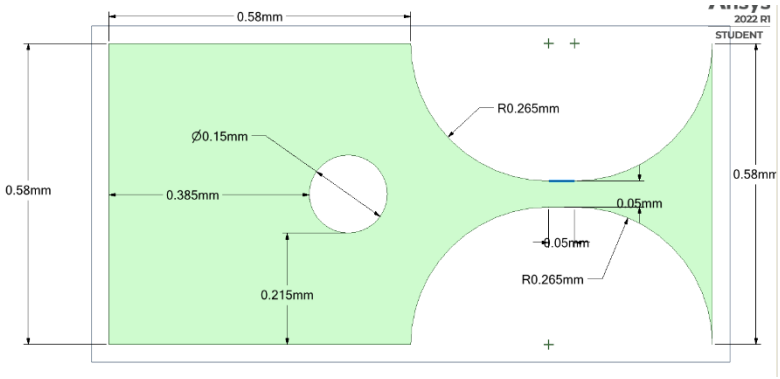

Figure 112: Micro-tensile specimen geometry with a 50 µm x 50 µm (length to width) gauge.

Prior to machining the 415 micro-tensile specimens, the base component wedge must be prepared. Preparation of the 415 wedge includes steps to reduce the initial thickness down to a target thickness of 50-100 µm and polished to an EBSD quality surface finish. Initially, the 415 wedges were cut from the bulk material through EDM machining at IREQ. The length and width of the EDM-machined wedges were of 15 mm x 15 mm (length to width). The initial thickness of the wedges from the EDM cuts ranged from 340 µm to 550 µm. A brief description on the preparation steps of the 415 wedges can be seen in Figure 113.

To reduce the thickness of the wedges to a reasonable thickness size for micro-tensile specimen fabrication, a series of grinding and polishing steps were performed on the metal surface. The 415-steel wedge was initially mounted in an epoxy stub with one surface of the wedge exposed on the exterior of the mount for performing grinding and polishing using the auto-polisher. Initially, a damage layer exists consisting of rust on both surfaces of the wedge from the thermal process of EDM. One of the damage layers was removed using the auto-polisher. SiC papers of different grit roughness and blue diamond suspension polishing clothes were used to refine the surface cracks. A final polishing using colloidal silica was used to etch the surface and expose the grains and grain boundaries for performing 2D EBSD of one of the wedge surfaces.

After one side of the surface is polished to EBSD quality, the epoxy mount was broken using hacksaw, while the EBSD quality surface was protected using Paraview tape from the epoxy debris. Once the mount was removed, the thickness of the wedge was measured to be approximately 200-250 µm. The remaining thickness of the wedge was removed using a TEM lapping tool. Melted crystal bond was used to attach the wedge onto a cylindrical metal holder with the heat damaged EDM surface exposed for grinding. The amount of target material was to be removed was controlled using a dilator on the lapping tool. Each increment on the dilator removes 20 µm of material. Small increments of the wedge's cross-sectional thickness were removed to control the rate of material removed. In addition, the thickness of the wedge was measured between each grinding step by removing the crystal bond (using acetone solution) for taking the thickness measurements and reapplying the crystal bond onto the wedge to secure it onto the metal holder. The grinding process using the lapping tool was continued until the thickness of the wedge has reached a uniform target thickness of approximately 100 µm over the entire wedge. Due to the manual grinding process with the lapping tool, the thickness of the

wedge was not perfectly uniform. Significantly large thickness variations across the wedge surface should be avoided by keeping the lapping took flat when performing the grinding. The final preparation process was to clean the debris of SiC paper and contaminants off the wedge surfaces by dipping the wedge in a bath of ethanol solution. Once the wedge was finally prepared, the specimen was cut to the appropriate dimensions to fit into the PFIB chamber for machining the micro-tensile specimens and to fit into specimen holder of the micro-tensile bench for mechanical testing.

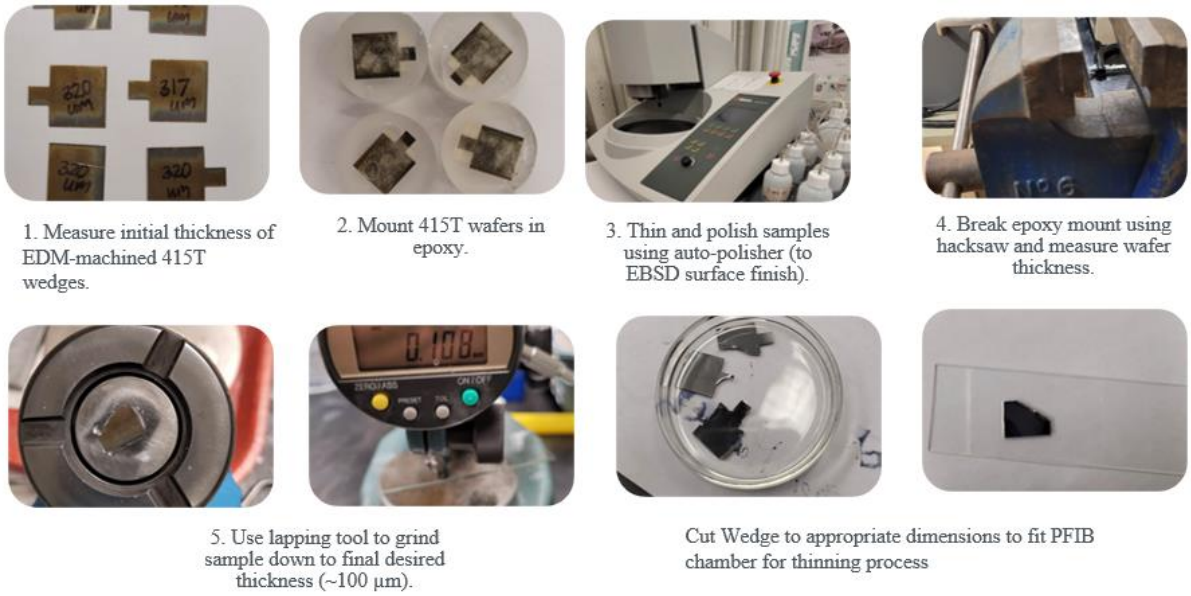

Figure 113: Sample preparation recipe for 415 steel wedges.

7.4. Targeting of 415 Steel Grains

Once the 415-steel wedge was prepared, the process of identifying grains of interest for tensile specimen machining was performed. The process of identifying the position of individualized grains and their crystallographic orientations was through the use of 2D EBSD scans of the surface microstructure. The EBSD analysis was performed using the Oxford Symmetry S2 camera on the Helios 5 PFIB. From the 100 µm magnification scale of the 2D EBSD maps, specific grains of interest were chosen. The size of the martensite laths and sub-blocks were of approximately 50 µm or smaller. The location of the grains of interest were referenced to a grid of X-shaped fiducial marks that were spaced out 500 µm apart from each other in the lateral direction. The fiducial marks were deposited using tungsten precursor gas provided by the multi-chem injector of the PFIB. A global fiducial mark was placed at the corner of the wedge to identify the positions of the grid fiducial marks in reference to the global fiducial mark. Once the grains of interest were identified, measurement boxes are used to measure the X and Y distances between the nearby grid fiducial mark and the grains of interest, as seen in Figure 114 for the third (out of four) specimen's site of interest detected. An SEM image was taken as a reference image to relocate the grain of interest when the 415 wedge was transferred

to the fs-laser chamber of the 350 Crossbeam for machining out the tensile specimen geometries with the grains of interest contained within the gauge. To indicate the specimen number for the grains of interest to be machined by the fs-laser, thin rectangular lines were milled (with an ion current of 10 nA) at approximately 500 µm above the region of interest, where the number of rectangular lines indicate the specimen number.

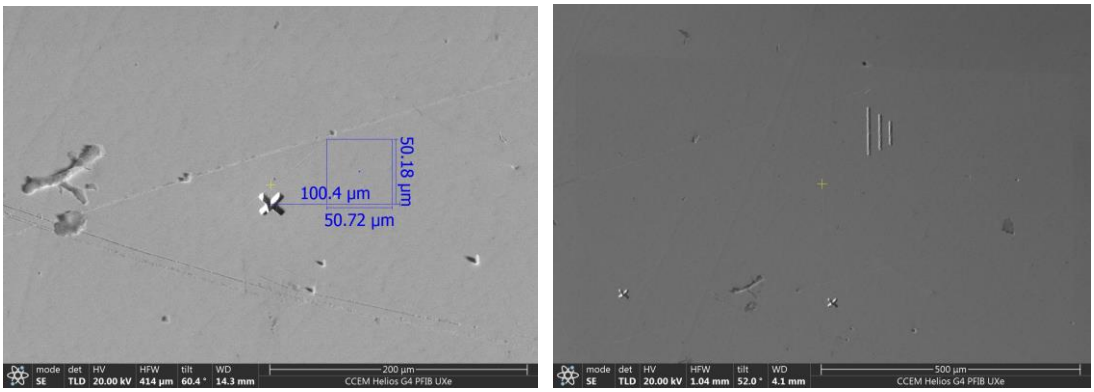

Figure 114: Locating grains of interest on the surface of 415 steel using measurement boxes at the vicinity of X-shaped fiducial marks in the SEM (left image). Ion-milled lines indicate the specimen number for the tensile specimen to be machined (right image).

The EBSD maps would pick up the fiducial marks as non-indexed patterns in the post-EBSD IPF orientation maps produced by the Aztec EBSD analysis software, as seen in Figure 115. Both the IPF maps and the ISE image of the fiducial marks with the rectangular measurement boxes at the vicinity of the grains of interest were used to relocate the grains during laser-machining of the tensile specimen geometries in the Crossbeam 350.

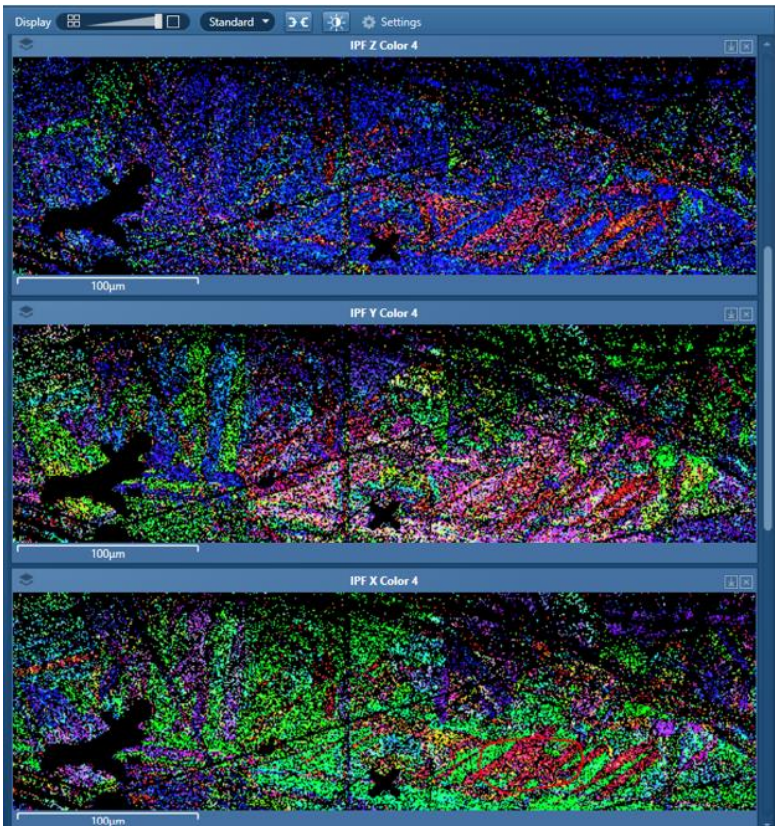

Figure 115: IPF maps from a 2D EBSD scan of the 415-steel surface. Potential grains of interest located at the vicinity of a fiducial mark (circles in red). EBSD image corresponds to same ROI as for the SEM images shown in Figure 114.

In the 350 Crossbeam CAD software, the tensile specimen geometry was drawn with the exact dimensions as the ANSYS SpaceClaim sketch, as seen in Figure 116. The CAD drawing consists of a single tensile specimen geometry as opposed to a line-up of several tensile specimens, which was done for the fs-laser-machined copper tensile specimens. The individual tensile specimens are placed at the location of each grain of interest with the help of the fiducial marks and EBSD maps to navigate towards the region of interest. Initially, the specimen number is located with the help of the rectangular deposition boxes. Afterwards, the fiducial mark at the vicinity of the region of interest was located. SEM images produced by the PFIB showing the X- and Y-distances between the fiducial and the region of interest was used to determine the location of the grains of interest. Afterwards, the gauge section of the tensile specimen pattern was placed on top of the grain of interest. This process of relocating the grains in the SEM of the 350 Cross beam was repeated for four specimens for their corresponding grains of interest in the 415-steel wedge.

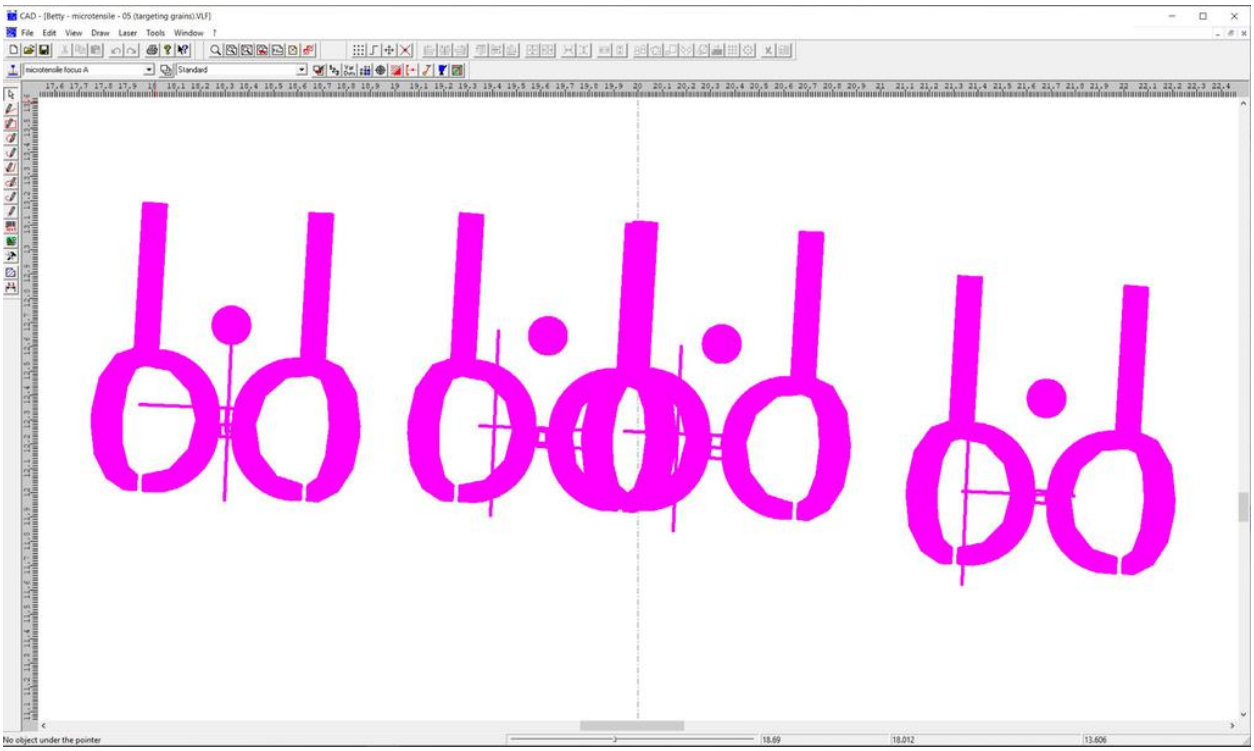

Figure 116: Tensile specimen geometry patterns layout for machining grain-targeted fs-laser-machined 415 micro-tensile specimens. Image by *Travis Casagrande, CCEM (2023).*

Once the tensile specimen patterns were placed at the locations of the grains of interest, the 415 wedge was transferred into the fs-laser chamber for machining using the interlock system between the dual beam chamber and the laser chamber. The four tensile specimens were cut out in less than 6 minutes. Due to the larger thickness of the 415-steel wedge compared to the copper wedge, a taper of approximately 6 degrees was exhibited on the edges of the tensile specimen cutouts, as shown by the SEM image in Figure 117.

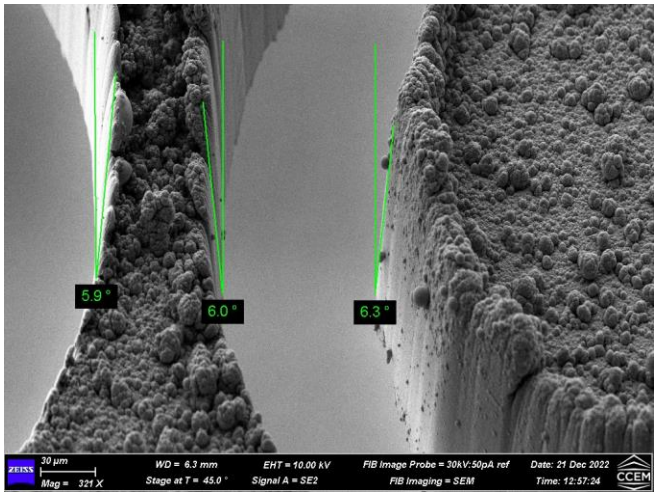

Figure 117: Tapering exhibited at the gauge edges of a fs-laser-machined 415 micro-tensile specimen. Image by *Travis Casagrande, CCEM (2023).*

One major machining error that occurred during the machining of the tensile specimens was the shift of the 415-steel wedge on the stub holder attached to the stage of the fs-laser. The shift occurred during the initial laser-machining process. The wedge was attached on the surface of the stub using carbon tape with the edge of wedge hanging free for the tensile specimens to be machined. The slippage of the wedge on the carbon tape caused the wedge to move out of position in the X-direction. Therefore, the grains of interest were out of the place on the gauge section after machining. In addition, the pinhole was misaligned to the center of the grip due to the shift of the wedge, as seen by the SEM images in Figure 118. Therefore, the specimens could not be used be further processed or used for mechanical testing.

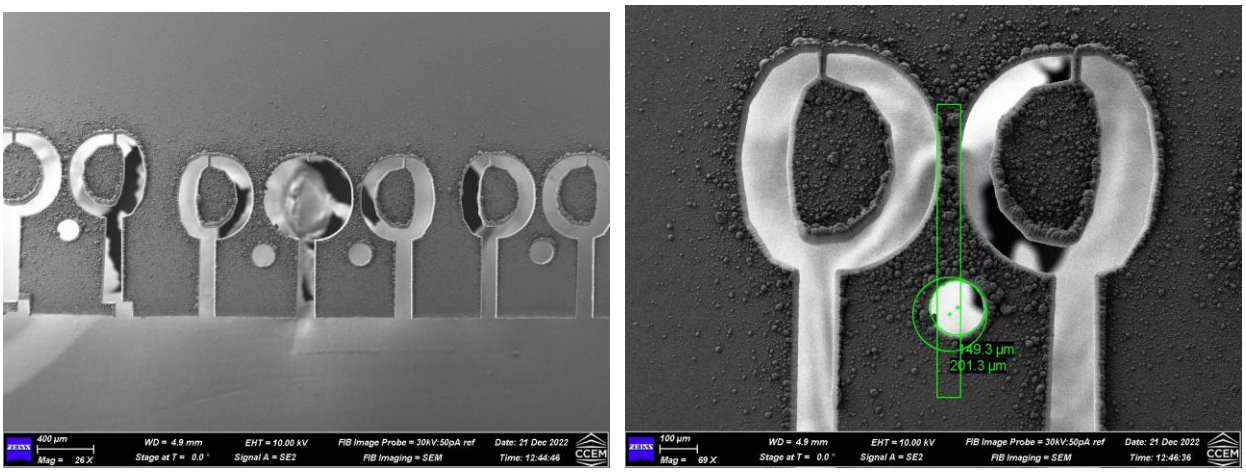

Figure 118: SEM images of fs-laser-machined (grain-targeted) 415 tensile specimen geometries (left image). Shift of the pinhole in the X-direction is exhibited for all the 415 specimens during laser-machining process (right image). *Images by Travis Casagrande, CCEM (2023).*

Potentially, the next steps towards fabrication of the grain-targeted specimens after the tensile specimen cut-outs with the fs-laser was to perform a thorough sonication cleaning of the steel wedge using ethanol to remove the laser debris on the top surface of the laser-machined tensile specimens (with the gauge section being the most important section to be cleaned from the laser debris). Afterwards, the gauge sections of the tensile specimens would be thinned using the same thinning method performed for thinning the copper-tensile specimens. The thickness of the gauge would be kept to a constant value of 10 µm for the gauges of all the tensile specimens. To perform the thinning process, the specimens would be transferred into the PFIB chamber and the same sample configuration as the copper specimens to produce the tilted gauge section after the thinning process. Afterwards, the wedge would be taken out of the chamber and remounted on the wafer holder and stub to perform low ion milling to remove the rough edges along the gauge length originating from laser curtaining. Once the edges are cleaned, two X-shaped tungsten fiducial marks would be deposited onto the edges of the gauge surface (at the same sample configuration in the PFIB used for cleaning the edges). The fiducial marks would be used to track the elongation during image acquisition of the micro-tensile test and for the calculation of the accumulated strain of the specimen during post-image analysis of the SEM images.

7.5. PFIB-Machined 415 Micro-Tensile Specimens

Prior to the development of the grain-targeted single crystal and bicrystal 415 micro-tensile specimens, non-targeted 415 micro-tensile specimens were produced using the PFIB. Initially, the tensile samples were cut out of a prepared 415 steel wedge an approximate thickness of 100 µm using the sample preparation procedure discussed previously in this chapter.

Two different tensile specimen geometries were used to determine the existence of the Hall Petch effect where the number of grains contained in the gauge section plays a role on the strength and deformation behaviour of the respected tensile specimen. Therefore, the geometries consist of three tensile specimens with a 50 µm x 50 µm (length to width) gauge section using the tensile specimen geometry shown in Figure 112, and three tensile specimens with a 180 µm x100 µm (length to width) gauge section using the copper tensile specimen geometry shown in Figure 32. Initially, the tensile specimen cutouts were performed using high-ion current milling parameters with the Helios 5 PFIB. The tensile specimen patterns were produced using the arrangement of milling patterns provided by the FEI user interface. The tensile specimen pattern was milled in parallel configuration with each tensile specimen taking about 3-4 hours to cut out at a 2.5 µA ion current. Therefore, the fs-laser would have decreased the machining time during the geometry cutout process significantly. The specimens were line-up towards edge of steel wedge. Although the grips were not exposed freely at the edge of the wedge, sufficient clearance between the grip and the wedge materials was produced to take into account of the elongation of the specimen during mechanical testing.

After the tensile specimen geometry cutouts were produced, the specimens were thinned using the method adopted from *Robert Wheeler*. Initially, the specimens were taken out of the chamber and remounted with the wafer holder only. The cross-section of the wedge faced normal to the ion beam at the 52-degrees milling configuration. A small tilt of 5 degrees offset was used to expose the surfaces of the gauge of each tensile specimen. Cleaning cross-section milling boxes were used to thin the gauge section. Table 11 lists the milling times and final gauge thickness values of each sample. During the process of fabricating the 415 micro-tensile specimens, the idea of removing the roughness from the gauge edges and the deposition of the fiducial marks for tracking the elongation of the gauge was not established yet. Therefore, the thinning process was the final step for fabricating the first batch of the PFIB-machined 415 micro-tensile specimens. Figure 119 shows the final fabricated PFIB-machined (non-grain targeted) 415 micro-tensile specimens.

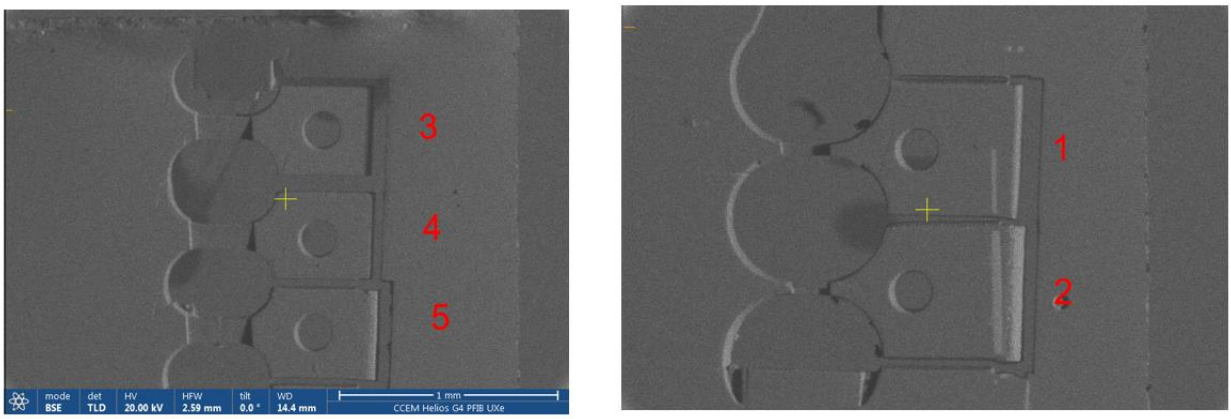

Figure 119: Final state of the fabricated (non-grain targeted) 415 micro-tensile specimens.

Table 11: Final Gauge Thickness and Milling Times for 415 Micro-Tensile Specimens

Sample	Target Gauge Y and X Dimensions (μm^2)	Milling Time for Thinning (Mins)	Final Gauge Thickness (µm)
1	50x50	25	14.56
2	50x50	25	28.98
3	180x100	17	18.50
4	180x100	8	20.81
5	180x100	60	10.79

7.6. EBSD Analysis Set-Up and Configurations

Prior to the mechanical testing of the 415 micro-tensile specimens, 2D EBSD analysis was performed on the surface of the thinned gauge sections. Figure 120 shows two 2D EBSD scans of the gauge surface of two of the fabricated specimens with different gauge geometries using Aztec EBSD analysis software. Initially, the specimen was taken out of the chamber and remounted with both the stub and wafer holder. The surface of the wedges faced normal to the ion beam at the 52-degrees milling configuration. Once alignments and the eucentric height was set at a working distance of 4 mm, the stage is over-tilted to the highest tilt of 61 degrees of the PFIB stage and with a working distance set to 12-15 mm from the SEM column. The configuration allowed the EBSD camera to detect the specimen wedge when the EBSD detector was inserted into the chamber. In addition, tilting the sample to the optimal tilt angle closest to 72 degrees allowed the optimal output of BSEs from the subsurface of the specimen. To perform the EBSD analysis, the SEM voltage and current was set to 30 keV and 26 nA, respectively. The high SE current allows for a high count of BSEs to be collected by the EBSD detector.

Prior to inserting the EBSD detector into the PFIB chamber, the tensile specimens were located in the field-of-view in the SEM window. It is important to note that the EBSD analysis was performed one specimen at a time. Therefore, five EBSD maps after post thinning process

was produced to see the grain size, number of grains, and crystal orientation of the grains contained at the gauge surfaces. The gauge section of each individual tensile specimen was focused to a magnification of 100 µm for performing the EBSD scans of the surface. The EBSD scans were performed using the fore-scatter electron (FSE) detectors of the EBSD detector and SE imaging. Afterwards, the phases of BCC and FCC iron were added to the indexing library of phases to identify the phases picked up by the EBSD scans and to produce a phase map of the gauge surfaces. Once the surface was scanned, the resolution of the Kikuchi patterns was optimized by selecting the binding resolution of the pixels. Binding is the process of combining neighboring pixels (e.g., 2x2, 3x3, 4x4, etc.) together into a single pixel by averaging out the pixel resolution. Averaging of the pixels reduces the background noise of the Kikuchi patterns to produce higher resolution Kikuchi patterns. In addition, the mean angular deviation (MAD) value (which is the misfit between the measured and calculated angles) should be less than 0.7 for detected Kikuchi patterns on the surface. The Kikuchi patterns detected by the EBSD software were referenced to a library of indexed patterns for the certain phases contained in the material. Therefore, the quality of the EBSD surface was important to allow for distinguishable patterns to be detected by the Aztec EBSD software.

The map of the scanned surface was cropped to fit the entire gauge surface. In addition, a step size was specified in accordance with appropriate processing time and grain size of the microstructure. As a rule of thumb, a step size of 1/5 the average grain size of the material should for performing EBSD analysis. During the EBSD pattern acquisition, the post-EBSD maps of the scan of the specimen's gauge section are developed, including band contrast, inverse pole figure (IPF) maps, and phase maps. The IPF maps were the most important maps to determine the crystallographic orientation of the grains. In addition, it is also beneficial to take the 2D EBSD after the mechanical testing of the tensile specimens to misorientation of the strained grains and the possible formation of twins and martensite in the material microstructure. This is part of the future work on the post-mechanical testing of future fabricated 415 micro-tensile specimens.

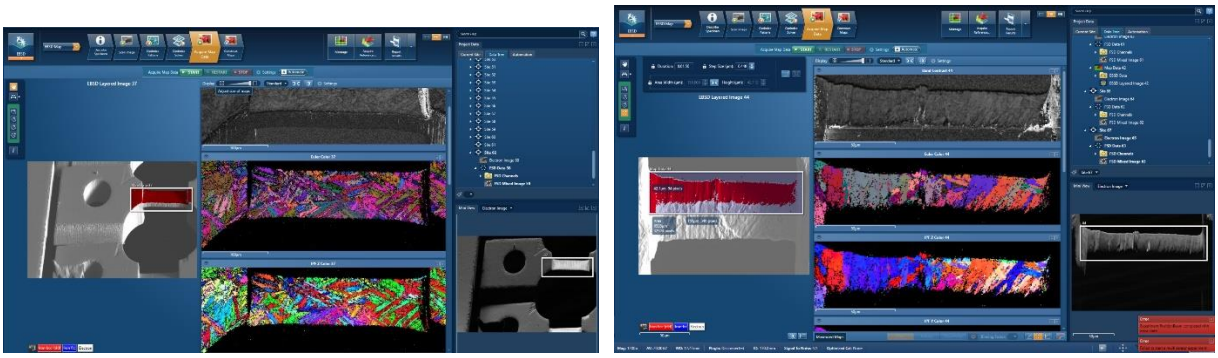

Figure 120: EBSD scan of 415 tensile specimen gauge surface (prior to mechanical testing) performed using Aztec EBSD analysis software.

7.7. Mechanical testing of 415 Micro-Tensile Specimens

The mechanical testing of the 415-micro-tensile specimens was performed using the custom-built micro-tensile bench. Out of the 5 fabricated PFIB-machined 415 tensile specimens, 4 of the

specimens were mechanically strained, due to the bending of specimen 4's gauge section from handling of the specimens prior to mechanical testing. The mechanical testing for the 415 tensile specimens followed the same procedure as that of the mechanical testing of the copper tensile specimens discussed in Chapter 6. The specimens were loaded in the micro-tensile bench and into the Hitachi S-3700 N SEM microscope. Alignments were performed to ensure the gauge section was flat and aligned parallel to the tensile loading axis. The pinhole of the grip section was loaded onto the tungsten pin with a small tension of 5 mN or less applied on the specimen prior to starting the test. For all 4 tensile specimens, a strain rate of $5x10^{-4}s^{-1}$ was used to strain the specimens. Load intervals of 5 mN and 10 mN were used for performing image acquisition in the SEM. Therefore, images of the gauge section were taken to track the elongated specimen during periods of constant loading. Once the SEM image was taken, the test was resumed by increasing the load at the specified strain rate and the process of taking an image was repeated at every 5 mN or 10 mN (respectively for each specimen) up to the fracture point.

The yield stress was identified from the converted load-versus-time to stress-versus-time staircase curve. The dip in the staircase curve indicates the onset of plasticity, which can be seen for the stress-versus strain curve of specimen 1 in Figure 121. The yield point of the 415 specimens were identified very close UTS point in the stress-versus-time curve for each tensile specimen. This was an indication that the martensite steel is highly brittle material compared to the ductile material of copper. Copper had a more gradual transition from elastic-to-plastic behaviour where energy from the plastic deformation is absorbed by the material prior to necking of the specimen. On the contrary, the 415 steel specimens absorbed very little energy and no necking was present prior to the fracture of the specimen from the micro-tensile test. From the stress-versus-time curve for specimen 1, the yield stress was identified to be approximately 994.5 MPa. In comparison to engineering stress-strain obtained from the tension test performed on a 415 micro-tensile specimen by *Robert Wheeler* (true stress-strain data used to simulate the 415 tensile Fe-models in tension), the yield stress was measured to be 504 MPa. The result is almost half the yield strength difference for the same material between the two specimens in the micro-scale size. However, the mechanical tests of the 415 tensile specimens were affected by the drift of the micro-tensile machine. The tests were run during significant drift, due to the immediate testing of the specimens when the tensile bench was placed in the SEM chamber. The drift caused the load to increase at a relatively small rate. Due to the drift, the point at which specimen exhibited the onset of yielding from the dip of the staircase curve is affected by the drift. Therefore, the yield stress depicted from the curve maybe higher than the true yield stress if the specimen were tested without the presence of drift in the micro-tensile bench.

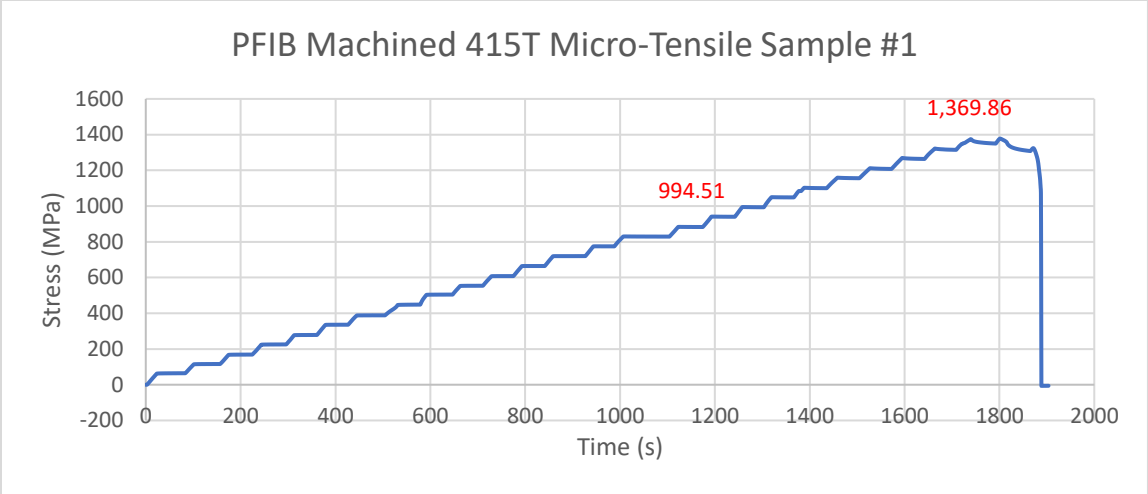

Figure 121: Stepwise stress-versus-time curve for PFIB-machined (non-grain targeted) 415 micro-tensile specimen 1. The onset of plasticity (yield stress) is indicated by initial dip in stress of the staircase curve. A yield stress of 994.51 MPa and an ultimate tensile strength of 1369.86 MPa was measured for the tensile specimen.

In addition, the 415 micro-tensile specimen that was fabricated and tested by *Robert Wheeler* only contained 1 to 2 martensite grains at the gauge section, while 415 micro-tensile specimen 1 contained a large number of grains, as depicted by the EBSD scan in Figure 122. Therefore, due to the large number grains and grain size relative to the dimensions and thickness of the specimen, the Hall Petch effect can be seen where the strength of the specimen increases with decreasing grain size. Although, this theory cannot be confirmed with the mechanical results, because of the drift effect. More mechanical tests of the 415 micro-tensile specimens with reproducible results is needed to validate the Hall Petch theory in 415 (non-grain targeted) micro-tensile specimens. In addition, the strength of bicrystal tensile specimens (depicted by the specimen fabricated by *Robert Wheeler*) can be affected by multiple roles of the GB such as the angle and volume fraction of the GB. For example, a high-angle GB is more efficient in impeding the motion of dislocations compared to a low-angle GB. Also, as seen from the bicrystal compression experiments on Cu by *Zhang et al., (2015*), the specimen dimensions at the sub-micron-level caused the buildup of dislocations at the vicinity of the GB that impeded dislocation motion and increased the flow stress in the bicrystal specimens [17].

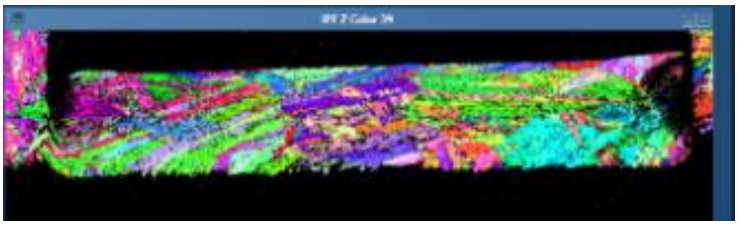

Figure 122: IPF map of PFIB-machined (non-grain-targeted) 415 micro-tensile specimen 5 exhibiting substructures of martensitic packets, blocks, and laths.

Table 12 lists the yield stress (onset of plasticity) identified from the corresponding stress-versus-time curves, as well as their gauge volumes for all four strained 415 tensile specimens.

The yield stress for specimen 3 could not be determined from the staircase curve due to the occurrence of a large harmonic that occurred during mechanical testing prior to the transition from elastic to plastic deformation of the specimen. Therefore, the yield point in the stress versus time curve (as well as the measurement of the additional caused by the harmonic and stress applied manually to overcome the harmonics) was difficult to determine. In the elastic region, the first harmonic occurred where the stress drastically increased from 700 MPa to 1350 MPa.

Table 12: Measured Gauge Volume and Yield Stress for Strained (Non-Grain Targeted) 415 Micro-Tensile Specimens.

Sample	Gauge Volume (μm^3)	Yield Stress (MPa)
1	41860	994.5
2	184875	614
5	335030	766

Prior to reaching the fracture point, sharp slip bands were observed through the SEM images taken of the 415 tensile specimen gauge sections, as seen in Figure 123, Figure 124, and Figure 125 for specimens 1, 2, and 5, respectively. The slip bands ran at arbitrary locations across the gauge length at angles of approximately 40-47 degrees normal to the gauge edge. Severe curtaining was observed at the freshly milled surface from the thinning process of the gauge section. The rippling pattern of ion milling-induced curtaining on the gauge surface can influence the mechanical behaviour of the specimens, such as adding addition stress concentrators at the ripples. Therefore, it would be viable to minimize the curtaining effect on the gauge surface as much as possible. Curtaining can be minimized by reducing the ion current used during milling and reducing the initial thickness of the gauge section. Another possible artifact that could have affected the mechanical behaviour of the 415 tensile specimens was the non-uniform rough edges of the gauge sections. Without the removal of the rough edges through the process of low-ion milling, localized stress concentrators exist at the ripples of the edges (produced from ion-induced curtaining during the geometry cutout process).

The location of the slip bands on the gauge surface provided insight on the deformation mechanisms occurring at the microstructure. Unfortunately, SEM imaging of the gauge section (during mechanical testing of the specimens) was performed on the opposite side of the gauge surface where the initial EBSD analysis took place. Therefore, it was difficult to determine where the slip bands originated from by looking at the EBSD scans taken prior to testing. Possible origins to the slip bands could be along martensite block boundaries, GBs between martensite laths, or across the grain themselves. A better depiction on the development of the slip bands would be through the tracking the strained grains and their orientations with in-situ EBSD analysis of the gauge section. During image acquisition, both an SEM image and a 2D EBSD scan of the gauge surface would be taken. Although, this could not be done for the 415 specimens batched tested, but it would providing valuable insight on the misorientation and morphology of the grains for the testing of future 415 micro-tensile specimens.

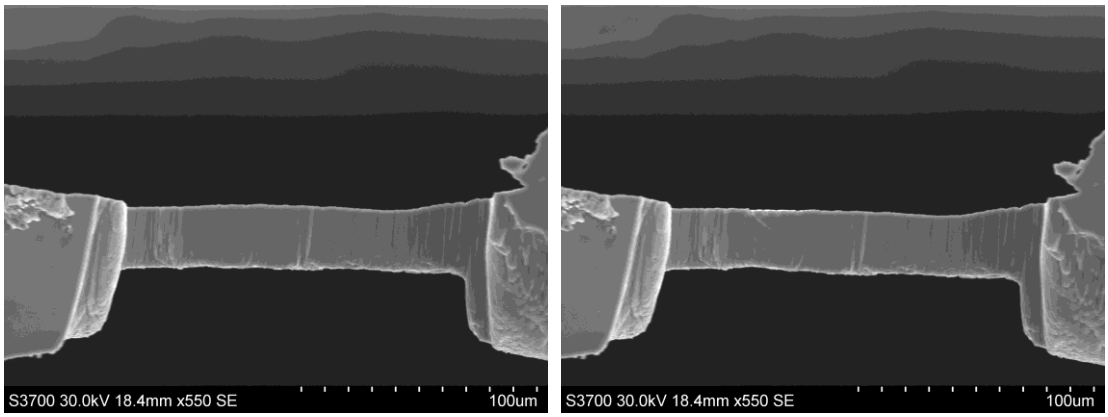

Figure 123: SEM images taken before and after micro-tension test of PFIB-machined (non-grain-targeted) 415 micro-tensile specimen 1.

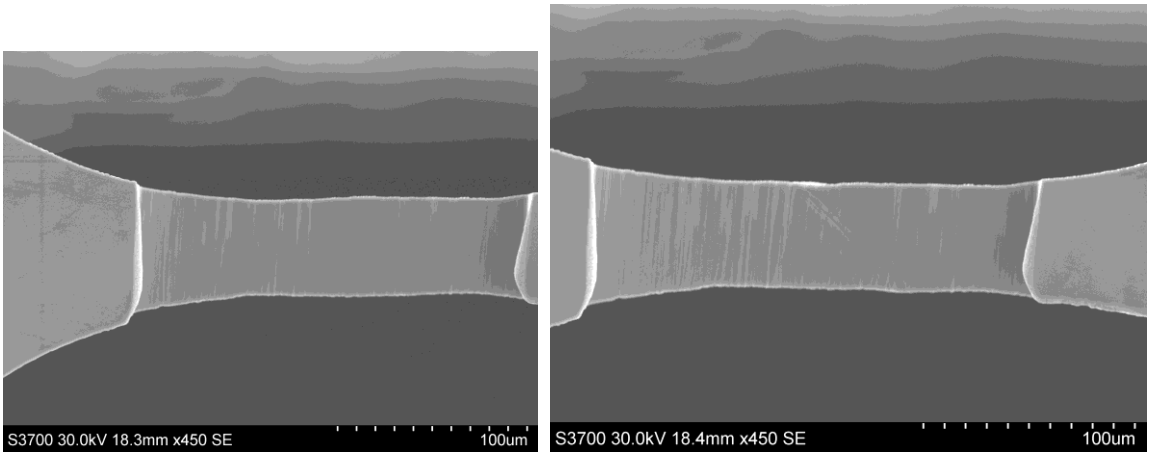

Figure 124: SEM images taken before and after micro-tension test of PFIB-machined (non-grain-targeted) 415 micro-tensile specimen 2.

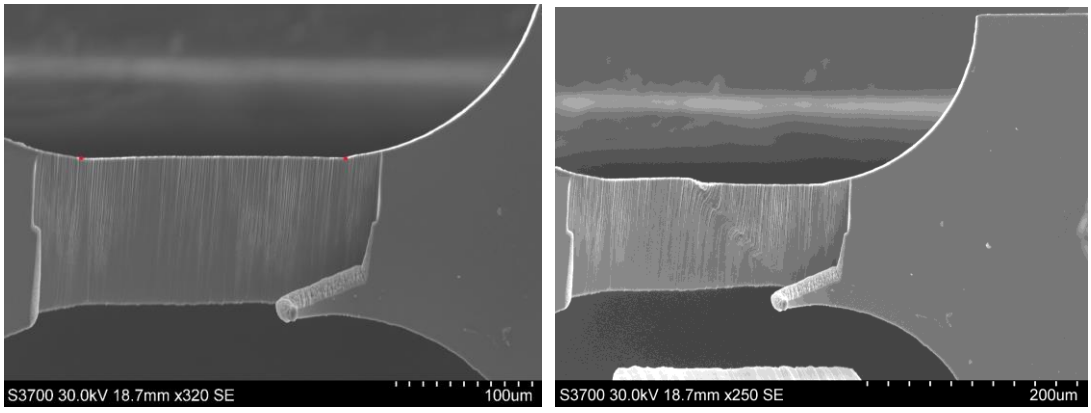

Figure 125: SEM images taken before and after micro-tension test of PFIB-machined (non-grain-targeted) 415 micro-tensile specimen 5.

The typical structure of a prior austenite grain is depicted in Figure 126, where the composition of one PAG consists of packets of martensitic laths, blocks, and sub-blocks of martensitic laths. Typically, there are 24 variants of martensitic laths contained in each PAG. Although, since the blocks run parallel to each other in each packet block, the number of variants can be reduced to 6. In addition, the sub-blocks of S and K variants have a misorientation angle of approximately 10 degrees from one another [53]. Therefore, it is controversial to understand which boundaries provide the most resistance to dislocation motion. Micro-tension experiments can provide the capability of determining localized strain of a partial, single, or a few PAGs contained at the gauge section. From the EBSD scan of the gauge surface of 415 tensile specimen 5 prior to mechanical testing in Figure 122, several packets containing parallel martensitic blocks and laths of various orientations were observed.

In a micro-tension test performed on 304 austenitic stainless carbon steels consisting of martensitic laths and PAGs by *Mine et al., (2013),* it was determined that the orientation of block boundaries plays a significant role in impeding the motion of dislocations. This finding was confirmed through the measurement of the critically resolved shear stress of martensitic laths, where the value was greater in the in-plane slip system compared to the out-of-plane slip system of the laths. Therefore, it was confirmed from Mine's experiment that the yield stress of martensitic laths was orientation dependent on the block packets. In addition, it was observed through EBSD analysis, that the impediment of dislocation glide by the packet boundaries during straining caused the rotation of the blocks and subblocks of martensitic laths [54].

For future work on the 415 micro-tensile specimens, it is desirable to produce a comparable study on the strength of the steel microstructure. Two different sizes of micro-tensile specimens would be produced, where the first batch of specimens would be of a larger scale to include several packets of block boundaries, and the second batch would be of smaller scale to contain only 1-2 martensitic laths at the gauge section. The first fabrication of the larger scale tensile specimens would be used to study the strength effects of neighboring substructures of PAGs. The mechanical testing and post-EBSD analysis of the specimens will help to determine which substructures provide the most resistance to dislocation glide and determine how the response of each substructure under tension would affect the morphology and misorientation of the other substructures. The second fabrication of the smaller scale tensile specimen would be used to determine the mechanical strength difference of martensite interface-interphase specimens through the distinct crystal orientation of two martensitic laths contained at the gauge section. The slip systems present at the gauge section would be analyzed through the calculation of the critically resolved shear stress and Schmid Factor of each interface-interphase specimen by taking SEM image on both sides of the gauge surfaces and the gauge cross-section surfaces.

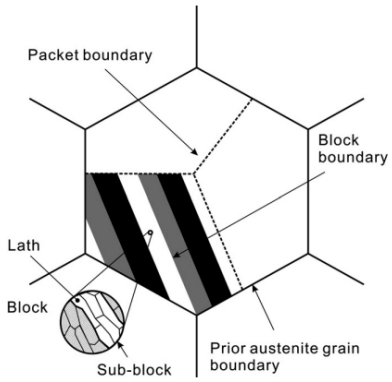

Figure 126: Schematic showing the structure of a prior austenite grain [53].

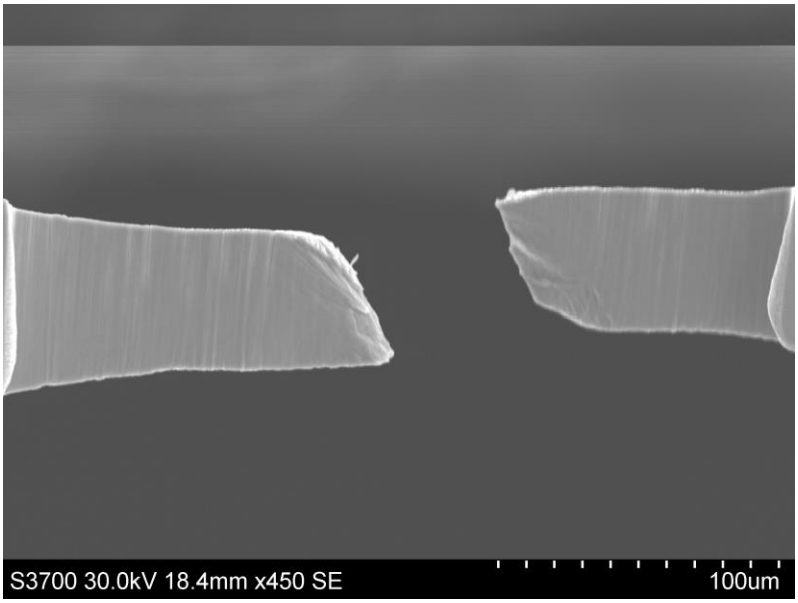

Figure 127: SEM image taken of the fracture point of PFIB-machined (non-grain-targeted) 415 micro-tensile specimen 2.

7.8. Post-Strain Analysis of PFIB-Machined 415 Micro-Tensile Specimens

The strain was calculated for each strained 415 tensile specimen using the SEM images taken during constant interval loading. The same procedure for calculating strain performed in Chapter 6 for the copper specimens was adopted for the 415 specimens. Although, the 415 specimens did not have fiducial marks deposited on the edges of the gauge surface for tracking the elongation of the specimen. Instead, the strain was tracked using the edges of the gauge section. The X and Y coordinates of two points were taken from the ends of the reduced section to determine the distance between the two points. The initial gauge length and accumulated strain were calculated using Equation 18 and Equation *19*. Figure 128 shows the constructed

stress-strain curve for 415 tensile specimen 5, where the calculated strain values from each SEM image taken was plotted against their corresponding stress values. The stress values for the corresponding strain were much higher in comparison with the stress-strain data from the micro-tension test performed by *Robert Wheeler.* As mentioned previously, this could be caused by the effect of drift from the micro-tensile bench. Another discretion from the stress-strain curves was the negative strain associated with the bending of the gauge section, due to the large mass of the grip section weighing down the specimen. The thickness of the grip was approximately 100 µm while the thickness of the gauge for specimen 5 was 10.79 µm. Negative strain was exhibited at the elastic region of the curves. The negative to positive strain transition occurred when the specimen was straightened out during the micro-tension test. Negative strain was measured for all three 415 specimens. Therefore, the grip should be thinned out to the approximate thickness of the gauge section to prevent the gauge section from bending. A large scattering of data points was seen near the elastic region of the curve. This conveys the poor accuracy of the tracking the strain with the edges of the gauge. Therefore, deposition of fiducial marks on the gauge section is necessary to calculate the strain of the specimen with higher accuracy.

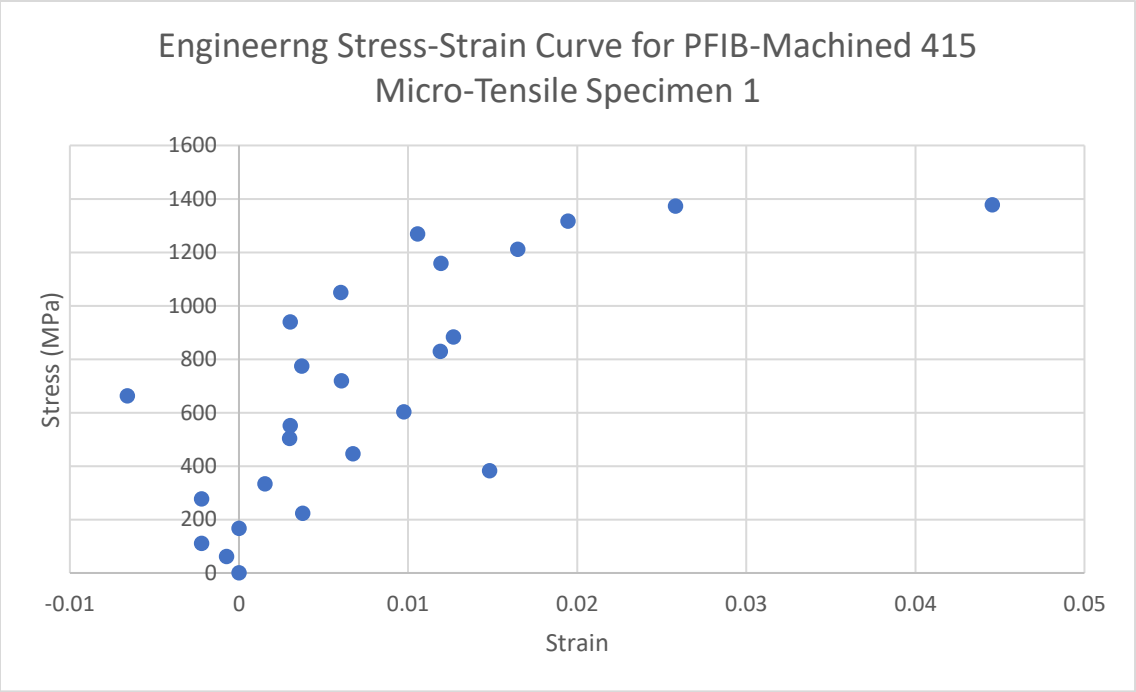

Figure 128: Engineering stress-strain curve for PFIB-machined (non-grain targeted) 415 micro-tensile specimen 1.

7.9. Size of Heat-Affected Zone (HAZ) for 415 Micro-Tensile Specimens

The fs-laser will be used to machine more grain-targeted 415 micro-tensile specimen cutouts in the future. Therefore, it is important to measure the size of the HAZ zone from the fs-laser machining in the 415-steel prior to producing a large number of specimens for mechanical testing. A HAZ zone can be produced through the interaction between the laser irradiation and

the specimen, which causes both chemical and physical changes in the material. When the laser energy is dissipated into the material, a melt pool is formed. The solidification rate of the melt is dependant on the physical properties of material's temperature and the material's thermal diffusivity rate. For example, *Wemanet al., (2003*) discovered that materials with high thermal diffusivity produce a smaller HAZ zone (due to the higher cooling rate of the material) compared to low thermal diffusivity materials where heat dissipates out of the material at a slower speed [55]. In addition, the laser's process parameters of pulse duration, laser fluence, cutting speed, and laser power can also determine the size of the HAZ zone produced.

The pulse duration of the fs-laser is very short and the energy of the laser in the form of heat energy does not typically have enough time to dissipate into the material lattice. Therefore, the fs-laser hypothetically should leave behind a negligible HAZ zone. If a temperature gradient is formed by the laser-material interaction, the process of solidification causes modifications in the microstructure such as grain growth, phase transformations, and variations in the material's hardness.

Experiments in literature have discovered that the fs-laser's process parameters and the physical properties of the specimen material can play a role in how large a HAZ is produced in the material. Through many experiments on the measurement of the HAZ zone in various materials such as copper, aluminum, and low carbon steels, it was discovered that the laser fluence (energy of the laser per unit area illuminated by the laser beam) can determine whether a small or large HAZ zone is formed on the subsurface of the laser-ablated material. For example, it was discovered by *Schnell et al. (2021*) in the fs-laser ablation of Ti6Al4V titanium alloy that self organized features extended several micrometers into the base material from the ablated surfaces at high laser fluence of $4.76\ \frac{J}{cm^2}$ [56]. In addition, there was an increase in chemical composition changes (with new oxidation states introduced) as the laser fluence increased as observed through XRD (X-ray diffraction) and XPS (X-ray photoelectron spectroscopy) analysis of the laser-ablated surface. In addition, a HAZ zone ranging 0.5-3.5 μm for low to high laser fluence was seen in copper in an experimental procedure performed by *Hirayama et al., (2005)* where it extended out to the non-ablated material [57].

In addition, it was discovered that the power and cutting speed of a laser also plays a significant role in determining the size of the HAZ zone produced. In an experiment performed by *Zaied et al., (2013)* on low carbon steel S235, it was determined that a high cutting speed and low power of a high power CO2 laser can minimize the size of the HAZ zone produced in the material [58]. With a high cutting speed, the heat energy from the laser has a shorter period of time to diffuse into the material. In addition, a higher cutting speed reduces roughness of the ablated surface. With a high laser power, the surface of the material heats up and in turn, causes a larger fusion zone between the beam and material interaction. The affect of the CO2 laser's cutting speed and power on the size of the HAZ zone produced in S235 can be seen in plots produced by *Zaied et al., (2013)* in Figure 129. This size of the HAZ zone was measured by *Zaied et al., (2013)* with SEM and optical imaging of the S235 carbon steel cross-section, as seen in Figure 130 [58].

With low carbon steels, it was also discovered by *Lancaster et al., (1987)* that the existence of a HAZ in carbon steels can result to the formation of martensite (or additional formation of finer martensitic laths) when the thermal gradient of the melt undergoes rapid cooling [59]. The result of the martensitic phase change increases the hardness of the material at the localized HAZ zone, which can be undesirable for certain engineering applications. Additionally, grain growth that occurs at the HAZ can cause embrittlement and susceptibility for micro-cracks and crack growth to occur, which was seen in an experiment carried out by *Moskovicet al., (2003)* on a ductile ferritic steel weldment [60].

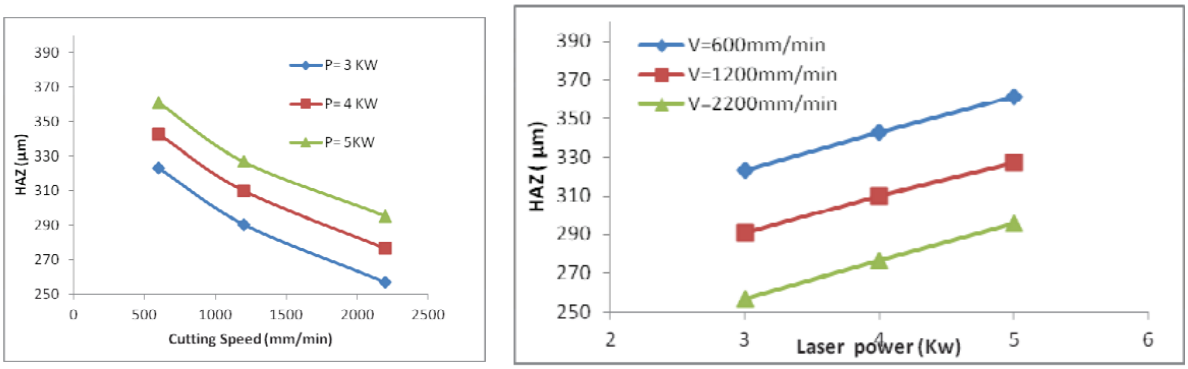

Figure 129: Effect of cutting speed and power of a CO2 laser on the size of the heat effected zone seen in S35 carbon steels (experiments performed by Zaied et al., (2013)) [58].

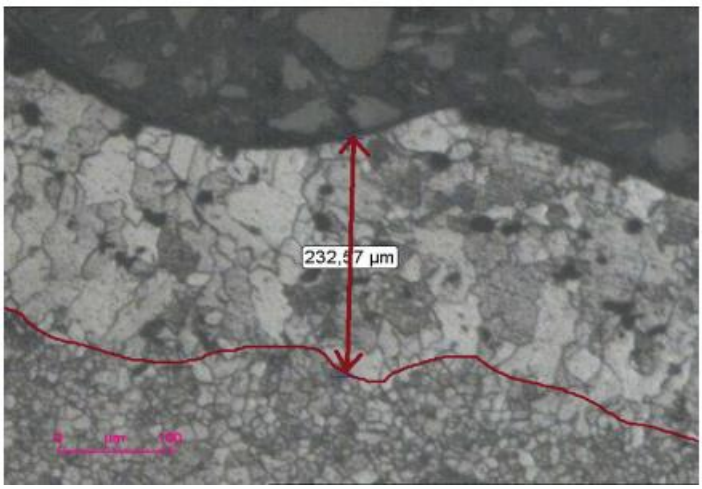

Figure 130: Size of HAZ zone measured for an S35 carbon steel from SEM imaging at CO2 laser-ablated surface (experiment performed Zaied et al., (2013)) [58].

The future process for measuring the size of the HAZ zone for the laser-ablated 415 micro-tensile specimens is through EBSD analysis. The fs-laser from the Zeiss Crossbeam 350 would be used to machine a laser-ablated surface of a prepared 100 µm-thick 415 steel wedge. A laser cut would be made perpendicular to the wedge surface, creating two separate wedge surfaces. The laser's process parameters that will be used to create the laser cut are listed in Table 7. Afterwards, one of the wedge surfaces would be transfer into the dual-beam chamber of the

Helios 5 UXe FIB-SEM microscope, where the analysis of the freshly prepared laser surface and HAZ zone would be analyzed using EBSD analysis. The wedge would be placed on the wafer holder with the cross-section facing normal to the SEM beam when the stage is at a 0-degree tilt configuration to examine the HAZ zone. Afterwards, the position of the stage and specimen would be set up to perform EBSD analysis of the cross-section. A 2D EBSD scan of the cross-section would be produced to determine the grain size difference between the base material and HAZ zone. The width of the HAZ zone would be measured from the EBSD band contrast or IPF maps. The measurement of the HAZ zone would extend from the modified microstructure by the laser and up to the non-laser modified microstructure.

XV. Conclusions

The underlying object of this research project was to develop an efficient and reliable fabrication process for micro-tensile specimens. With the aide of both the plasma-FIB and fs-laser, an optimal fabrication route was developed to be the most time-effieicnt in providing reliable mechanical results from the straining of the micro-tensile specimens. The tensile specimen geometry produced from the optimal fabrication method and instrumental accuracy of the custom-built micro-tensile bench was validated through the machining of micro-tensile specimens made out of (100) single crystal copper. The copper specimens were machined with various gauge thicknesses to determine the exisitence of the mechanical size effect of increasing yield strength with decreasing specimen dimensions. After validating the existence of the mechanical size effect seen in the copper micro-tensile speomens, the tensile specimen geometry and micro-tensile bench were used to fabricate and test specimens made out of the hydro-turbine 415 martensitic stainless. A recipe for targeting grains at the local microstructure of 415 steel for fabricating bicrystal and interphase interface micro-tensile specimens have been developed using electron backscattered diffraction (EBSD) for locating grains of interest. Future work includes the process of producing numerous bicrystal and interphase interface micro-tensile specimens out of the turbine steels used at Hydro-Quebec. The experimental data from the mechanical testing of the micro-tensile specimens would be used to aide researchers at Hydro-Quebec in validating the results of their crystal plasticity finite element models. The future goal for the digital twin models of the steel microstructures is to provide predictiablity on how the material at the microstructure level would deform under immense loads of cycliing stress during operations of the turbines. In addition, the digital twin models can provide insight on improvements that can be made on the composition and thermal processing of the turbine steels to increase the service life of the hydro-turbines.

XVI. References

[1] H. D. Espinosa and B. C. Prorok, “Effects of film thickness on the yielding behavior of Polycrystalline Gold Films,” MRS Proceedings, vol. 695, 2001.

[2] S. Ghosh, C. Woodward, and C. P. Przybyla, *Integrated Computational Materials Engineering (ICME): Advancing Computational and Experimental Methods*. Cham, Switzerland: Springer Nature, 2020.

[3] M. D. Uchic, D. M. Dimiduk, J. N. Florando, and W. D. Nix, "Specimen dimensions influence strength and crystal plasticity," *Science*, vol. 305, no. 5686, pp. 986–989, 2004.

[4] N. Kheradmand and H. Vehoff, "Orientation gradients at boundaries in Micron-sized bicrystals," *Advanced Engineering Materials*, vol. 14, no. 3, pp. 153–161, 2011.

[5] D. Kiener, W. Grosinger, G. Dehm, and R. Pippan, "A further step towards an understanding of size-dependent crystal plasticity: In situ tension experiments of miniaturized single-crystal copper specimens," *Acta Materialia*, vol. 56, no. 3, pp. 580–592, 2008.

[6] V. S. Deshpande, A. Needleman, and E. Van der Giessen, "Plasticity size effects in tension and compression of SCs," *Journal of the Mechanics and Physics of Solids*, vol. 53, no. 12, pp. 2661–2691, 2005.

[7] Z. Zong, J. Lou, O. O. Adewoye, A. A. Elmustafa, F. Hammad, and W. O. Soboyejo, "Indentation size effects in the nano- and micro-hardness of FCC SC Metals," *Materials Science and Engineering: A*, vol. 434, no. 1-2, pp. 178–187, 2006.

[8] Y. Liu and A. H. W. Ngan, "Depth dependence of hardness in copper SCs measured by nanoindentation," *Scripta Materialia*, vol. 44, no. 2, pp. 237–241, 2001.

[9] J. Wang, T. Volz, S. M. Weygand, and R. Schwaiger, "The indentation size effect of single-crystalline tungsten revisited," *Journal of Materials Research*, vol. 36, no. 11, pp. 2166–2175, 2021.

[10] A. Pandey, R. Wheeler, A. Shyam, and T. B. Stoughton, "Onset of plasticity via relaxation analysis (OPRA)," *Experimental Mechanics*, vol. 56, no. 6, pp. 1095–1107, 2016.

[11] S. Lee, J.-H. Kim, T. Ohba, Y. S. Kim, and T.-S. Kim, "A study on mechanical properties of thinned SC silicon wafer: Effect of size and direction," *2018 International Conference on Electronics Packaging and iMAPS All Asia Conference (ICEP-IAAC)*, 2018.

[12] D. Terentyev, A. Bakaev, A. Serra, F. Pavia, K. L. Baker, and N. Anento, "Grain boundary mediated plasticity: The role of grain boundary atomic structure and thermal activation," *Scripta Materialia*, vol. 145, pp. 1–4, 2018.

[13] Y. Kihara, T. Nagoshi, T.-F. M. Chang, H. Hosoda, S. Tatsuo, and M. Sone, "Tensile behavior of micro-sized specimen made of single crystalline nickel," *Materials Letters*, vol. 153, pp. 36–39, 2015.

[14] C. Du, J. P. M. Hoefnagels, L. I. Bergers, and M. G. Geers, "A uni-axial nano-displacement micro-tensile test of individual constituents from bulk material," *Experimental Mechanics*, vol. 57, no. 8, pp. 1249–1263, 2017.

[15] R. LUMLEY, A. MORTON, and I. POLMEAR, "Nanoengineering of metallic materials,"

Nanostructure Control of Materials, pp. 219–250, 2006. doi:10.1533/9781845691189.219

[16] N. Kheradmand, A. Barnoush, and H. Vehoff, "Investigation of the role of grain boundary on the mechanical properties of metals," *Journal of Physics: Conference Series*, vol. 240, p. 012017, 2010.

[17] L. L. Li, Z. J. Zhang, J. Tan, C. B. Jiang, R. T. Qu, P. Zhang, J. B. Yang, and Z. F. Zhang, "Stepwise work hardening induced by individual grain boundary in Cu Bicrystal micropillars," *Scientific Reports*, vol. 5, no. 1, 2015.

[18] D. Terentyev, A. Bakaev, A. Serra, F. Pavia, K. L. Baker, and N. Anento, "Grain boundary mediated plasticity: The role of grain boundary atomic structure and thermal activation," *Scripta Materialia*, vol. 145, pp. 1–4, 2018.

[19] Zhang, Z. F. & Wang, Z. G. Grain boundary effects on cyclic deformation and fatigue damage. Prog. Mater. Sci. 53, 1025–1099 (2008)

[20] Li, L. L., Zhang, Z. J., Zhang, P., Wang, Z. G. & Zhang, Z. F. Controllable fatigue cracking mechanisms of copper bicrystals with a coherent twin boundary. Nat. Commun. 5, 3536 (2014).

[21] C. A. Volkert and A. M. Minor, "Focused ion beam microscopy and micromachining," *MRS Bulletin*, vol. 32, no. 5, pp. 389–399, 2007. doi:10.1557/mrs2007.62

[22] N. S. Smith, J. A. Notte, and A. V. Steele, "Advances in source technology for focused ion beam instruments," *MRS Bulletin*, vol. 39, no. 4, pp. 329–335, 2014. doi:10.1557/mrs.2014.53

[23] N. Bassim, K. Scott, and L. A. Giannuzzi, "Recent advances in focused ion beam technology and applications," *MRS Bulletin*, vol. 39, no. 4, pp. 317–325, 2014. doi:10.1557/mrs.2014.52

[24] N. Bassim and J. Notte, "Focus Ion Beam Instruments," in ASM Handbook: Volume 10

Materials Characterization, vol. 10, Ohio: ASM International, 1986, pp. 636–670.

[25] J. Liu *et al.*, "Effect of ion irradiation introduced by focused ion-beam milling on the mechanical behaviour of sub-micron-sized samples," *Scientific Reports*, vol. 10, no. 1, 2020. doi:10.1038/s41598-020-66564-y

[26] A. E. Mayer, V. S. Krasnikov, and V. V. Pogorelko, "Homogeneous nucleation of dislocations in copper: Theory and approximate description based on molecular dynamics and

Artificial Neural Networks," *Computational Materials Science*, vol. 206, p. 111266, 2022. doi:10.1016/j.commatsci.2022.111266

[27] H.X. Qian et al., Appl. Surf. Sci. 240, 140 (2005).

[28] X. Zhong *et al.*, "Comparing XE + pfib and ga + fib for Tem sample preparation of Al Alloys: Minimising fib-induced artefacts," *Journal of Microscopy*, vol. 282, no. 2, pp. 101–112, 2020. doi:10.1111/jmi.12983

[29] B. Tordoff *et al.*, "The LaserFIB: New Application Opportunities Combining a high-performance FIB-SEM with femtosecond laser processing in an integrated second chamber," *Applied Microscopy*, vol. 50, no. 1, 2020. doi:10.1186/s42649-020-00044-5

[30] M. P. Echlin, A. Mottura, C. J. Torbet, and T. M. Pollock, "A new TriBeam system for three-dimensional multimodal materials analysis," *Review of Scientific Instruments*, vol. 83, no. 2, 2012. doi:10.1063/1.3680111

[31] A. R. Neale *et al.*, "Electrochemical performance of laser micro-structured nickel oxyhydroxide cathodes," *Journal of Power Sources*, vol. 271, pp. 42–47, 2014. doi:10.1016/j.jpowsour.2014.07.167

[32] "LaserFIB for Zeiss crossbeam," LaserFIB for ZEISS Crossbeam. [Online]. Available:

https://www.zeiss.com/microscopy/int/cmp/mat/20/nanomaterials/fslaser/laserfib.html?utm_sour

ce=googleppc&utm_medium=search&utm_campaign=ft-nanomaterials-laserfib2020&gclid=Cj0KCQiA4b2MBhD2ARIsAIrcB-RWsC5VEPzqXUcedmH5N5xZF3otiPyPMMP7Q259OyPuZTKib_6yPMaAiUeEALw_wcB. [Accessed: 03-Dec2021].

[33] N. Nishimura, C. B. Schaffer, and D. Kleinfeld, "In vivo manipulation of biological systems with femtosecond laser pulses," *SPIE Proceedings*, 2006. doi:10.1117/12.668886

[34] J. G. Gigax *et al.*, "Micropillar compression response of femtosecond laser-cut single crystal CU and Proton irradiated Cu," *Scripta Materialia*, vol. 170, pp. 145–149, 2019. doi:10.1016/j.scriptamat.2019.05.004

[35] M. A. Chilbert *et al.*, "Effects of intensity and fluence upon DNA single-strand breaks induced by excimer laser radiation," *Photochemistry and Photobiology*, vol. 47, no. 4, pp. 523–525, 1988. doi:10.1111/j.1751-1097.1988.tb08839.x

[36] O. Armbruster, A. Naghilou, M. Kitzler, and W. Kautek, "Spot size and pulse number dependence of femtosecond laser ablation thresholds of silicon and stainless steel," *Applied Surface Science*, vol. 396, pp. 1736–1740, 2017. doi:10.1016/j.apsusc.2016.11.229

[37] I. A. Salimon, S. Mailis, A. I. Salimon, E. Skupnevskiy, S. A. Lipovskikh, I. Shakhova, A. V.

Novikov, T. F. Yagafarov, and A. M. Korsunsky, "FIB-SEM investigation of laser-induced

periodic surface structures and conical surface microstructures on D16t (AA2024-T4) alloy,"

Femtosecond Laser FIB-SEM

[38] W. Liu *et al.*, "Manipulation of LIPSS orientation on silicon surfaces using orthogonally polarized femtosecond laser double-pulse trains," *Optics Express*, vol. 27, no. 7, p. 9782, 2019. doi:10.1364/oe.27.009782

[39] M. J. Pfeifenberger *et al.*, "The use of femtosecond laser ablation as a novel tool for rapid micro-mechanical sample preparation," *Materials & Design*, vol. 121, pp. 109–118, 2017. doi:10.1016/j.matdes.2017.02.012

[40] T. Voisin *et al.*, "Tem sample preparation by femtosecond laser machining and ion milling for high-rate tem straining experiments," *Ultramicroscopy*, vol. 175, pp. 1–8, 2017. doi:10.1016/j.ultramic.2016.12.001

[41] D. W. Eastman, P. A. Shade, M. D. Uchic, and K. J. Hemker, "Microscale testing and characterization techniques for benchmarking crystal plasticity models at microstructural length scales," *Integrated Computational Materials Engineering (ICME)*, pp. 91–125, 2020. doi:10.1007/978-3-030-40562-5_4

[42] H. Sönnerlind, "What is the difference between plane stress and plane strain?," *COMSOL*, 20-May-2021. [Online]. Available: https://www.comsol.com/blogs/what-is-the-difference-between-plane-stress-and-plane-strain. [Accessed: 02-Oct-2022].

[43] "Test Methods for Tension Testing of Metallic Materials," *ASTM International (Standard E8/E8M)*, Jun. 2012.

[44] L. U. 2023, "How do ultrasonic cleaners work: 7 things you should know," L&R Ultrasonics, https://www.lrultrasonics.com/blog/post/7-things-you-should-know-about-ultrasonic-cleaners#:~:text=The%20Frequency%20of%20Ultrasonic%20Cleaning&text=Most%20ultrasonic%20cleaning%20occurs%20around,and%20more%20detailed%20cleaning%20action. (accessed Aug. 30, 2023).

[45] tec-science Tec-Science, "Deformation process in single crystals - tec-science," tec-science, https://www.tec-science.com/material-science/ductility-of-metals/deformation-process-in-single-crystals-stress-strain-curve/ (accessed Aug. 30, 2023).

[46] "Chapter II. Linear Elasticity," *An Introduction to Modern Anistropic Elasticity*, 1998. doi:10.1615/1-56700-107-6.85

[47] "Hooke's Law," Hooke's law, http://labman.phys.utk.edu/phys221core/modules/m3/Hooke%27s%20law.html#:~:text=The%20force%20exerted%20by%20a,directed%20towards%20its%20equilibrium%20position.&text=F%20%3D%20%2Dkx.,is%20called%20the%20spring%20constant. (accessed Aug. 31, 2023).

[48] S. Shoja, O. Alm, S. Norgren, H.-O. Andrén, and M. Halvarsson, “Calculated and experimental Schmid factors for chip flow deformation of textured CVD α-alumina coatings,” *Surface and Coatings Technology*, vol. 412, p. 126991, 2021. doi:10.1016/j.surfcoat.2021.126991

[49] Department of Materials Science and Metallurgy - University of Cambridge, “Slip in Single Crystals (All Content),” Cambridge University, https://www.doitpoms.ac.uk/tlplib/slip/printall.php (accessed Aug. 31, 2023).

[50] Department of Materials Science and Metallurgy - University of Cambridge, “Slip geometry: the critical resolved shear stress,” Cambridge University, https://www.doitpoms.ac.uk/tlplib/slip/slip_geometry.php (accessed Aug. 31, 2023).

[51] Libretexts, “7.5: Climb and cross slip,” Engineering LibreTexts, https://eng.libretexts.org/Bookshelves/Materials_Science/TLP_Library_II/7%3A_Mechanisms_of_Plasticity/7.5%3A_Climb_and_Cross_Slip (accessed Aug. 31, 2023).

[52] T. Takeuchi, “Work hardening of copper single crystals with multiple glide orientations,” *Transactions of the Japan Institute of Metals*, vol. 16, no. 10, pp. 629–640, Feb. 1975. doi:10.2320/matertrans1960.16.629

[53] Y. Mine, K. Hirashita, H. Takashima, M. Matsuda, and K. Takashima, “Micro-tension behaviour of lath martensite structures of Carbon Steel,” *Materials Science and Engineering: A*, vol. 560, pp. 535–544, Oct. 2012. doi:10.1016/j.msea.2012.09.099

[54] [Y. Mine, K. Koga, O. Kraft, and K. Takashima, “Mechanical characterisation of hydrogen-induced quasi-cleavage in a metastable austenitic steel using micro-tensile testing,” *Scripta Materialia*, vol. 113, pp. 176–179, Mar. 2016. doi:10.1016/j.scriptamat.2015.11.013

[55] K. Weman, Welding Process Handbook. CRC Press LLC, New York. (2003).

[56] G. Schnell *et al.*, “Heat accumulation during femtosecond laser treatment at high repetition rate – a morphological, chemical and crystallographic characterization of self-organized

structures on ti6al4v," *Applied Surface Science*, vol. 570, p. 151115, Dec. 2021. doi:10.1016/j.apsusc.2021.151115

[57] Y. Hirayama and M. Obara, "Heat-affected zone and ablation rate of copper ablated with femtosecond laser," *Journal of Applied Physics*, vol. 97, no. 6, 2005. doi:10.1063/1.1852692

[58] M. Zaied, I. Miraoui, M. Boujelbene, and E. Bayraktar, "Analysis of heat affected zone obtained by CO2 laser cutting of Low Carbon Steel (S235)," *AIP Conference Proceedings*, Dec. 2013. doi:10.1063/1.4849285

[59] J. F. Lancaster, Metallurgy of Welding: The Mechanical Properties of the Heat Affected Zone. 4th Edition, Allen and University, London.p45. (1987).

[60] R. Moskovic, N. O. Dowd and P. Flewitt, Experimental and Numerical Study of Crack Growth in the Heat-AffectedZone of a Ferritic Steel Weldment, Transactions of the 17th International Conference on Structural Mechanics in Reactor Technology (2003).

[61] "Iron alloy," MakeItFrom.com, https://www.makeitfrom.com/material-properties/AISI-415-S41500-Stainless-Steel (accessed Sep. 4, 2023).

[62] A. Basavalingappa, M. Y. Shen, and J. R. Lloyd, "Modeling the copper microstructure and elastic anisotropy and studying its impact on reliability in nanoscale interconnects," *Mechanics of Advanced Materials and Modern Processes*, vol. 3, no. 1, 2017. doi:10.1186/s40759-017-0021-5

[63] P.-A. Deschênes *et al.*, "Micromechanical properties of low-carbon martensitic stainless steel by microtensile experiments," *Materials Science and Engineering: A*, vol. 858, p. 144030, Jun. 2022. doi:10.1016/j.msea.2022.144030

[64] Defining a Multilinear Plasticity Hardening Model Using Ansys Mechanical — Lesson 1. YouTube, 2020.

XVII. Appendix

A1. 2D 1-Element Model (Linear Elastic) Stress-Strain Calculations for (100) Copper

Material Assignment: (100) Copper

Applied Load: 3.01 N

Length: 1 mm

Width: 1 mm

Thickness: 0.0123 mm

With Applied Load Force:

Cross-Sectional Area: 1 mm x 0.0123 mm= 0.0123 mm^2

$$\sigma = \frac{F}{A}$$

$$\sigma = \frac{3.01\ N}{0.0123\ mm^2}$$

$$\sigma = 244.28\ MPa$$

$\sigma = \varepsilon E$ (Hooke's Law)

$$\varepsilon = \frac{\sigma}{E}$$

$$\varepsilon = \frac{244.28\ MPa}{66700\ MPa}$$

$$\varepsilon = 3.66x10^{-3}\frac{mm}{mm}$$

ANSYS results:

$\varepsilon = 3.662x10^{-3}$ mm/mm

$\sigma = 244.28\ MPa$

With Applied Displacement Load:

$$\Delta l_y = \varepsilon_y l_{0y}$$

$$\Delta l_y = \left(3.66x10^{-3}\ \frac{mm}{mm}\right)(1\ mm) = 3.66x10^{-3}mm$$

$$U = \frac{x}{l_{0x}}\Delta U = \frac{3.66x10^{-3}mm}{1\ mm} = 3.66x10^{-3}\frac{mm}{mm}$$

$$V = -v\Delta U\frac{y}{l_{0x}} = -0.42\left(\frac{3.66x10^{-3}mm}{1\ mm}\right) = -1.54x10^{-3}\ \frac{mm}{mm}$$

A2. Young's Modulus and Poisson's Ratio Plots for 2D Tensile Specimen Half Model (With Free-End)

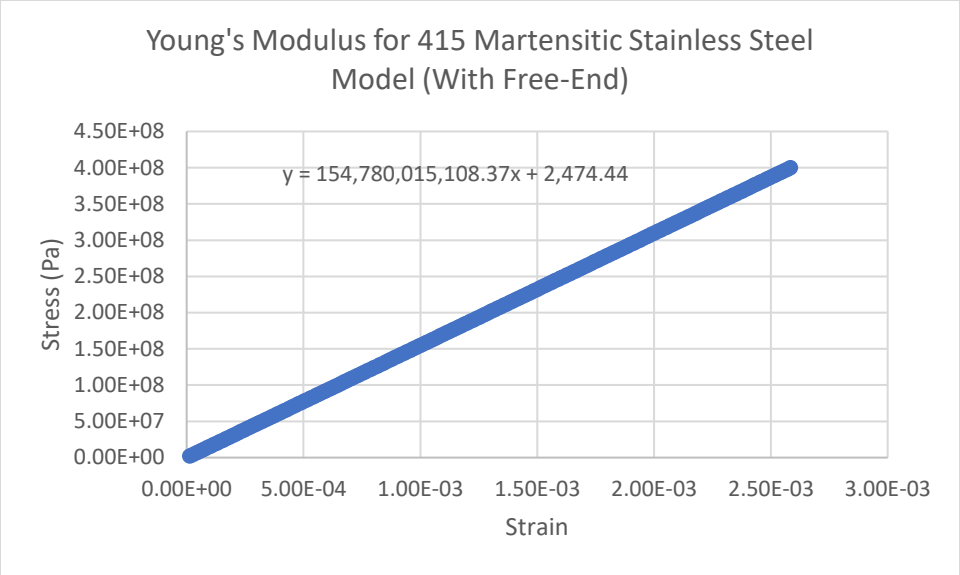

Figure 131: Model results for the Young's Modulus value exhibited by the 2D micro-tensile specimen half model (without the wedge component) simulated in pure tension under the assigned material properties of 415 martensitic stainless steel.

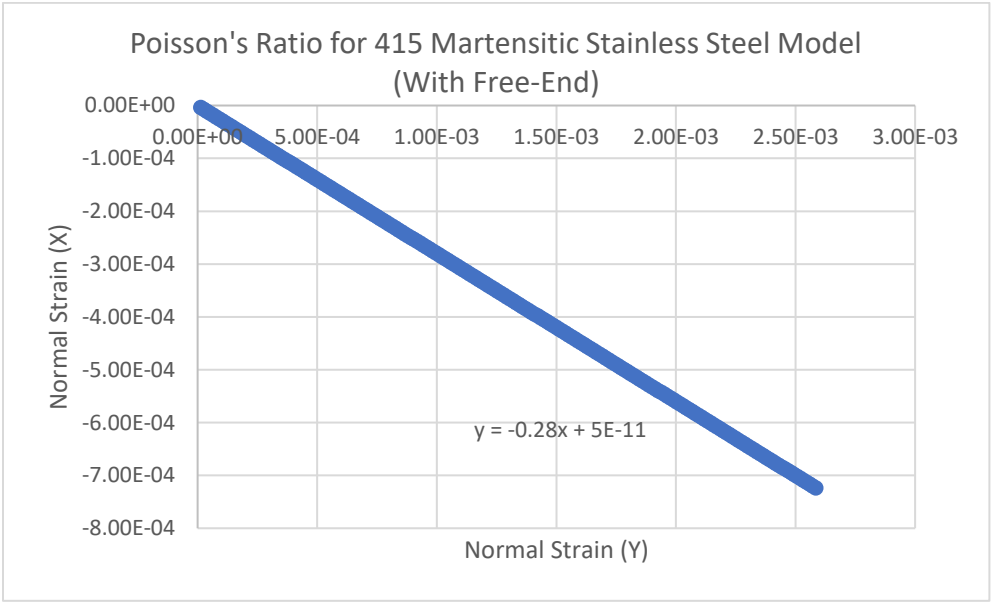

Figure 132: Model results for the Poisson's ratio exhibited by the 2D micro-tensile specimen half model (without the wedge component) simulated in pure tension under the assigned material properties of 415 martensitic stainless steel.

A3. Experimental Plastic Strain Data for ANSYS Multilinear Isotropic Plasticity Hardening Model

Table 13: Experimental data of true plastic strain and corresponding stress values for 415 martensitic stainless steel.

True Stress (Pa)	True Plastic Strain (μm/μm)
$5.08x10^{8}$	0
$5.32x10^{8}$	$2.30x10^{-4}$
$5.58x10^{8}$	$4.68x10^{-4}$
$6.07x10^{8}$	$9.63x10^{-4}$
$6.11x10^{8}$	$1.74x10^{-3}$
$6.35x10^{8}$	$1.99x10^{-3}$
$6.61x10^{8}$	$3.03x10^{-3}$
$6.81x10^{8}$	$4.11x10^{-3}$
$7.07x10^{8}$	$5.55x10^{-3}$
$7.31x10^{8}$	$7.40x10^{-3}$
$7.52x10^{8}$	$8.87x10^{-3}$
$7.69x10^{8}$	$1.08x10^{-2}$
$7.86x10^{8}$	$1.30x10^{-2}$
$8.02x10^{8}$	$1.49x10^{-2}$
$8.11x10^{8}$	$1.69x10^{-2}$
$8.21x10^{8}$	$2.00x10^{-2}$
$8.24x10^{8}$	$2.23x10^{-2}$
$8.27x10^{8}$	$2.46x10^{-2}$

Table 14: Experimental data of true plastic strain and corresponding stress values for (100) copper.

True Stress (Pa)	True Plastic Strain (μm/μm)
$7.23x10^{7}$	0
$8.72x10^{7}$	$8.40x10^{-3}$
$9.37x10^{7}$	$1.61x10^{-2}$
$1.01x10^{8}$	$1.74x10^{-2}$
$1.09x10^{8}$	$2.12x10^{-2}$
$1.15x10^{8}$	$2.16x10^{-2}$
$1.23x10^{8}$	$2.53x10^{-2}$
$1.31x10^{8}$	$2.72x10^{-2}$
$1.46x10^{8}$	$3.47x10^{-2}$
$1.54x10^{8}$	$4.19x10^{-2}$
$1.63x10^{8}$	$4.95x10^{-2}$
$1.70x10^{8}$	$5.28x10^{-2}$
$1.78x10^{8}$	$5.46x10^{-2}$
$1.87x10^{8}$	$6.61x10^{-2}$
$2.04x10^{8}$	$7.95x10^{-2}$
$2.13x10^{8}$	$8.90x10^{-2}$
$2.22x10^{8}$	$1.06x10^{-1}$
$2.35x10^{8}$	$1.23x10^{-1}$
$2.44x10^{8}$	$1.33x10^{-1}$

A4. Mechanical Testing Results

Table 15: Strain Copper Tensile Specimens and Their Corresponding Measured Yield-Stress Value.

Specimen	Gauge Thickness (μm)	Measured Yield Stress (MPa)
Laser-Wedge 3-Sample 1	33.92	137.5693
Laser-Wedge 3-Sample 3	30.06	75.10282
Laser-Wedge 3-Sample 2	32.32	114.2468
Laser-Wedge 3-Sample 4	29.29	66.39341
Laser-Wedge 3-Sample 5	29.71	87.61081
Laser-Wedge 3-Sample 6	26.56	83.62021
Laser-Wedge 1-Sample 2	4.384	199.8575
Laser-Wedge 1-Sample 3	6.266	194.9467
Laser-Wedge 1-Sample 6	5.811	179.2946
Laser-Wedge 4-Sample 5	16.52	119.1508
Laser-Wedge 4-Sample 6	19.42	101.3572
Laser-Wedge 4-Sample 3	19.51	101.7723
Laser-Wedge 4-Sample 1	18.26	119.9816
Laser-Wedge 2-Sample 1	10.38	150.303
Laser-Wedge 2-Sample 3	9.131	231.28
Laser-Wedge 2-Sample 4	12.87	94.15273
Laser-Wedge 2-Sample 6	9.588	168.7899
Laser-Wedge 2-Sample 5	12.87	109.8039
PFIB-Wedge 1-Sample 1	19.1	85.12189
PFIB-Wedge 1-Sample 2	20.04	98.23137
PFIB-Wedge 1-Sample 3	13.49	109.9286
PFIB-Wedge 1-Sample 4	18.5	89.04168
PFIB-Wedge 1-Sample 5	18.5	108.8846
PFIB-Wedge 1-Sample 6	14.11	119.6825
PFIB-Wedge 1-Sample 7	15.42	126.3044
PFIB-Wedge 1-Sample 8	18.14	103.3069
PFIB-Wedge 1-Sample 9	12.33	92.06022
PFIB-Wedge 1-Sample 10	20.81	83.77632
PFIB-Wedge 3-Sample 1	26.21	77.75544
PFIB-Wedge 3-Sample 2	25.44	104.0394
PFIB-Wedge 3-Sample 3	31.6	53.79653
PFIB-Wedge 2-Sample 6	12.33	109.6074